Search for new phenomena in events with a highly energetic jet and missing transverse momentum with the ATLAS detector[a]

Cora Fischer

Ph.D. thesis

Institut de Física d'Altes Energies
Universitat Autònoma de Barcelona
Departament de Física
Facultat de Ciències
Edifici Cn E-08193 Bellaterra (Barcelona)

Programa de doctorat en Física

June 2017

supervised by:
Prof. Dr. Mario Martínez Pérez
Institució Catalana de Recerca i Estudis Avançat
Institut de Física d'Altes Energies
Universitat Autònoma de Barcelona
Edifici Cn E-08193 Bellaterra (Barcelona)

CERN-THESIS-2017-219
25/09/2017

[a] Ph.D. dissertation

Contents

1 Introduction **1**

2 The Standard Model of Particle Physics **3**
2.1 Particle Content . . . 3
2.2 Fundamental Interactions . . . 4
2.2.1 The Strong Interaction . . . 5
2.2.2 The Electroweak Interaction . . . 6
2.3 Electroweak Symmetry Breaking . . . 8
2.4 Open Questions in the SM . . . 10

3 Theories Beyond The Standard Model **13**
3.1 Extra Spatial Dimensions . . . 13
3.1.1 The Arkani-Hamed Dimopoulus Dvali Model . . . 14
3.2 Supersymmetry . . . 16
3.2.1 The Hierarchy Problem . . . 16
3.2.2 Basic Theory . . . 17
3.2.3 SUSY Breaking . . . 20
3.2.4 Collider Phenomenology . . . 21
3.3 Dark Matter . . . 22
3.3.1 Experimental Evidence . . . 22
3.3.2 Effective Field Theories . . . 27
3.3.3 Simplified Models . . . 28

4 Hadron Collider Physics **31**
4.1 Parton Distribution Functions . . . 31
4.2 Monte Carlo Simulation . . . 33
4.2.1 Monte Carlo Integration . . . 33
4.2.2 Event Generation . . . 34
4.2.3 Detector Simulation . . . 38
4.3 Monte Carlo Generators . . . 39

5 Experimental Setup **41**
5.1 The Large Hadron Collider . . . 41
5.1.1 Luminosity . . . 41
5.2 The ATLAS Detector . . . 43
5.2.1 Coordinate System . . . 43
5.2.2 The Inner Detector . . . 44
5.2.3 The Calorimeters . . . 46
5.2.4 The Muon Spectrometer . . . 49
5.2.5 The Magnet System . . . 50
5.2.6 Performance Goals . . . 51
5.2.7 The Trigger System . . . 51

5.2.8 Computing Facilities and Data Quality . . . 52

6 Object Definition **53**
6.1 Tag-and-Probe Method . . . 53
6.2 Vertex Reconstruction and Impact Parameters . . . 53
6.3 Electrons . . . 54
6.4 Photons . . . 55
6.5 Muons . . . 57
6.6 Jets . . . 58
6.6.1 Jet Reconstruction . . . 58
6.6.2 Jet Calibration . . . 59
6.6.3 b-tagging . . . 63
6.7 Overlap Removal . . . 65
6.8 Missing Transverse Momentum . . . 65

7 The Monojet Analysis **69**
7.1 Event Signature . . . 69
7.1.1 Analyses in ATLAS . . . 70
7.2 Data Sample . . . 72
7.3 Event Selection . . . 73
7.4 Background Processes . . . 74
7.4.1 V+jets Background . . . 74
7.4.2 Top-Quark Background . . . 74
7.4.3 Multijet Background . . . 75
7.4.4 Diboson Background . . . 75
7.4.5 Non-Collision Background . . . 75
7.5 Background Modelling . . . 75
7.6 Analysis Strategy . . . 77
7.6.1 Higher Order QCD and Electroweak Corrections . . . 78
7.6.2 Definition of Control Regions . . . 81
7.6.3 Multijet Background Estimation . . . 84
7.6.4 Non-Collision Background Estimation . . . 85
7.7 Statistical Analysis . . . 87
7.7.1 Maximum Likelihood Method . . . 87
7.7.2 Monojet Analysis Fit Model . . . 87
7.7.3 Inclusion of Uncertainties . . . 89
7.7.4 Different Fit Configurations . . . 89
7.7.5 Hypothesis Testing . . . 91
7.8 Systematics Uncertainties . . . 92
7.8.1 Experimental Uncertainties . . . 93
7.8.2 Modelling/Theoretical Uncertainties . . . 96
7.9 Pre-Fit Distributions . . . 100
7.9.1 Distributions in CR1e . . . 102
7.9.2 Distributions in CR1m . . . 105
7.9.3 Distributions in CR2m . . . 108
7.9.4 Distributions in CRtop . . . 111

8 Results **115**
8.1 Background-Only Fit . . . 115
8.1.1 Fit Parameters . . . 115
8.1.2 Post-Fit Distributions: Control Regions . . . 118
8.1.3 Background Estimation in the Signal Region . . . 129
8.1.4 Impact of Individual Uncertainties . . . 130
8.2 Goodness of Fit . . . 137
8.2.1 Post-Fit Distributions: Signal Region . . . 138
8.3 Model-Independent Limits . . . 140

9 Interpretation **143**
9.1 Extra Dimensions . . . 143
9.1.1 Signal Modelling . . . 143
9.1.2 Signal Uncertainties . . . 144
9.1.3 Exclusion Limits . . . 144
9.2 Squark Production in Compressed Scenarios . . . 146
9.2.1 Signal Modelling . . . 146
9.2.2 Signal Uncertainties . . . 147
9.2.3 Exclusion Limits . . . 147
9.3 Dark Matter Production . . . 150
9.3.1 Signal Modelling . . . 150
9.3.2 Signal Uncertainties . . . 151
9.3.3 Exclusion Limits . . . 151
9.4 Background Probability and Discovery Potential . . . 153

10 Summary and Conclusion **157**

A Additional Material/Studies **159**
A.1 Event Yields After CR-only Fit . . . 159
A.2 Limits on Alternative Dark Matter Models . . . 161
A.3 Inclusion of a γ+jets Control Region in the Likelihood Model . . . 161
A.4 TileCal Correction Tool . . . 167

B The 2015 Monojet Analysis **171**
B.1 Strategy . . . 171
B.2 Systematic Uncertainties . . . 173
B.3 Results . . . 173
B.4 Interpretations . . . 176
B.4.1 Signal Models . . . 177
B.5 Conclusion . . . 182

C On the WIMP Signal Interpretation using EFT **183**
C.1 Effective Field Theory and Truncation . . . 183
C.2 Simplified Models in Comparison with EFT . . . 187

D The ATLAS Tile Calorimeter **191**
D.1 Minimum Bias Data . . . 191
D.2 Luminosity Monitoring . . . 192

D.3 Irradiation Studies 193
D.3.1 Irradiation studies in 2015 195
D.3.2 Irradiation studies in 2016 196
D.4 Conclusion 197

Bibliography **203**

Chapter 1

Introduction

The Large Hadron Collider (LHC) at CERN is a machine that accelerates protons to almost the speed of light and brings them to collisions. In these high energetic collisions, particles can be produced that otherwise do not exist in nature. These particles and the interactions between them are explored in high energy physics research at the LHC. In 2012, the *Higgs boson* was discovered by the analysis teams of ATLAS and CMS [1, 2]. The Higgs boson was the last fundamental particle predicted by the Standard Model (SM) to be discovered. The SM is a theory developed in the 1970s that up to now has successfully described the fundamental particles and their interactions, and the Higgs boson was the last missing piece to complete the theory. The SM could not be disproven in any experiments up to now, however, theoretical considerations of naturalness and most importantly, cosmological and astrophysical observations call for theories beyond the SM (BSM). These theories seek answers to the questions on the nature of *dark matter*, *dark energy*, the matter−anti-matter asymmetry, etc.. Among those, the theory of *Supersymmetry* (SUSY) is the most appealing one: it predicts additional 'partner' particles to the known fundamental particles. Thereby SUSY is able to provide a candidate for dark matter and a natural solution to the *hierarchy problem*. Many more theories exist, among them *Large Extra Dimensions*, in an attempt to include the gravitational force into the quantum field theory. The additional particles predicted by these theories can potentially be produced at the LHC. Therefore, a wide physics program is pursued at both ATLAS and CMS in order to discover these particles. Most anticipated are scenarios, where new particles produced leave the detector untraced since they only interact weakly with the detector material. Therefore, if other visible objects recoil against these particles, there will be a momentum imbalance measured, called *missing transverse momentum*. The objects most prominent in hadron collision final states are jets. The monojet analysis searches for jets recoiling against invisible particles. It is a search for an additional abundance of events with high missing transverse momentum over a rapidly decreasing background of SM production. Many models can be searched for with such a final state. This makes this analysis very powerful, since it enables to explore the highest regions of missing transverse momentum where signals from new theories are easier distinguished from backgrounds. With the advent of a highly increased dataset and a high centre-of-mass energy of 13 TeV, the LHC is more likely than ever to discover new particles if they actually exist in nature.
This thesis is devoted to the monojet search using proton-proton collisions at $\sqrt{s} = 13$ TeV. Two analyses were carried out based on the data collected by the ATLAS experiment. The first analysis used 3.2 fb^{-1} of data collected in 2015 and the second analysis is based on the full 2015+2016 dataset with a total integrated luminosity of 36.1 fb^{-1} and constitutes the main body of this thesis.

The thesis is organised as follows: Chapter 2 introduces the theoretical framework of the SM and poses some questions that are not answered within. Theories beyond the SM are introduced in Chapter 3 along with their expected phenomenology in collider experiments. The physics of

hadron colliders is described in Chapter 4. The experimental setup of the ATLAS detector is presented in Chapter 5. The objects measured in ATLAS have to be classified and their definition and use in the analysis is explained in Chapter 6. The monojet analysis is introduced in Chapter 7 along with its signature, former analyses' results and the strategy followed in this thesis. It contains the statistical fit model including uncertainties of the measurement as well as pre-fit event yields and kinematic distributions. The results of a background-only fit are presented and discussed in Chapter 8. These are finally interpreted in terms of BSM scenarios including the ADD model of large extra dimensions, SUSY compressed scenarios and dark matter models and 95% CL limits on these are discussed in Chapter 9. A summary and conclusion can be found in Chapter 10.
This thesis is complemented with a number of appendices related to both detector and analysis aspects. In particular, appendix B presents a summary of the 2015 monojet analysis carried out with a dataset of 3.2 fb^{-1}.

The material presented in this thesis contributed to the following publications:

- *Search for new phenomena in final states with an energetic jet and large missing transverse momentum in pp collisions at* $\sqrt{s} = 13$ *TeV using the* ATLAS *detector* (Physical Review D **94**, 032005 (2016)).
- *Dark matter benchmark models for early* LHC *Run-2 searches: Report of the* ATLAS/CMS *dark matter forum* (arXiv.1507.00966, 2015).
- *Search for dark matter and other new phenomena in events with an energetic jet and large missing transverse momentum using the* ATLAS *detector* (ATLAS-CONF-2017-060), submitted for publication to JHEP.

Chapter 2

The Standard Model of Particle Physics

This chapter introduces the theoretical basics of the Standard Model of Particle Physics (SM). The SM is up to now the model known to describe experimental data best and no significant deviations from SM predictions have been found to date. The fundamental particles and forces that are described within the SM are shortly presented here as well as the mechanism of electroweak symmetry breaking that predicts a scalar boson in the SM, the so-called *Higgs boson*. This particle represented the last missing piece of the SM and was discovered in 2012 [1, 2]. Although no deviations from SM predictions have been found so far, studies to test the SM still continue as the SM does not satisfactorily describe all observations and leaves some open questions. To address these questions and provide solutions new theories have been developed that are commonly referred to as Beyond the Standard Model (BSM) theories. Selected BSM theories, relevant for this thesis, will be described in Chap. 3.

The SM is a theory that has been developed by various physicists mainly in the 1960s and 1970s [3–7]. The SM describes the elementary particles - point-like particles with no further substructure - and the interactions between them. The SM does not predict the fundamental particles but it rather incorporates the particles we know up to now in a common theoretical framework. The particle content of the SM is introduced in Sec. 2.1, the three fundamental forces described within the SM are introduced in Sec. 2.2. As a fourth force gravity exists, but it is not described within the SM since there is no complete theory description of it up to date. Due to its weakness it does not play a role in high energy collider physics and will therefore not be discussed here further.

2.1 Particle Content

The elementary particles in the SM are grouped in *fermions* with spin $s = 1/2$ and *bosons* with integer spins. The fermions are the matter particles and the spin-1 bosons are the so-called *gauge bosons* that mediate the three forces (see next Sec. 2.2). The fermions are arranged in three generations and are divided into *leptons* and *quarks*. The visible matter is made up of particles belonging to the first generation: the *up* and *down* quarks form protons and neutrons, the constituents of atomic nuclei. The charged electrons e^- together with the nuclei form atoms. The second and third generations of quarks and leptons can only be produced in collision experiments or high-energetic cosmic showers and are not stable. They differ from the first generation by increasing masses of the particles. In total there are six different *flavours* of quarks: *up (u), down (d), charm (c), strange (s), top (t)* and *bottom (b)*. The electron is accompanied by an electrically neutral neutrino, the electron-neutrino ν_e, which is the weak isospin partner of the electron (see Sec. 2.2). The muon (μ) and muon-neutrino (ν_μ), the tau (τ) and the tau-neutrino (ν_τ) make up the second and third lepton generation, respectively, and only differ from the first generation by increasing mass of the charged leptons. The leptons carry *lepton numbers* L_e, L_μ

and L_τ according to their lepton family. The fundamental fermions together with their charge and measured masses are given in Tab. 2.1. All particles are accompanied by their anti-particles which have the same spin and masses but opposite electric charges (except for the neutrinos) and are denoted by a bar, e. g.: the $\bar{t}$ is the anti-particle of the top-quark. The generations of fermions

	Quarks			**Leptons**		
Generation	Symbol	$Q[e]$	Mass [MeV/c^2]	Symbol	Q [e]	Mass [MeV/c^2]
1	u	$+\frac{2}{3}$	$2.3^{+0.7}_{-0.5}$	ν_e	0	$< 2.2 \cdot 10^{-6}$
	d	$-\frac{1}{3}$	$4.8^{+0.5}_{-0.3}$	e^-	-1	0.511
2	c	$+\frac{2}{3}$	$(1.275 \pm 0.025) \cdot 10^3$	ν_μ	0	< 0.170
	s	$-\frac{1}{3}$	95 ± 5	μ^-	-1	105.7
3	t	$+\frac{2}{3}$	$(173.21 \pm 0.87) \cdot 10^3$	ν_τ	0	< 18.2
	b	$-\frac{1}{3}$	$(4.18 \pm 0.03) \cdot 10^3$	τ	-1	1776.82 ± 0.16

Tab. 2.1: The generations of quarks and leptons, their charge Q in units of e and their measured masses [8]. Upper limits on neutrino masses are given at 95% CL from Ref.[9, 10] (ν_e), Ref. [11] (ν_μ) and Ref. [12] (ν_τ).

follow a striking mass hierarchy. The masses span a range of about 9 orders of magnitude, where the top-quark is by far the heaviest fermion. In the SM, neutrinos are considered to be massless. But experimental findings of neutrino oscillations require neutrinos to have masses (see e. g. [13–17]). In Tab. 2.1, upper limits on the neutrino masses from direct mass measurements are given. Besides the described fermions, the SM also incorporates force carriers, the gauge bosons γ, the photon, g, the gluons and $W^\pm, Z^0$, the *weak* bosons[a]. These bosons mediate different forces and will be further described in the next section.

2.2 Fundamental Interactions

Three fundamental forces, the electromagnetic, weak and strong force, are described within the SM. They are mediated by gauge bosons. The gauge bosons gather their name from the basic principle through which they emerge in the theory: the requirement of the Lagrangian $\mathscr{L}$, that mathematically describes the particles and interactions, to be invariant under *local* gauge transformations. This requirement can only be met if additional terms are introduced into $\mathscr{L}$ that contain the fields of the gauge bosons. All particles and mediators are described by quantised fields in the framework of quantum field theory. The quantisation of the gravitational field has not been successfully performed up to now.

The electromagnetic force is mediated by massless photons, the weak force by the massive Z^0 and $W^\pm$-bosons and the strong force by eight massless gluons. All particles participate in the weak interaction, only charged particles participate in the electromagnetic interaction and only those particles that carry a so-called *colour-charge* participate in the strong interaction, namely quarks and gluons. The three interactions are summarised in Tab. 2.2. A more thorough description of the three forces is given in the following.

[a] The *graviton* as the hypothesised force carrier of the gravitational interaction is not included in the SM.

Interaction	Couples to	Mediator	Mass $[\mathrm{GeV}/c^2]$	Relative strength
strong	colour	8 gluons (g)	0	~ 1
electromagnetic	electric charge	photon (γ)	0	$\sim 10^{-2}$
weak	weak charge	$W^{\pm}$-boson	80.385 ± 0.015	$\sim 10^{-5}$
		Z^0-boson	91.1876 ± 0.0021	

Tab. 2.2: The three interactions with their gauge bosons described in the SM [8]. The relative strength of the interaction is given by the respective couplings, $\alpha_s, \alpha_{\mathrm{em}}$ and G_F (not pure coupling, modified by mediator mass).

2.2.1 The Strong Interaction

The gauge group that characterises the strong interaction is the $SU(3)_C$ group, where C stands for colour, to which the eight mediators, the gluons g, couple. Accordingly, the theoretical framework that describes the strong interaction is called quantum chromo dynamics, QCD. The colour charge is an additional quantum number[b] that only quarks and gluons carry. Gluons carry both colour and anti-colour. Quarks can only be observed in so-called *hadrons* which are bound states, either mesons ($q\bar{q}$) or baryons (qqq), and not as free particles. This is due to the non-abelian character of the $SU(3)_C$ group. The generators of the $SU(3)_C$ group $t^a = \frac{1}{2}\lambda^a$, where λ^a are the eight 3×3 *Gell-Mann-matrices*, do not commute: $[t^a, t^b] = if^{abc}t^c$, where f^{abc} are the structure constants of QCD. The impact of the non-abelian gauge group is visible by looking at the classical[c] QCD Lagrangian:

$$\mathscr{L}_{\mathrm{QCD}} = -\frac{1}{4}F^{\mu\nu}_a F^a_{\mu\nu} + \sum_q \bar{\psi}_{q,i}(i\gamma^\mu \partial_\mu \delta_{ij} - g_s(t^c A^c_\mu)_{ij} - m\delta_{ij})\psi_{q,j} \tag{2.1}$$

$$\text{with} \qquad F^a_{\mu\nu} = \partial_\mu A^a_\nu - \partial_\nu A^a_\mu - g_s f^{abc} A^b_\mu A^c_\nu. \tag{2.2}$$

The gluon fields are denoted by A^a_μ, the spinor $\psi_{q,i}$ represents the field of the quark q (the sum in Eq. 2.1 is over all quark flavours) with the colour i. This Lagrangian is invariant under the gauge transformation

$$\psi_i \to \exp\left[i(t^a\theta^a(x))_{ij}\right]\psi_j,$$

with $\theta(x)$ being a locally dependent phase factor. The term proportional to $g_s\bar{\psi}_{q,i}(t^c A^c_\mu)_{ij}\psi_{q,j}$ in Eq. 2.1 represents the quark-gluon interaction. The last term in Eq. 2.2 stems from the commutator $[t^a, t^b]$ and does not vanish; g_s is related to the strong coupling constant α_s via $g_s = \sqrt{4\pi\alpha_s}$. Inserting Eq. 2.2 into Eq. 2.1 one finds terms that are proportional to $(\partial_\mu A^a_\nu - \partial_\nu A^a_\mu)A^b_\mu A^c_\nu$ and $A^a_\mu A^b_\nu A^\mu_c A^\nu_d$ that represent three gluon and four gluon interactions, respectively. This means that gluons couple to themselves: the consequence is that the potential between two quarks increases with increasing distance, due to the effect of anti-screening[d]. When separating two quarks from each other, the energy in the field between them will at one point be large enough to create a new

[b] The colour charge quantum number was initially introduced to explain the existence of qqq bound states with same quark flavours and spins to avoid the violation of Pauli's principle.

[c] Here, only the classical QCD Lagrangian is shown. A 'gauge fixing' part (to ensure invertibility of the gluon propagator) and a so-called 'ghost term' (to cancel unphysical polarisation states of the gluon) are left out, since this is a short introduction to QCD and the terms are not needed for the general understanding.

[d] Pictorially, the self-coupling terms of gluons lead to a cloud of gluons that carry colour charge around a single quark which increases the colour charge with increasing distance to the single quark.

quark−anti-quark pair. Instead of separating two quarks from each other, another quark pair will be created which makes it impossible to observe single quarks. Only colour singlet states such as baryons and mesons can be observed in nature. This is what is called *quark confinement*. It requires the strong coupling to increase with decreasing energy, thus increasing distance. In renormalisable gauge theories, the couplings are energy dependent due to vacuum polarization effects. The quantities, such as couplings are parameterised depending on bare couplings and a starting energy scale μ_0^2. The bare quantities have to be independent of the energy μ^2 which leads to the so-called *renormalisation group equations* (RGE). The solution of the RGE yields in the case of the strong coupling α_s:

$$\alpha_s(\mu^2) = \frac{\alpha_s(\mu_0^2)}{1 + \frac{\alpha_s(\mu_0^2)}{4\pi}\beta_0 \ln\left(\frac{\mu^2}{\mu_0^2}\right)} \quad \text{with} \quad \beta_0 = 11 - \frac{2}{3}N_f \quad \text{at the one-loop level.} \tag{2.3}$$

N_f is the number of quark flavours that are relevant at a scale μ^2. For six quark flavours β_0 is always positive and α_s diverges to high values for low energies. At high energies, α_s is small and therefore one speaks of *asymptotic freedom* of quarks at small distances. The scale at which the divergence occurs (the denominator becomes zero) is often denoted as Λ_{QCD}. Below this scale, perturbation theory in α_s is no longer possible. The coupling can be rewritten in the form:

$$\alpha_s(\mu^2) = \frac{4\pi}{\beta_0 \ln\left(\frac{\mu^2}{\Lambda_{\mathrm{QCD}}^2}\right)}. \tag{2.4}$$

From measurements of $\alpha_s(m_Z^2)$ with m_Z being the Z-boson mass it is deduced that $\Lambda_{\mathrm{QCD}} \sim 200$ MeV [8]. Knowledge of this behaviour of α_s is important to understand and model hadron collider phenomenology (see Chapter 4).

2.2.2 The Electroweak Interaction

In this chapter, the electromagnetic and weak force are described. A common theoretical framework that describes both forces was introduced by Glashow, Weinberg and Salam [4, 6, 18]. The electromagnetic and weak interaction unify to the *electroweak* interaction, mediated by the massless photon γ, two charged massive $W^{\pm}$-bosons and an electrically neutral, massive Z^0-boson. While the photon only couples to electric charge the massive weak bosons couple to the *weak isospin* T. Only left-handed particles carry weak isospin. Therefore, left-handed doublets of fermions participate in the weak interaction, while right-handed particles transform as singlets under the corresponding symmetry transformation, thus they do not take part in the weak interaction. The corresponding gauge group of the electroweak interaction is $SU(2)_L \otimes U(1)_Y$. The group $SU(2)_L$ describes the weak interaction where the subscript L indicates the coupling to left-handed particles. The group $U(1)_Y$ describes the electromagnetic part of the interaction where the subscript Y refers to the so-called *hypercharge* that is defined as: $Y = 2(Q - T_3)$ with T_3 being the third component of the weak isospin. The fermion doublets and singlets together with their isospin T and third component T_3 and the hypercharge are listed in Tab. 2.3. No right-handed neutrinos are listed as in the SM they are *a priori* considered to be massless and the helicity measurement performed by Goldhaber et al. [19] implies that neutrinos are only left-handed (when they are produced in a weak interaction). The doublets consist of so-called flavour eigenstates, eigenstates of the weak interaction. Only in charged $W^{\pm}$-boson exchange it is possible to change the flavour of a quark. This is because mass eigenstates are not equal

	Fermion Multiplets			T	T_3	Y
Leptons	$\begin{pmatrix} \nu_e \\ e^- \end{pmatrix}_L$	$\begin{pmatrix} \nu_\mu \\ \mu^- \end{pmatrix}_L$	$\begin{pmatrix} \nu_\tau \\ \tau^- \end{pmatrix}_L$	$1/2$	$+1/2$ $-1/2$	-1
	e_R^-	μ_R^-	τ_R^-	0	0	-2
Quarks	$\begin{pmatrix} u \\ d' \end{pmatrix}_L$	$\begin{pmatrix} c \\ s' \end{pmatrix}_L$	$\begin{pmatrix} t \\ b' \end{pmatrix}_L$	$1/2$	$+1/2$ $-1/2$	$+1/3$
	u_R	c_R	t_R	0	0	$+4/3$
	d_R	s_R	b_R	0	0	$-2/3$

Tab. 2.3: Fermions and their corresponding weak isospin T with third component T_3 and hypercharge Y [8].

to flavour eigenstates but mixings of these. Conventionally, the mass eigenstates and flavour eigenstates of the up-type quarks (u, c and t) are set equal and the mixing is ascribed only to the down-type quarks (d, s and b). Therefore, in Tab. 2.3 the flavour eigenstates are denoted as d', s' and b' and are related to the mass eigenstates via the CKM-Matrix V_{CKM}:

$$\begin{pmatrix} d' \\ s' \\ b' \end{pmatrix} = \begin{pmatrix} V_{ud} & V_{us} & V_{ub} \\ V_{cd} & V_{cs} & V_{cb} \\ V_{td} & V_{ts} & V_{tb} \end{pmatrix} \begin{pmatrix} d \\ s \\ b \end{pmatrix} = V_{CKM} \begin{pmatrix} d \\ s \\ b \end{pmatrix}. \tag{2.5}$$

This formalism has been developed by Cabibbo and extended by Kobayashi and Maskawa in 1973 [20, 21]. The matrix V_{CKM} is characterised by three mixing angles and one complex phase that leads to the violation of the CP-symmetry[e]. The matrix is non-diagonal which allows transitions between different generations via the weak interaction. The diagonal elements are nevertheless close to 1, transitions between different generations are possible but suppressed, especially between first and third generation particles. An equivalent formalism to the CKM-Matrix can be introduced in the lepton sector. This has been done by Pontecorvo, Maki, Nakagawa and Sakata who included the so-called PMNS-Matrix into the theory as an analogue to the CKM-Matrix that can describe transitions between different neutrino flavours[f] [22–24].

The generators of the non-abelian $SU(2)_L$ group are the Pauli matrices τ_i, the generator of the $U(1)_Y$ abelian gauge group is the hypercharge Y. A $SU(2)_L \otimes U(1)_Y$ transformation is of the form

$$\psi_L \to \exp\left[i\frac{1}{2}g\boldsymbol{\alpha}(x)\cdot\boldsymbol{\tau} + ig'\beta(x)Y\right]\psi_L \qquad \text{and} \qquad \psi_R \to \exp\left[ig'\beta(x)Y\right]\psi_R \tag{2.6}$$

with arbitrary phases $\boldsymbol{\alpha}(x)$ and $\beta(x)$. The vector $\boldsymbol{\tau}$ consists of the Pauli matrices τ_i and ψ_L and ψ_R are left-handed and right-handed spinors. The parameters g and g' are the couplings of $SU(2)_L$ and $U(1)_Y$, respectively. For the electroweak Lagrangian $\mathscr{L}_{\text{ew}}$ to be invariant under the transformation in Eq. 2.6, an isotriplet field $\boldsymbol{W}_\mu = (W_{1\mu}, W_{2,\mu}, W_{3\mu})$ and a singlet field B_μ

[e] C is the charge conjugation operator and P is the parity operator. Both symmetries are maximally violated in the weak interaction. The combination of both transformations is mildly violated in the SM.

[f] This PMNS-Matrix is not part of the SM, it only becomes relevant if neutrinos have non-zero masses.

have to be added. The corresponding Lagrangian takes the form:

$$\begin{aligned}\mathscr{L}_{\text{ew}} = &-\frac{1}{4}\boldsymbol{W}_{\mu\nu}\boldsymbol{W}^{\mu\nu} - \frac{1}{4}B_{\mu\nu}B^{\mu\nu} \\ &+ i\bar{L}\gamma^{\mu}\left[\partial_{\mu} + i\frac{g}{2}\boldsymbol{W}_{\mu}\cdot\boldsymbol{\tau} + i\frac{g'}{2}YB_{\mu}\right]L + i\bar{R}\gamma^{\mu}\left[\partial_{\mu} + i\frac{g'}{2}YB_{\mu}\right]R.\end{aligned} \tag{2.7}$$

The tensor $\boldsymbol{W}_{\mu\nu}$ is given by $\boldsymbol{W}_{\mu\nu} = \partial_{\mu}\boldsymbol{W}_{\nu} - \partial_{\nu}\boldsymbol{W}_{\mu} - g\cdot\boldsymbol{W}_{\mu}\times\boldsymbol{W}_{\nu}$ and $B_{\mu\nu}$ is $B_{\mu\nu} = \partial_{\mu}B_{\nu} - \partial_{\nu}B_{\mu}$. L and R denote left-handed doublets and right-handed singlets, respectively (see Tab. 2.3). The first two terms in Eq. 2.7 are kinetic energy terms of the gauge fields, the other terms represent interaction terms of particles with the gauge fields.
After *electroweak symmetry breaking* the fields mix to form the physical $\gamma, W^{\pm}$ and Z^0-bosons. The neutral bosons, represented as fields A_{μ} (photon) and Z_{μ} (Z^0-boson), are linear combinations of $W_{3\mu}$ and B_{μ}:

$$\begin{pmatrix} A_{\mu} \\ Z_{\mu} \end{pmatrix} = \begin{pmatrix} \cos\theta_W & \sin\theta_W \\ -\sin\theta_W & \cos\theta_W \end{pmatrix}\begin{pmatrix} B_{\mu} \\ W_{3\mu} \end{pmatrix}.$$

The charged W-bosons are linear combinations of the first and second isotriplet field components:

$$W^{\pm}_{\mu} = \frac{1}{\sqrt{2}}\left(W_{1\mu} \mp iW_{2\mu}\right).$$

The weak mixing angle or also called Weinberg angle θ_W relates the two couplings g and g':

$$\sin\theta_W = \frac{g'}{\sqrt{g^2 + g'^2}} \qquad \text{or} \qquad \tan\theta_W = \frac{g'}{g}. \tag{2.8}$$

They again can be related to the electromagnetic coupling g_{em} ($= e = \sqrt{4\pi\alpha_{\text{em}}}$) via

$$g_{\text{em}} = g\sin\theta_W \qquad \text{and} \qquad g_{\text{em}} = g'\cos\theta_W.$$

The *fine structure constant* α_{em} is used to quantify the relative strength of the electromagnetic interaction in Tab. 2.2, whereas the *fermi-constant* $G_F (= \frac{\sqrt{2}}{8}\frac{g^2}{m_W^2})$ is used to quantify the relative strength of the weak interaction in Tab. 2.2, where the mass m_W of the W-boson enters the definition. In Eq. 2.7, there are no mass terms for the gauge bosons as they would break the invariance under local gauge transformations. This is in conflict with the experimental measurements: the weak bosons are massive particles with masses of $m_W = (80.385 \pm 0.015)$ GeV/c^2 and $m_Z = (91.1876 \pm 0.0021)$ GeV/c^2 [8]. A solution to this problem is given by the mechanism of electroweak symmetry breaking.

2.3 Electroweak Symmetry Breaking

To ensure invariance of the Lagrangian under gauge transformation including mass terms for the massive gauge bosons, six authors proposed the mechanism of spontaneous symmetry breaking [25–27]. This mechanism is named after Peter Higgs the *Higgs-mechanism*. The basic idea is to add a potential to the Lagrangian of the following form:

$$V(\phi) = \mu^2(\phi^{\dagger}\phi) + \lambda(\phi^{\dagger}\phi)^2. \tag{2.9}$$

The field ϕ is a complex scalar $SU(2)$-doublet field that can be written as:

$$\phi = \frac{1}{\sqrt{2}} \begin{pmatrix} \phi_1 + i\phi_2 \\ \phi_3 + i\phi_4 \end{pmatrix}. \tag{2.10}$$

The potential in Eq. 2.9 exhibits a rotational symmetry around $\phi = 0$. If the parameters are chosen as $\mu^2 < 0$ and $\lambda > 0$, then the potential has the form that is sketched in Fig. 2.1. This potential is still symmetric around $\phi = 0$, but special is that the minima of the potential lie on a circle with radius $v = \sqrt{-\mu^2/2\lambda}$ around the symmetry axis. The parameter v is called the vacuum expectation value (VEV) and is non-zero. A theory always has to be developed around

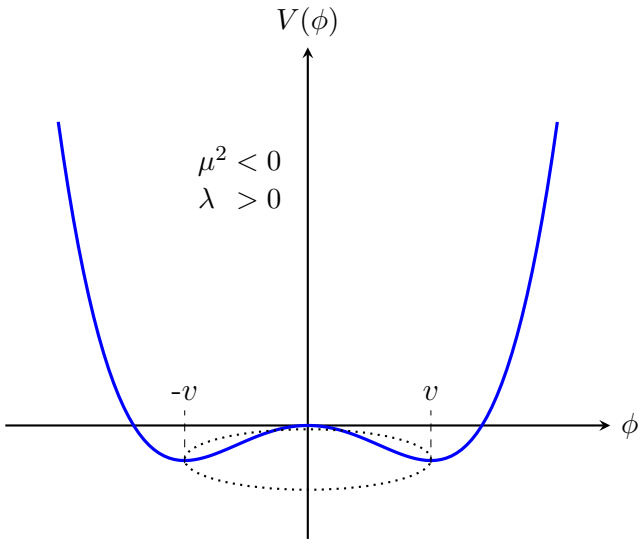

Fig. 2.1: A 2-dimensional sketch of the potential $V(\phi)$ for $\mu^2 < 0$ and $\lambda > 0$. The minima are given by -v and v. Extending to three dimensions means to rotate the potential around the y-axis, indicated by the ellipse at the bottom.

the ground state of a system. In this case the ground state is degenerated, choosing a particular ground state and developing around this state spontaneously breaks the rotational symmetry of the potential $V(\phi)$. Choosing a ground state ϕ_0 with small perturbations $h(x)$ (real scalar field) around it is conveniently written as:

$$\phi_0 = \frac{1}{\sqrt{2}} \begin{pmatrix} 0 \\ v + h(x) \end{pmatrix}. \tag{2.11}$$

Adding the potential $V(\phi)$ and a term of the form $(D^\mu\phi)^\dagger(D_\mu\phi)$ with the covariant derivative $D_\mu = \partial_\mu + i\frac{g}{2}\boldsymbol{W}_\mu \cdot \boldsymbol{\tau} + i\frac{g'}{2}B_\mu Y$ and substituting ϕ for ϕ_0 yields the desired additional mass terms in the Lagrangian:

$$\mathscr{L}_{\text{mass}} = -\lambda v^2 h^2 + \frac{1}{4}g^2 v^2 W_\mu^+ W^{-\mu} + \frac{1}{8}(g^2 + g'^2)v^2 Z_\mu Z^\mu. \tag{2.12}$$

The excitation of the Higgs-field $h(x)$ gives the scalar Higgs boson with the mass $m_h = \sqrt{2\lambda}v$. The interaction of the weak bosons with the Higgs-field generates the mass terms $m_W = \frac{1}{2}vg$

and $m_Z = \frac{1}{2}v\sqrt{g^2 + g'^2}$. The photon remains massless. Inserting the relation in Eq. 2.8 yields:

$$\frac{m_W}{m_Z} = \cos\theta_W,$$

which is consistent with the Glashow-Weinberg-Salam-theory. The VEV can be determined via the knowledge of m_W and amounts to $v \approx 246$ GeV, which sets the scale for electroweak symmetry breaking. The mass of the Higgs boson cannot be predicted due to the unknown parameter λ. After the discovery in 2012, the most recent combined measurement (Run 1) of the Higgs mass from ATLAS and CMS yields $m_h = 125.09 \pm 0.21\,(\text{stat}) \pm 0.11\,(\text{syst})$ GeV/c^2 [28]. Mass terms for fermions can be created by allowing a *Yukawa*-coupling of the Higgs-field to the fermions. Thereby further coupling constants g_f have to be introduced. The masses of the fermions are then proportional to g_f:

$$m_f = \frac{1}{\sqrt{2}} g_f \cdot v.$$

Since the coupling g_f is unknown, the masses of the fermions can not be predicted and have to be measured in experiments.

Altogether, the SM incorporates the mechanism of electroweak symmetry breaking producing a Higgs boson and the three above introduced forces are described by the $SU(3)_C \otimes SU(2)_L \otimes U(1)_Y$ symmetry groups.

2.4 Open Questions in the SM

The SM is a successful theory that could not be disproven in any experimental measurement up to now. Nevertheless, it does not include gravity. Measurements of rotational velocities of and inside galaxies gave an indication about the existence of the so-called dark matter [29, 30]. The cosmic microwave background measurement performed by WMAP and PLANCK indicate that this dark matter component makes up about 25% of the content of our universe, while the visible matter described by the SM represents only 5% of the universe [29, 31, 32]. The rest is made up by *dark energy*. The SM provides no answer to the question of what dark matter and dark energy are made of. It also has to be extended to include neutrino masses: oscillation measurements of neutrino flavours require neutrinos to have non-zero masses. Including neutrino mass terms is not straight-forward: the question that also arises is of which nature neutrinos are, are they Dirac- or Majorana-particles [33]? Depending on the answer, neutrino mass terms are different. Another problem arises if we consider the huge matter-antimatter asymmetry in our universe: the CP-violation incorporated in the SM via the CKM-mechanism cannot account for the observed matter-antimatter asymmetry. Therefore, one seeks for additional sources of CP-violation, but not successfully up to now.
On the theoretical side, the *hierarchy problem*, or also called *fine-tuning* problem emerges: the fact that the Higgs boson as a scalar particle receives corrections to its mass via loop contributions of fermions that are 17 orders of magnitude higher than the Higgs mass itself. This is considered to be *unnatural* and requires a fine-tuning. A solution to this problem is e. g. provided by the model of *Supersymmetry* (see Sec. 3.2). There is also a cosmological hierarchy problem referring to the cosmological constant λ describing the energy density of free space-time: the difference between its magnitude and the Planck-scale is of 120 orders of magnitude.

Furthermore, the SM has many free parameters, especially all particle masses that cannot be predicted but have to be measured by experiments. These parameters remain arbitrary and yet, changes of these would have dramatic influences on our world (see e. g. [34]). The origin of the generations of fermions and gauge symmetries is not explained, the three forces do not unify (as anticipated by Big Bang models). The latter problem can be solved by certain theories, but there is no theory known, to satisfactorily answer the former questions.

All these short-comings motivate to further test the SM and to search for BSM physics. The following chapter will introduce BSM physics concepts that partly provide solutions to the above posed questions. The focus is in particular on models that predict particles a monojet search may be sensitive to.

Chapter 3

Theories Beyond The Standard Model

Chapter 2 already pointed out some of the short-comings of the SM as we know it to date. There is a multitude of theories being developed to solve at least some of them. However, new theories are regarded as extensions of the SM, since it describes most of our observations correctly. In general, the BSM theories around are based on the principle to extend the number of symmetries from the SM to include further symmetries that might hold in nature. Here, the focus is on models that actually predict modified physics at a certain energy scale that is above the energy probed up to now. The new physics manifests itself in new particles that influence cross sections or other properties we are able to measure in collision experiments. These kind of theories include the prediction of extra spatial dimensions, a symmetry between bosons and fermions or simplified models describing the production of dark matter particles. These models have in common to predict heavy particles that can escape a particle detector unseen. The presence of such heavy particles can be detected if these are recoiling against ordinary matter particles. Thereby a momentum imbalance is created that can be traced in the detector. These are the event topologies relevant for a monojet, mono-boson search strategy. The theory behind these models is shortly introduced in the following.

3.1 Extra Spatial Dimensions

The theory of extra spatial dimensions adds Poincaré symmetries related to translational invariances in the corresponding extra dimensions. A first introduction of the idea of extra dimensions by Kaluza in 1921 [35] had the goal to unify gravity and electromagnetism. Both forces would have the same origin with different manifestations in the different dimensions. However, if extra dimensions existed they would have to modify Newton's law from a $1/r^2$ behaviour, one would 'experience' the extra dimensions. To accommodate this idea with experimental observations the idea of *compact* extra dimensions was introduced by Klein [36]: this means that the extra dimension is curled up, like a cylinder with radius R, where R is the size of the extra dimension. Let y be the variable of the 4th spatial dimension, then $y = 2\pi R + y$ would hold for such a compactified dimension. Any function describing a moving particle in this dimension has to obey periodical boundary conditions. A scalar field φ in this dimension can be written as

$$\varphi(x^\mu, y) = \sum_{n=-\infty}^{\infty} \varphi_n(x^\mu, y) \exp\left(\frac{iny}{R}\right).$$

The mass term of such a scalar field can be identified with $m_n = n^2/R^2$ (inserting φ into the Klein-Gordon equation). This means there is an infinite amount of particles with mass m_n, referred to as *Kaluza-Klein tower*. This is not only valid for a scalar field but also for fields with non-zero spin, like the graviton, a spin-2 particle. The mass spectrum is discrete and the mass difference dependent on the size of the compact extra dimension. The presence of

such particles and extra dimensions would modify the gravitational potential at small scales r. Models that make predictions to be tested at the LHC are those introduced by Randall and Sundrum (RS model) [37] and Arkani-Hamed, Dimopoulus and Dvali (ADD model) [38]. The RS model predicts resonances in event signatures of e. g. dilepton or dijet final states. The ADD model predicts invisible particles escaping the detector leaving a signature the monojet analysis is sensitive to, therefore the latter model will be discussed next.

3.1.1 The Arkani-Hamed Dimopoulus Dvali Model

The basic idea of the ADD Ansatz is to explain the difference of the electroweak energy scale and the Planck scale by introducing n compactified extra dimensions into the theory. That is, there is only one scale, the electroweak scale M_{EW}, at the core of the model. The assumption is that all known SM particles are bound to a so-called *3-brane*, the known dimensions, while the mediator of gravity, the graviton, can travel into the extra dimensions, into the *bulk*. The extra dimensions all have the same radius R. To understand the implications, one can consider the gravitational potential between two masses m_1 and m_2. If the distance r between the masses is much larger than R, the potential takes the known form as in Eq. 3.1, that is a $1/r$ behaviour[a].

$$V(r) \sim \frac{m_1 m_2}{M_D^{n+2} R^n} \frac{1}{r} \qquad \text{for} \quad r \gg R \tag{3.1}$$

Here, M_D labels the Planck mass in $n+4$ dimensions. The formula in Eq. 3.1 essentially tells us that if extra dimensions exist, one can only probe them if the scale r is small enough, is close enough to 'feel' the extra dimensions. If these small distances can be probed than the potential transforms to the one in Eq. 3.2:

$$V(r) \sim \frac{m_1 m_2}{M_D^{n+2}} \frac{1}{r^{n+1}} \qquad \text{for} \quad r < R. \tag{3.2}$$

This effectively means that the gravitational strength is modified by the presence of extra dimensions, that is the connection between the Planck mass in four dimensions and the actual Planck mass if n extra dimensions existed can be written as

$$M_{\mathrm{Pl}}^2 \sim M_D^{2+n} R^n. \tag{3.3}$$

The pure existence of these extra dimension could thus explain the smallness of $1/M_{\mathrm{Pl}}$ and would thus resolve the hierarchy problem between the electroweak scale and the Planck scale if $M_D \sim M_{\mathrm{EW}}$. If indeed the scale M_D is identified with the electroweak scale one can obtain the radius of the extra dimensions as

$$R \sim 10^{\frac{30}{n}-17}\ \mathrm{cm} \left(\frac{1\ \mathrm{TeV}}{M_{\mathrm{EW}}} \right)^{1+\frac{2}{n}}. \tag{3.4}$$

If there was only one extra dimension R would be of the order of 10^{13} cm which would modify the motion of objects at solar system scales and is thus ruled out. However, if $n = 2$ R could be in the $10^2\,\mu$m range which is not ruled out and accessible at the LHC. Therefore, the name *large extra dimensions* is used in the context of the ADD model.

[a] The form of the potential can be derived by employing Gauss laws for both scenarios with $r < R$ and $r \gg R$. A known analogue is the electrical potential of an extended charge, where the potential takes a different form for the distance inside the charge area and the distance outside.

The hypothetical graviton with spin-2 is the only particle respecting the Einstein equation in $4+n$ dimensions. From there the gravitational Lagrangian can be derived with an interaction term:

$$\mathscr{L}_{\text{grav}} = -\frac{\sqrt{8\pi}}{M_{\text{Pl}}}\mathcal{G}_{\mu\nu}\mathcal{T}_{\mu\nu}. \tag{3.5}$$

The graviton field is denoted by $\mathcal{G}_{\mu\nu}$ and the energy-momentum tensor is $\mathcal{T}_{\mu\nu}$. From there Feynman-rules for the interaction of gravity with SM particles can be derived. Fig. 3.1 shows

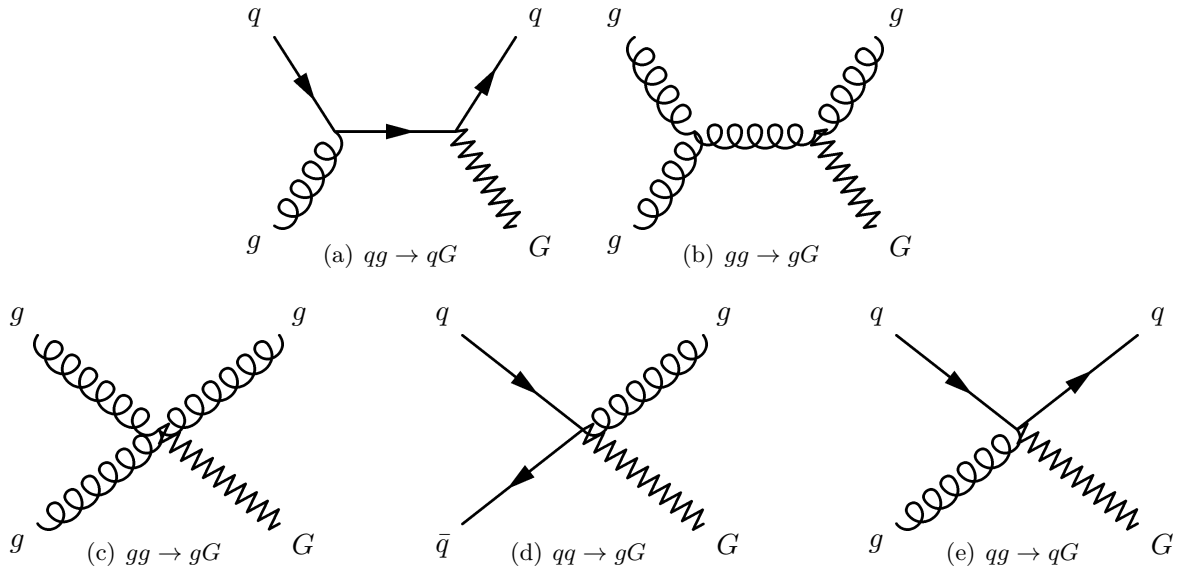

Fig. 3.1: LO Feynman diagrams for the production of a graviton G in pp collisions.

possible production modes of the graviton at the LHC at LO. If the coupling to only one graviton with $1/M_{\text{Pl}}$ would be considered the cross section for the diagrams in Fig. 3.1 would be too low to be measurable. But since there is a tower of graviton modes, the amplitude for the processes needs to be summed up over all these modes and finally yields a cross section at the weak scale. The decay of the graviton is suppressed by M_{Pl}^2/m_n^3 and therefore the graviton can escape the detector as a stable particle. Therefore, graviton production at the LHC could yield in final states with one jet and large missing transverse momentum, $\not{E}_T$. Not only for this reason is the ADD model so appealing: it has the electroweak scale as a natural cut-off of the theory. It introduces no new fields apart from the graviton field and thus also only two new parameters: n and M_D. The ADD model can also be nicely connected with string-theory: in this theory SM particles are excitations of open strings with a certain extension and gravitons are excitations of closed strings. The SM particles are confined to the 3-brane by the length of the string, they cannot penetrate further into the bulk in contrast to the gravitons. The string theory relies on extra dimensions and is up to now the only viable way to quantise the gravitational field.

As mentioned, the underlying theory for gravity is not an exact theory, also the string-model is not worked out as a complete quantum field theory. A solution is to make use of so-called *effective field theories* (EFT). They will be discussed in Sec. 3.3.2. Using EFT one can derive

the production cross section. The dependence on n and M_D is shown in Eq. 3.6:

$$\sigma_G \propto \frac{C_n}{M_D^{n+2}}, \tag{3.6}$$

where C_n is a term dependent on n and relevant for the kinematics of the ADD graviton production while M_D determines the cross section magnitude. The EFT and this cross section formula is only valid if $\hat{s} \ll M_D$ holds. For cases where the transferred momentum is comparable to M_D the validity of the theory is questioned. Section. 3.3.2 will show how the cross section is *truncated* to estimate the impact of the limited EFT validity.

3.2 Supersymmetry

Supersymmetry is the theory that introduces a symmetry between fermions and bosons and is an extension of the space-time symmetry. It is a complete theory that has been and is being developed from the 1970s onwards. It is maybe the most appealing theory among theorists as it is able to resolve several observational and mathematical short-comings of the SM. Supersymmetry, short SUSY, provides a candidate for the dark matter component in the universe, involves unification of forces at the Planck scale, includes gravity to some extend and offers a solution to the mentioned *hierarchy problem*. Here, the theoretical basics shall be shortly described as well as the implications for collider searches and in particular the phenomenology relevant to monojet searches. An extensive discussion of SUSY can be found for e. g. in Ref. [39].

3.2.1 The Hierarchy Problem

As any particle in the SM, the Higgs mass receives corrections via loop contributions to its propagator. Figure 3.2(a) shows a fermionic loop modifying the Higgs propagator. The fermion f is any fermion that has a coupling to the Higgs boson. The form of the fermionic correction to the Higgs mass m_H is:

$$\Delta m_H^2 = -\kappa |\lambda_f|^2 \Lambda_{UV}^2 + \cdots \gg m_H^2, \tag{3.7}$$

where Λ_{UV} is an ultraviolet cut-off parameter and κ is some constant prefactor. If Λ_{UV} has the energy scale of the Planck mass M_{Pl} then it is of the order 10^{19} GeV. The Higgs mass itself however is at the electroweak scale with just more than 10^2 GeV. This requires a correction from the Planck mass all the way down to the electroweak scale which is called *fine-tuning*. This problem only affects the Higgs boson as a scalar particle, since fermions are protected by their chiral symmetries which leads to a logarithmic divergence in Λ_{UV} via loop corrections and does not require fine-tuning. The ADD model discussed before resolves this discrepancy of energy scales by introducing compact extra dimensions. The theory of SUSY provides a different solution: scalar particles S are introduced into the theory. If they would couple to the Higgs boson they would produce contributions to the Higgs mass correction via the loop diagram shown in Fig. 3.2(b). The corrections are of the form:

$$\Delta m_H^2 = \frac{\kappa}{2} \lambda_s \Lambda_{UV}^2 + \dots. \tag{3.8}$$

This correction has the opposite sign of the fermionic correction to the Higgs mass. If $|\lambda_f|^2 = \lambda_s$, meaning the couplings are equal, and two complex scalars are introduced for each Dirac fermion

then these two correction terms in Eq. 3.7 and Eq. 3.8 cancel each other and no fine-tuning would be needed anymore.



(a) (b)

Fig. 3.2: Loop contributions to the Higgs mass: (a): corrections from fermionic loops, (b) corrections from scalar loops to the Higgs propagator.

3.2.2 Basic Theory

The solution of the hierarchy problem by introducing new scalar particles is the basic underlying concept of SUSY. These scalars are so-called *superpartners* of the SM fermions. The supersymmetric operator Q carries itself spin 1/2 and behaves as a spinor. It allows the transformations of the form

$$Q|\text{fermion}\rangle = |\text{boson}\rangle,$$
$$Q|\text{boson}\rangle = |\text{fermion}\rangle,$$

thus it changes the spin of particles by half a unit and thereby transforms fermions to bosons and vice versa. The SUSY particles and the SM particles are grouped together in so-called *supermultiplets*. The 'chiral' supermultiplet consists of a complex scalar Φ and a Weyl fermion Ψ. The representation of such a supermultiplet is therefore given by

$$\begin{pmatrix} \Phi \\ \Psi \end{pmatrix} \quad \text{with spin} \quad \begin{pmatrix} 0 \\ \frac{1}{2} \end{pmatrix}.$$

Not only do the SM fermions have scalar superpartners but also the SM bosons have fermionic superpartners. They form the the so-called 'gauge' supermultiplet. It groups together vector-bosons A with 'gauginos', Weyl fermions, λ. The gauge supermultiplet can be written as

$$\begin{pmatrix} A \\ \lambda \end{pmatrix} \quad \text{with spin} \quad \begin{pmatrix} 1 \\ \frac{1}{2} \end{pmatrix}.$$

SUSY does also include a gravity supermultiplet containing the spin-2 graviton G and the spin-3/2 gravitino $\tilde{G}$. Particles that share the same supermultiplet must have same quantum numbers and a priori same masses.
Supersymmetric particles are shortly called *sparticles*. For the scalar superpartners an 's' is put in front of the name of the SM partner, e. g. the selectron is the supersymmetric scalar partner of the electron. Supersymmetric fermionic partners of the gauge bosons receive their name by appending 'ino' at the end, e. g. the wino is the superpartner of the W-boson. The Tables 3.1 and 3.2 summarise the particle content of the minimal supersymmetric extension of the standard model, called MSSM. Table 3.1 shows the chiral supermultiplets. The Weyl notation is used in this table. The indices R and L in the case of scalars refer to the helicity of their superpartners.

Names		spin 0	spin 1/2	$SU(3)_C$	$SU(2)_L$	$U(1)_Y$
squarks, quarks	Q	$(\tilde{u}_L \tilde{d}_L)$	$(u_L d_L)$	**3**	**2**	$+\frac{1}{3}$
(×3 families)	$\bar{u}$	$\tilde{u}_R^*$	$u_R^\dagger$	$\bar{\mathbf{3}}$	**1**	$-\frac{4}{3}$
	$\bar{d}$	$\tilde{d}_R^*$	$d_R^\dagger$	$\bar{\mathbf{3}}$	**1**	$+\frac{2}{3}$
sleptons, leptons	L	$(\tilde{\nu}_L \tilde{e}_L)$	$(\nu_L e_L)$	**1**	**2**	-1
(×3 families)	$\bar{e}$	$\tilde{e}_R^*$	$e_R^\dagger$	**1**	**1**	$+2$
Higgs, higgsinos	H_u	$(H_u^+ H_u^0)$	$(\tilde{H}_u^+ \tilde{H}_u^0)$	**1**	**2**	$+1$
	H_d	$(H_d^0 H_d^-)$	$(\tilde{H}_d^0 \tilde{H}_d^-)$	**1**	**2**	-1

Tab. 3.1: The particle content of the MSSM (non-gauge sector). The Weyl notation has been chosen, therefore conjugates like $\tilde{u}_R^*$ appear in the table. On the right, the quantum numbers of the particles with respect to the symmetry groups are shown.

Names	spin 1/2	spin 1	$SU(3)_C$	$SU(2)_L$	$U(1)_Y$
gluino, gluon	$\tilde{g}$	g	**8**	**1**	0
winos, W-bosons	$\tilde{W}^\pm \tilde{W}^0$	$W^\pm W^0$	**1**	**3**	0
bino, B-boson	$\tilde{B}^0$	B^0	**1**	**1**	0

Tab. 3.2: Gauge sector of the MSSM without the gravity supermultiplet.

Superpartners of right-handed fermions are also singlets under the $SU(2)$ gauge symmetry. The quantum numbers under the symmetry groups of the supermultiplets are shown on the right. The Higgs sector in SUSY models is extended: there are two Higgs doublets H_u and H_d to generate the masses of up-type and down-type fermions, respectively. One cannot conjugate the Higgs field in order to generate down-type fermion masses as is done in the SM Higgs sector. Introducing two Higgs doublets thus leads to eight degrees of freedom with four higgsinos and also charged higgses. A linear combination of H_u^0 and H_d^0 would correspond to the SM scalar boson.
The same mechanism introduced for mixing of photon and Z-boson fields is assumed here: $\tilde{W}^0$ and $\tilde{B}^0$ mix to form the states of the *zino* and the *photino*. In Tab. 3.1 the neutrino is listed with the same quantum numbers as the higgsino. However, it cannot be the superpartner of the SM Higgs because of lepton number violation and the implication that at least one neutrino has to have a huge mass which is forbidden by phenomenology. Thus all supersymmetric partners are indeed new particles.

States with same quantum numbers can mix. In this case it means, that particles which have the same quantum numbers can mix to form mass eigenstates that are different from the interaction eigenstates. These mass eigenstates are then linear combinations of the interaction eigenstates. The names of these mass eigenstates are shown in Tab. 3.3. For the first two sfermion generations, mixing is often assumed to be negligible. Important for the collider phenomenology is the formation of the so-called *neutralino*. The so-called *chargino* is a mixing of charged winos and higgsinos. To understand how all these different states, gauginos, sfermions, interact with each other and with SM particles, the supersymmetric interaction Lagrangian $\mathscr{L}_{\text{gauge}}$ is presented:

$$\mathscr{L}_{\text{gauge}} = -\frac{1}{4} F_{\mu\nu}^a F_a^{\mu\nu} - i\bar{\Psi}\bar{\sigma}^\mu D_\mu \Psi - D^\mu \Phi^* D_\mu \Phi - i\lambda^{ta}\bar{\sigma}^\mu D_\mu \lambda^a. \tag{3.9}$$

Name	Interaction Eigenstate	Mass Eigenstate
squarks	$\tilde{u}_L\tilde{u}_R\tilde{d}_L\tilde{d}_R$	same
	$\tilde{c}_L\tilde{c}_R\tilde{s}_L\tilde{s}_R$	same
	$\tilde{t}_L\tilde{t}_R\tilde{b}_L\tilde{b}_R$	$\tilde{t}_1\tilde{t}_2\tilde{b}_1\tilde{b}_2$
sleptons	$\tilde{e}_L\tilde{e}_R\tilde{\nu}_e$	same
	$\tilde{\mu}_L\tilde{\mu}_R\tilde{\nu}_\mu$	same
	$\tilde{\tau}_L\tilde{\tau}_R\tilde{\nu}_\tau$	$\tilde{\tau}_1\tilde{\tau}_2\tilde{\nu}_\tau$
Higgs	$H_u^0 H_d^0 H_u^+ H_d^-$	$h^0 H^0 A^0 H^\pm$
neutralino	$\tilde{B}^0\tilde{W}^0\tilde{H}_u^0\tilde{H}_d^0$	$\tilde{\chi}_1^0\tilde{\chi}_2^0\tilde{\chi}_3^0\tilde{\chi}_4^0$
chargino	$\tilde{W}^\pm\tilde{H}_u^+\tilde{H}_d^-$	$\tilde{\chi}_1^\pm\tilde{\chi}_2^\pm$
gluino	$\tilde{g}$	same

Tab. 3.3: The supersymmetric particles and their mixings.

The individual terms will be discussed in the following. The first term includes the vector boson fields from the SM, generalised (see also Eq. 2.2) written as

$$F^{\mu\nu} = \partial^\mu A^\nu - \partial^\nu A^\mu - g f^{abc} A^\mu A^\nu.$$

The SM vector-boson self-interaction (not for the photon field!) terms are depicted in Fig 3.3 (a) and (b). The second term in Eq. 3.9 is also familiar from the SM, it contains:

$$D_\mu \Psi = \partial_\mu \Psi + igA_\mu T\Psi,$$

describing the fermion interaction with the gauge fields A_μ as depicted in diagram (f). The third term of Eq. 3.9 includes the scalar particle interactions with the gauge fields A_μ which can be seen from

$$D_\mu \Phi = \partial_\mu \Phi + igA_\mu T\Phi,$$

which produces the interaction diagrams (d) and (g) in Fig. 3.3, the latter being present in the SM as well via Higgs boson interactions. Note that appearing couplings g are equal to the SM couplings. The last term in Eq. 3.9 is new w. r. t. the SM Lagrangian: The covariant derivative D_μ can be written as

$$D_\mu \lambda^a = \partial_\mu \lambda^a - g f^{abc} A_\mu^b \lambda^c.$$

Thus, the last term produces a vector-boson-gaugino-gaugino coupling as can be seen in diagram (c). The supersymmetric Lagrangian also contains a scalar potential. From this scalar potential the additional terms

$$\Phi^* T^a \Psi\lambda \qquad \text{and} \qquad (\Phi^* T^a \Phi)^2$$

are expected which lead to the diagrams (h) and (i) in Fig. 3.3, respectively. In general the gauginos only couple to the particles their superpartners also couple to. This means that e. g. the gluino only couples to quarks and squarks and the wino only couples to left-handed particles and right-handed anti-particles. There is also a so-called *Superpotential* present in the SUSY

Lagrangian. This superpotential contains Yukawa couplings and mass terms of scalars and fermions. Additional interactions from this superpotential are the diagrams (e) and (j).

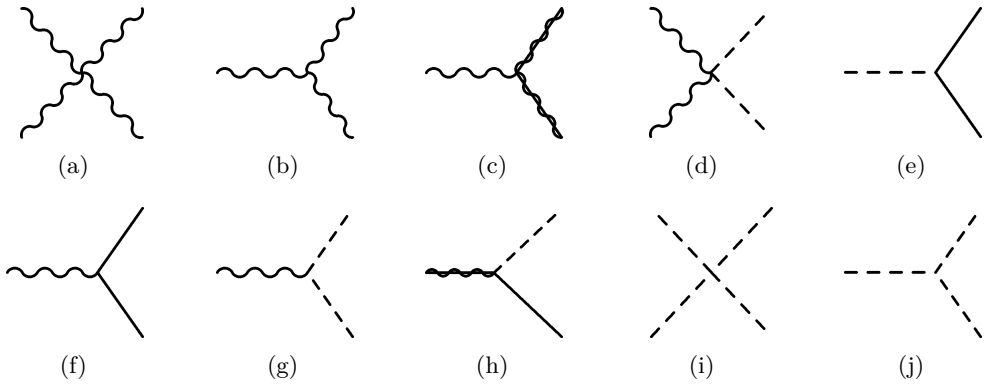

Fig. 3.3: Gauge interactions in SUSY. Dashes indicate scalars, solid lines indicate fermions. Wavy lines indicate vector bosons and solid lines drawn on top of wavy lines are gauginos.

Canonical Scenario

The aforementioned superpotential in the SUSY Lagrangian $\mathscr{L}_{\text{SUSY}}$ contains lepton number L and baryon number B violating terms. In the SM they happen to be conserved quantum numbers without an underlying symmetry demanding the conservation of these numbers. However, if L and B can be violated in SUSY interactions, the proton could decay into leptons and mesons via a squark exchange. But such a proton decay has never been observed until now (SuperKamiokande measurement, see Ref. [40]). To circumvent the conflict with experimental measurements, a new symmetry can be added: the *R-parity*. The conserved quantum number R is then calculated as

$$R = (-1)^{3(B-L)+2S},$$

where S is the spin quantum number. R is a multiplicative quantum number. Consequently SM particles have $R = +1$ and sparticles have $R = -1$. The conservation of R has several consequences for the collider phenomenology of SUSY:

- no mixing between SUSY and SM particles is possible,
- sparticles can only be produced in pairs,
- the lightest sparticle (LSP) is stable,
- all sparticles but the LSP decay into a final state with an odd number of LSPs.

The scenario in which R is conserved is also called canonical scenario and determines the signatures looked for in SUSY searches at colliders (see Sec. 3.2.4).

3.2.3 SUSY Breaking

As introduced in Sec. 3.2.2, particles that share the same supermultiplet must have the same masses. This assumption leads to the question why we have not already observed SUSY particles if SUSY really exists. Experiments tell us that e. g. there is no selectron with a mass of 0.511... MeV, which is the mass of the electron [8]. Therefore, if SUSY is realised in nature,

it must be a broken symmetry. If the masses of superpartners are not equal then there is no exact cancellation of the loop corrections to the Higgs mass. In order to preserve the attractive property of SUSY solving the fine-tuning problem, a 'soft SUSY breaking' is required. This leads to additional terms in the SUSY Lagrangian,

$$\mathscr{L} = \mathscr{L}_{\text{SUSY}} + \mathscr{L}_{\text{soft}},$$

which are denoted by $\mathscr{L}_{\text{soft}}$. If the heavy sparticles have masses of the scale m_{soft} then the correction to the Higgs mass becomes:

$$\Delta m_H^2 = m_{\text{soft}}^2 \left[\frac{\lambda}{16\pi^2} \ln\left(\frac{\Lambda_{UV}}{m_{\text{soft}}}\right) + \dots \right]. \tag{3.10}$$

The parameter λ denotes a dimensionless coupling. The term in Eq. 3.10 is now logarithmically divergent in Λ_{UV}. Mathematically, one can still handle this sort of divergence if the mass scale of m_{soft} is not too huge to preserve a cancellation of Higgs mass corrections. Assuming the ultraviolet cut-off at M_{Pl} and a coupling λ of the order ~ 1 then m_{soft} should not be much larger than 1 TeV. Present SUSY searches aim at this energy range. The terms of $\mathscr{L}_{\text{soft}}$ can be parameterised containing fermionic and scalar mass terms, cubic scalar couplings, mixing angles and CP-violating phases invoking 105 new parameters. No fundamental theories can be build up with this amount of free parameters. A popular model that reduces this number down to only five free parameters is called *minimal supergravity*, mSUGRA. It assumes that SUSY breaking is taking place in a 'hidden' sector that is only weakly coupled to the visible sector of the MSSM. SUSY breaking is assumed to be mediated by gravity or other new physics entering at the Planck scale. The mSUGRA model includes an effective field theory of gravity which is non-renormalisable. Similar to the electroweak symmetry breaking a production of a massless fermion, the *goldstino* is assumed in SUSY breaking. This goldstino is absorbed by the gravitino which thereby acquires a mass of $m_{\tilde{G}} \approx m_{\text{soft}}$, the graviton stays massless. The gravitino coupling is estimated to be of the order $\mathcal{O}(10^{-15})$ and therefore does not play any role for collider phenomenology. In the mSUGRA model the coupling strengths of the forces unify at $M_U \approx 2 \cdot 10^{16}$ GeV as do the masses of the sparticles down to one universal scalar mass m_0, one universal fermionic mass $m_{1/2}$ and one universal Higgs mass. Evolving these down to lower energy scales yields a splitting into many different scalar and fermionic masses. The LSP in mSUGRA is always the lightest neutralino, denoted by $\tilde{\chi}_1^0$. This neutralino is stable and neutral and only interacts weakly, thus it is an excellent dark matter candidate (in particular a cold dark matter candidate, see Sec. 3.3).

3.2.4 Collider Phenomenology

In the canonical scenario (universal masses and R-parity conservation), SUSY event signatures will always contain $\not{E}_T$ from the undetected LSP, the neutralino. The dominant production of sparticles in pp collisions is via the strong force. Processes like $pp \to \tilde{g}\tilde{g}, \tilde{g}\tilde{q}, \tilde{q}\tilde{q}$ are expected to be dominant. Which process of sparticle production is dominant depends on the mass spectrum. If the masses of squarks are much lighter than the gluino masses, $m_{\tilde{q}} \ll m_{\tilde{g}}$, then the production $pp \to \tilde{q}\tilde{q}$ will be dominant. If $m_{\tilde{q}} \gg m_{\tilde{g}}$, then the production of gluinos $pp \to \tilde{g}\tilde{g}$ will be dominant. If both masses are about the same, $m_{\tilde{q}} \sim m_{\tilde{g}}$, then all productions $pp \to \tilde{g}\tilde{g}, \tilde{g}\tilde{q}, \tilde{q}\tilde{q}$ would equally contribute to the production of sparticle pairs. Produced gluinos will decay to squarks which will then decay to SM particles and neutralinos. In the monojet search, three basic productions are looked for. Figure 3.4 shows the Feynman diagrams for the production of

sbottom-pairs (a) and stop-pairs (b) and (c). While it is apparent that such production will lead to a multi-particle final state, the mass splitting Δm between the neutralino and the produced squark determines if these particles can be detected: in the case of small Δm, the SM particles from the decay will only be low energetic and thus might not be reconstructed in the detector. In Fig. 3.4(a) the sbottom quarks decay into b-quarks and neutralinos. If the b-jets are not measured the event would not lead to any signature in the detector at all. Such events can only be recognised if an ISR jet recoils against the squark system. Thus, a monojet search is sensitive in cases of small Δm, of the order of a few GeV. In case of stop pair production, two scenarios are shown in Fig. 3.4(b) and (c): (b) shows a decay into a charm-quark and a neutralino. This happens if $\Delta m < m_b + m_W$ and the phase space does not allow a decay to $\tilde{t} \to bW\tilde{\chi}_1^0$. If the phase space is large enough, the four body decay can occur, as depicted in Fig. 3.4(c). Third generation squarks are shown here, because they are assumed to possibly be the lightest squarks. In general, one can replace $\tilde{b}$ in diagram (a) with a generic $\tilde{q}$. In the monojet search, the flavour of the produced sparticles is not important since the events are tagged by an ISR jet, which is often initiated by a gluon.

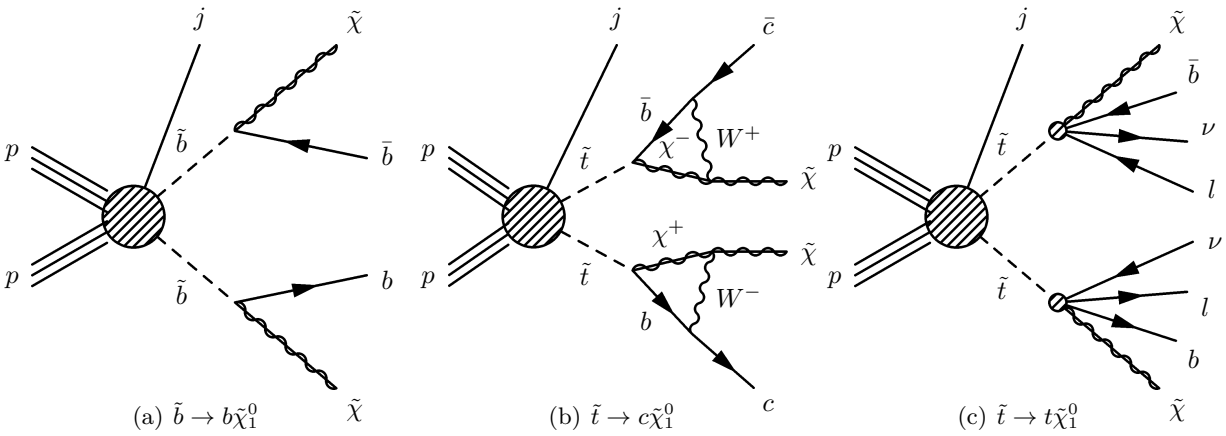

Fig. 3.4: Pair production of squarks in association with a jet j in pp collisions and their subsequent decays. (a) Production of $\tilde{b}\tilde{b}$ with decay mode: $\tilde{b} \to b\tilde{\chi}_1^0$. (b) Production of $\tilde{t}\tilde{t}$ with decay mode: $\tilde{t} \to c\tilde{\chi}_1^0$, and (c) the decay mode: $\tilde{t} \to \ell^{\pm}\nu b\tilde{\chi}_1^0$ (four body decay).

As already mentioned, SUSY is a complete theory that provides a dark matter candidate, the LSP, here the neutralino. The next section discusses the need for dark matter and alternative approaches besides SUSY that try to model it.

3.3 Dark Matter

3.3.1 Experimental Evidence

There is a number of observations from the present and past universe that point to the existence of dark matter (DM). It has been first postulated by Fritz Zwicky in 1933 to explain orbital velocities of galaxies in galaxy clusters [29]. He measured these in the Coma cluster (also called 'Abell 1656') and found that the amount of luminous matter is not accountable for keeping the galaxies on their orbits. The velocities measured would lead to a diffusion of galaxy clusters. In spite, Zwicky proposed the existence of a 'dark 'component with a mass 400 times the mass of the luminous matter to keep Newton dynamics valid. The term *dark* refers to the property of non-interaction with electromagnetic radiation.

Later on in the 1970s, measurements of rotation curves of spiral galaxies supported the existence of an unknown DM component [30]: the rotation curves $v(r)$ are measured as the tangential velocity of stars moving around the galactic centre at a distance r from the centre. Measurements of this kind give information on the mass distribution $M(r)$ inside a galaxy. In general, the velocity obtained by assuming gravitational force and centripetal force equal has the form

$$v(r) \propto \sqrt{\frac{M(r)}{r}}. \tag{3.11}$$

At large distances, where the visible mass becomes constant, the velocity should decrease as $1/\sqrt{r}$. Instead, in most spiral galaxies it was observed that the velocity is rather constant with increasing r (sometimes even increasing, see e. g. Ref. [41–43]). Figure 3.5 shows the measured data for $v(r)$ for the galaxy `ngc4157` in red [44, 45]. The model for $v(r)$ including a disk and a bulge component that make up the visible matter of the galaxy is shown as the green curve. In order to resolve the discrepancy between the green curve and the data an additional dark matter halo component is introduced (then: $v_{\text{tot}} = \sqrt{v^2_{\text{disk+bulge}} + v^2_{\text{halo}}}$). The model of the halo is shown in blue. The velocity v_{tot} was fitted to the data, the fitted components are the curves shown. The dark halo mass component has to increase linearly with r to explain the data. While both Zwicky's observations and the rotation curves of galaxies can have alterna-

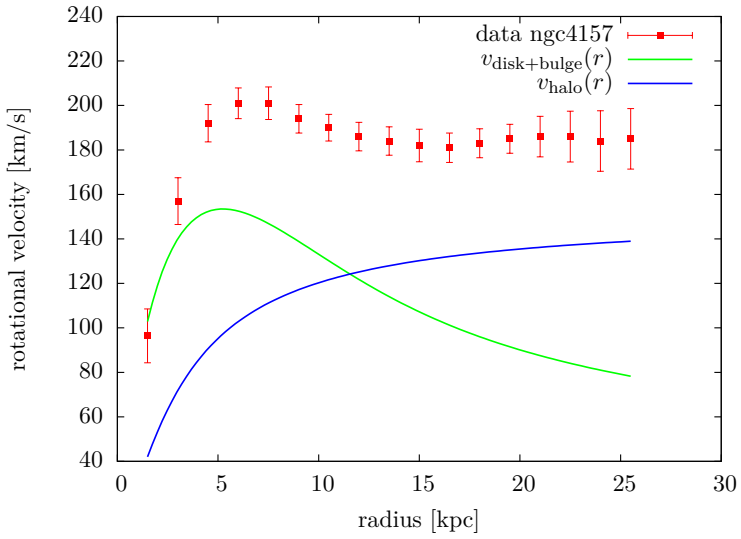

Fig. 3.5: Rotation curve of the spiral galaxy `ngc4157` with fitted disk+bulge component (green) and halo component (blue).

tive explanations other than DM, like modified Newtonian Dynamics ('MOND' theories), data from gravitational lensing cannot be explained by these alternatives. Gravitational lensing is a model independent tool to obtain mass distributions of galaxies and galaxy clusters by studying deflection of light from the gravitational potential of a foreground object. The most prominent measurement w. r. t. DM evidence is the one from the bullet cluster [46]: the bullet cluster is the result of two colliding galaxy clusters. The observation from radiative gas distributions inside the cluster point to an interaction that has taken place between the two colliding clusters since the gas is prominent in the centre. Gravitational lensing data however measures gravity centers displaced w. r. t. the centre. MOND theories would not predict such a behaviour, instead

a present DM component could explain the displacement: when the clusters collided the DM components barely interacted with each other and instead travelled undisturbed.

While these observations from the present universe are already compelling, there is an even more substantial observation from the early universe: the *cosmic microwave background* (CMB). The CMB is the photon radiation originating from about 380 000 years after the Big Bang. The Big Bang initiated the early phase of the hot universe where all photons and nuclei where in thermal equilibrium constantly interacting with each other. When the universe cooled down photons decoupled from the rest of the particles and began to travel freely. Therefore, the CMB is also called *surface of last scattering*. The latest most precise measurements of this radiation yield a temperature of $T = 2.7255 \pm 0.0006$ K[b][8]. The CMB is extremely isotropic supporting the model of *inflation*: it is the same all over the sky, in every direction. There are only small anisotropies of the order of μK. They are these anisotropies that reveal a lot of information about our universe. Therefore, the *angular power spectrum* is examined: it is the temperature difference between two positions as a function of the angular separation (and not orientation, since the CMB is isotropic). Since the temperature fluctuations lie on a sphere they are expressed in a series of spherical harmonics:

$$\frac{\Delta T(\theta,\phi)}{T_0} = \frac{T(\theta,\phi) - T_0}{T_0} = \sum_{l,m} a_{lm} Y_{lm}(\theta,\phi). \tag{3.12}$$

In Eq. 3.12, l denotes the multipole order and is connected to the angle θ via $\theta = \pi/l$ and thus is a measure for the distance on a spherical surface. The modes a_{lm} are assumed to be Gaussian and uncorrelated [47]. For an isotropic sky, all modes m are equivalent. The power spectrum is finally obtained as

$$P_l = \frac{l(l+1)C_l}{2\pi} \qquad \text{with} \quad C_l = \langle |a_{lm}|^2 \rangle. \tag{3.13}$$

The power spectrum as measured by the PLANCK satellite [48] is shown in Fig. 3.6. It exhibits some striking maxima and minima. They originate from acoustic oscillations in the early universe at the time of the photon decoupling. The oscillations are a product of the competing pressure and gravitational force. While the gravitational force leads to compression of dense areas the pressure leads to the exact opposite effect causing the oscillations. At the time of decoupling, these oscillations were frozen. More dense regions exhibit higher temperatures as lower density regions. The first peak in Fig. 3.6 gives information about the geometry of the universe, the second, smaller peak about the baryon density and the abundance of dark matter influences the third peak. The damping tail at high l is due to the surface of last scattering having a finite thickness where not all photons decoupled at exactly the same time. From these peaks we know that the DM is making up about 25.9% of our universe where baryonic matter only contributes ∼4.9% [48]. The open question is what is: this 'dark matter'?.

We know that DM is interacting gravitationally. It must be at most weakly interacting with SM particles, paying respect to the term 'dark', otherwise it likely would have been already detected. It has to be stable on a cosmological time scale (otherwise a decay would imply an exponentially small abundance of dark matter at the present) and has to have the right relic

[b] It is obtained from the intensity of the black-body radiation that is the CMB.

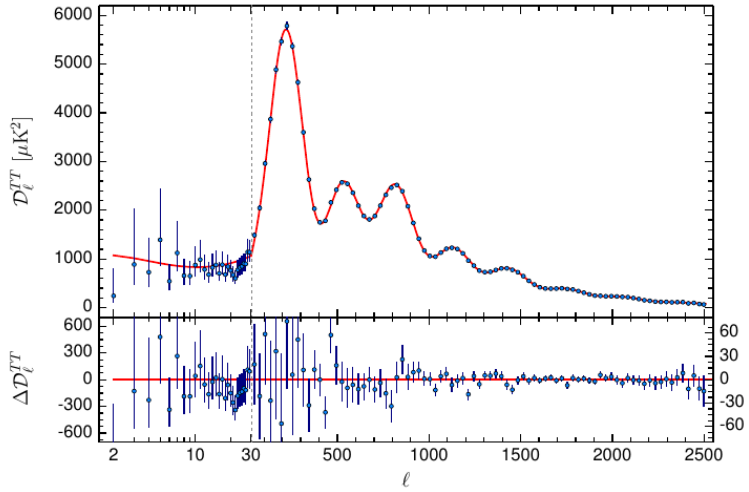

Fig. 3.6: Measured Power Spectrum by PLANCK [48]. The overlayed curve is fitted to the data. The underlying model is the ΛCDM theory.

density consistent with cosmological measurements. There are three different concepts for dark matter:

- **Cold DM**: "Cold" refers to the non-relativistic speed ($v < 0.1c$) of the DM particles. Cold DM is necessary to explain large structure formation in the universe like galaxies and galaxy clusters. Cold DM can play the role of a compactor of structure. The most popular candidate for cold DM is the **W**eakly **I**nteracting **M**assive **P**article (**WIMP**). Other candidates are the sterile neutrino, the axion and primordial black holes[c].
- **Warm DM**: "Warm" refers to the relativistic speed ($0.1c < v < 0.95c$) of the DM particles. These particles move too quickly to be bound to galaxies or clusters and they do not form gravitational lenses. A candidate for warm DM is also the sterile neutrino that is required in certain theories. This scenario is also favoured by some measurements of haloes of 'satellite galaxies' (see e. g. Ref. [49]).
- **Hot DM**: These DM particles travel at ultra-relativistic speeds ($v > 0.95c$). These particles are needed to explain the lensing data of the Abell cluster and in certain theories. But they are assumed to be too light to be responsible for the DM component predicted from cosmology. We already know an example for hot DM which is the neutrino as a Weakly Interacting Light Particle (WILP).

These concepts are not mutually exclusive and can coexist. However, the most favoured concept is the one that DM consists of WIMPs. WIMPs are expected to interact weakly with normal matter. The expected WIMP masses m_χ range from about 10 GeV to a few TeV. Lower masses are excluded by experiments and higher masses are excluded by cosmological considerations. It is assumed that WIMPs were in thermal equilibrium with the SM particles after inflation. This means that they were equally transforming into SM particles as SM particles were transforming

[c] *Sterile neutrinos* denote heavy, right-handed neutrinos that do not couple to the Z-boson and only interact via mixing with SM neutrinos. *Axions* are a consequence of a spontaneously broken "Peccei-Quinn" $U(1)$ symmetry introduced to solve the absence of CP violation in QCD. *Primordial black holes* denote black holes formed during the first second of the universe's existence from a gravitational collapse of density fluctuations.

into WIMPs. When the universe cooled down, WIMP production was suppressed by their mass. One speaks of a 'freeze out' of WIMPs at the temperature $T_F \simeq \frac{m_\chi}{20}$, when the transforming probability into SM particles fell under a certain threshold [8]. From the relic density, the present abundance of DM, it is possible to determine the interaction cross section of DM with SM particles. This indeed leads to a cross section at the weak scale which lends support to the WIMP picture for DM. A favoured WIMP candidate is the lightest supersymmetric particle, the neutralino.

If WIMPs exist, we should be able to detect them. There are three categories of WIMP search experiments:

- **Direct Detection:** A search for WIMP-nucleon interactions is performed: a WIMP might scatter on nuclei of detector material and thereby transfer recoil energy. This recoil energy can be measured e. g. by phonon detection. There are many experiments targeting direct DM detection such as XENON [50], CDMS [51], LUX [52], CRESST [53], etc.. All of these have slightly different materials and background suppression, are sensitive to spin-dependent or spin-independent interactions.
- **Indirect Detection:** A search for annihilation products of WIMP-WIMP interaction. Space experiments detect photons/neutrinos/electrons/positrons/antiprotons and search for a feature in the energy spectrum. Experiments such as Fermi-LAT [54] and MAGIC [55] are space telescopes. Earth based experiments are IceCube [56] or ANTARES [57].
- **Pair Production:** Collider searches aim at the production of WIMPs in pairs. If they really interact weakly there is a chance of producing them directly in collisions with a sufficiently high centre-of-mass energy above $2m_\chi$. The WIMPs will escape the detector just like neutrinos and will leave a signature of missing transverse momentum.

All methods are complementary to each other. This thesis focuses on the pair production of WIMPs using the ATLAS experiment at the LHC (see Chap. 5). This production can be depicted as shown in Fig. 3.7[d]. An advantage with respect to direct detection searches is the better sensitivity to low WIMP masses, that hardly lead to a measurable recoil in a WIMP-nucleon scattering but can be produced in particle collisions. The underlying modelling of WIMPs is discussed in the following.

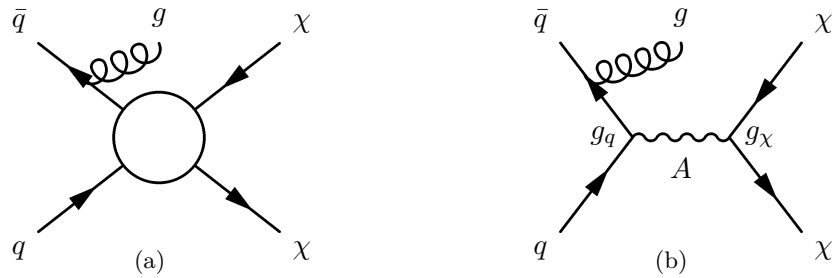

Fig. 3.7: Possible pair production of WIMPs at the LHC: (a) in context of an effective field theory where the blob represents the unresolved physics, a new mediator; (b) in context of a simplified model where A denotes the exchanged mediator with couplings g_q and q_χ to quarks and WIMPs, respectively. The mediator diagram is an example for s-channel production. In both diagrams initial state radiation is added that recoils against the invisible WIMPS.

[d] Rotation of the time axis yields the Feynman diagrams for direct detection (90°) and indirect detection (180°).

3.3.2 Effective Field Theories

A convenient approach to model new physics of which the underlying exact theory is unknown is to employ the use of EFTs. Its advantage lies in the model independence and therefore allows application to different fields of new physics. In general, the EFT simply introduces a new energy scale at which new physics can be probed. This energy scale is a substitute for introducing a new mediator with mass M_{med} and decay width Γ_{med}. The propagator term of the mediator is simplified in EFTs as follows:

$$\frac{1}{q^2 - M_{\text{med}}^2 + im\Gamma_{\text{med}}} \rightarrow -\frac{1}{M_*^2}, \tag{3.14}$$

where q^2 is the transferred momentum and M_* is the new energy scale substituting the new mediator properties. Equation 3.14 only holds if $q^2 \ll M_{\text{med}}^2$, that is, the actual mediator mass cannot be resolved at the energies probed. Figure 3.7(a) illustrates this approach by drawing a blob as the unknown interaction, the mediator mass integrated out. Analogous to Fermi's contact interaction theory replacing the exchange of a W-boson in weak decays like the β-decay of a nucleus, a *contact operator* can be introduced in the Lagrangian to model the production of dark matter particles χ. In general, these terms can be written as

$$\mathscr{L}_{\text{WIMP}} = \frac{g_*}{M_*^2}\mathscr{O}. \tag{3.15}$$

The coupling g_* describes the effective coupling of the four-point vertex between $\bar{q}q$ and $\bar{\chi}\chi$. The operator $\mathscr{O}$ can have different natures: it can be a vector operator ($\mathscr{O} = (\bar{q}\gamma^\mu q)(\bar{\chi}\gamma_\mu\chi)$), an axial-vector operator ($\mathscr{O} = (\bar{q}\gamma^\mu\gamma^5 q)(\bar{\chi}\gamma_\mu\gamma^5\chi)$), a tensor operator ($\mathscr{O} = (\bar{q}\sigma^{\mu\nu}q)(\bar{\chi}\sigma_{\mu\nu}\chi)$, $\sigma^{\mu\nu}$ is a tensor) etc.. An extensive list of such LO operators can be found in Ref. [58]. The dark matter particles χ can be either fermions or scalars. If they are fermions they can have Dirac or Majorana nature, if they are scalars they can be real or complex. The operator examples are given for Dirac WIMPs. In the EFT approach, the different operators will influence the kinematics of the dark matter pair production and the scale M_* will only determine the cross section magnitude. In the case of the WIMP pair production the cross section scales as

$$\sigma_{\text{WIMP}} \propto \left(\frac{1}{M_*}\right)^k, \tag{3.16}$$

where k is determined by the contact operator, for the shown examples $k = 4$ holds.

In the case of direct dark matter search experiments the EFT approach is valid since the transferred momentum is of the order of several keV. However, at the LHC the transferred momentum (q^2) can be as large as several TeV. In this energy regime it is possible to resolve new mediators with masses at the weak scale. In such cases the EFT is not a valid approach anymore, since $q^2 \ll M_*^2$ no longer holds. To assess the sensitivity of the unknown UV completion of the EFT, a *truncation* procedure is introduced. The truncation procedure constrains the production cross section to the valid phase space. The convenient choice is to truncate the cross section if $q^2 > M_*^2$. In ATLAS, the truncation in case of WIMP production requires to discard any events with $q^2 > M_*^2$. Studies on this kind of truncation are presented in App. C.1. Likewise, as introduced for the ADD model, the EFT breaks down if $\hat{s} > M_D^2$. Here, the approach is to deplete the cross section (see Eq. 3.6) by a factor of $M_D^4/\hat{s}^2$.
In any case, the truncation serves to simply illustrate the limitations of the EFT approach.

Instead, the solution followed by the LHC experiments is to employ mainly *simplified models* that include a heavy, Z'-like mediator in the theory [59]. The next section will describe these models.

3.3.3 Simplified Models

In the simplified model approach, a new mediator is introduced that is exchanged between SM particles and the WIMPs. Figure 3.7(b) shows an examples for s-channel WIMP pair production with an additional ISR jet (here: gluon radiation). The couplings to SM particles and WIMPs are denoted by g_q and g_χ, respectively. The connection with the EFT is as follows:

$$M_{\text{med}} \sim M_* \sqrt{g_q g_\chi}. \tag{3.17}$$

For s-channel production this means that in order to produce WIMPs in pairs the mediator mass has to be $M_{\text{med}} \gtrsim 2m_\chi$. In the case of the EFT and maximal couplings ($\sqrt{g_q g_\chi} \leq 4\pi$ to ensure perturbative expansion of the theory) another condition for M_* is $M_* \gtrsim m_\chi/2\pi$. Naturally, a mediator exchange in the t-channel is also possible. The simplified model converges to the EFT if $M_{\text{med}} \gtrsim 10$ TeV.
The nature of the new mediator (A in Fig. 3.7(b)) remains a parameter of the model. A simple model is the assumption of a Z'-like mediator: this is a heavy relative of the SM Z-boson originating from a broken $U'(1)$ gauge symmetry additionally introduced into the theory. A composite vector mediator is another possibility. In either case, the following terms need to be added to the Lagrangian:

$$\begin{aligned}\mathscr{L}_{\text{med}} = &-\frac{1}{4} Z'_{\mu\nu} Z'^{\mu\nu} + \frac{1}{2} M^2_{\text{med}} Z'^{\mu} Z'_{\mu} + i\bar{\chi}\gamma^\mu \partial_\mu \chi - m_\chi \bar{\chi}\chi \\ &+ Z'_\mu \bar{\chi}\gamma^\mu \left(g_{\chi V} - g_{\chi A}\gamma^5\right)\chi + Z'_\mu \sum_q \bar{q}\gamma^\mu \left(g_{qV} - g_{qA}\gamma^5\right) q.\end{aligned}$$

The mediator in this case is either an axial-vector or a vector mediator with the couplings g_A and g_V, respectively. The vector and axial vector couplings to quarks are assumed to be the same for all flavours for simplicity. In general the Z' also has couplings to leptons and gauge bosons. They are not included here since they are not relevant in a monojet search in pp collisions (see next chapter on hadron collider phenomenology). The simplified model introduces four new parameters: the mediator mass M_{med}, the couplings g_q and g_χ and the dark matter mass m_χ. The mediator in Fig. 3.7(b) is denoted A for the reason that the case of an axial-vector mediator will be studied here. The advantage is that the axial-vector interaction is non-zero for Majorana dark matter (in contrast to the vector interaction). It is also a spin-dependent interaction which is more competitive when comparing LHC results with limits from direct detection searches. Here, the mediator width is assumed to be the minimal width as defined in Ref. [60]:

$$\Gamma_{\text{min}} = \frac{g_\chi^2 M_A}{12\pi} \beta_\chi^3 \theta\left(M_A - 2m_\chi\right) + \sum_q \frac{3 g_q^2 M_A}{12\pi} \beta_q^3 \theta\left(M_A - 2m_q\right),$$

where M_A is the mass of the axial-vector mediator ($M_{\text{med}} \equiv M_A$), $\theta(x)$ is the Heaviside step function and $\beta_f = \sqrt{1 - \frac{4m_f^2}{M_A^2}}$ is the velocity of the fermion f with mass m_f in the rest frame of the mediator A. Finally, the cross section of WIMP pair production via a mediator exchange in

the s-channel is

$$\sigma_{\text{WIMP,med}+X} \propto \frac{g_q^2 g_\chi^2}{\left(q^2 - M_A^2\right)^2 + \Gamma_A^2/4} \hat{s}^2.$$

The partonic centre-of-mass energy $\hat{s}$ is not equal to q^2 if additional particles X are produced, like jets from gluon/quark radiation in the case of a monojet-like signature. In the limit case where M_A is $\gtrsim$10 TeV the cross section is the EFT one and the limits for both EFT and simplified models coincide [59, 61].

The t-channel exchange of a heavy mediator can also be considered as a model monojet searches are sensitive to. The physics behind such a simplified model are different as it considers interaction terms of the form (e. g. [62, 63]):

$$\mathscr{L}_{\text{int}} = \lambda_q \bar{\chi} \Phi^* q + h.c., \tag{3.18}$$

meaning a vertex where a heavy mediator Φ couples the dark matter particles directly to SM particles with a cubic coupling λ_q. This coupling scenario and the t-channel production of WIMP pairs is illustrated in Fig. 3.8(a). The interaction term in Eq. 3.18 has the following implications: (1) the mediator Φ must be coloured, (2) to guarantee the stability of the produced WIMPs the mass of Φ has to be larger than m_χ, (3) the term introduces flavour violation into the theory: this is strongly constrained by experiments. Therefore, a minimum flavour violating scheme assumes that the couplings and masses are flavour independent. In order for the masses to be invariant under electroweak gauge symmetries the mediator Φ has to be a complex scalar if χ is a fermion (if χ is a scalar, Φ has to be a fermion). Thus, this simplified model is very close to the MSSM where the squark plays the role of Φ, which can be viewed as the superpartner of q. The width of the mediator can be expressed as a function of the three new parameters in this model: m_Φ, m_χ and the coupling λ_q:

$$\Gamma_\Phi = \frac{\lambda_q m_\Phi}{16\pi} \left(1 - \frac{m_\chi^2}{m_\Phi^2}\right)^2.$$

As already mentioned, the monojet signature can be produced via the process in Fig. 3.8(a). Also possible in pp-collisions is the exchange of the WIMP in the t-channel which leads to a pair production of Φ that decay in turn to quarks and WIMPs. This is depicted in Fig. 3.8(b) and would lead to a final state with 2 jets and $\not{E}_T$.

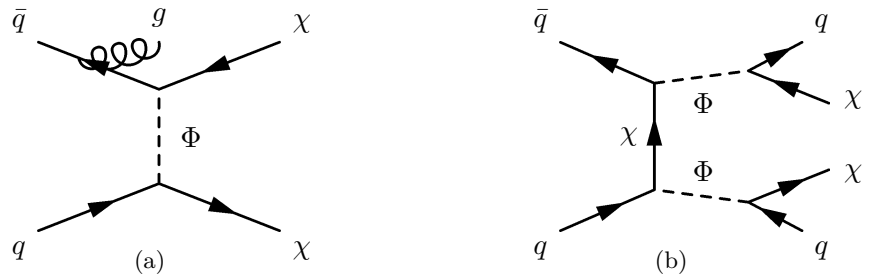

Fig. 3.8: WIMP pair production with 1 additional jet (a) and 2 additional jets (b) involving the mediator Φ: t-channel exchange of Φ (a) and χ (b).

Finally, it has to be noted that the approaches presented above are indeed *simplified* ones: only few parameters have been introduced. The simplified model itself is not a full theory (unlike Supersymmetry) and has some short-comings (axial-vector coupling to fermions breaks SM gauge symmetry and leads to divergence in mono-W cross section [64]). However, more complete models introduce thousands of new parameters and therefore it is still sensible to work with simplified models as introduced here.

Chapter 4

Hadron Collider Physics

In the previous chapters, the basics of the SM and BSM theories have been introduced via the Lagrangian formalism describing particles and their interactions mathematically. This chapter now focuses on the collider phenomenology: the production of particles, the final states produced via decays, the resulting signature in a detector and the modelling of all these physics processes. At the LHC, protons are brought to collision with protons. The proton is a hadron, a composite object, consisting of three valence quarks (uud) and additional quarks and gluons. Thus, the strong force plays a dominant role in hadron collisions.
The physics processes involved in pp collisions can be approximately factorised in the following elements:

- *parton distribution functions* describing the proton,
- the hard scattering of proton constituents with cross section $\hat{\sigma}$,
- *parton showers* involving initial and final state radiation of additional quarks/gluons via QCD parton splitting,
- the *hadronisation* of produced particles to form mesons/baryons,
- the decay of unstable hadrons,
- the *underlying event* resulting from proton remnant interactions and
- electroweak radiation.

All the listed physics processes are described along with their implementation in Monte Carlo simulations in Sec. 4.2.

4.1 Parton Distribution Functions

Figure 4.1 depicts processes in pp collisions in Feynman diagrams. The incoming protons are indicated by the three parallel lines. If the protons have the momenta P_1 and P_2 then the centre-of-mass energy of the pp collision is: $s = (P_1 + P_2)^2$. However, since the proton consists of partons, the actual hard scattering process indicated by the box with cross section $\hat{\sigma}$ on the left in Fig. 4.1 involves the parton momenta rather than P_1 and P_2. The partons interacting carry momentum fractions x_1 and x_2 of the respective protons. Thus, the partonic centre-of-mass energy $\hat{s}$ is defined as $\hat{s} = sx_1x_2$. The probability of a parton a to carry momentum fraction x is described by the *parton distribution function* (PDF) $f_a(x, Q^2)$, where Q^2 is the energy scale of the hard process. In Fig. 4.1 two parton distribution functions $f(x, Q^2)$ and $g(x, Q^2)$ are given for the general scenario of different incoming hadrons. At the LHC f and g are equally distributed. The Feynman diagrams show a simplified picture of what happens

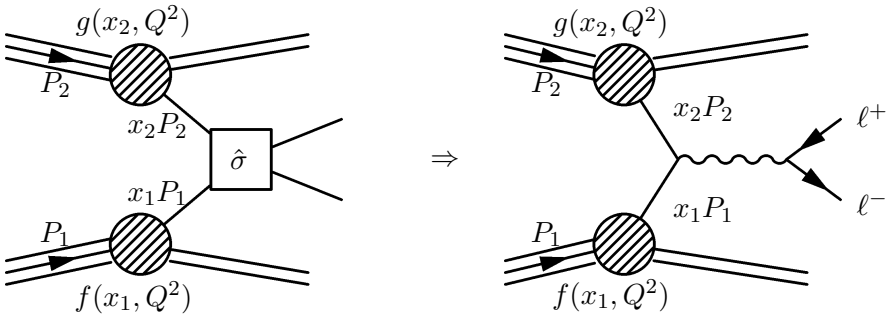

Fig. 4.1: Production mechanism in hadron-hadron collisions illustrating the factorisation theorem: The cross section of the hard-scattering process is denoted by $\hat{\sigma}$. The soft processes are included in the PDFs f and g of the hadrons. The right diagram shows a Drell-Yan production of $\ell^+\ell^-$ as an example for the hard process.

in a hadron collision. As already described in Sec. 2.2.1, the coupling strength of α_s is a running coupling dependent on the energy scale probed due to vacuum polarisation effects. The reference scale μ_R^2 for the renormalisation via the RGE that leads to Eq. 2.3 is introduced. The dependence of α_s on μ_R^2 is included in the cross section: $\hat{\sigma} \to \hat{\sigma}(\alpha_s(\mu_R^2))$. Apart from infinite loop corrections (ultraviolet (UV) divergences) that are renormalised, also *soft* and *collinear* divergences (infrared (IR) divergences) can occur when low energetic gluons are radiated or they are collinear with the mother particle. In that regime, perturbative calculations are not possible anymore. Instead, a so-called *factorisation* scale μ_F^2 can be introduced to separate perturbative (short distance physics) processes from non-perturbative (long distance physics) processes. The non-perturbative processes are parameterised by the DGLAP equations, which will be discussed in Sec. 4.2.2. Finally, the PDFs become $f \to f(x, \mu_F^2)$; the blobs in Fig. 4.1 are a symbol for the non-trivial physics contained in the PDFs. The general choice is to set $\mu_R^2 = \mu_F^2 = Q^2$, the energy scale of the hard scattering process which can be chosen to be $\hat{s}$ (or any other process specific scale, see Sec. 7.5).
The QCD **factorisation theorem** allows for the separation of short and long distance physics, where the PDFs include the long distance processes and $\hat{\sigma}$ contains the short distance processes such that the total cross section for a process $pp \to X$, like Drell-Yan production in Fig. 4.1 (right) as an example, can be written as:

$$\sigma_{pp\to X}(x_1, x_2, Q^2, \sqrt{s}) = \sum_{a,b} \int \mathrm{d}x_1 \int \mathrm{d}x_2 f_a(x_1, Q^2) g_b(x_2, Q^2) \hat{\sigma}_{ab\to X}(x_1, x_2, Q^2, \sqrt{s}).$$

The sum is over all possible partons a and b from the incoming hadrons. The parameters of the PDFs have to be measured in particle collisions, for example via deep-inelastic scattering[a] [65]. The kinematics of these processes give information on the proton content. Likewise, the rapidity[b] distributions of $W^{\pm}$- and Z^0-boson in hadron-hadron collisions can be used to measure the PDFs [66]. Figure 4.2 shows the PDFs for the partons of the proton at a scale of $Q^2 = 100$ GeV^2 for the CT10 PDF sets [67]. The biggest momentum fractions are carried by the valence quarks

[a] Deep inelastic scattering denotes collisions of electrons/positrons with protons. The lepton probes the structure of the proton by interacting with its components and thereby breaking the proton up. These processes have been intensively studied at the HERA collider at DESY.

[b] The rapidity is defined as $y = \frac{1}{2} \ln\left(\frac{E+p_z}{E-p_z}\right)$, where E is the energy of a particle and p_z its momentum along the beam direction.

up and *down*. It is also visible that for lower x gluons dominate the proton content. Quarks of flavours other than up or down constitute the *sea* part of the proton and their probability function is also present in Fig. 4.2.

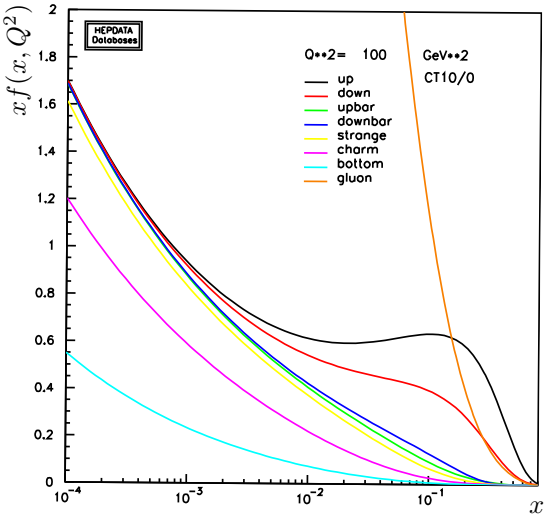

Fig. 4.2: CT10 PDF sets for the scale $Q^2 = 100$ GeV^2. The momentum fraction is denoted by x while $xf(x, Q^2)$ represents the amount of partons at a certain x. The plot is produced via `HEPDATA` [68].

4.2 Monte Carlo Simulation

The complete physics processes happening in particle collisions are simulated using Monte Carlo (MC) event generators. MC simulations are used to model the theory predictions. These predictions are then compared to data to either confirm or reject the theory modelled by the MC. This section gives an overview over the basic MC concepts which are crucial for particle physics analyses.

Monte Carlo methods are devised due to the fact that particle physics interactions are of quantum mechanical nature: Only probabilities for the outcome of a certain process can be predicted. Thus only ensembles of measurements can be used to compare the theory with observations. The fundament of MC generators is to use random number inputs, both used for the event generation and integration, that is discussed next.

4.2.1 Monte Carlo Integration

To calculate measurable quantities like cross sections and differential cross sections of a certain process, one encounters integrals that cannot be solved analytically. In this case, numerical integration can be performed. The best method to do so, is to use MC integration techniques. MC integration techniques use pseudo random numbers as input. Pseudo random numbers are random numbers generated according to a certain distribution. These are used to perform *importance sampling* of a function (see e. g. [69]). The hit-and-miss method is followed combined with the importance sampling to evaluate the integral of a function. The advantage of this method compared to other numerical methods (Simpson rule, trapezoidal rule) is, that the error on the integral scales with $1/\sqrt{N}$, N being the number of sampling points, independent of the function dimension d. There are also other MC integration algorithms.

4.2.2 Event Generation

Being able to calculate integrals makes it now also possible to generate whole events[c]. True random variables are used by MC generators as input as they represent quantum mechanical choices. With this it is possible to calculate the cross section of a given interaction. Every particle collision process is a complex process as illustrated in Fig. 4.3: it includes the hard scattering process, as an example the production of $t\bar{t}H$, as a complex final state, is shown as red blobs. It can be calculated using perturbative QCD (pQCD) with the matrix element (ME) and proton PDFs. The proton remnants can also interact, which is called *underlying event*, depicted in purple. If the initial or final state variables are quarks or gluons they will undergo QCD Bremsstrahlung and develop a *parton shower*. Eventually, the showered particles will form hadrons that can decay further, which is indicated in green. The task of the MC generator is to simulate all these processes, which means that there may be hundreds of particles present in the final state each with ∼10 degrees of freedom. In MC generators, the steps from hard process to final state are handled in a probabilistic way. Hadronisation has to be modelled, as it takes place in a regime, where perturbative calculations are not always possible. Several generators exist that handle different stages of event generation differently. Three general purpose generators are Pythia8 [71], Herwig [72] and Sherpa [73]. Basic principles for each of those and the various steps mentioned are described in the following.

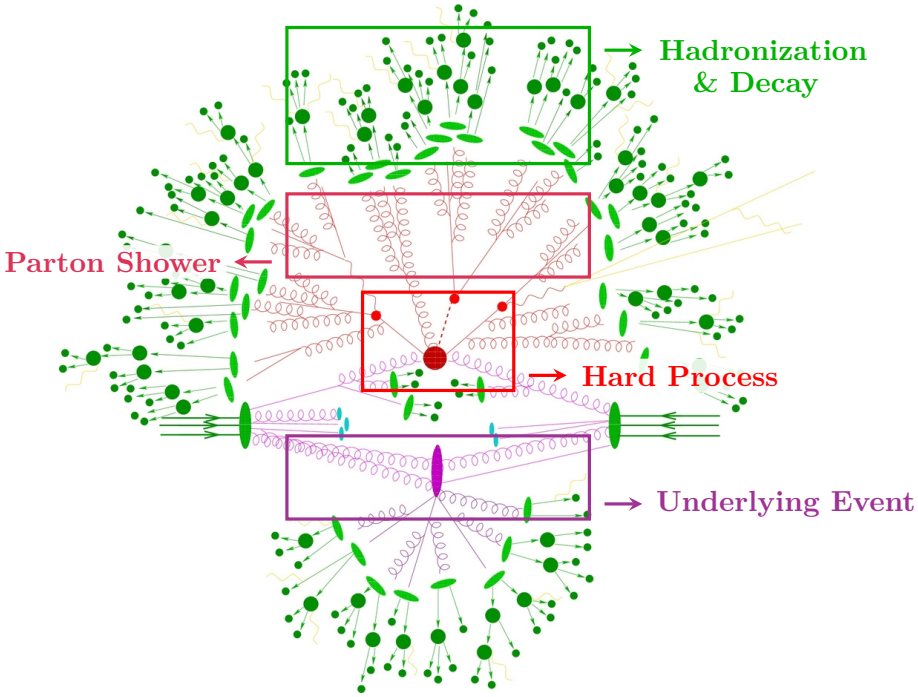

Fig. 4.3: Illustration of typical processes in hadron collisions: the hard process is indicated by the dark red blob, in this case $t\bar{t}H$ production. The three unstable particles decay (red blobs) and produce secondary particles. Another hard interaction can occur from proton remnants (purple blob), the underlying event. Parton shower, hadronisation and decay of hadrons and photon radiation are also indicated in this figure. Figure taken from [73].

[c] The following description is oriented on the introduction to Monte Carlo generators in Ref. [70].

Hard Process

The hard process, the interaction happening at high energy scales producing new particles, is calculated including the ME and the phase space factor. The ME is calculated from all contributing Feynman diagrams to a process. The hard scattering cross section turns out as

$$\hat{\sigma} \propto \int \mathrm{d}\Phi_n(\hat{s}, p_1, \ldots, p_n) \frac{|\mathcal{M}|^2}{\hat{s}}, \tag{4.1}$$

where Φ is the phase space factor dependent on the energy of the incoming particles and the four-momenta of the n outgoing particles. The phase space factor involves real emissions of n particles. The ME is $\mathcal{M}$, summed over all processes with identical final states. As an example for a hard scattering process we can look at the production of a Z- or W-boson in association with jets. These are the processes that make up the main background for the monojet analysis. The hard scattering cross section can be written in components of different jet multiplicity:

$$\begin{aligned} \hat{\sigma}_{V+1 \text{ jet}} &= a_1\alpha_s + a_2\alpha_s^2 + a_3\alpha_s^3 + a_4\alpha_s^4 \ldots \\ \hat{\sigma}_{V+2 \text{ jets}} &= b_2\alpha_s^2 + b_3\alpha_s^3 + b_4\alpha_s^4 + \ldots \\ \hat{\sigma}_{V+3 \text{ jets}} &= c_3\alpha_s^3 + c_4\alpha_s^4 + \ldots \\ &\ldots \end{aligned} \tag{4.2}$$

The sum of these cross sections yields the inclusive $\hat{\sigma}_{V+\text{jets}}$ cross section, where $V = Z, W$. The expansion is done here in α_s with coefficients a_i, b_i, c_i. The lowest order in α_s for the respective processes is called leading order (LO), here, including the terms with $a_1, b_2, c_3, \ldots$ calculated at tree-level. Next-to-leading order (NLO) contributions involve loop corrections to tree-level diagrams (virtual corrections) or real emissions of partons. This means the NLO cross section can be written as

$$\begin{aligned} \hat{\sigma}^{\text{NLO}}_{V+n \text{ jets}} &= \hat{\sigma}^{\text{virtual}}_{V+n \text{ jets}} + \hat{\sigma}^{\text{real}}_{V+n \text{ jets}} \\ &= \hat{\sigma}^{\text{1-loop}}_{V+n \text{ jets}} + \hat{\sigma}^{\text{tree-level}}_{V+n+1 \text{ jets}}. \end{aligned}$$

Next-to-next-to leading order (NNLO) calculations will consequently include 2-loop diagrams to the tree-level and one-loop corrections and real emission of a parton w. r. t. the NLO diagram. Higher order calculation in electroweak (EW) theory correspond to higher orders of α ($\alpha \equiv \alpha_{\text{em}}$). LO calculations usually have larger uncertainties due to their dependence on μ_R^2 and μ_F^2. The dependence is as strong as the first order in α_s not included in the calculation (i. e. dependence of α_s^2 on μ for LO, α_s^3 for NLO pQCD, likewise for EW calculations). Higher order calculations are therefore more precise but require a larger effort to take a multitude of diagrams into account. If the event generation is only available at LO but a theoretical cross section calculation is done at higher orders, so-called k-factors can be employed to normalise cross sections to higher order calculations. In the general case of normalising a N^{r}LO to N^{r+1}LO the k-factor is defined as

$$k = \frac{\sigma_{\text{N}^{r+1}\text{LO}}}{\sigma_{\text{N}^r\text{LO}}}, \qquad r = 0, 1 \ldots. \tag{4.3}$$

In full MC event generations orders of NLO in QCD in the ME are available. Higher orders beyond NLO are usually not simulated by the MC. To obtain higher precision other than normalising the overall cross section via the k-factor it is possible to reweight the simulation to a higher order via parton level theoretical calculation. This will be explained in Sec. 7.6.

The already mentioned occurrence of IR and UV divergences are separated from the hard process and modelled via parton showering and hadronisation.

Parton Shower

As already pointed out, colour charged particles will undergo QCD Bremsstrahlung and will create a shower and produce additional jets. At this step, parton showers (PS) are generated and can be viewed as approximations for higher order MEs. Considering the probability of a parton to split, meaning the probabilities for $q \to qg, g \to gg$ and $g \to q\bar{q}$, as a function of the energy scale, or virtuality Q^2, leads to the so-called DGLAP (Dokshitzer, Gribov, Lipatov, Altarelli, Parisi) equations [74–76], that have been already mentioned in the context of PDFs. They are shown in Eq. 4.4 and describe the probability of parton splitting with the help of the *splitting kernels* $P_{a\to bc}(z)$. The splitting kernels describe the probability of branching with the momentum fraction z for one of the partons after the branching.

$$\mathrm{d}\mathcal{P}_{a\to bc} = \frac{\alpha_s}{2\pi}\frac{\mathrm{d}Q^2}{Q^2}P_{a\to bc}(z)\mathrm{d}z \tag{4.4}$$

$$\text{with} \quad P_{q\to qg} = C_F\frac{1+z^2}{1-z},$$



$$P_{g\to gg} = C_A\frac{(1-z(1-z))^2}{z(1-z)},$$



$$P_{g\to q\bar{q}} = T_R \cdot N_f(z^2+(1-z)^2).$$



The colour factors, or *Casimir operators* of $SU(3)_C$, are $C_A = N_C = 3$ and $C_F = (N_C^2 - 1)/(2N_C) = 4/3$ and are associated to the branching of $g \to gg$ and $q \to qg$, respectively [77]. Therefore, gluon splitting is more likely than quark splitting. N_f is the number of quark flavours and $T_R = 1/2$ is the colour factor corresponding to $g \to q\bar{q}$. Eq. 4.4 describes the evolution of the probability of splitting with Q^2. The evolution can only start at a certain cut-off, about 1 GeV, where the region with singularities from soft and collinear splittings is avoided. Starting from DGLAP and performing successive emissions in several steps will develop a shower. When performing the iteration steps, conservation of probability has to be taken into account:

$$\mathcal{P}_{\text{branching}} + \mathcal{P}_{\text{nothing}} = 1. \tag{4.5}$$

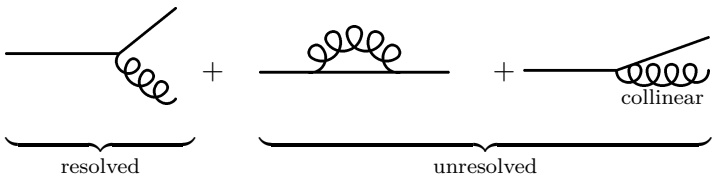

Here, the probability that nothing happens, no parton branching, can be seen as diagrams where also virtual contributions and collinear and soft contributions contribute that cannot be resolved (see Eq. 4.5, Feynman diagrams as examples). A resolvable example in Eq. 4.5 is the $q \to qg$ branching. The probability that at a given time T nothing has happened is the product of

probabilities that nothing happened in the time intervals before, e. g.:

$$\mathcal{P}_{\text{nothing}}(0 < t \leq T) = \mathcal{P}_{\text{nothing}}(0 < t \leq T_1) \cdot \mathcal{P}_{\text{nothing}}(T_1 < t \leq T). \tag{4.6}$$

Combining Eq. 4.5 and Eq. 4.6 leads to the probability that something happens at time T, if it did not happen already before:

$$\mathrm{d}\mathcal{P}_{\text{first}} = \mathrm{d}\mathcal{P}_{\text{branching}} \cdot \exp\left[-\int_0^T \frac{\mathrm{d}P_{\text{branching}}}{\mathrm{d}t}\mathrm{d}t\right] \tag{4.7}$$

This way it is ensured that the total probability for a branching cannot exceed unity. This concept is known as *Sudakov form factor*, the factor itself being the exponential term in Eq. 4.7 [78]. The relevant time scale in parton showers is $t \sim 1/Q$. Combining the Sudakov concept with DGLAP yields Eq. 4.8.

$$\mathrm{d}\mathcal{P}_{a\to bc} = \frac{\alpha_s}{2\pi}\frac{\mathrm{d}Q^2}{Q^2}P_{a\to bc}(z)\mathrm{d}z \exp\left[-\sum_{b,c}\int_{Q^2}^{Q^2_{\max}} \frac{\mathrm{d}Q'^2}{Q'^2}\frac{\alpha_s}{2\pi}\int P_{a\to bc}(z')\mathrm{d}z'\right] \tag{4.8}$$

In this way, the Sudakov factor provides a physical way to handle cancellations between real and virtual divergences. This approach is not exact but a sensible approximation. The cascade evolution until a lower cut-off scale can follow different paths: in SHERPA the evolution is Q^2 ordered. Other possibilities are evolutions in $E^2\theta^2$ with θ being the emission angle (HERWIG approach) or in p_T^2 (ARIADNE approach [79], PYTHIA8). The described procedure based on DGLAP and the Sudakov form factor can be applied to final state radiation (FSR). The application to initial state radiation (ISR) is more complicated as kinematics are different and the non-perturbative initial state of the colliding hadrons has to be taken into account. This is done by the PDFs which are themselves evolved via DGLAP:

$$\frac{\mathrm{d}f_b(x,Q^2)}{\mathrm{d}(\ln Q^2)} = \sum_a \int_x^1 \frac{\mathrm{d}z}{z} f_a(x',Q^2)\frac{\alpha_s}{2\pi}P_{a\to bc}\left(z = \frac{x}{x'}\right).$$

The splitting kernels agree to LO with the ones describing FSR evolution. They differ for higher orders. Whereas the FSR shower develops from high virtualities down to the on-shell mass of the particles, thus a space-like shower ($p^2 < 0$), the ISR shower goes from small virtualities to high virtualities as it approaches the hard process, thus a time-like shower ($p^2 > 0$). Conveniently, a backward evolution is performed starting from the hard process [80]. It involves the conditional probabilities included in the Sudakov factor reversed in time w. r. t. the description above.

Matching of Matrix Element and Parton Shower

ME calculation and PS are two essential steps in the event generation. The ME accurately describes well separated jets, whereas the PS produces a good description of the internal jet structure. Both ME and PS have to be matched to avoid double counting and ensure full phase space coverage. Double counting may occur when a certain process with n jets from the ME will also appear for an ME process with $n-1$ jets, that received an additional jet via PS. There are different strategies how to match ME and PS. Popular matching algorithms are the Catani-Krauss-Kuhn-Webber (CKKW [81] within SHERPA) and the Michelangelo L. Mangano (MLM [82] within ALPGEN [83]) scheme. These methods use different resolution parameters to divide the phase space in a region with high momentum, well resolved jets (ME description)

and low-momentum unresolved jets (PS description). The CKKW scheme generates a parton branching history for a given final state via the k_t-algorithm [84]. Then the ME is reweighted with α_s for every vertex and the Sudakov factor for lines between vertices. The initial condition for the PS is then reset to match the reweighted ME. If the parton shower produces a hard jet that is well separated according to the k_t algorithm the jet is vetoed. The MLM algorithm constructs jets with a cone algorithm for a certain final state after showering. The radius of the cone is R_{jet}. The jets can be matched to the original parton if $\Delta R(\text{jet, parton}) < R_{\text{jet}}$ holds. If every jet can be matched to a parton the event is accepted. Events with unmatched jets are vetoed. Individual jet multiplicities are combined. There is an extra sample with all events containing more jets than partons.

Hadronisation

Once the parton shower has been developed, the hadronisation step has to be simulated. Hadronisation cannot be described from first principles but rather models have to be utilised. There are two basic approaches to the hadronisation: one is the *string fragmentation* model [85], implemented in Pythia8, the other is the *cluster fragmentation* model [86], implemented in Herwig and Sherpa.
The string model is based on the assumption of linear confinement: the field between quarks of distance r to each other is $V = \kappa r$ with κ being a string tension: the field can be seen as a tube or string that stretches between the quarks. The field lines are the string, which breaks when a new $q\bar{q}$ pair is created. The string breaks into hadrons along its length with uniform probability in rapidity. Gluon emissions represent kinks on the strings. The string fragmentation proceeds until only on-shell hadrons remain. Charm quarks and heavier quarks are not expected to be produced in soft fragmentation.
The cluster model forces that all gluons branch according to $g \to q\bar{q}$ to form finally colour-singlet clusters, while keeping track of the colour flow. Eventually the clusters decay isotropically into hadrons according to their phase space weight.
Both approaches have advantages and disadvantages but serve their purpose. The hadrons may not be stable and have to be decayed further.

Underlying Event

Underlying events (UE) denote the interaction that can occur between proton remnants, such as the purple part of Fig. 4.3. These cannot be calculated in pQCD, but have to be simulated based on phenomenological models, with various approaches [87, 88]. These models are then tuned to observations in real collisions. For this, multijets events are used.

4.2.3 Detector Simulation

The full physics simulation of particle collisions is done in the previously described MC event generation. The final states of the events are described on particle level (hadrons, leptons, photons). These have to be further propagated to the detector level, to be able to compare actual measurements with MC outputs. In Atlas, detector simulation is performed via the Geant4 toolkit [89] or via the Atlfast II simulation tool [90]. The step of simulating the passage of produced particles through the experimental apparatus is called 'MC radiation transportation', or simply detector simulation. This step requires the most computation time. While the physics within the MC generators is the same for all experiments at a collider, the detector simulation is individual for each experiment, beginning from the beam pipe to the end of the cavern, the

detector is located in. Detector simulation is non-deterministic, meaning that random numbers are used as input to reproduce distributions instead of solving equations. The geometry of a detector and the material used must be modelled. If the lifetime of a particle is long enough, detector simulation may also take over the task of simulating its decay. When transporting a particle through the detector one has to simulate Bremsstrahlung, pair creation, multiple scattering etc.. Particles are transported through the detector until their energy (E_{kin}) falls below a certain threshold, where the simulation is over. Not only energy deposits, electric and magnetic field effects and the creation of new particles are modelled, but also the electric current and voltage signals, thus the detector response is simulated. Thereby same reconstruction chains can be used which are later on applied to real data.
When performing detector simulation one has to find a compromise between low CPU time and accuracy of the modelling: not too detailed physics models and detector geometry can be included (e. g. screws, cables etc. can never be modelled).

4.3 Monte Carlo Generators

A number of MC generators commonly used in data analyses have been already mentioned. The generators used for this thesis will be briefly mentioned here, a more detailed description of the modelling is given in Sec. 7.5.
The following MC generators are used:

- **Powheg** [91]: An event generator that simulates events with NLO ME calculation in pQCD. It is usually interfaced with Herwig or Pythia8 to simulate the PS and UE.
- **Sherpa**: As already mentioned, it is a multi-purpose generator. The ME is calculated to LO or NLO in pQCD precision depending on the respective process. It is specialised on simulating $2 \to n$ processes in inclusive samples, where the n real emissions are called *multi-legs*, stemming from the phase space element in Eq. 4.1. PS and UE event are also modelled within Sherpa. The cluster model is used for hadronisation, CKKW for ME and PS matching.
- **Pythia**: Like Sherpa a multi-purpose generator. The ME is calculated at LO, it is specialised on $2 \to 2$ processes, where additional jets can be added via PS. It can simulate underlying events and minimum bias events; the string model is utilised for hadronisation.
- **MadGraph** [92, 93]: Like Sherpa the generator is specialised on $2 \to n$ processes, that is a multi-leg generator with the ME calculation at LO or NLO in pQCD. MadGraph is interfaced with Pythia8 for PS, hadronisation and UE. MLM matching for the PS and ME overlap removal is used.

Corresponding physics processes, parameter choices, detector simulation and PDFs sets utilised in the thesis's analysis are detailed in Sec. 7.5.

Chapter 5

Experimental Setup

The monojet analysis uses data recorded by the ATLAS detector [94, 95] at the Large Hadron Collider, LHC. The LHC located at CERN (*Conseil Européen pour la Recherche Nucléaire*) near Geneva, provides accelerator facilities for various different experiments, amongst them the ATLAS experiment. The LHC is introduced in the next section followed by a description of the ATLAS detector.

5.1 The Large Hadron Collider

The Large Hadron Collider is a synchrotron accelerator with a circumference of about 27 km located in a tunnel on average 100 m underground traversing the border of France and Switzerland, that formerly hosted the Large Electron Positron collider, LEP. The LHC accelerates protons in two directions colliding them at four different interaction points. These are occupied by ATLAS, CMS (Compact Muon Spectrometer) [96], ALICE (A Large Ion Collider Experiment) [97] and LHCb [98]. The design centre-of-mass energy of 14 TeV can only be reached by making use of CERN's pre-accelerator facilities. First, protons are produced by ionising hydrogen atoms. They are then accelerated up to 50 MeV by the linear accelerator LINAC2. The protons are passed to the BOOSTER which is a circular accelerator. BOOSTER passes protons with an energy of 1.4 GeV to another synchrotron, the PS storage ring. PS accelerates the protons to 25 GeV before they are injected to the biggest pre-accelerator, the SPS synchrotron. SPS is able to increase the proton energy up to 450 GeV. Finally, bunches with about 10^{11} protons are injected to the LHC that reaches energies at the TeV scale. Proton bunches are accelerated in two opposite directions, requiring two distinct beam pipes. The bunch spacing for the majority of data taking periods in 2015 and 2016 is 25 ns. In order to bend the proton beams that consist of 2808 bunches on a circular path, dipole magnets with a magnetic field of about 8.6 T are installed. In addition, quadrupole and sextupole magnets take care of focusing the beams. Both magnets and accelerating elements (cavities) are super-conducting and need to be cooled down to temperatures of about 1.9 K by liquid helium kryostats. Apart from *pp* collisions that are produced for the majority of the running time, the LHC is also running with proton-lead ion collisions and lead ion-lead ion collisions, typically for a few weeks at the end of a year. In the following, the focus is on *pp* collisions only.

5.1.1 Luminosity

An important parameter of an accelerator is the so-called *luminosity*. The luminosity $\mathcal{L}$ relates the observed event rate $\mathrm{d}N/\mathrm{d}t$ with the cross section of a certain process, σ:

$$\frac{\mathrm{d}N}{\mathrm{d}t} = \sigma\mathcal{L}. \tag{5.1}$$

More precisely, the quantity $\mathcal{L}$ is called *instantaneous* luminosity, it has units of area^{-1}·time^{-1}. The higher this number, the higher the number of events that can be observed in collision experiments. Eq. 5.1 can be rewritten in the following way:

$$\mathcal{L} = f\frac{N_b \cdot \mu}{\sigma_{\text{obs}}}, \tag{5.2}$$

where μ denotes the interaction rate per bunch crossing, f the revolution frequency of bunches in the accelerator ring, N_b the number of bunches and σ_{obs} is the total interaction cross section in pp-collisions that can be observed in the detector[a]. The instantaneous luminosity is dependent on how well the colliding beams can be focused onto one interaction point where they meet. Therefore, the spread of a beam has to be small to obtain a high $\mathcal{L}$. The cross sectional area of the beam can be expressed by $4\pi a_x a_y$, assuming the beam spread a_x and a_y in both x- and y-directions to be Gaussian. The values for a_x and a_y are measured in a *Van-der-Meer scan*: the beam positions are scanned in both x- and y- directions and simultaneously μ is measured. For maxima of μ the beams overlap fully, for minima of μ the edges can be determined. Finally, Eq. 5.2 transforms to

$$\mathcal{L} = f\frac{N_b \cdot n_1 n_2}{4\pi a_x a_y}, \tag{5.3}$$

and $\mathcal{L}$ can be calculated, where n_1 and n_2 are the number of protons in the two colliding bunches. During a run, $\mathcal{L}$ will decrease in time due to fewer protons from former bunch crossings being left that can interact and the widening of the beam spread. Typically, in ATLAS a run is divided in time intervals, the so-called `lumiblocks`. These are time intervals in which the instantaneous luminosity is about constant. Figure 5.1 shows just exactly this behaviour in an example run of 2010. The *integrated* luminosity, $\int \mathcal{L} dt$, is a measure for the total data collected in a given time-

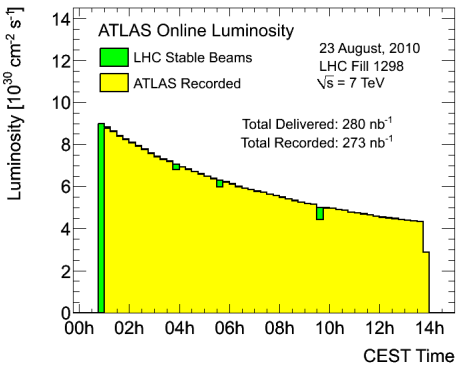

Fig. 5.1: Example of a data run during pp collisions in 2010 recorded by ATLAS [99]. The time axis is divided in lumiblock intervals that have a defined $\mathcal{L}$. The slope seen is characteristic.

span. The LHC has produced pp collision data in Run 1 (2010-2013) and Run 2 (2015 onwards) with a 2 year technical stop in between allowing for upgrade activities of both the accelerator and detectors. During Run 1 the LHC has run with a centre-of-mass energy of 7 TeV (2010-2011) and 8 TeV (2012). In Run 2 the centre-of-mass energy was ramped up to $\sqrt{s} = 13$ TeV, close to the design centre-of-mass energy of 14 TeV. Figure 5.2(a) shows the integrated luminosity

[a] $\sigma_{\text{obs}} = \mathcal{A} \cdot \sigma_{pp}$, where $\mathcal{A}$ accounts for the capability of a detector to detect all events happening in pp collision with a cross section of σ_{pp} that is not 100%.

achieved throughout Run 1 and Run 2. The record is set by 2016, where the total delivered integrated luminosity amounts to $\sim 39\ \mathrm{fb}^{-1}$. The design peak luminosity of $10^{34}\ \mathrm{cm}^{-2}\mathrm{s}^{-1}$ has been reached and slightly surpassed during 2016 data taking (see Fig. 5.2(b): peak luminosity of $1.37{\cdot}10^{34}\ \mathrm{cm}^{-2}\mathrm{s}^{-1}$).

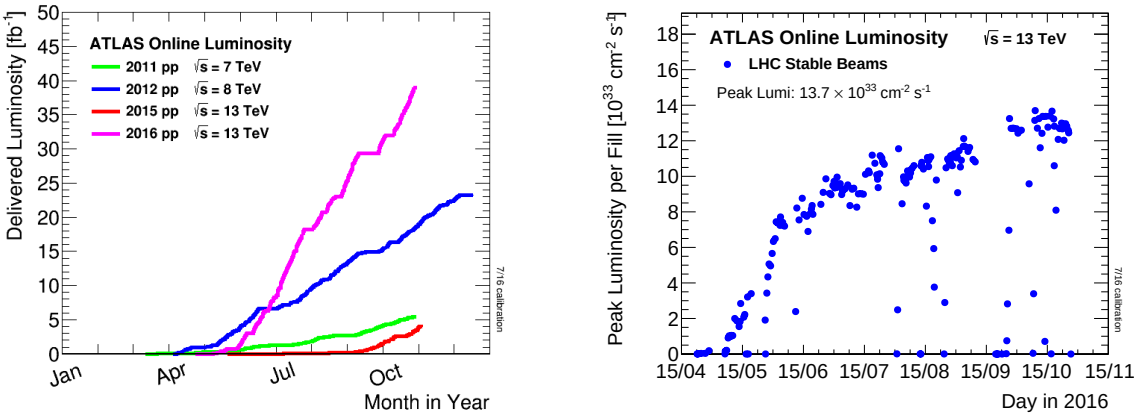

(a) (b)

Fig. 5.2: (a): Integrated luminosity $\int \mathcal{L}\mathrm{d}t$ recorded by ATLAS in the years 2011, 2012, 2015 and 2016 as a function of time. (b) Instantaneous luminosity $\mathcal{L}$ as a function of time for 2016 [100] runs.

5.2 The ATLAS Detector

Being located at one of the four interaction points of the LHC, ATLAS (A Toroidal LHC ApparatuS) is one of two multi-purpose detectors, initially designed to search for the Higgs boson and other yet unknown physics that may be present at the high-energy frontier explored at the LHC. With its mass of 7 000 tons, length of 44 m and diameter of 25 m, the ATLAS detector represents the largest high-energy physics detector worldwide [94, 95]. It is a cylindrical shaped detector, forward-backward symmetric around the interaction point (IP) covering almost the full solid angle. It consist of four main subcomponents: the inner detector (ID), responsible for particle tracking, the calorimeters for measuring the energy of particles, the muon spectrometer for identifying muons and measuring their momentum and the magnet system consisting of solenoidal and air-cored toroidal magnets. Fig. 5.3 shows a computer simulated cut-away view of the full detector displaying the mentioned subcomponents and their position. The subcomponents are described in more detail in the following.

5.2.1 Coordinate System

Variables of particles traversing the detector are described in a right-handed cartesian coordinate system (x, y, z). The z-axis points along the beam axis. The x-axis points to the centre of the LHC, while the y-axis points vertically upwards. The so-called *transverse* plane is spanned by the x, y-plane and is orthogonal to the original proton-direction. The azimuthal angle ϕ is measured in the transverse plane. The polar angle θ is the angle between the particle's momentum and the z-axis. Commonly used variables such as the transverse momentum p_T and the transverse energy E_T can thus be obtained via $p_T = p \sin\theta$ and $E_T = E \sin\theta$, respectively, where p is the magnitude of the 3-momentum vector and E the total energy of a particle measured in the

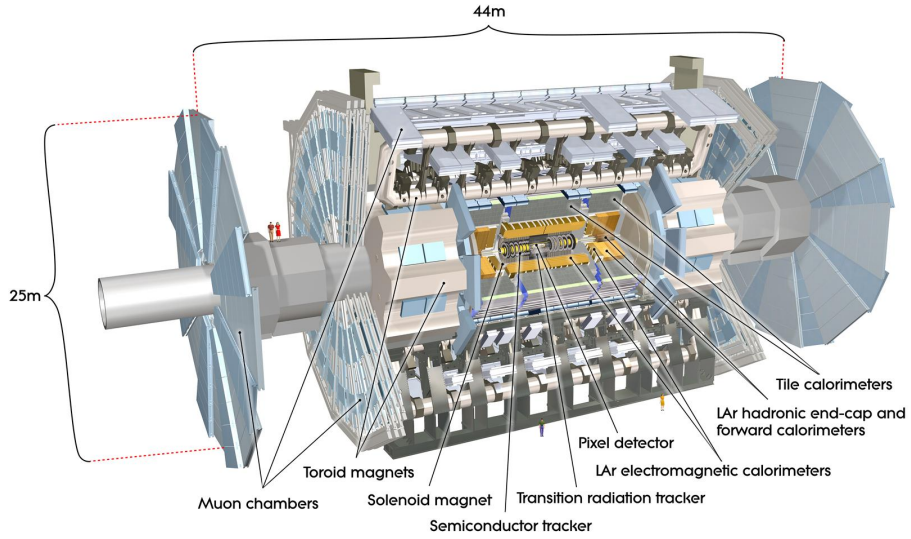

Fig. 5.3: Cut-away view of the ATLAS detector. The various components are indicated as well as the measures in length and diameter of the detector [95].

calorimeters and the muon system. An important variable is the *pseudo-rapidity* η, defined by:

$$\eta = -\ln\left(\tan\left(\frac{\theta}{2}\right)\right).$$

Differences in η are invariant under Lorentz boosts along the z-axis for massless particles. Various different detector components cover different regions in η. The transverse plane with $z = 0$ corresponds to $\eta = 0$ and the beam pipes to both $\pm z$ directions correspond to $\eta = \pm\infty$. Spatial distances are expressed by ΔR:

$$\Delta R = \sqrt{\Delta\eta^2 + \Delta\phi^2}.$$

5.2.2 The Inner Detector

In particle collisions, charged particle tracks are reconstructed by detecting ionisation signals, scintillation signals, Cherenkov photons or photons from transition radiation. The goal is to measure the particle momentum via the deflection of the track in a magnetic field, which also serves to determine the charge of the particle and to reconstruct interaction vertices or decay vertices. The latter is crucial in terms of flavour tagging, where a long-lived particle may decay into other charged particles and produce a secondary vertex (e. g. c-/b-tagging). The inner detector of ATLAS is the first subdetector traversed by particles created in the pp collision and is closest to the beam pipe. The ID of ATLAS is surrounded by a solenoid magnet that provides a magnetic field of 2 T in order to bend the tracks. Typically, the momentum resolution of the tracking detector decreases with increasing momentum since high energetic particle tracks are hardly bend in the magnetic field. Thus, the relative momentum resolution behaves like $\sigma_p/p \propto p$. The ID consists of the pixel detector closest to the beam pipe, followed by the semiconductor tracker (SCT) and the transition radiation tracker (TRT). The pixel and the SCT are made of silicon sensors where charged particles create a signal via ionisation: the semiconductor material is doped and possesses np-junctions and traversing charged particles produce electron-

hole pairs in the depleted region of the silicon sensors. The electron-hole pairs then travel to opposite poles and thereby create an electrical signal that can be readout. Since May 2014, before the start of LHC Run 2, the so-called Insertable B-Layer (IBL) has been installed as the closest pixel layer to the beam axis. The radius of the beryllium beam pipe was decreased to 25 mm to allow room for the IBL. It sits now 3.2 cm away from the beam axis and its purpose is to improve vertexing and provide additional information to the pre-existing three pixel layers. The pixel size of the IBL is 50×250 µm^2 [101]. Two different kind of sensors are used: planar sensor in the centre and 3D sensors for large $|\eta|$. The other pixel sensors are planar sensors with a size of 50×400 µm^2. The pixel detector possesses about 80.4 million readout channels. It is required to be radiation hard since its close proximity to the beam pipe means the largest particle flux in the whole detector. At the same time the pixel detector is build out of light material in order to avoid multiple scattering.

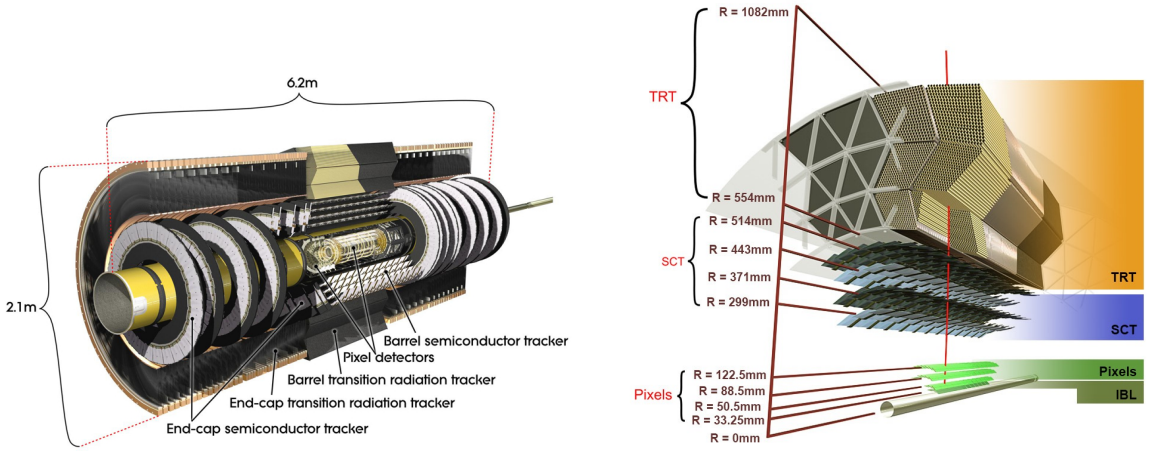

Fig. 5.4: View of the ID tracking detector [95]: Left: components of the ID are shown with barrel and end-cap regions. Right: Transverse view of the central ID illustrating a path of a traversing particle through the various layers (red line). The numbers given are distances to the beam axis. The IBL is installed since May 2014 [102].

The SCT that is installed behind the pixel detector uses silicon microstrip sensors with a strip pitch of 80 µm. It employs the same working principle as the pixel detector only with a larger dimension. Both SCT and pixel consist of a central region with concentric cylindrical layers around the beam axis and two end-cap regions at each side of the IP where the pixel/strip sensors are arranged on disks perpendicular to the beam pipe. The SCT consists of 4 layers in the central region and is readout by 6.3 million channels. Both the SCT and pixel detector cover a region of $|\eta| < 2.5$. The sensors are operated at low temperatures of -5°C to -10°C which are achieved via CO_2 cooling.
The final component of the ID that is furthest away from the beam axis is the TRT. It consists of Kapton straw tubes with a conductive coating and a diameter of 4 mm that are filled with a gas-mixture of 70% Xenon, 27% CO_2 and 3% O_2. In the centre of the tube, a gold-plated tungsten wire (30 µm) acts as anode while the straw tube is the cathode. In the barrel region they are aligned parallel to the beam axis, in the end-caps they are arranged radially in wheels. The TRT covers a region in pseudo-rapidity of $|\eta| < 2.0$. The tracking information in the TRT stems from the ionisation of the gas molecules when a charged particle traverses. The drift time of the

created charge to the anode/cathode is measured and allows to reconstruct spatial information in R-ϕ of the particle. It uses information from 351 000 readout channels. Although only two space dimensions can be reconstructed, the TRT provides significant information on the tracks due to the longer lever arm and almost continuous tracking. In addition, information on the identity of traversing particles is obtained by detecting transition photons: these are produced if a relativistic particle crosses the interface of two materials with different refractive indices, i. e. $n_1 \neq n_2$. Therefore, the drift tubes are interleaved with radiators (polypropylene foils or fibres) that will produce measurable X-rays if an electron passes through and thus provides electron-pion separation.
Figure 5.4 shows two different views of the ID. The left side illustrates the different components in barrel and end-cap regions while the right side figure displays an example path a particle produced at the IP may take and gives the distances of each tracking layer to the beam axis.

5.2.3 The Calorimeters

Calorimeters are used to measure the energy of particles, such as photons, electrons and hadrons (neutral or charged). The principle of calorimetry is to absorb the particle fully and detect their released energy. The released energy can be measured from so-called particle *showers* evolving when a particle is stopped in dense material and produces either a charge signal via ionisation or a light signal in a scintillating medium. The particle showers contain secondary particles produced via interaction with the calorimeter material. One distinguishes electromagnetic and hadronic calorimeters. In an electromagnetic shower electrons or photons lose energy via Bremsstrahlung and e^+e^--pair creation, respectively. The evolving shower of N secondary particles will stop if the energy of the secondaries is not high enough to produce in turn other secondary particles. The same occurs in hadronic showers, the difference being that hadrons interact strongly with the nuclei of the calorimeter material. The evolution of the remaining energy of a particle with initial energy E_0 passing through the detector as a function of travelled distance x is given in the following:

$$\langle E(x) \rangle = E_0 \cdot \mathrm{e}^{-x/X_0}.$$

The parameter X_0 is called radiation length and describes the average distance a particle travels in which it loses a fraction of 1/e of its original energy. The value of X_0 is dependent on the detector material. The particle energy can only be measured if the shower is fully contained in the calorimeter and thus X_0 should be a small number. Electromagnetic calorimeters typically have a length of several X_0 ($\sim 20 \cdot X_0$).
In hadronic showers, the radiation length is replaced by the parameter λ, which is a scale for the shower length. Hadrons lose their energy in nuclear interactions and λ is typically larger than X_0 which explains why hadronic calorimeters are bigger and are placed behind the electromagnetic calorimeters. Hadronic calorimeters have a lower response than electromagnetic calorimeters due to the different nature of hadronic showers: not all the energy can by transformed into a measurable signal when muons or neutrinos are produced in a hadronic shower, that can not be absorbed and carry away their energy fraction. Energy can also get lost in nuclear reactions that do not lead to scintillation light or charge production. A hadronic shower will always contain an electromagnetic component due to the production of neutral π^0 mesons which decay instantly via $\pi^0 \to \gamma\gamma$. Since the response to electromagnetic and hadronic components is different this leads to a non-linear response of the calorimeter. The energy resolution of the calorimeter improves

with increasing particle energy and can be described by Eq. 5.4[b].

$$\frac{\sigma(E)}{E} = \frac{a}{\sqrt{E}} \oplus \frac{b}{E} \oplus c. \tag{5.4}$$

The first term proportional to a is the stochastic term stemming from Poissonian fluctuations of the particle number N in a shower, where $\sqrt{N} \sim \sqrt{E}$ holds. The second term with b stems from noisy detector components. The constant term c accounts for dead detector material (support structure, electronic readout), calibration uncertainties, non-uniformity and non-compensation of the calorimeter.

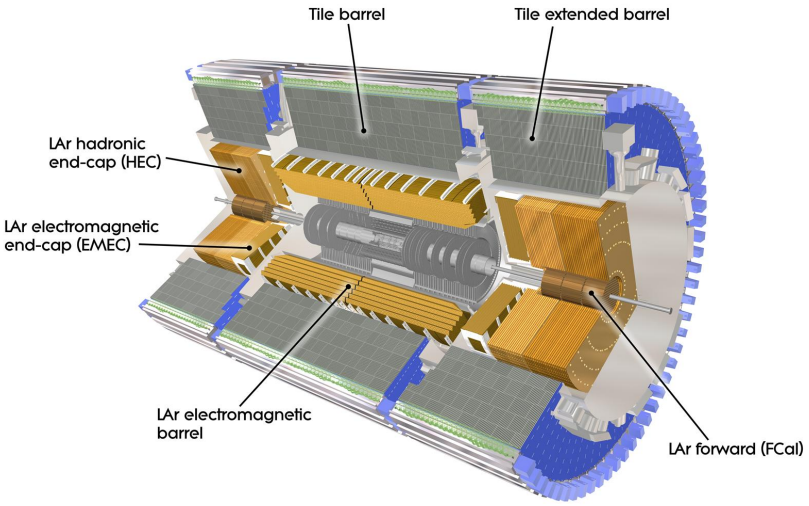

Fig. 5.5: Cut-away view of the electromagnetic and hadronic calorimeter that are located outside the solenoid magnet that houses the ID [95].

Both electromagnetic and hadronic calorimeters of ATLAS are *sampling* calorimeters: this means they consist of alternating layers of stopping material and active material that produces a measurable signal output[c]. The electromagnetic and hadronic calorimeters are also divided into a barrel region and two end-cap regions. They exhibit a high granularity in order to also provide position information. Additional forward calorimeters exist that cover high-$|\eta|$ regions. All calorimeter parts are depicted in Fig. 5.5. The electromagnetic calorimeter shown in copper-colour is composed of alternating lead and liquid Argon layers (LAr). The lead stops particles, their secondaries produce charge signals in the LAr via ionisation. An external electric field is applied and charge signal read out by accordion-shaped Kapton electrodes. The LAr calorimeter is assembled from modules, segmented in ϕ and η with a high granularity as can be seen in Fig. 5.6. The modules are also segmented in three layers in y-direction. The first one is called presampler which provides identification and position information. The second layer is the longest ($16X_0$) and contains the shower maximum. Fast readout from the electrodes is used for triggering (see Sec. 5.2.7). The barrel and end-cap components cover the region $|\eta| < 3.2$. An additional forward calorimeter covers the region of $3.2 < |\eta| < 4.9$. The first layer is made of copper/LAr for electromagnetic measurements and the second and third layer

[b] $\oplus$: add the terms in quadrature: $a \oplus b \to \sqrt{a^2 + b^2}$.

[c] A *homogeneous* calorimeter consists of one material that can stop particles and at the same time create a signal output.

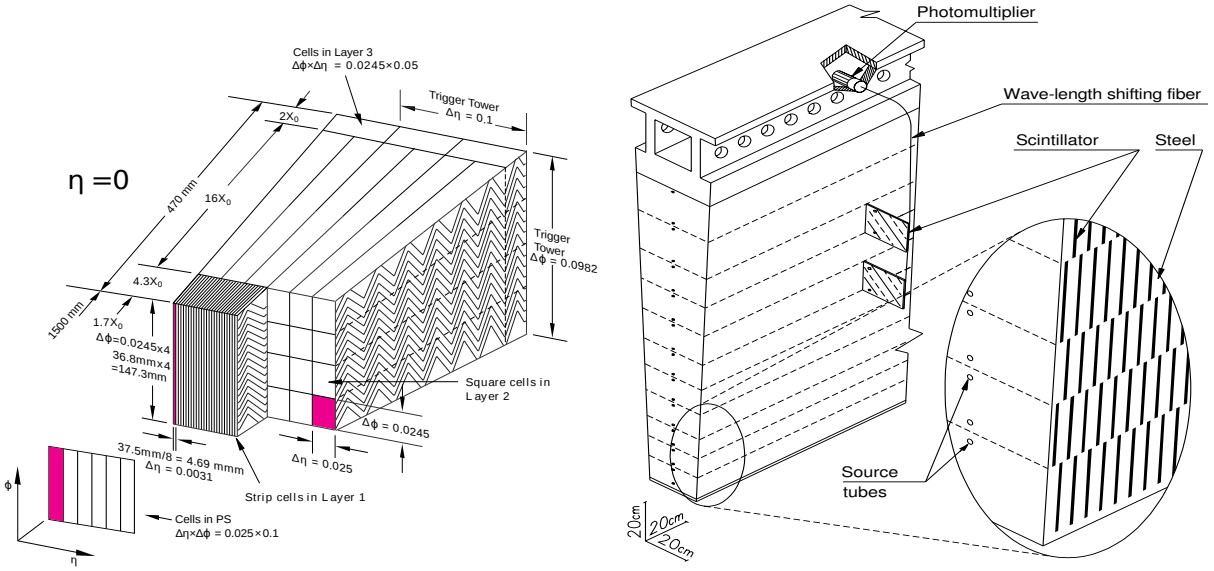

Fig. 5.6: Concept of LAr (left) and Tile (right) modules: length measures are given, also in terms of X_0 and the accordion shape is displayed for the LAr module. The layers of a Tile module and their readout is shown. Also tubes for moving a ^{137}Cs source for calibration are shown.

use tungsten as stopping material with LAr as active material for hadronic measurements. The hadronic calorimeter is made of low-carbon steel plates alternating with plastic scintillator tiles as active material. The tiles will produce scintillation light that is read out by photo multiplier tubes, connected from both sides in a module via wavelength shifting fibres (see Fig. 5.6 right). There are 64 modules each in long barrel and extended barrels covering the full azimuthal angle. They are segmented in three layers and additionally in η. The central region extends to about 11λ for full shower containment and avoiding of punch-through effects into the muon system. Long barrel and extended barrel cover a region in pseudo-rapidity of up to $|\eta| = 1.7$. Tile cells are also installed in the transition region between barrel and end-cap of the electromagnetic calorimeter. In this so-called *crack* region they provide information for the electron energy calibration and improve the resolution. Additional tile calorimeter paddles are installed closer to the beam axis covering a region of $2.12 < \eta < 3.85$. They are called MBTS (Minimum Bias Trigger Scintillators), used for triggering. There is also a hadronic end-cap calorimeter made of lead/LAr covering $1.5 < |\eta| < 3.2$. The η coverage of the mentioned components of the hadronic calorimeter is summarised in Tab. 5.1 and the $\Delta\eta \times \Delta\phi$ granularity of each is specified.

	Hadronic Calorimeter			
	Scintillator Tile		**LAr Hadronic**	
	Barrel	Extended Barrel	End-cap	
$\|\eta\|$ coverage	< 1.0	0.8-1.7	1.5-2.5	2.5-3.2
Number of layers	3	3	4	4
Granularity ($\Delta\eta \times \Delta\phi$)	0.1×0.1	0.1×0.1	0.1×0.1	0.2×0.2
(last layer)	0.2×0.1	0.2×0.1		

Tab. 5.1: Granularity and η coverage of the sub-components of the hadronic calorimeter.

5.2.4 The Muon Spectrometer

The muon spectrometer (MS) is the outermost detector component of ATLAS. Only muons are expected to reach the MS. Since high-energetic muons have the nature of minimum ionising particles they lose only little of their energy when passing through the calorimeters. This means they are not absorbed and leave the detector crossing the MS detectors. The MS consists of four types of detectors: the *Monitored Drift Tubes* (MDT), *Cathode Strip Chambers* (CSC), *Resistive Plate Chambers* (RPC) and *Thin Gap Chambers* (TGC). Figure 5.7 shows ATLAS with a focus on these components. The right-hand figure illustrates the position of each of these in the y, z-plane. The MDT chambers are installed in three cylindrical layers in the barrel at distances of 5 m, 7.5 m and 10 m from the beam axis. MDT end-cap chambers are installed on three wheels perpendicular to the beam axis, the outermost wheel being located at $|z| = 21.5$ m. The CSC is installed in the very forward region at $|z| = 7$ m, just in front of the end-cap toroids. The

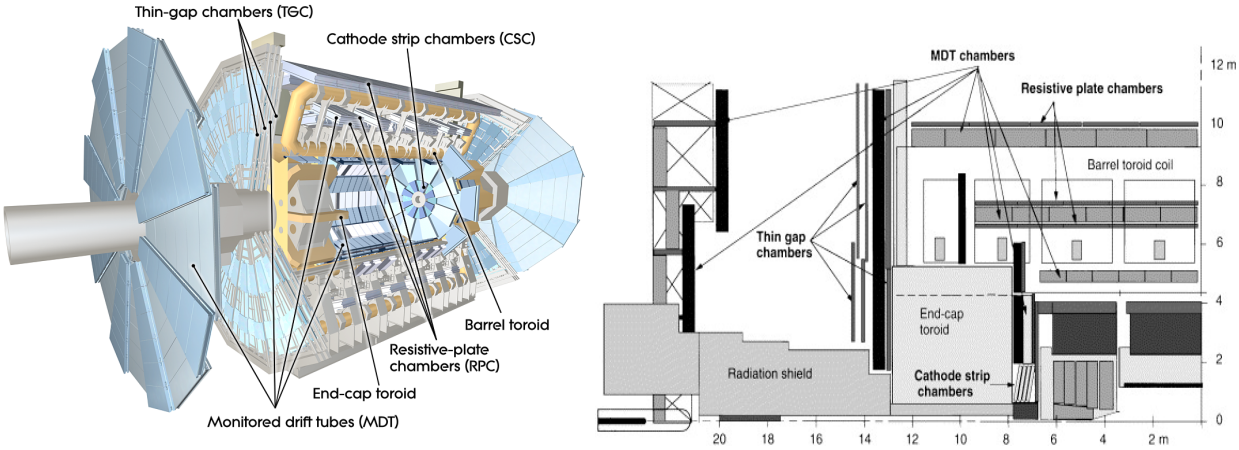

Fig. 5.7: Left: Cut-away view of the ATLAS muon spectrometer system with indicated subsystems. Right: Same for the view in the y, z-plane showing one quadrant and length measures [95].

MDT and CSC cover a range in pseudo-rapidity of $|\eta| < 2.7$ and their function is to measure muon tracks precisely. From the deflection of the tracks in the magnetic field of up to 4 T provided by the toroids the muon momentum can be reconstructed. All MS chambers are multi-wire proportion chambers which means that they detect the charge produced by ionisation of traversing muons in a gas mixture and measure the drift times. The MDT consists of aluminium tubes with a gas mixture of Ar/CO_2 (93%/7%). The tubes are arranged in two multilayers per chamber, where each of the multilayers provide spatial resolution of 50 µm. The CSC are multi-wire proportional chambers with a strip readout and a gas content of Ar/CO_2 (80%/20%) and can provide spatial resolution of 60 µm. The drift time in MDT and CSC is of the order of 700 ns and thus longer than the bunch spacing. In order to distinguish muons from different bunch crossings, timing information from the RPC is used. The RPC and TGC chambers have the purpose of triggering on muon events. The RPC has a timing resolution of 2 ns. It is composed of two plates filled with gas (capacitor) and operated in avalanche mode. The RPC at the middle station triggers on low-p_T muons, the outer chambers trigger on high-p_T muons. The TGC chambers provide the end-cap trigger. For this multiwire chamber the cathode-anode distance is only 1.4 mm. The timing resolution is 4 ns. Both RPC and TGC also provide information on ϕ. They trigger tracks that point approximately to the IP. For the muon momentum the information from the MS and ID is combined. Typically, the MS provides a better resolution

than the ID for high p_T muons from $p_T > 50$ GeV onwards [103]. A summary of the properties of the subcomponents of the MS is given in Tab. 5.2.

	MDT	CSC	RPC	TGC
$\|\eta\|$ coverage	< 2.7 (innermost layer < 2.0)	2.0-2.7	< 1.05	1.05-2.7 (1.05-2.4 trigger)
Number of chambers	1 150	32	606	3 588
Number of channels	354 000	310 000	373 000	318 000
Function	Precision tracking	Precision tracking	Triggering, ϕ-coordinate	Triggering, ϕ-coordinate

Tab. 5.2: Function and properties of the subcomponents of the muon spectrometer and their η coverage.

5.2.5 The Magnet System

A unique feature of ATLAS is the employment of two magnet systems. The solenoid magnet and the air-cored toroidal magnets both work with super-conducting technologies. The solenoid serves to bend the tracks of charged particles traversing the ID. Instead of installing a dense iron return yoke to ensure a magnetic field outside the solenoid, the concept of ATLAS makes use of eight toroids that are assembled with an eight-fold azimuthal coil symmetry outside the calorimeters in the barrel. Also in both end-cap regions behind the calorimeters eight smaller toroids are installed in a closed insulating vessel reaching to a diameter of 10 m. They provide the magnetic field for bending the tracks of muons in the muon spectrometer. The end-cap toroids are rotated w. r. t. the barrel toroids to ensure radial overlap and optimise the bending power at the interface of the two systems. This is illustrated in Fig. 5.8. The absence of a return yoke ensures that muons can reach the MS without disturbance from multiple scattering in dense material. The magnetic field however is more complicated and non-uniform at the position of the muon chambers.

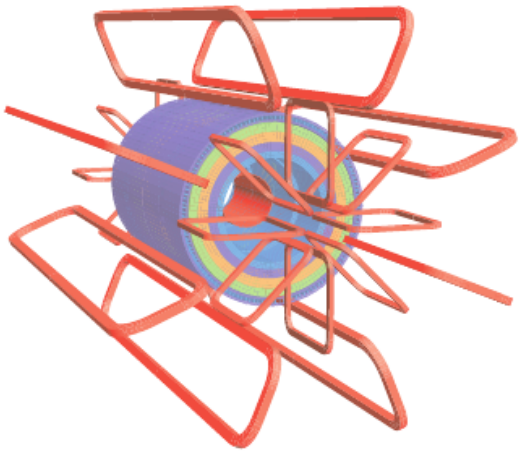

Fig. 5.8: Geometry of barrel and end-cap toroidal magnet windings (red). In the centre, the solenoid is displayed with the tile calorimeter plus outside return yoke. The different colours illustrate different magnetic properties of the tile calorimeter.

5.2.6 Performance Goals

Table 5.3 summarises the subdetectors comprised within ATLAS and their $|\eta|$ coverage as introduced in the previous sections. In order to fulfill the physics goals of ATLAS these subdetectors have to deliver a certain resolution power that allows for precision measurements. These requirements are also shown in Tab. 5.3. The discussed resolutions as a function of p_T or E are shown here (omitting the noise terms). The resolution of the electromagnetic calorimeter is better than the one of the hadronic calorimeter due to the reasons discussed in Sec. 5.2.3.

Detector Component	Required Resolution	$\|\eta\|$ Coverage
Tracking (ID)	$\sigma_{p_T}/p_T = 0.05\% p_T \oplus 1\%$	< 2.5
EM calorimetry	$\sigma_E/E = 10\%/\sqrt{E} \oplus 0.7\%$	< 3.2
Hadronic calorimetry:		
barrel and end-cap	$\sigma_E/E = 50\%/\sqrt{E} \oplus 3\%$	< 3.2
forward	$\sigma_E/E = 100\%/\sqrt{E} \oplus 10\%$	3.1-4.9
Muon spectrometer	$\sigma_{p_T}/p_T = 10\%$ at $p_T = 1$ TeV/c	< 2.7

Tab. 5.3: Performance goals of the different detector components and their η coverage. The units for E and p_T are in GeV and GeV/c, respectively [94].

5.2.7 The Trigger System

With a targeted peak luminosity of 10^{34} cm^{-2}s^{-1} in pp collisions during Run 2, events occur with an expected rate of 40 MHz. It is neither possible to store this amount of data on disks nor to reconstruct and analyse all these events in time. Most of the processes in pp collisions are scattering events where no new particles are produced and therefore they are largely uninteresting for physics analyses. Therefore, ATLAS deploys a trigger system to filter out only interesting events: the first trigger level is called L1, the final trigger decision is made by the so-called *High Level Trigger*, HLT [104]. The L1 trigger is fully hardware based: it uses information from the MS (L1Muon) and the calorimeters (L1Calo). While L1Muon relies on the RPC and TGC in the end-cap and barrel region of the MS to provide identification of muons, the L1Calo triggers on jets, electrons, hadronically decaying τ-leptons, large E_T and large $\not{E}_T$. It uses a *sliding window* algorithm to search for energy clusters in η-ϕ space. The then identified objects are called *Trigger Objects*, TOB. Information on the type, location in η-ϕ, energy and isolation status of the TOB is passed on to the *L1Topo* trigger component. It combines geometrical and kinematic information and allows a larger variety of trigger requirements on entire events. The final L1 trigger decision is made by the *Central Trigger Processor*, CTP, that provides 512 different possible trigger selections. Each selection has a prescale of $n \geq 1$[d]. The CTP accepts at random $1/n$ events that pass the selection. The event rates are reduced to up to 100 kHz. The CTP passes events on to the HLT. The HLT is a large computer farm that uses event reconstruction and selection algorithms. Event selections in the HLT are a chain of selection steps events have to pass through. The collection of such chains is called *trigger menu*. Events that pass the final step are accepted and stored on disk at the CERN Tier-0 centre. The final event rate is reduced to 1 kHz.

[d] Typically, for physics analyses it is desired to have unprescaled triggers, i. e. $n = 1$. However, if event rates are too high, a prescaled trigger has to be employed.

5.2.8 Computing Facilities and Data Quality

The CERN Tier-0 is the largest computing centre at the top of the so-called Worldwide LHC Computing Grid (WLCG). It stand on top of the hierarchy that has 13 Tier-1 sites at its second instance and more than 160 Tier-2 and Tier-3 sites. They are large computer centres operated by institutes worldwide, where the data is distributed. From top to bottom of the hierarchy the level of detailed event information is reduced to the analysis specific content.
To ensure a high quality of recorded and analysed data, a data quality infrastructure is developed at Tier-0 and Tier-1 level. The data quality is constantly monitored, starting from online data taking - to spot detector failures as soon as possible - continuing with offline analyses, calibration and reprocessing. ATLAS data is recorded in different streams: apart from the data stream for `physics` analyses, crucial data is also stored in `calibration` and `express` streams. The streams are coupled with certain triggers. The calibration and express stream (fast monitoring of all subsystems) are promptly processed. The different detector parts might suffer from irradiation damage or other failures during the data taking period. In general, the response of different components will change over time. Therefore, databases are constantly updated with calibration information and the detector status (dead channels, inefficiencies, etc.). In addition, runs without beams are used to access detector noise and appearance of cosmic muons. After the fast processing of calibration and express streams, physics data will be available a few days later. If further problems with the taken data appear, the runs have to be reprocessed, which happens a few months later. In the meanwhile the data can still be used via masking lumiblocks with problematic data (employing so-called *GoodRunsLists*).

Chapter 6

Object Definition

The monojet analysis defines signal and background control regions for which it makes use of events containing electrons, photons, muons, jets and $\not{E}_T$. The object definitions are described in the following. The analyses distinguishes between so-called *baseline* and *good* objects in case of electrons, photons, muons and jets. Baseline objects are used in the overlap removal (see Sec. 6.7) and for preselection criteria (see Sec. 7.3); good objects are used in the actual analysis selection to define signal and control regions. All particles have a trigger, reconstruction, identification and isolation efficiency attached to them. They should be ideally close to 100% and must be measured in both MC and data events. This is done via the *tag-and-probe method* described in the following.

6.1 Tag-and-Probe Method

Trigger, reconstruction, identification and isolation efficiencies are determined for electrons, photons, muons and b-jets. Therefore, the tag-and-probe method is used, which is explained here shortly, in more detail e. g. in Refs. [105–107]. Clean decay channels such as $Z \to \ell\ell$ or $J/\psi \to \ell\ell$ are used to determine the efficiency in data. Considering the case of a decay $Z \to \ell\ell$: first, events are selected with opposite signed leptons, ℓ^+ and ℓ^-. Their invariant mass is required to be close to the Z-mass peak. One of the leptons fulfils tight criteria (or a certain trigger criterion, etc.). This lepton is the *tag* lepton. The other lepton is the *probe* lepton that fulfils looser criteria than the tag lepton. The efficiency is now determined by how often the probe lepton also passes tight selection criteria:

$$\varepsilon = \frac{N_{\text{probe}}^{\text{pass}}}{N_{\text{probe}}^{\text{total}}}.$$

This efficiency is measured both in data and MC events. MC events need to be weighted if ε in data is not the same as in MC. This weight is included in the scale factors SF, determined by:

$$SF = \frac{\varepsilon_{\text{data}}}{\varepsilon_{\text{MC}}}. \tag{6.1}$$

SF is usually parameterised in η and p_T (or ϕ), since the detector components used are different in different areas and have different p_T dependent responses.

6.2 Vertex Reconstruction and Impact Parameters

Most objects that are introduced in the following are charged objects that can leave a track in the ID. Tracks are reconstructed using the information from hits in IBL, pixel, SCT and TRT that are combined in track finding algorithms. Charged particles produced in the same event

may come from the same interaction vertex or different vertices. A vertex can be reconstructed by finding tracks that meet in one point. The vertex that is associated with tracks which have the biggest summed p_T^2 is the so-called *primary vertex* (PV). Secondary vertices can be displaced from the PV due to particles that travel a short distance in the detector and decay before they reach the first pixel layer. In order to match a track with the PV the *impact parameters* have to be small[a]: they are called d_0 and z_0. The parameter d_0 is the distance of closest approach of a track to the PV in the transverse plane, likewise z_0 is the distance of closest approach in z-direction. In the following sections, they will be used. Related parameters like σ_{d_0}, the uncertainty on d_0, Δz_0, the distance between PV and beamspot and θ, the polar angle of the track are taken into account for the definition of good objects.

6.3 Electrons

Electrons are reconstructed from tracks in the ID and electromagnetic clusters in the calorimeter. A cluster is formed out of adjacent calorimeter cells with an energy deposition. Electromagnetic clusters are built with the help of the *sliding window* algorithm [107]: a window of fixed size 3×7 in units of $\Delta\eta \times \Delta\phi = 0.025 \times 0.025$, corresponding to the middle layer granularity of the electromagnetic calorimeter, scan longitudinal layers ('towers') to search for cluster seeds with an energy $E_T > 2.5\,\text{GeV}$. Clusters are than formed around the seeds using clustering algorithms [108]. The window size is 5×5 in the end-cap. The transverse energy is calculated via

$$E_T = \frac{E_{\text{cluster}}}{\cosh(\eta_{\text{track}})}.$$

The energy information is taken from the calorimeter cluster, the position information is provided by the ID (within $|\eta| < 2.5$, for forward electromagnetic clusters the positions stems from the calorimeter as well). An electron is reconstructed if at least one track can be matched to the energy cluster (where tracking is possible). A track is matched to a cluster if $\Delta\eta$ between the track direction an the seed cluster is smaller than 0.05. If more than one track can be matched, tracks with silicon hits are preferred and finally the track with the smallest ΔR is chosen. For the electron identification a multivariate likelihood technique is employed. It uses shower shape variables, track information, track-to-cluster matching and TRT information. A cut on the multivariate likelihood represents different working points for electron identification efficiencies [109, 110]. The working points are *loose*, *medium* and *tight*, with increasing background rejection and decreasing identification efficiency, respectively. The working points were opimised in bins of η and E_T and created such that they are a subset of one another (tight electrons as subset of medium electrons, as subset of loose electrons). The efficiencies vary between 78% and 90% for $E_T > 25$ GeV [110].
In addition, isolation criteria can be required in order to make sure that prompt electrons are selected and not e. g. those from leptonic decays inside a jet. Isolation can be required on both tracks and energy depositions in the calorimeter. Ideally, they should be independent of pileup[b] activity. For both track and calorimeter isolation a cone of a certain size ΔR around the electron direction is considered and cuts are performed on the p_T or E_T not associated to the electron inside the cone .

[a] Quality criteria on impact parameters are applied to electrons, muons, jets.
[b] Pileup describes the interaction between various protons in a single bunch crossing or from neighbouring bunch crossings happening in the detector at the same time.

The total associated energy of the electron is a sum of the energy cluster deposit plus the estimated components from (1) energy deposited in front of the electromagnetic calorimeter, (2) energy deposited outside the cluster (lateral leakage) and (3) energy deposited beyond the electromagnetic calorimeter (longitudinal leakage). To estimate these additional components MC simulation is used. Further corrections are applied to data and MC: the energy of electrons is calibrated in a $Z \to ee$ control sample (*in-situ* calibration): the energy is corrected such that the invariant mass of the electrons reproduces the Z-mass peak. The corrected energy is then $E_{\text{corrected},i} = E_i/(1+\alpha_i)$. The indices label bins in η. Also, the energy resolution in simulation is corrected to match the data. The resolution can be parameterised as seen in Eq. 5.4. The difference of this term in data and MC can be corrected with a constant term c_i:

$$\left(\frac{\sigma(E)}{E}\right)_i^{\text{data}} = \left(\frac{\sigma(E)}{E}\right)_i^{\text{MC}} \oplus c_i'.$$

The terms α_i and c_i' are extracted from a template fit to data to correct the energy scale in data and the energy resolution in MC, respectively [111]. Figure 6.1 shows the obtained correction factors in a fit to the 2015 data set. It is visible that electrons are measured with less accuracy in the *crack* region of the detector which is poorly instrumented ($1.37 < |\eta| < 1.52$). In the following, criteria for baseline and good electrons used for the monojet analysis are listed:

- **baseline electrons:** $E_T > 20$ GeV, $|\eta| < 2.47$, loose likelihood + B-layer cut (require a hit in the IBL[c]), survive overlap removal (Sec. 6.7),
- **good electrons:** tight likelihood cut for $p_T < 300$ GeV, medium likelihood cut for $p_T > 300$ GeV, $d_0/\sigma_{d_0} < 5$ and $|\Delta z_0 \sin\theta| < 0.5$ mm, `FixedCutTight` isolation: `ptcone20`$/p_T <$ 0.06 and `topoetcone20`$/p_T < 0.06$, crack region is excluded.

The cut on the impact parameters is applied to assure the electron originating from the PV. The FixedCutTight isolation requires track isolation and calorimeter isolation. The variables ptcone20 and etcone20 refer to the energy/momentum measured around the electron in a cone with size $\Delta R = 0.2$ not associated to the electron. Efficiency scale factors, as defined in Eq. 6.1 are applied for identification, reconstruction, isolation and triggering.

6.4 Photons

Photon candidates are reconstructed within the same cluster finding algorithm as electrons. This serves to solve any possible electron-photon ambiguity. One distinguishes between converted and unconverted photons. Unconverted photons do not have a track associated to the energy cluster. Converted photons are those that undergo $\gamma \to e^+e^-$ when interacting with the material upstream of the electromagnetic calorimeter. Thus, they can have two tracks stemming from the electrons pointing to the cluster. It is also possible that either one electron or positron has low p_T (asymmetric pair creation) and only one track can be found matching the cluster. These tracks from photon conversion often do not have hits in the first ID layers and the energy/momentum measurement is not consistent with prompt electrons. To resolve the ambiguity between electrons and converted photons one can either require that two tracks can be fitted to originate from one massless particle or finding tracks without hits in the first pixel layer[d]. These two findings would point to converted photons. If a cluster with the best matched high-p_T track only has TRT hits

[c] For discrimination against converted photons, non-prompt electrons.
[d] If the missing inner layer hit can be due to dead pixel modules in the track direction no photon is reconstructed.

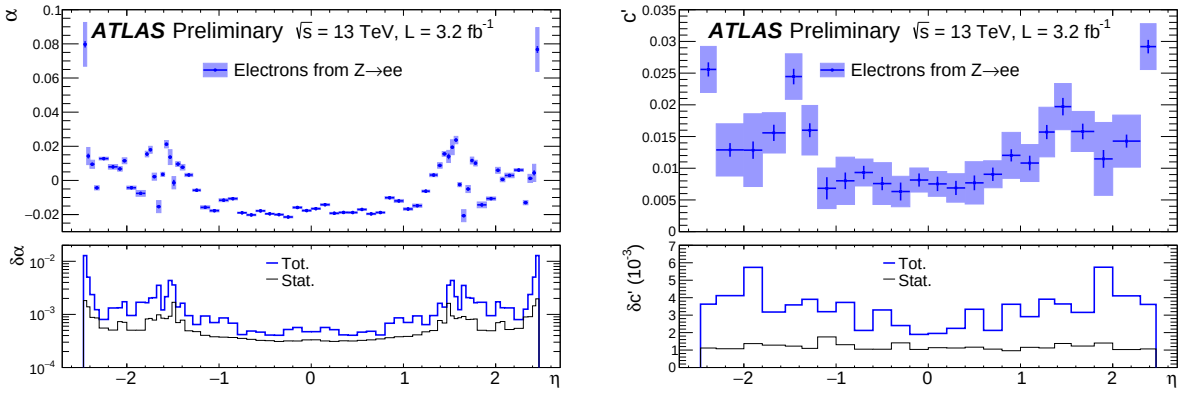

(a) (b)

Fig. 6.1: Energy scale correction (a) and energy resolution correction (b) as a function of η as obtained in $Z \to ee$ template fits to data in 2015 [111]. Uncertainties are displayed. The energy scale correction is applied to data, the resolution correction to simulation.

it is considered as originating from a converted photon. A further distinction between electrons and photons (also unconverted photons which have a track assigned by mistake) can be achieved by examining the E/p ratio of the object which is large for real photons. The four-momentum of a reconstructed photon is computed only from the calorimeter cluster. Shower shape variables and energy variables as described in Ref. [112, 113] are used for the identification of photons. These variables rely on the high-granularity of the LAr calorimeter. A hadron decaying to two photons, e. g. $\pi^0 \to \gamma\gamma$ can be distinguished with the help of the first LAr layer granularity. Clusters from two photons are broader and exhibit a second energy maximum. Hadron jets can be distinguished also by broader shower shapes and more energy deposition in the hadronic calorimeter. Independent requirements on the shower shape variables are imposed to define *loose* and *tight* photons. Tight photons use more shower shape classifiers. They are excluded in the region of $1.37 < |\eta| < 1.52$ as well as beyond $|\eta| = 2.37$ due to the coarser calorimeter granularity. In order to avoid photons being double-counted as jets, an overlap removal is applied (Sec. 6.7). The energy calibration is the same as for electrons (using $Z \to ee$), the only difference being that the energy loss upstream of the calorimeter is slightly different for photons than for electrons due to their different interaction nature. The requirements on photons are:

- **baseline photons:** $E_T > 20$ GeV, $|\eta| < 2.37$, tight identification,
- **good photons:** additional isolation: `FixedCutTight`: `topetcone40`$< 0.022E_T + 2.45$ GeV, `ptcone20`$/p_T < 0.05$.

An isolation requirement is applied to good photons: a calorimeter isolation, called `topetcone40`: this refers to the energy in a topological cluster in a cone of size $\Delta R = 0.4$ around the photon direction not associated to the photon. The track isolation variable used is `ptcone20` referring to the track momentum in a cone of size $\Delta R = 0.2$ around the photon track (in case of converted photons). The details of the isolation prescription are important for theoretical cross section calculations (brief discussion in App. A.3). For determining photon efficiencies in data the tag-and-probe method can only be used in radiative Z-boson decays ($Z \to \ell\ell\gamma$). Other methods are extrapolation from the lepton case to the photon case or employing a *matrix method* which determines background contamination with varying isolation cuts [114].

6.5 Muons

Muons are reconstructed using track informations from the ID and the MS. Their tracks are first independently reconstructed in ID and MS before the information is combined for physics analyses. The track reconstruction in the ID works just like for electrons as mentioned in the previous sections. In the MS, the information from MDT and CSC is used: tracks are formed from fitting hits from segments in different layers. Like in cluster algorithms, also here segment seeds are used. In the MDT the hit segments are fitted with a straight line. A separate combinatorial search in $\eta \times \phi$ is performed in the CSC. There is a certain requirement on the hit multiplicity and the quality of the fitted track (χ^2-fit). In the barrel, at least two matching segments are required to form a track, while one high-quality segment in the end-cap is sufficient. Since muons can pass the whole detector, there are several ways of detecting them and using the information from the whole detector. Thus, muons are classified as [115]:

- **Combined muons (CB):** A global refit is performed to tracks in the ID and MS. Tracks can be be either build from starting in the MS and extrapolating back to the IP, matching up the information from the ID (main strategy), or starting from tracks in the ID.
- **Segment-tagged muons (ST):** A muon is reconstructed from a track in the ID if at least one matching segment in the MDT or CSC can be found. This is helpful to recover low-p_T muons and muons outside the MS acceptance ($|\eta| < 2.7$).
- **Calorimeter-tagged muons (CT):** If an ID track can be matched with an energy deposit in the calorimeter that is compatible with the one from a minimum ionising particle, a muon is reconstructed. This set of objects has the lowest muon purity but recovers acceptance in regions where the MS is only partially instrumented ($|\eta| < 0.1$)
- **extrapolated muons (ME):** This muon type is reconstructed from an MS track that is compatible with stemming from the IP, but has no ID track. This extends the detection of muons to larger η-regions where no ID tracking is possible ($2.5 < |\eta| < 2.7$).

To avoid one muon being reconstructed as different types an overlap removal is performed, where preference is given to CB muons if ID tracks overlap with other muons (likewise ST muons are preferred if they overlap with CT muons). In this analysis, CB muons are further analysed. Also muons are selected with different identification criteria: *loose*, *medium*, *tight* and *high-p_T*. Variables used for this classification are ID and MS momenta and measured charge, reduced χ^2 of the track fit[e], number of hits in ID and MS. The medium muon is the standard selection applied with minimal systematic uncertainties from reconstruction and calibration. A medium muon is a CB or ME muon. Loose muons can be reconstructed with the highest efficiency and allow all muon types. The tight selection has the highest purity and consists of only CB muons. High-p_T muons are those with $p_T > 100$ GeV. The analysis described later on will consider medium muons with the following distinction:

- **baseline muons:** $p_T > 10$ GeV, $|\eta| < 2.5$,
- **good muons:** additional cuts on impact parameters: $d_0/\sigma_{d_0} < 3$ and $|\Delta z_0 \sin\theta| < 0.5$ mm.

No isolation requirement is applied. To calculate identification efficiencies, the tag-and-probe method in decays of $J/\psi \to \mu\mu$ and $Z \to \mu\mu$ is used. They are also used to correct the momentum

[e] The reduced χ^2 is defined as χ^2/dof, where dof denotes the degrees of freedom in a χ^2 minimisation fit.

scale and resolution in MC simulation. Similar to the electron energy calibration, a template fit to the data is performed to obtain the correction. In an analysis performed with 2015 data an accuracy of up to 0.05% in the momentum scale and 1.7% in the momentum resolution is found [115]. The medium efficiency scale factors measured are shown in Fig. 6.2 as a function of muon-p_T. The left plot shows the efficiencies measured in data and MC used to calculate the weight scale factors according to Eq. 6.1. The right plot shows the total uncertainty on the efficiency scale factor.

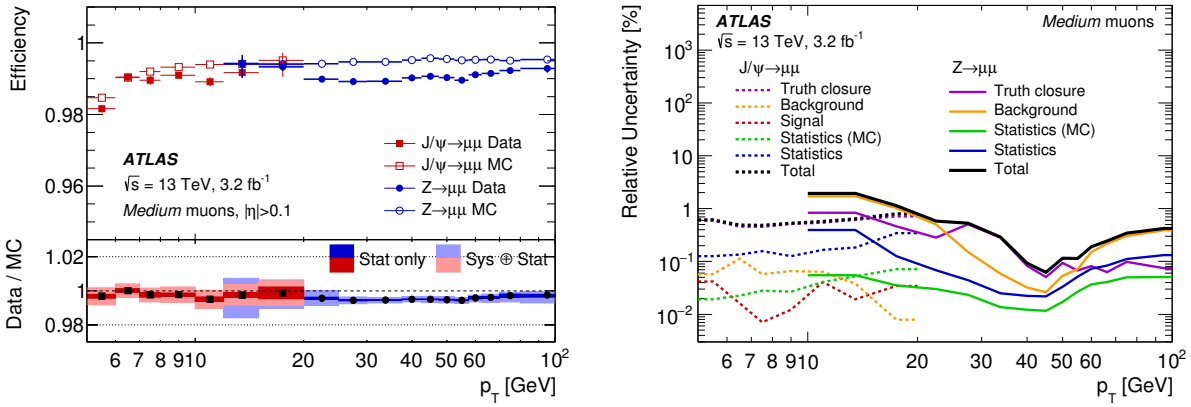

(a) (b)

Fig. 6.2: Muon medium identification efficiency measured in 2015 data as function of p_T (a) [115]. The total uncertainty on the obtained efficiency scale factors is shown with its components in (b).

6.6 Jets

Jets are the most common objects present in collision events at the LHC. They denote particle bundles that leave tracks in the ID and energy in the calorimeters. The particle bundle originates from quarks and gluons that undergo hadronisation and form hadron jets. Due to the involvement of the strong force, jet production is very likely in an event. They are complex objects and their understanding is not only important to obtain the right jet properties but also to extract the correct $\not{E}_T$ (see Sec. 6.8), both of them are crucial for the analysis presented later on.

6.6.1 Jet Reconstruction

In ATLAS, jets are reconstructed with the anti-k_t algorithm [116] as implemented in FASTJET [117, 118]. It uses as inputs so-called *topoclusters* [119]. The formation of topoclusters and the anti-k_t algorithm are explained in the following.
Topoclusters represent 3-dimensional energy clusters distributed over neighbouring calorimeter cells. They are seeded if the measured energy lies above a certain threshold that is dependent on the noise term σ_{noise}. It consists of two components and is defined as

$$\sigma_{\text{noise}} = \sqrt{\left(\sigma_{\text{noise}}^{\text{electronics}}\right)^2 + \left(\sigma_{\text{noise}}^{\text{pileup}}\right)^2}. \tag{6.2}$$

The first term is the electronics noise. The second term takes energy deposition from pileup-jets into account. It is essential in environments with high instantaneous luminosity to suppress contributions from soft interactions in the same proton-proton bunch-crossing (in-time pileup) or neighbouring bunch-crossings (out-of-time pileup). The pileup term is defined based on an assumption of the average number of interactions per bunch crossing, $\langle\mu\rangle$[f] (introduced in Eq. 5.2) dependent on $\mathcal{L}$. Also, underlying event activity from interactions of proton remnants adds to the noise term. Clusters are seeded by finding cells with a significant signal $E_{\text{cell}}^{\text{EM}}$, defined by: $\left|E_{\text{cell}}^{\text{EM}}/\sigma_{\text{noise}}\right| > 4$. EM denotes the electromagnetic scale, uncorrected for energy loss of hadrons in the non-compensating hadronic calorimeter. Once a cluster seed is found, the neighbouring cells are checked and if they have $\left|E_{\text{cell}}^{\text{EM}}/\sigma_{\text{noise}}\right| > 2$ they are added to the cluster. Again, their neighbours are checked for significant signal. Finally, if a neighbouring cell has $\left|E_{\text{cell}}^{\text{EM}}/\sigma_{\text{noise}}\right| > 0$ but not $\left|E_{\text{cell}}^{\text{EM}}/\sigma_{\text{noise}}\right| > 2$ it is added to the cluster and the clustering is stopped. The now called proto-clusters can also have negative energy induced by out-of-time pileup. This is allowed to achieve a cancellation of random cell signals in global variables like the $\not{E}_T$. If proto-clusters exhibit more than one energy peak ($E > 500$ MeV, ≥ 4 neighbours with lower signal), the cluster is splitted. Cells can be part of at most two proto-clusters, their energy is split according to the energy distribution and geometrical distance to the respective seeds. After this step the final topoclusters are formed. The direction of a topocluster in η, ϕ is calculated as signal-weighted barycentres. The topoclusters are treated as massless pseudo-particles.
Only topoclusters with $E^{\text{EM}} > 0$ are used as input for the anti-k_t algorithm. The topocluster i has a momentum $k_{t,i}$, then the following quantities are defined:

$$d_{ij} = \min\left(\frac{1}{k_{t,i}^2}, \frac{1}{k_{t,j}^2}\right)\frac{\Delta R_{ij}^2}{R^2},$$
$$d_{iB} = \frac{1}{k_{t,i}^2}.$$

The algorithm considers two clusters i and j at a time. In ATLAS, mostly $R = 0.4$ is used. It is a measure for the maximal cone size a jet will have and ΔR_{ij} is the distance between cluster i and j. If d_{ij} is smaller than d_{iB} (effectively the 'distance' of i to the beam axis), then i and j are recombined to one cluster, else, i is called a jet and the merging stops. This algorithm is insensitive to soft or very collimated radiation of particles inside a jet (infrared save). It starts from clusters with high momentum and picks up the soft constituents to form a jet. The final jet will have a defined cone area which is important for further pileup-corrections and calibration which will be discussed next.

6.6.2 Jet Calibration

After jets are reconstructed as described before, they have an assigned energy at the EM scale, as measured in the electromagnetic calorimeter. The jet properties still need to be calibrated for a number of reasons: as introduced in Sec. 5.2.3, the ATLAS hadronic calorimeter is non-compensating, meaning its response is lower than the electromagnetic calorimeter response, furthermore energy can be lost in inactive material, accidentally signals can be lost (via the noise suppression derived from pileup conditions) and very high-p_T jets might not be absorbed and its constituents penetrate through the calorimeter into the muon chambers.
One possibility is to correct for some of these effects via the *local cluster weighting* (LCW) [123].

[f] The value of $\langle\mu\rangle$ can be measured for ATLAS by the dedicated luminosity monitors LUCID and BCM [120–122]

It is a hadronic calibration to correct for non-compensation and out-of-cluster energy deposition using simulation which is validated with data. In general, there are a number of steps in the calibration scheme, starting either from EM-scale or LCW-scale:

- a correction of the jet direction to point back to the hard-scatter vertex instead of the detector center (by default in jet reconstruction) using track information,
- a correction for pileup contributions to jet energy,
- a jet energy scale correction to MC particle level (truth particles),
- a *global sequential correction* (see page 62) to remove dependencies on jet shower shapes to improve the resolution,
- a residual in-situ calibration to resolve remaining differences in MC and data, only applied to data.

The first step of correcting the jet direction takes track information from the ID into account. A good determination of the primary vertex is important here. Tracks are associated to the calorimeter cluster using a *ghost-association* where tracks are extrapolated into the calorimeters, which have an infinitesimal p_T and will not change the energy of the jet [124]. By using these tracks in the clustering one can identify the tracks belonging to a jet. Not only is the vertex finding crucial for this correction, it is also crucial to obtain an estimation of in-time pileup contributions to the jet by reconstructing the number of primary vertices N_{PV}. The pileup corrections and further corrections listed above will be discussed in the following.

Pileup Corrections

As already mentioned, due to the high luminosity and short bunch spacing of 25 ns in 2015 and 2016 data runs, in-time and out-of-time pileup play an important role in the measurements of jets. The LAr calorimeter readout is sensitive to out-of-time pileup but pulse shaping in signals has been optimised for Run 2 conditions. The tile calorimeter is less sensitive to pileup due to the absorption of mostly soft jets in the LAr and a faster readout time. As outlined in Eq. 6.2, pileup influences on the object reconstruction are already suppressed by the noise term when building topoclusters. However, this will not remove all contributions. One needs to further estimate the pileup contribution and correct the jet energy accordingly. A pileup subtraction depending on the jet area in $\eta \times \phi$ has been established. The energy density is defined as p_T/A, where the area A can also be obtained by clustering 'ghost' contributions into the jet and evaluating how many ghosts end up in a jet. The median energy density ρ of all jets with $|\eta| < 2.0$ is used as an estimator for pileup contributions. The correction is now of the following form [125]:

$$p_T^{\text{corr}} = p_T^{\text{EM}} - \rho \cdot A - \alpha(N_{\text{PV}} - 1) - \beta\langle\mu\rangle. \tag{6.3}$$

Here, the pileup term with ρ is subtracted from the original p_T^{EM} at EM scale. A residual effect remains, which is expressed by the terms depending on N_{PV} and $\langle\mu\rangle$. Figure 6.3(a) shows the measured μ during 2015 and 2016 data taking. It is around values of 20. The number of primary vertices N_{PV} peaks at values around 15 (Fig. 6.3(b)). The first one is an indicator for the amount of out-of-time pileup, the latter for the amount of in-time pileup. The parameters α and β are derived from simulation and paramaterised in η.

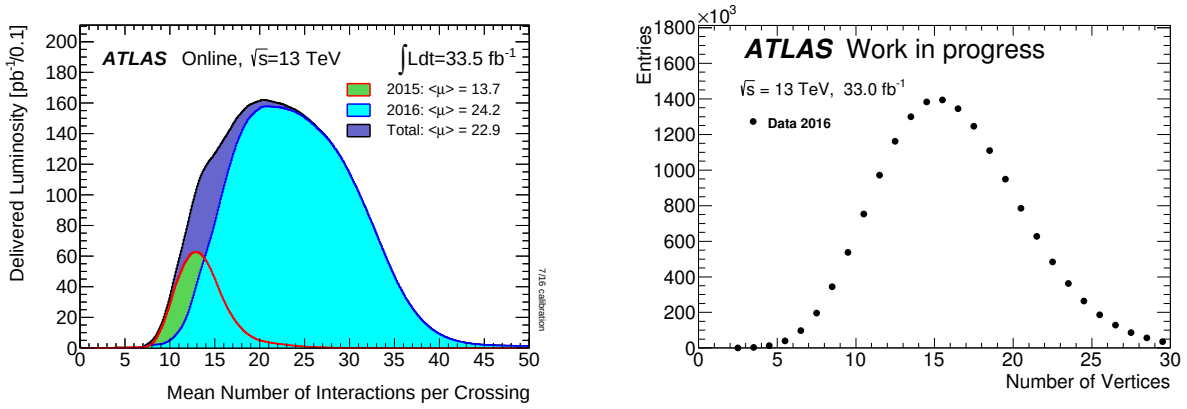

(a) (b)

Fig. 6.3: (a): Mean number of interactions per bunch crossing, μ during 2015 and 2016 data taking [100]. The y-axis shows the corresponding amount of integrated luminosity. During 2016, the average $\langle\mu\rangle$ amounts to ~ 24 interactions per bunch crossing [100]. (b): Number of primary vertices in 2016 data taking.

Jet Energy Scale

After the pileup correction the jet energy scale is corrected to the particle level. Again, simulation is used: reconstructed jets have to be matched to jets known at truth level (by $\Delta R < 0.3$). Isolated jets with no other jets of $p_T > 5\,\text{GeV}$ inside $\Delta R = 1.0$ allowed are used for the study. The jet energy response is defined as $\mathcal{R} = E^{\text{reco}}/E^{\text{truth}}$. The average jet energy response corresponds to the mean of $\mathcal{R}$ fitted by a Gaussian. The standard deviation of this Gaussian is the jet energy resolution. The jet calibration factor applied is the inverse of the average jet energy response. After application of this factor a bias in η remains. Figure 6.4 shows this behavior: on the right side the response is shown as a function of η where transitions between different detector regions are apparent. The jet calibration might give a jet that lies in between different detector components a larger energy only in one part of the jet, hence the bias seen on the left-hand in regions of η with transitions. This residual bias in η is corrected for.

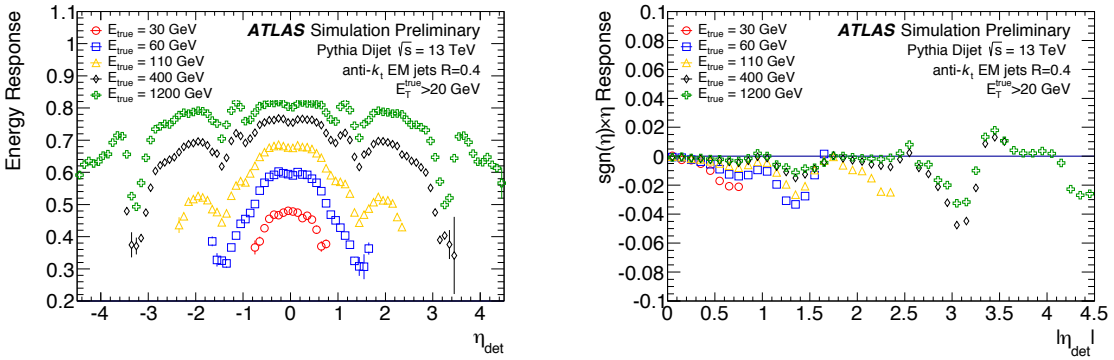

Fig. 6.4: Jet energy response for jets with different truth energies as a function of η (left). The right plot shows the residual bias in η after correcting the jet energy scale [125].

Global Sequential Corrections

The next step in the calibration process is to remove remaining dependencies on transverse and longitudinal features of the jets with the goal to improve the resolution. Therefore, a sequence of multiplicative correction factors is derived depending on different variables describing the jet shower shape. This procedure is called global sequential correction [126] and is used in ATLAS regarding the following dependencies:

1. the fraction of energy measured in the first layer of the tile calorimeter ($|\eta| < 1.7$),
2. the fraction of energy measured in the third layer of LAr ($|\eta| < 3.5$),
3. the width: p_T-weighted distance of jet four-momentum to all tracks with $p_T > 1\,\text{GeV}$ associated to a jet ($|\eta| < 2.5$),
4. the number of tracks associated to a jet ($|\eta| < 2.5$),
5. the number of muon segments associated to a jet ($|\eta| < 2.7$).

All these variables are provided by tracking, calorimeter and MS information and present dependencies on jet flavours (quark/gluon initiated), punch-through effects of high-p_T jets (using muon segments behind a jet) and general shower shape fluctuations. In the case of LCW calibrated jets, the energy is already corrected from information about fractional energy in calorimeter layers and energy outside the cluster, thus for LCW calibrated jets only the tracking and muon segment correction is used. The corrections are multiplied sequentially to the energy. The correction on the variable x is derived from MC as $\mathcal{R}^{-1}(x)$. In this way the dependency on x is removed. The average jet response is left unchanged. The resolution however can be improved, depending on η and p_T, by up to 35% [126].

In-situ Calibration

Finally, as a last step an in-situ calibration is applied only to data: it corrects for differences in data and MC which can arise from imperfect modelling of the detector details and the electromagnetic and hadronic interactions therein. Data samples enriched in processes such as γ+jets, Z+jets and multijets are selected. Similar to the tag-and-probe method a well known reference object can be used. In the case of dijet events this may be a jet in the central region balancing another jet in the forward region, which is measured with less accuracy. The response correction of forward jets from the better known central jet for those events is called η-intercalibration. The quantity

$$r = \frac{p_T^{\text{jet}}}{p_T^{\text{ref}}}$$

can be determined in both data and MC events. The correction applied from this in-situ measurement is $r^{\text{MC}}/r^{\text{data}}$, applied to data only.

Jet Vertex Tagger

The pileup correction in form of a subtraction of average pileup contribution to a jet has been mentioned. However, pileup activity may give rise to local fluctuations and reconstruction of spurious pileup jets. In order to distinguish such jets from hard-scatter jets the *jet vertex tagger* (JVT) has been developed for use in Run 2 analyses [127]. This tagger uses as input two variables

resulting in a 2-dimensional likelihood discriminant. In Run 1, mostly a cut on the *jet vertex fraction* (JVF) has been applied to suppress pileup jets. This variable was defined as the fraction of tracks associated to a jet stemming from the primary hard scatter vertex. The performance of the JVF cut in terms of efficiency and fake rate is however dependent on N_{PV}. In order to correct for this dependence, the first of two input variables to JVT has been defined as following:

$$\text{corrJVF} = \frac{\sum p_T^{trk}(PV_0)}{\sum p_T^{trk}(PV_0) + \frac{\sum_n \sum p_T^{trk}(PV_n)}{k \cdot n_{trk}^{\text{PU}}}}.$$

The term $\sum p_T^{trk}(PV_0)$ is the summed p_T of tracks originating from the hard-scatter vertex associated to a jet. The term $\langle p_T^{\text{PU}} \rangle = \sum_n \sum p_T^{trk}(PV_n)$ is the summed up p_T of all tracks associated to a jet stemming from a different primary vertex other than the hard-scatter vertex. The factor $k \cdot n_{trk}^{\text{PU}}$ has been introduced to correct for a dependence on N_{PV}, where n_{trk}^{PU} is the total number of pileup tracks per event and k has been chosen to be 0.01, the slope[g] of $\langle p_T^{\text{PU}} \rangle$ vs. n_{trk}^{PU}. The higher corrJVF the more likely it is that the jet is a hard scatter jet. The second variable is defined as:

$$\text{R}_{\text{pT}} = \frac{\sum p_T^{trk}(PV_0)}{p_T^{\text{jet}}}.$$

The p_T^{jet} is the fully calibrated jet p_T as outlined above. This variable will be peaked at zero and steeply falling for pileup jets, while hard scatter jets will have a broader distribution in this variable. The JVT variable now is the 2-dimensional likelihood of corrJVF and R_{pT}. It has been obtained using MC simulation where pileup is simulated by overlaying minimum bias events produced with Pythia8 [71]. Figure 6.5(a) shows the likelihood discriminant for pileup and hard scatter jets. A good separation between those distributions is visible. Jets without any matched track are assigned a negative JVT value. Figure 6.5(b) shows the performance of the tagger and its input variables and the JVF variable in terms of fake rate vs. efficiency for a given cut on the respective variable. One can see how the JVT improves the individual performance of the input variables and the JVF variable. The JVT tagger has been validated with different data samples.

Jet Requirements for Analysis

In the studies presented in this thesis, the `antikt4EMTopo` jet calibration is applied to jets. A loose jet cleaning is applied to all jets. Jets have $p_T > 30$ GeV and $|\eta| < 2.8$. The JVT variable is utilised to suppress jets from pileup interactions by requiring JVT> 0.59 for jets with $p_T < 60$ GeV and $|\eta| < 2.4$. Further requirements on jet properties will be introduced in the event selection in Sec. 7.3.

6.6.3 *b*-tagging

The flavour of a jet is generally categorised as b, c or light flavour depending on the quark that initiated the jet. The light flavour category also includes jets initiated by gluons. To identify a jet as a b-jet by experimental means is called b-tagging. This b-tagging is a useful tool to select events that are enriched in certain processes: the top-quark almost always decays into a b-quark

[g] Different choices of k have been tested in simulation and no dependence of the performance on k has been found.

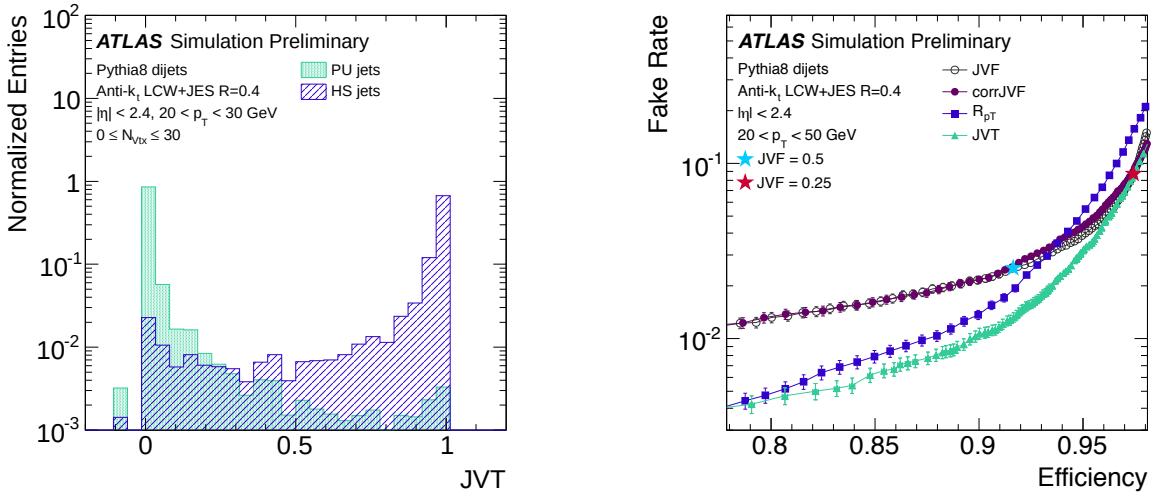

(a) (b)

Fig. 6.5: (a): JVT discriminant in simulation for pileup and hard-scatter jets with 20 GeV$< p_T <$ 30 GeV and (b): performance of the JVT variable compared with the two input variables and the formerly used JVF variable [127].

and a W-boson. Therefore, top-quark events will always produce b-jets and through b-tagging top-quark enriched samples can be selected. In ATLAS, a multivariate b-tagging algorithm [128] is used to identify jets stemming from b-quarks. This multivariate technique uses three individual taggers that use different information as input. The three algorithms are based on

- impact parameters,
- secondary vertex reconstruction,
- decay chain multi-vertex reconstruction.

If a b-quark is produced, it may travel a significant distance from the primary vertex before it decays further ($c\tau \sim 450$ µm). Thus, a b-jet may have tracks that do not point back to the primary vertex, but rather to a secondary vertex and it may have more vertices inside from leptonic decays initiated by heavy quark content. To develop the exact criteria to distinguish b-jets from c-jets and light flavour jets, the algorithms are tested on simulated $t\bar{t}$ samples. Again, a truth level matching of reconstructed objects is performed to know the true quark content ($\Delta R < 0.3$ for matching truth and reco jets). The IPD2 and IPD3 algorithms rely on the impact parameters d_0 and $z_0 \sin\theta$ and their significances. They also incorporate information from hit patterns in the pixel and SCT. A SV2 algorithm is designed to find a secondary vertex. It also uses hit informations in pixel and SCT. It suppresses fake vertices (due to material interaction) by also requiring that the reconstructed invariant mass does not exceed 6 GeV which would be too heavy for a b-quark. The invariant mass is also used to distinguish $\Lambda(uds)$ and kaon ($c\bar{s}/\bar{c}s$) decays. The third algorithm used is the JetFitter that searches for topological structures of weak decays inside a b- or c-jet by finding a common line of the PV and subsequent decays. All three taggers are used in a boosted decision tree (BDT) that form the multivariate discriminant MV2. The BDT is trained on a $t\bar{t}$ sample. Different background compositions have been tested and the one that contains a background of 7% c-jets and 93% light flavour jets has the best c-jet and

light flavour jet rejection while having a high b-tag efficiency. This discriminant is called `MV2c10` and is the standard b-tagging algorithm in ATLAS analyses. The analysis in this thesis uses the working point with 60% efficiency. Table 6.1 shows the corresponding background rejection rates for this working point and the working point with 77% and 85% efficiencies. The rejection rate is the inverse of the fake rate (rate of tagging non-b-jets).

BDT cut value	b-jet efficiency [%]	c-jet rejection	light-jet rejection	τ rejection
0.9349	60	34	1538	184
0.6459	77	12	381	55
0.1758	85	3.1	33	8.2

Tab. 6.1: Three operating points of the `MV2c10` b-tagging algorithm for 60%, 77% and 85% efficiencies and the corresponding background rejection rates. The values have been obtained with a $t\bar{t}$ test sample [128].

6.7 Overlap Removal

After the reconstruction of electrons, photons, muons and jets a residual ambiguity is possible if one particle is reconstructed as different objects. To avoid this double counting of objects an overlap removal is applied. This is performed for baseline objects in two steps:

1. **step:** if $\Delta R(\text{jet},e/\mu) < 0.2$ (b-tagging WP with 85%):
   - if jet is not b-tagged: remove the jet, keep electron/muon,
   - if jet is b-tagged: keep the jet, remove electron/muon,
2. **step:** after this continue with:
   - if $\Delta R(\text{jet},e) < 0.4$: remove electron, keep jet,
   - if $\Delta R(\text{jet},\mu) < 0.4$ and jet with ≥ 3 ID tracks: keep jet, remove muon,
   - if $\Delta R(\text{jet},\mu) < 0.4$ and jet with < 3 ID tracks: keep muon, remove jet.

Further, for the overlap of photons and other objects the procedure is:

- if $\Delta R(\gamma,\mu) < 0.4$: keep muon, remove photon,
- if $\Delta R(\gamma, \text{jet}) < 0.4$: keep photon, remove jet.

6.8 Missing Transverse Momentum

The most important signature of monojet finals states besides jets is a large amount of missing transverse momentum, $\not{E}_T$. It is reconstructed if the vector sum over all transverse momenta in an event does not vanish. The momentum conservation requires $\not{E}_T$ to be close to zero[h], unless there are particles escaping the detector untraced. In general, the $\not{E}_T$ is defined as the negative

[h] Due to imperfect detector resolution, the reconstructed $\not{E}_T$ may not be zero although all produced particles are measured.

vectorial sum of all objects in an event. Energy deposits in the calorimeter are associated to objects in the following order: electrons, photons, hadronically decaying τ-leptons, jets and muons. Their respective energy is calibrated as outlined in the sections above. Energy deposits in the calorimeter that cannot be assigned to any of these objects are taken into account via a so-called *soft-term*. They can arise from underlying event activity or soft radiation of hard particles. In Run 2, there are three different definitions of the $\not{E}_T$: CST $\not{E}_T$, track $\not{E}_T$ and TST $\not{E}_T$ [129]. CST stands for calorimeter based soft term and TST for track based soft term. In the CST $\not{E}_T$ only topoclusters are included in the calorimeter soft term, they are calibrated to the LCW scale. The track $\not{E}_T$ is based entirely on track information in the ID. The TST $\not{E}_T$ uses a track based soft term and combines the information with the calorimeter and the muon system. The CST $\not{E}_T$ has been vastly used as the $\not{E}_T$ definition throughout Run 1 analyses. However, a disadvantage is that the CST is sensitive to pileup which influences the overall $\not{E}_T$ resolution and performance [129]. The track $\not{E}_T$ is independent of pileup via the exact association of tracks to primary vertices. But it does not use calorimeter information and therefore does not take neutral particles into account. The TST $\not{E}_T$ definition is the default definition in ATLAS for Run 2: the track soft term is stable w. r. t. different pileup conditions and therefore improves the $\not{E}_T$ resolution. Finally the x- and y-components of the $\not{E}_T$ can be written down for the TST $\not{E}_T$ as:

$$\not{E}_{x,y} = \not{E}_{x,y}^{\text{electron}} + \not{E}_{x,y}^{\text{photon}} + \not{E}_{x,y}^{\tau} + \not{E}_{x,y}^{\text{jets}} + \not{E}_{x,y}^{\text{muon}} + \not{E}_{x,y}^{\text{soft}},$$

where the soft term depends on tracking information. Tracking information is only available inside $|\eta| < 2.5$, information on the soft term from the forward calorimeters is only used in the CST term. For the TST $\not{E}_T$ a JVT cut is applied on the jets. Tracks of a jet that fail this cut enter in the TST. Requirements for the rest of the objects correspond to the ones used in the analyses for the respective objects. Here, baseline objects after overlap removal are used to calculate the $\not{E}_T$. The performance of the $\not{E}_T$ can be measured in MC in $Z \to \ell\ell$ events or $W \to \ell\nu$ events. They are clean channels to study the resolution ($Z \to \ell\ell$) and overall scale ($W \to \ell\nu$). Important in this respect is the overall event activity, captured by the $\sum E_T$ variable:

$$\sum E_T = \sum p_T^{\text{electron}} + \sum p_T^{\text{photon}} + \sum p_T^{\tau} + \sum p_T^{\text{jets}} + \sum p_T^{\text{muon}} + \sum p_T^{\text{soft}}.$$

The $\not{E}_T$ resolution can be accessed in $Z \to \ell\ell$ events as the width of $\not{E}_T$. Since these events do not have genuine $\not{E}_T$ the distribution should be centered around zero. Genuine $\not{E}_T$ is expected in $W \to \ell\nu$ due to the produced neutrino that escapes the detector. Therefore, the $\not{E}_T$ scale is accessible in these measurements. In 2015 data taking, these events have been studied in data and the $\not{E}_T$ resolution has been compared to the MC expectation. The $\not{E}_T$ distribution in $Z \to \mu\mu$ events is shown in Fig. 6.6(a). Figure 6.6(b) shows the resolution vs. the overall $\sum E_T$. Also jets are allowed in the events. An increasing $\sum E_T$ is usually characterised by the presence of jets. The overall resolution increases with $\sum E_T$. It is however stable against N_{PV} which can be seen from Fig. 6.6(c). In all cases the data agrees well with the MC.

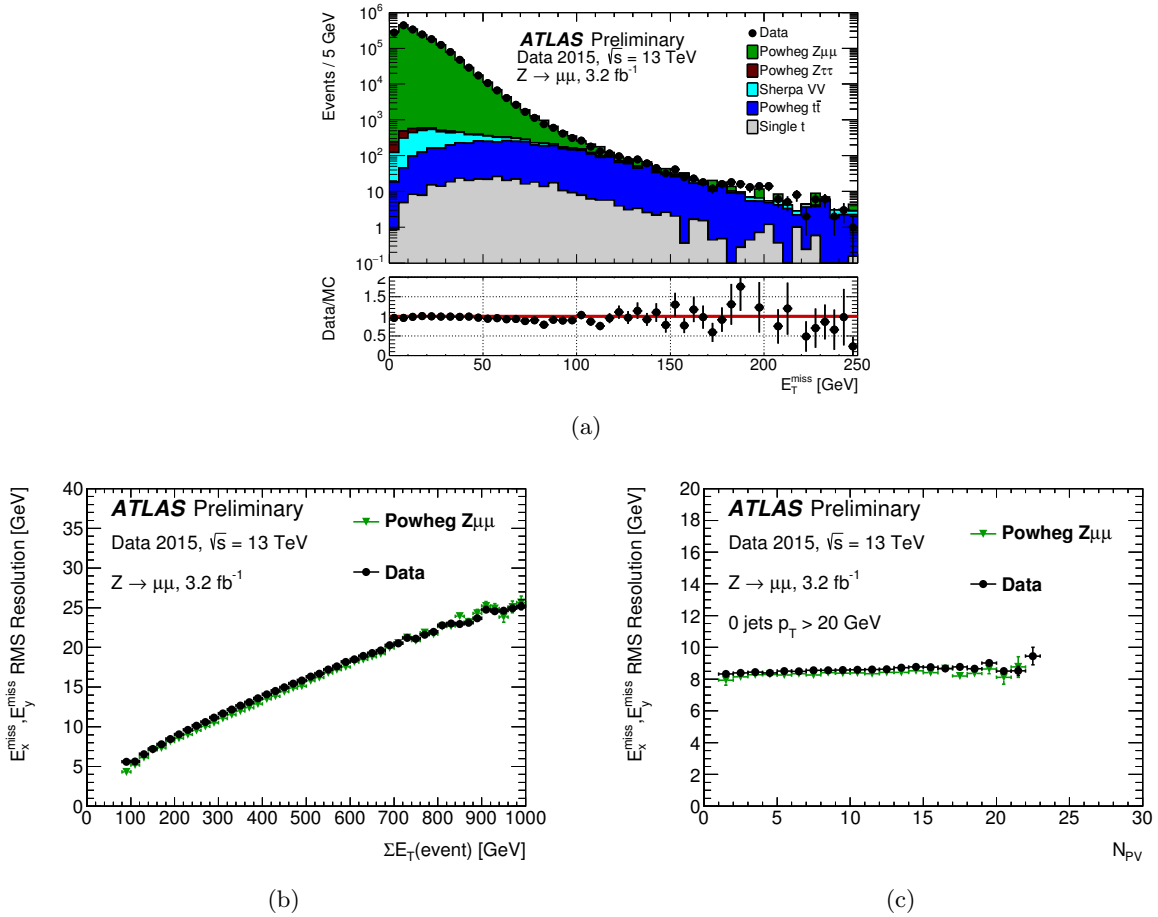

(a)

(b)

(c)

Fig. 6.6: $\not\!\!E_T$ resolution studies in 2015 data:(a): $\not\!\!E_T$ distribution in $Z \to \mu\mu$ events in MC and data. (b) $\not\!\!E_T$ resolution vs. $\sum E_T$ and (c) $\not\!\!E_T$ resolution vs. N_{PV} in selected events of $Z \to \mu\mu$ in MC and data [130].

Chapter 7

The Monojet Analysis

7.1 Event Signature

The monojet event signature at hadron colliders is traditionally a sensitive search channel for BSM physics: Its clear signature of one energetic jet and large missing transverse momentum, $\not{E}_T$, offers a variety of search possibilities: most prominent are the examples introduced in Chap. 3: large extra dimensions, Supersymmetry and WIMP dark matter searches. All these new physics scenarios have the monojet signature in common: in case of the ADD model, a graviton can be produced together with a quark or gluon. The graviton will escape the detector unseen and thereby produce $\not{E}_T$. The quark or gluon will form a jet in the detector. In the case of SUSY production, the sparticles will eventually decay into neutralinos which in turn can only be recognised via $\not{E}_T$. Usually, the production of SUSY particles is accompanied with a multitude of jets. However, if the mass splitting between the sparticle and the neutralino is of the order of a few GeV then the visible decay product, a quark jet, cannot be measured because its energy falls below the threshold of the detector acceptance. The monojet signature in this case is caused by initial state radiation (ISR): a gluon can be radiated off the initial incoming partons before the hard interaction. Likewise, it can be radiated off of a produced squark/gluino as final state radiation (FSR). Both ISR and FSR jets can recoil against the neutralinos and produce a monojet signature. In the case of WIMP pair production, the monojet signature is of particular interest: here, an ISR jet recoils against the WIMP pairs that cannot be detected as they are at most weakly interacting with the detector. All these scenarios will leave signatures in the detector as seen in the ATLAS event display in Fig. 7.1. It shows an event that was recorded during 2015 at $\sqrt{s} = 13$ TeV with the highest $\not{E}_T$ measured for monojet events of $\not{E}_T \approx 954$ GeV.
SM processes can also produce a monojet signature: the most dominant one is the production of Z-bosons in association with a jet, where the Z-boson decays into two neutrinos. This background process is essentially irreducible.
The production of monojet events involves the strong interaction via a coupling of α_s. The cross section of production of higher jet multiplicities is roughly suppressed by α_s^n, where n is the number of jets[a]. Besides monojet searches also mono-γ and mono-W/mono-Z searches are performed with the same goal of testing the mentioned BSM scenarios. The cross section for these productions involves the electroweak coupling strength and is therefore lower than the production cross section of monojet processes. Thus, the monojet search is in general more sensitive, since the statistical power allows an extended search range at higher $\not{E}_T$, where the signal over background ratio is increased. The particular strength of a monojet search is its model independence: not only the introduced BSM models can be tested, but a large variety of many different processes may produce a monojet signature in the detector. The monojet analysis is therefore designed to cover a large amount of BSM models that may predict new particles in

[a] The behaviour of production cross sections to decrease with the number of jets is known as 'Berends scaling' [132].

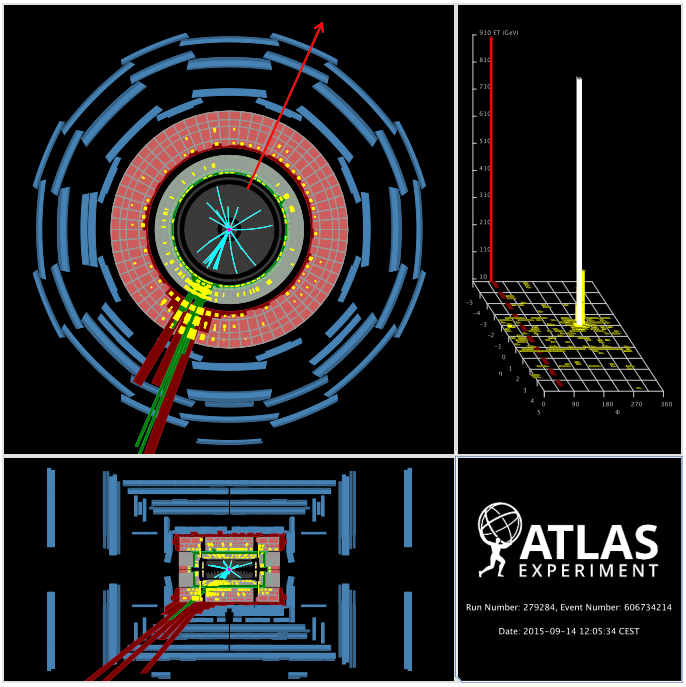

Fig. 7.1: ATLAS event display of a monojet event during 2015 data taking with $\sqrt{s} = 13$ TeV [131]: One jet is measured with transverse momentum of $p_T = 973$ GeV, indicated by the red and green bars corresponding to the energy deposition in the calorimeters. The red arrow in the opposite ϕ direction indicates the missing transverse momentum with $\not{E}_T = 954$ GeV. Tracks with p_T above 2 GeV are displayed in the ID.

different kinematic regions.

A monojet analysis has been carried out in the past with ATLAS data taken in Run 1 and Run 2. The analyses performed previously are briefly discussed in the following. The event selection, data sample and background processes are discussed as well as the background modelling.

7.1.1 Analyses in ATLAS

This section will present results of (a) a monojet analysis performed with Run 1 data aimed at WIMP and ADD extra dimension searches, (b) a monojet analysis performed with Run 1 data aimed at SUSY searches in compressed scenarios and (c) a monojet analysis performed with the first Run 2 data of 2015 aimed at WIMP, ADD extra dimensions and SUSY searches.

The name 'monojet' suggests that such events contain only one jet which is balanced by $\not{E}_T$. In fact, monojet searches performed at ATLAS in the past allowed for more jets in their event signature. The reason is that the presence of additional jets is very likely and the inclusion of such events allows to decrease the statistical uncertainty. In Run 1, the monojet analysis in ATLAS did not apply any upper cut on the jet multiplicity [133]. Instead the recoil energy of the leading jet (the one with the highest p_T) in the event was required to be of the order of the $\not{E}_T$ ($p_T/\not{E}_T > 0.5$). This analysis was performed using data taken at $\sqrt{s} = 8$ TeV and a luminosity of 20.3 fb^{-1}. Different signal regions were defined by applying various inclusive cuts on the $\not{E}_T$ starting from $\not{E}_T > 150$ GeV going up to $\not{E}_T > 700$ GeV. Background predictions were compared to various BSM models and limits on those were set: ADD production (limit on number of ex-

tra dimension n vs. M_D), WIMP production (EFT scale M_* and simplified model), gravitino production in Gauge Mediated SUSY Breaking (GMSB) models and on the branching ratio of $H \rightarrow$invisible particles, where the SM Higgs was assumed. A different analysis was optimised for SUSY compressed scenarios [134]: an upper limit of at most three jets in the events was set. Different inclusive regions were defined which set lower limits on the leading jet p_T and $\not{E}_T$ from 220 GeV up to 600 GeV. As signal, $\tilde{q} \rightarrow q + \tilde{\chi}_1^0$ processes were considered. For each signal scenario the region that has the best exclusion power was used. This was obtained by comparing the background and signal predictions with the data in each region. Figure 7.2 shows selected results from the two 8 TeV analyses: (a) the obtained limit on M_* as a function of WIMP mass m_χ for a contact operator with vector coupling in the EFT framework. The untruncated limit on M_* for low WIMP masses assuming EFT to be 100% valid is of the order of 1 TeV. The observed and expected limits coincide. (b) shows the limit on stop pair production where the stop decays into a charm-quark and a neutralino. In the degenerate case where $m_{\tilde{t}} \approx m_{\tilde{\chi}_1^0}$, the 95% CL lower limit on neutralino masses reaches as high as $\sim$ 275 GeV.

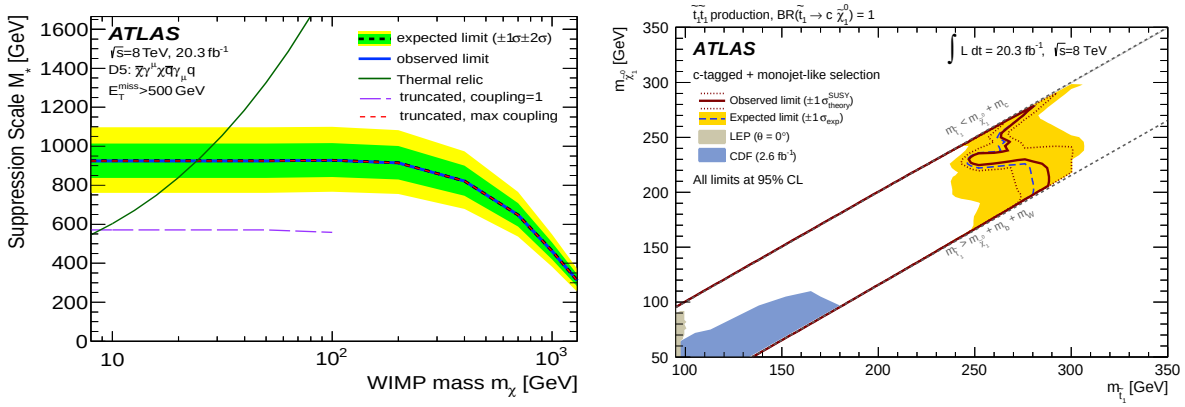

(a) (b)

Fig. 7.2: (a): Limit on M_* vs m_χ in the context of WIMP production with the contact operator D5 (vector coupling) as obtained in Ref. [133]. (b): Limit on $m_{\tilde{\chi}_1^0}$ vs $m_{\tilde{t}}$ as obtained in Ref. [134]. The limit is obtained by combining a monojet analysis and a charm-tagged analysis that is more sensitive to higher mass splittings between stop and neutralino.

For the 2015 data analysis, both efforts have been unified: the monojet analysis at ATLAS is aimed at both SUSY compressed scenarios and WIMP and ADD production searches. The analysis applies an upper cut of at most four jets on the jet multiplicity and a lower cut of 250 GeV on the $\not{E}_T$ and the leading jet p_T [131]. A shape fit to the resulting $\not{E}_T$ distribution has been performed and limits have been extracted with a dataset of 3.2 fb^{-1} taken at $\sqrt{s} = 13$ TeV. This analysis is presented in more detail in App. B. The higher centre-of-mass energy in Run 2 enabled more stringent limits despite of the reduced luminosity w. r. t. Run 1. This can be seen in Fig. 7.3(a), where the result is compared with the Run 1 exclusion limit. The limits on the effective Planck mass M_D vary between 4 and 7 TeV depending on the number of extra dimensions n. A limit on WIMP production was derived in the framework of simplified models with a mediator production of mass m_A and an axial vector coupling. The limits from the plane m_χ vs. m_A can be translated into a WIMP-nucleon cross section limit. This can be seen in Fig. 7.3(b), where the ATLAS result is compared to direct detection experiments like LUX [135], XENON100 [136] and PICO [137, 138]. As already outlined in Sec. 3.3, the direct detection

searches have limited sensitivity to low WIMP masses. The LHC is able to provide a unique sensitivity in this range.

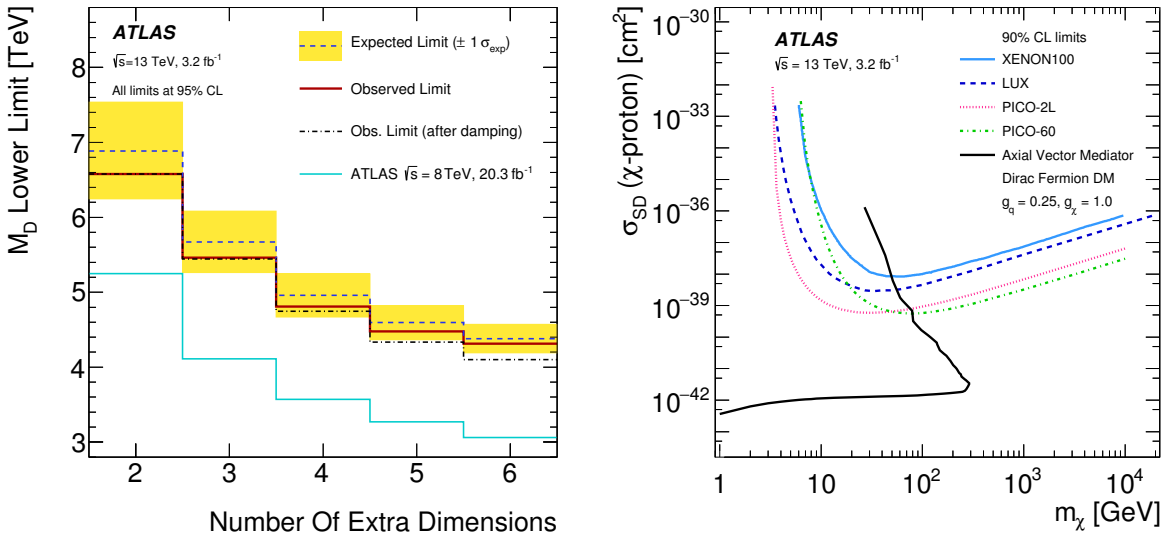

(a) (b)

Fig. 7.3: (a): Limits on M_D vs n extra dimensions. The 2015 result [131] is compared with the Run 1 result [133]. (b): Comparison of ATLAS limits on WIMP-nucleon scattering for spin-dependent interactions with direct detection experiments [131].

The monojet analysis presented in this thesis is a continuation of the 2015 analysis. It uses data taken in both 2015 and 2016 and optimises the analysis strategy to gain higher sensitivity. The dataset and the corresponding event selection are introduced in the following.

7.2 Data Sample

ATLAS Run 2 data with a centre-of-mass energy of $\sqrt{s} = 13$ TeV has been collected in 2015 and 2016. For both 2015 and 2016, data periods that satisfy the criteria of the Good Runs List (GRL) are considered. They are flagged as good physics data with a fully functional detector. The amount of data collected in 2015 is 3.2 fb^{-1}, in 2016 the integrated luminosity amounts to 32.9 fb^{-1}. Therefore, a total dataset corresponding to $\int \mathcal{L} dt = 36.1$ fb^{-1} is analysed. The monojet analysis utilises $\not{E}_T$-triggers for the data event selection. These $\not{E}_T$-triggers are calorimeter based and take into account the information from the L1Calo. This implies that at trigger level, muons are considered as invisible particles, since the MS information is not used. The triggers vary for different data periods where the trigger menu is adjusted to the changing luminosity conditions. Throughout the 2015 data taking the `HLT_xe70` trigger was applied. It requires $\not{E}_{T\,\mathrm{calo}} > 70$ GeV and is fully efficient at $\not{E}_T > 150$ GeV. During the 2016 data taking the threshold of the lowest unprescaled trigger changed due to increasing instantaneous luminosity conditions. Table 7.1 gives an overview of the different data periods with different $\not{E}_T$-triggers. Finally, to select the data of interest over all periods a logical `OR` of the mentioned triggers is applied.
During the 2016 data taking, one of the tile calorimeter modules was switched off due to a leakage problem from the water cooling system. All data taking from August 2016 onwards

(affecting ~ 8 fb^{-1}) therefore suffers from an inefficiency in the jet reconstruction for jets lying in the region of $-0.85 < \eta < 0$ and $0.39 < \phi < 0.49$. An additional module was masked during the whole 2016 period affecting the region $0. < \eta < 0.85$ and $-1.17 < \phi < -1.27$. Studies of the impact of these 'holes' have been performed and the results are collected in App. A.4. The impact was found to be negligible for the monojet analysis.

Data Period	$\not{E}_T$-trigger
Period A-C	`HLT_xe90_mht_L1XE50` `HLT_xe80_tc_lcw_L1XE50`
Period D1-D3	`HLT_xe90_mht_L1XE50`
Period D4-L11	`HLT_xe110_mht_L1XE50` `HLT_xe130_mht_L1XE50`

Tab. 7.1: Data periods in 2016 and corresponding lowest unprescaled $\not{E}_T$-triggers. The numbers indicate the threshold on $\not{E}_{T\,\text{calo}}$ in GeV.

7.3 Event Selection

The event selection of the monojet analysis has been optimised to gain the best sensitivity with respect to the models discussed (ADD, SUSY, WIMP production). After the objects are reconstructed and selected with the criteria listed in Chap. 6, a preselection is applied to select the monojet topology. The preselection criteria are listed in Tab. 7.2. The events are required to have at least one primary vertex with at least two associated tracks ($|\eta| < 2.4$) and at least one jet with $p_T > 250$ GeV. To suppress events from non-collision backgrounds[b], a tight jet cleaning is applied to the leading jet. The pseudo-rapidity of the leading jet is limited to the central region where tracking information is available. The jet cleaning takes the following variables into account:

- $f_{\text{ch}} = \sum p_T^{\text{track}}/p_T^{\text{jet}}$: the fraction of the jet momentum associated to tracks in the inner detector,
- f_{max}: the maximal energy fraction deposited in a single layer of the calorimeter.

The charge fraction f_{ch} is high for jets coming from the IP and low for non-collision jets. Likewise f_{max} is high for jets generated via muon-induced calorimeter signals or noise bursts (especially in the LAr calorimeter). The requirement on the leading jet is finally $f_{\text{ch}}/f_{\text{max}} > 0.1$ to reduce non-collision backgrounds.
Apart from one leading jet, up to three additional jets are allowed in the events. In order to reduce contamination from multijet backgrounds, where the $\not{E}_T$ emerges from a mismeasurement of a hard jet, a cut is applied on the angular separation of the $\not{E}_T$ and any selected jet in the event. The requirement $\Delta\phi(\not{E}_T, \text{jet}) > 0.4$ ensures that the $\not{E}_T$ is not aligned with a jet. The signal region (SR) is optimised to be enriched in signal processes and to have a reduced contribution from SM backgrounds.

[b] For example beam induced backgrounds due to protons interacting before the actual IP, events induced by cosmic muons or calorimeter noise bursts are non-collision backgrounds.

Category	Selection Criteria
Trigger	(HLT_xe70 && 2015 data) OR ((HLT_xe80_tc_lcw_L1XE50 OR HLT_xe90_mht_L1XE50 OR HLT_xe100_mht_L1XE50 OR HLT_xe110_mht_L1XE50) && 2016 data)
GRL	PHYS_StandardGRL_all_Good_25ns
Vertex	≥ 1 vertex with $N_{\text{trk}} \geq 2$
Event cleaning	all subdetectors ok
Jet cleaning	No baseline jet failing Loose cleaning criteria (after overlap removal)
Leading jet	$p_T > 250$ GeV, $\lvert\eta\rvert < 2.4$ Passes tight jet cleaning criteria
Jet multiplicity	$N_{\text{jets}} \leq 4$ (good jets)
Multijet suppression	$\Delta\phi(\not{E}_T, \text{jet}) > 0.4$

Tab. 7.2: Preselection cuts applied in the monojet analysis.

The following requirements are applied in addition to the preselection:

- $\not{E}_T$ >250 GeV: in this regime all $\not{E}_T$-triggers are fully efficient;
- no baseline lepton as defined in Chap. 6.

Background processes that are relevant in this signal region (SR) are discussed in the following.

7.4 Background Processes

A number of SM background processes contribute to the monojet-like signature. The various different contributions are listed below.

7.4.1 *V*+jets Background

The dominant background in the SR originates from Z-boson production in association with jets, where the Z decays into two neutrinos, $Z \to \nu\bar{\nu}$. This background is irreducible as it exhibits the same topology that leads to a monojet final state. Other weak boson production in association with jets can also contribute. In the case of $Z \to \ell\ell$ decays the event might still be selected if the leptons are not reconstructed in the detector because they lie outside the acceptance. This may produce large fake $\not{E}_T$. In the case of $W \to \ell\nu$ production with additional jets the neutrino from the decay produces genuine $\not{E}_T$ ($\ell = e, \mu, \tau$). These events are selected if the lepton is either low-energetic or lies outside the detector acceptance or in case of $\ell = \tau$ if the τ-lepton decays hadronically. For leptonically decaying bosons, dedicated control regions can be defined to estimate their contribution in the SR (see Sec. 7.6.2).

7.4.2 Top-Quark Background

Top quarks can be either produced in pairs via the strong interaction, as $t\bar{t}$, or as single top quarks via the weak interaction together with a b-quark or accompanied by a W-boson. The produced top-quark will decay almost exclusively into a W-boson and a b-quark. The b-quark

gives rise to a b-jet in the detector. The W-bosons can decay leptonically and thus produce $\not{E}_T$. Top-quark events can be selected if the lepton from the W-decay is not reconstructed. Top-quark production, especially in pairs, usually produces higher jet multiplicities. Therefore, it is a small background in the SR due to the applied jet multiplicity requirement.

7.4.3 Multijet Background

Multijet events are events in which only quarks or gluons are produced in the final state. The production cross section for these processes is very high. They originate from parton-parton scattering or fully hadronic final states of top-quark or V+jets production. However, the multijet event rate decreases rapidly with increasing jet p_T. Fake high $\not{E}_T$ can be produced by these events if a high-p_T jet is mismeasured. This background is significantly reduced by applying the $\Delta\phi(\not{E}_T,\text{jet}) > 0.4$ cut and thus contributes with less than 1% to the SR.

7.4.4 Diboson Background

In diboson production, two weak bosons are produced together: either WW, WZ or ZZ. These events can lead to a monojet-like topology if e. g. one Z-boson decays into jets and the other into neutrinos. For other combinations and decay channels this background contributes if leptons are not reconstructed. The production cross section for these processes is comparatively low since two weak couplings are involved. This background is expected to be small in the SR.

7.4.5 Non-Collision Background

Momentum imbalances in jet events can also be induced by noisy detector material or fake jets from non-collision events, like beam-induced backgrounds and cosmic muon induced backgrounds. This non-collision background is reduced by the jet cleaning requirements. The non-collision background is expected to constitute a minor background contribution to the SR ($< 1\%$).

7.5 Background Modelling

The described SM background processes are modelled with the help of various MC event generators. The modelled backgrounds are used as input to the analysis; Sec. 7.6 describes how the MC simulation is used.

The ***V*+jets** backgrounds are modelled by Sherpa version 2.2.1. The ME contains up to four jets. Processes with $V + 0, 1, 2$ jets in the final state are generated at NLO accuracy, while $V + 3, 4$ jets processes are modelled at LO. Additional jets may be added in the PS. The NLO NNPDF30nnlo [139] set with $\alpha_s = 0.118$ is used. The ME calculation assumes massless quarks, while the charm and bottom-quarks are treated as massive in the PS. The CKKW scale for matching ME and PS is set to 20 GeV. The renormalisation/factorisation scale choice is $\mu = H'_T$, the scalar sum of all objects' transverse momenta in an event. In order to guarantee a good statistical accuracy, the event generation is performed in exclusive slices of the max(H'_T, truth boson-p_T). There are also exclusive flavour samples: a sample with b-quarks (`BFilter`), with c-quarks (`CFilterBVeto`) and a sample with light-flavour quarks/gluons (`BVeto`). Individual samples are produced for different lepton flavours as well. The inclusive V+jets processes are the sum of the respective samples.

Processes involving the production of **top quarks** are simulated with POWHEG-BOX v2 ($t\bar{t}$, s-channel) and v1 (t-channel, Wt) interfaced to PYTHIA8 for the PS using the Perugia 2012 tune [140] for the underlying event. The top-quark mass is set to $m_t = 172.5$ GeV. The CT10 NLO PDF set [67] is used for the incoming partons. The LO CTEQ6L1 [141] set is utilised for the PS. EVTGEN v1.2.0 [142] takes over the decay of unstable hadrons after PS. The single-top processes are individually generated for s-channel, t-channel and associated Wt production. The factorisation scale is equal to the renormalisation scale and set to:

- $t\bar{t}$ production: $\mu = \sqrt{m_t^2 + p_T(t)^2}$, where the top-quark transverse momentum is denoted by $p_T(t)$,
- single-top t-channel: $4\sqrt{m_b^2 + p_T(b)^2}$, where m_b and $p_T(b)$ are the mass and transverse momentum of the spectator b-quark,
- single-top s-channel and Wt channel: m_t.

Diboson production is simulated with two different versions of SHERPA. SHERPA 2.2.1 uses NNPDF30nnlo PDFs while SHERPA 2.1.1. uses the CT10 PDF set. The samples are generated with up to 2 additional partons in the final state. Samples are individually produced for the different production channels and number of charged leptons and gluons/quarks in the final state. Productions of 4ℓ and $2\ell 2\nu$ final states with up to one additional parton include NLO ME generation as well as inclusive final states with $3\ell\nu, \ell 3\nu$ and 4ν decays. The rest is generated at LO. A generator level cut of 5 GeV on the two highest p_T leptons is applied to all samples. Samples are generated for inclusive lepton flavours. The standard SHERPA scale setting on CKKW matching and resummation are used.

All MC samples are generated with full detector simulation with the GEANT4 tool. The simulated samples, except for diboson production, normalised to NNLO calculations in pQCD using DYNNLO [143] and Top++2.0 [144–149] for top-production (NNLO+NNLL accuracy in the case of $t\bar{t}$ production). The diboson production is normalised at NLO precision.
The event normalisation takes properly into account event-by-event weights associated to lepton scale factors as defined in Eq. 6.1, the luminosity of the dataset, filter efficiencies (fraction of events passing generator cuts) and event-by-event generator weights. The MC simulation is overlayed by minimum-bias interactions simulated with PYTHIA8 in order to take pileup interactions into account. These events are simulated according to an a-priori chosen $\langle\mu\rangle$. The choice should ideally be close to the actual $\langle\mu\rangle$ in recorded data. If this is not the case and the relevant variables used in the analysis are affected then MC events need to be reweighted to restore the actual μ-distribution in data. Since the amount of events and the kinematics in the SR are sensitive to pileup contributions the pileup reweighting is applied.

Multijet and non-collision backgrounds are difficult to model using MC simulations. They are obtained using data-driven techniques as introduced in Sec. 7.6.3 and 7.6.4.

7.6 Analysis Strategy

This section describes the determination of the SM background entering the monojet signal regions. The statistical analysis and evaluation of systematic uncertainties will be introduced as well as the methods for the extraction of exclusion limits in the case the background model agrees with the observed data.
To discriminate background from signal in the monojet signal region the $\not{E}_T$ distribution is utilised. As can be seen from the two plots in Fig. 7.4, the number of background events is steeply falling as $\not{E}_T$ increases, while the aforementioned signal processes exhibit an enhanced tail in the $\not{E}_T$ distribution. Thus, the monojet analysis is a search for an extraordinary abundance of events at very high $\not{E}_T$. For the statistical analysis the $\not{E}_T$-distribution is divided into

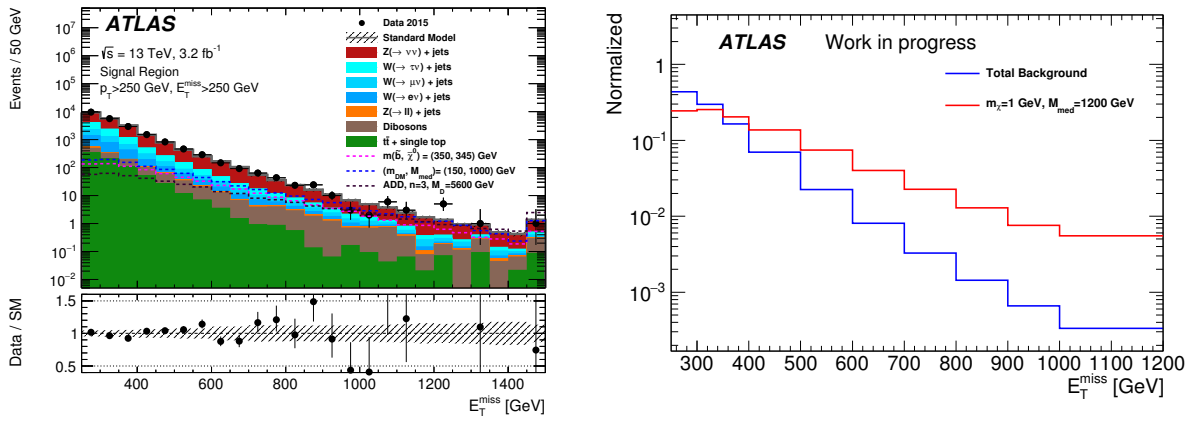

(a) (b)

Fig. 7.4: (a): $\not{E}_T$-distribution in 2015 monojet signal region after the background only fit [131]. Three examples of signal processes that have been just excluded are overlayed on top of the SM prediction, namely ADD ($n = 3, M_D = 5.6$ TeV), sbottom pair production ($m(\tilde{b}, \tilde{\chi}^0) = (350, 345)$ GeV) and DM production ($(m_\chi, M_{\text{med}}) = (150, 1000)$ GeV).(b): Shape comparison of SM background and example DM signal in $\not{E}_T$.

ten exclusive bins optimised to be sensitive to signal shapes while maintaining a high statistical accuracy (see Fig. 7.4(b)). The exact binning is presented in Tab. 7.3, where inclusive and exclusive regions in $\not{E}_T$ are defined and the naming convention is introduced. The inclusive regions will be evaluated in order to determine model-independent limits where the kind of BSM signal is unknown. In the case of specific models, the exclusive bins in $\not{E}_T$ will be used in a simultaneous fit to data to determine the sensitivity. Both methods will be explained later in Sec. 7.7.

The major background in the SR stems from $Z(\to \nu\nu)$+jets production followed by $W(\to \tau\nu)$+jets production. The next highest contributions are expected from $W(\to \mu\nu)$+jets and $W(\to e\nu)$+jets events. The top-quark background is a small contribution, minor contributions stem from $Z(\to \mu\mu/\tau\tau)$+jets, diboson production and multijet and non-collision backgrounds. The $Z(\to ee)$+jets background is negligible in the SR. The listed backgrounds are estimated employing different strategies.

The main backgrounds of W/Z+jets production are estimated using a combined method of *MC simulation modified by higher-order theory corrections* whith the overall normalisation ob-

Inclusive Regions		**Exclusive Regions**	
Name	Range [GeV]	Name	Range [GeV]
IM1	$250 < \not{E}_T$	EM1	$250 < \not{E}_T < 300$
IM2	$300 < \not{E}_T$	EM2	$300 < \not{E}_T < 350$
IM3	$350 < \not{E}_T$	EM3	$350 < \not{E}_T < 400$
IM4	$400 < \not{E}_T$	EM4	$400 < \not{E}_T < 500$
IM5	$500 < \not{E}_T$	EM5	$500 < \not{E}_T < 600$
IM6	$600 < \not{E}_T$	EM6	$600 < \not{E}_T < 700$
IM7	$700 < \not{E}_T$	EM7	$700 < \not{E}_T < 800$
IM8	$800 < \not{E}_T$	EM8	$800 < \not{E}_T < 900$
IM9	$900 < \not{E}_T$	EM9	$900 < \not{E}_T < 1000$
IM10	$1000 < \not{E}_T$	-	-

Tab. 7.3: Definition of various signal regions used in the statistical analysis.

tained from the data in *background enriched control regions*. The higher-order theory correction modifies the boson-p_T, $p_T(V)$, distribution to NLO QCD+NNLO EW theory predictions by reweighting the differential $p_T(V)$ cross section in the MC simulation. In the following, the $\not{E}_T$ used in various background enriched control regions is defined such that it approximates the $p_T(V)$. Thereby, background constraints from the control regions can be extrapolated to the $\not{E}_T$-distribution in the SR. The theory reweighting provides a better understanding of the $\not{E}_T$-shapes. This is crucial to establish the relation between the $W(\to \ell\nu)$+jets and $Z(\to \ell\ell)$+jets processes and the dominant background from the $Z(\to \nu\nu)$+jets production. The $\not{E}_T$ in the SR resembles the $p_T(V)$ of the $Z(\to \nu\nu)$-boson. There are no possibilities to estimate this background in an orthogonal control region to the SR. Thus, it has to be estimated using similar processes, namely, $W(\ell\nu)$+jets and $Z(\ell\ell)$+jets, that can be constrained in orthogonal control regions. The precise theory modelling of all V+jets events allows for the extrapolation from $W/Z(\ell\ell)$+jets predictions in the control regions to the $Z(\nu\nu)$+jets estimate in the signal region. The theory higher-order corrections come with uncertainties related to NLO QCD, NNLO EW calculations. These uncertainties are mostly correlated across processes.
In a simultaneous shape fit to the $\not{E}_T$-distributions in background-enriched control regions these uncertainties can be propagated to the dominant background and enable a precise determination of the overall background estimate in the SR. The procedure to obtain higher-order theory corrections is discussed in the next section (Sec. 7.6.1). The definition of the background enriched control regions follows in Sec. 7.6.2. Table 7.4 lists the different methods to obtain the various background predictions. The described method is denoted as "theory shape, data normalisation". The top-quark background is estimated similarly in a control region. The $\not{E}_T$-shape is not reweighted but supplied by the MC simulation, since this background is not used to extrapolate the V+jets backgrounds ("MC shape, data normalisation"). The diboson production is entirely estimated by MC simulation. Multijet and non-collision background are data-driven.

7.6.1 Higher Order QCD and Electroweak Corrections

The understanding of the V+jets backgrounds is the key point of the analysis and the best sensitivity is obtained by being able to precisely determine the contribution of these backgrounds and most importantly estimate the $Z(\nu\nu)$+jets background. In order to do so, higher-order perturbative corrections both in QCD and EW processes are included. Namely, NLO QCD

Background Process	Estimation Method	Control Region
$Z \to \nu\nu$+jets	theory shape, data normalisation	$W(\to \mu\nu)$+jets
$W \to e\nu$+jets	theory shape, data normalisation	$W(\to e\nu)$+jets
$W \to \mu\nu$+jets	theory shape, data normalisation	$W(\to \mu\nu)$+jets
$W \to \tau\nu$+jets	theory shape, data normalisation	$W(\to \mu/e\nu)$+jets
$Z/\gamma^* \to ee$+jets	theory shape, data normalisation	-
$Z/\gamma^* \to \mu\mu$+jets	theory shape, data normalisation	$Z(\to \mu\mu)$+jets
$Z/\gamma^* \to \tau\tau$+jets	theory shape, data normalisation	$W(\to e\nu)$+jets
$t\bar{t}$, single top	MC shape, data normalisation	$W(\to \mu\nu)$+b-jets
Diboson	MC only	-
Multijet	data driven	$\Delta\phi(\not{E}_T,\text{jets}) < 0.4$
Non-collision	data driven	-

Tab. 7.4: Background processes and their estimation method.

and NNLO EW corrections are provided for the $p_T(V)$ of the boson (V being both W- and Z-boson) at particle level and theoretical uncertainties are taken into account. For the MC simulations, the backgrounds are modelled at NLO precision in pQCD and LO precision in EW theory. The cross sections are normalised to NNLO in pQCD. The MC generation at NLO pQCD and NNLO EW can be circumvented by applying a reweighting scheme. The reweighting is done w. r. t. $p_T(V)(\equiv p_T^V)$. The following prescriptions summarise the reweighting procedure as worked out by Lindert et al. in Ref. [150][c]. The reweighting of the background MC prediction is done as follows:

$$\frac{\mathrm{d}}{\mathrm{d}p_T^V}\frac{\mathrm{d}}{\mathrm{d}\vec{y}}\sigma^{(V)}(\vec{\varepsilon}_{\mathrm{MC}},\vec{\varepsilon}_{\mathrm{th}}) = \frac{\mathrm{d}}{\mathrm{d}p_T^V}\frac{\mathrm{d}}{\mathrm{d}\vec{y}}\sigma^{(V)}_{\mathrm{MC}}(\vec{\varepsilon}_{\mathrm{MC}}) \left[\frac{\frac{\mathrm{d}}{\mathrm{d}p_T^V}\sigma^{(V)}_{\mathrm{th}}(\vec{\varepsilon}_{\mathrm{th}})}{\frac{\mathrm{d}}{\mathrm{d}p_T^V}\sigma^{(V)}_{\mathrm{MC}}(\vec{\varepsilon}_{\mathrm{MC}})}\right]. \tag{7.1}$$

The term in brackets thereby is the reweighting factor applied to the fully differential cross section as predicted by the MC, where $\vec{y}$ denotes all other observables but p_T^V and the dependence on $\vec{y}$ is integrated out for terms of $\frac{\mathrm{d}}{\mathrm{d}p_T^V}\sigma$. The nominator of the bracket-term in Eq. 7.1 is provided by theoretical calculations. The nuisance parameters are described by $\vec{\varepsilon}_{\mathrm{MC}}, \vec{\varepsilon}_{\mathrm{th}}$, where the theory uncertainties are provided in addition to the calculation. The term

$$R_{\mathrm{MC}} = \frac{\frac{\mathrm{d}}{\mathrm{d}p_T^V}\frac{\mathrm{d}}{\mathrm{d}\vec{y}}\sigma^{(V)}_{\mathrm{MC}}}{\frac{\mathrm{d}}{\mathrm{d}p_T^V}\sigma^{(V)}_{\mathrm{MC}}} \tag{7.2}$$

is obtained from the MC inputs to the analysis. Both denominator and nominator of R_{MC} need to have the same scales, PDFs and input parameters. On the other hand, the bracket term in Eq. 7.1 must use the same selection cuts for denominator and nominator. While the nominator of R_{MC} is the nominal MC background prediction used in the analysis, the denominator of Eq. 7.1 r. h. s. needs to be adopted to comply with the independent theory calculation. In order to use the reweighting some requirements have to be fulfilled: the theory prediction needs to be at least as precise as the MC prediction and the correlations among p_T^V and $\vec{y}$ need to be more

[c] The quoted note already includes NNLO QCD corrections and updates on PDF uncertainties which were not available at the time of the analysis.

or at least as precisely described by the MC compared to the theory calculations. Furthermore, the variable p_T^V needs to have minimal sensitivity to soft QCD interactions, which is the case for p_T^V with values $\gtrsim 250$ GeV. The reweighting is only useful for inclusive p_T^V distributions and insensitivity of the analysis to multijets emission. The components of the theory calculation are the following:

$$\frac{\mathrm{d}}{\mathrm{d}p_T^V}\sigma_{\mathrm{th}}^{(V)} = \frac{\mathrm{d}}{\mathrm{d}p_T^V}\sigma_{\mathrm{QCD}}^{(V)} + \frac{\mathrm{d}}{\mathrm{d}p_T^V}\sigma_{\text{QCD-EW}}^{(V)} + \frac{\mathrm{d}}{\mathrm{d}p_T^V}\Delta\sigma_{\mathrm{EW}}^{(V)} + \frac{\mathrm{d}}{\mathrm{d}p_T^V}\sigma_{\gamma\text{-ind}}^{(V)}. \tag{7.3}$$

The subscripts refer to the higher order corrections of QCD, EW, mixed QCD-EW calculations and photon-induced contribution, respectively. The individual terms will be discussed briefly in the following.
The photon induced term refers to production of the form $q\gamma \to Vq'$ with the photon stemming from the photon PDF inside the proton. The impact on Z+jets production is negligible. The impact on the W+jets production is evaluated via the comparison of different PDFs (LUXqed [151] vs. CT14qed_inc [152]).

The QCD prediction is given at NLO ($\mathcal{O}(\alpha\alpha_s^2)$). The QCD higher order calculations are applied as factors $K_{\mathrm{NLO}}(x, \vec{\mu})$ to the LO prediction:

$$\frac{\mathrm{d}}{\mathrm{d}p_T^V}\sigma_{\text{NLO QCD}}^{(V)}(\vec{\mu}) = K_{\mathrm{NLO}}(p_T^V, \vec{\mu})\frac{\mathrm{d}}{\mathrm{d}p_T^V}\sigma_{\text{LO QCD}}^{(V)}(\vec{\mu}_0). \tag{7.4}$$

The correction factor is a function of p_T^V and $\vec{\mu} = (\mu_F, \mu_R)$. The central scale is $\vec{\mu}_0 = (H_T'/2, H_T'/2)$, where H_T' is the scalar sum of all transverse momenta of objects at parton level in the event. This includes the boson transverse energy and radiated quarks, gluons and photons. The uncertainties on the NLO QCD correction consist of three components ($\vec{\mu}$-related, shape related and process correlation uncertainties, see Sec. 7.8.2).
Contributions including higher order electroweak corrections are denoted as

$$\frac{\mathrm{d}}{\mathrm{d}p_T^V}\sigma_{\mathrm{EW}}^{(V)} = \frac{\mathrm{d}}{\mathrm{d}p_T^V}\sigma_{\text{LO QCD}}^{(V)} + \frac{\mathrm{d}}{\mathrm{d}p_T^V}\Delta\sigma_{\text{NLO EW}}^{(V)} + \frac{\mathrm{d}}{\mathrm{d}p_T^V}\Delta\sigma_{\text{NNLO Sud}}^{(V)}.$$

The electroweak correction is split in exact NLO ($\mathcal{O}(\alpha^2\alpha_s)$) contributions and NNLO EW Sudakov logarithms in NLL (next-to-leading-logarithm) approximation. EW Sudakov logarithms enter at the level of $pp \to V$+jets production. Also the EW corrections are applied as factors to the LO QCD cross section:

$$\frac{\mathrm{d}}{\mathrm{d}p_T^V}\sigma_{\mathrm{EW}}^{(V)}(\mu) = \left[1 + K_{\mathrm{EW}}(p_T^V, \vec{\mu})\right]\frac{\mathrm{d}}{\mathrm{d}p_T^V}\sigma_{\text{QCD LO}}^{(V)}(\vec{\mu}). \tag{7.5}$$

In contrast to Eq. 7.4, the LO QCD cross section is taken at the same scale $\vec{\mu}$ as the EW correction, thus the relative EW correction is essentially independent of μ: $K_{\mathrm{EW}}(p_T^V, \vec{\mu}) \mapsto K_{\mathrm{EW}}(p_T^V)$. This factor is split into its components:

$$K_{\mathrm{EW}}(p_T^V) = K_{\text{NLO EW}}(p_T^V) + K_{\text{NNLO Sud.}}(p_T^V).$$

The corrections include virtual EW corrections to $q\bar{q} \to Vg$, photon Bremsstrahlung ($q\bar{q} \to Vg\gamma$), virtual QCD corrections to $q\bar{q} \to V\gamma$ to cancel singularities arising from photon Bremsstrahlung and $q\bar{q} \to Vq'\bar{q}'$ Bremsstrahlung. Real boson emission is not included as this leads

to diboson final states already covered by the actual diboson background modelling. For high momentum transfers with $Q \gg m_{W/Z}$ the coupling becomes large and so-called Sudakov logarithms of the form $\ln^k(Q^2/m_W^2)$ $(k = 2, 1)$ have to be taken into account for NNLO corrections (two loops) [78]. They are evaluated at NLL precision. Related to the Sudakov evaluation and NLO EW correction are three uncertainty components (see Sec. 7.8.2).

Combining both QCD and EW corrections leads to an overall correction factor of:

$$K_{\text{th}}(p_T^V, \vec{\mu}) = K_{\text{NLO}}(p_T^V, \vec{\mu}) \left[1 + K_{\text{EW}}(p_T^V)\right]. \tag{7.6}$$

This multiplicative approach leads to mixed correction terms of the order $\mathcal{O}(\alpha\alpha_s)$. An uncertainty is applied to account for non-factorised mixed EW-QCD effects (see Sec. 7.8.2).

The final correction factor has the form in Eq. 7.6. Uncertainties on the theory prediction are taken into account in the statistical fit model and will be referred to in Sec. 7.8.2. Figure 7.5 shows the final reweighting factors as a function of the boson-p_T for the different processes. The correction factor includes QCD+EW corrections. The correction is shown for $Z(ee)$+jets (a), $W(e\nu)$+jets (b) and $Z(\nu\nu)$+jets (c) and lepton universality is assumed, meaning the corrections is the same for boson-decays with $\ell = e, \mu, \tau$. The NLO QCD correction is applied to the NLO MC prediction to be consistent with the theory calculation. The corrections correspond to the reweighting term in Eq. 7.1. In addition, theory systematic uncertainties are drawn. Solid lines correspond to high-variations, dotted lines to low-variations. From these correction values it is anticipated that the overall number of events for W/Z+jets processes is decreased w.r.t. the nominal MC prediction, since they are always below 1. For the region $p_T(V) \sim 300$ GeV the correction factors are around 0.85 for $W(\ell\nu)$+jets and $Z(\nu\nu)$+jets processes and slightly higher for $Z(\ell\ell)$+jets (~ 0.87). The correction factor continuously decreases with increasing $p_T(V)$. It stays constant at values above $p_T(V) = 1$ TeV. In this region the $W(\ell\nu)$+jets cross section is modified by a factor of 0.72. The same factors are around 0.82 for $Z(\ell\ell)$+jets and 0.78 for $Z(\nu\nu)$+jets. While $Z(\nu\nu)$+jets and $W(\ell\nu)$+jets processes are similarly reweighted at low $p_T(V)$, the correction differs for high boson-p_T where the $W(\ell\nu)$+jets process receives larger corrections stemming from the EW higher-order calculation. The correction factors among $Z(\ell\ell)$+jets and $Z(\nu\nu)$+jets are more similar, but also here a slight difference appears for higher $p_T(V)$ of about 4%. The impact of systematic variations is similar among all processes.

7.6.2 Definition of Control Regions

The control regions (CR) are defined orthogonal to the SR, meaning there is no overlap of events between control regions and signal regions. The same preselection criteria as listed in Tab. 7.2 are applied to the control regions to ensure the kinematic proximity and a minimal kinematic extrapolation from control regions to signal regions. As anticipated, crucial to the application of higher-order theory corrections is the $\not{E}_T$-definition. In the respective regions the $\not{E}_T$ includes muons or electrons as invisible particles. In $W \to \mu\nu$ and $Z \to \mu\mu$ decays the definition of $\not{E}_T$ (muons invisible) is used. Likewise, for $W \to e\nu$ decays the $\not{E}_T$ (electrons invisible) resembles the W-boson p_T. There is no special control region defined for the $Z(ee)$+jets (since it is a negligible background) but it is treated consistently with all other V+jets background estimations.
Four different CRs are defined that reverse the lepton veto and add cuts depending on the specific region which are described in the following.

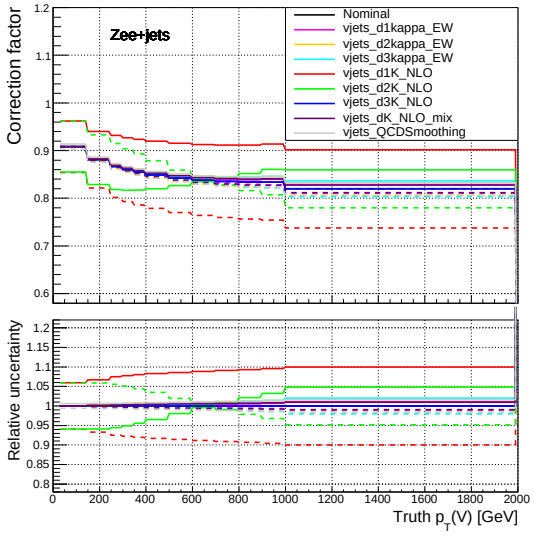

(a) $Z(ee)$+jets

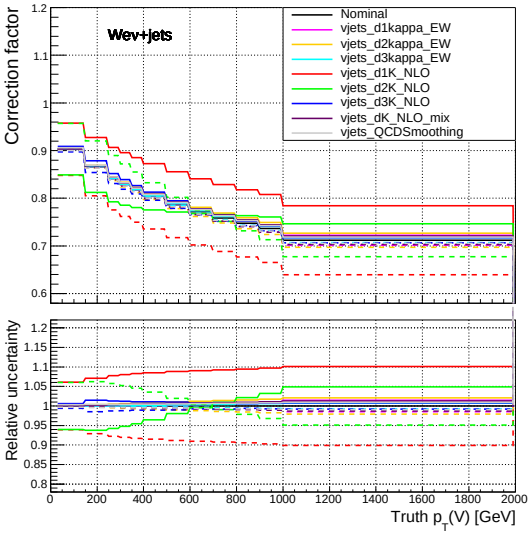

(b) $W(e\nu)$+jets

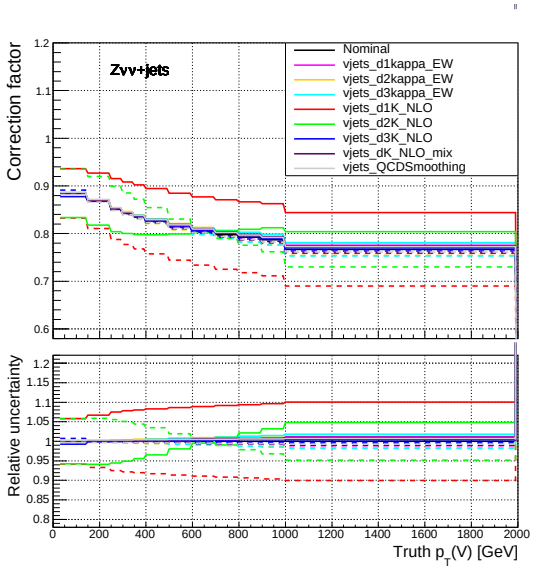

(c) $Z(\nu\nu)$+jets

Fig. 7.5: Reweighting factor obtained from theory correction to be applied to the truth boson-p_T. (a) Correction applied to $Z(\ell\ell)$+jets processes, (b) correction applied to $W(\ell\nu)$+jets processes and (c) correction applied to the $Z(\nu\nu)$+jets process.

Muon Control Region

The muon control region is denoted as CR1m. It is enriched in $W(\rightarrow \mu\nu)$+jets processes ($\sim 85\%$ of all processes). Additionally to the preselection criteria, the following requirements need to be fulfilled:

- $\not{E}_T > 250$ GeV (includes muons as invisible),
- no reconstructed baseline electrons,

- exactly one baseline and signal muon is reconstructed,
- the *transverse mass*, $m_T(W)$ has to fulfil: 30 GeV$< m_T(W) <$ 100 GeV,
- no reconstructed jet is b-tagged.

The transverse mass of the W-boson is defined as

$$m_T(W) = \sqrt{2p_T^\ell \not{E}_T(1 - \cos(\phi^\ell - \phi^\nu))}, \tag{7.7}$$

where p_T^ℓ and ϕ^ℓ denote the transverse momentum and azimuthal angle of the lepton from the W-decay and $\not{E}_T$ is the energy of the escaping neutrino with angle ϕ^ν in the transverse plane. This quantity has a maximum at around ~ 70 GeV for W-decays and a cut on it ensures that events containing a leponically decaying W-boson are selected. The b-jet veto is applied to ensure orthogonality with the top control region.

Top Control Region

The top control region is designed to be dominated by top-quark production processes and is defined with the same criteria as CR1m with one exception: The event has to contain at least one jet that is b-tagged with a 60% b-tag WP. This region has a reduced statistics compared to CR1m by a factor of 10. This region is called CRtop. Top-quark events (almost) always produce an on-shell W-boson and a b-jet. With the introduced selection criteria, top-quark events with $W \to \mu\nu$ are selected. The region is dominated by $t\bar{t}$ events while single top-quark production contributes about a quarter of the total top-quark background. The purity of this region is about 75% for all top-quark processes.

Electron Control Region

The electron control region (CR1e) is designed to be enriched in the process $W(\to e\nu)$+jets. A single electron trigger is used in this region. It is fully efficient for an electron with $p_T > 30$ GeV. All criteria to be fulfilled in addition to the preselection criteria are:

- pass single electron trigger:
  2015 data: `HLT_e24_lhmedium_L1EM20VH` OR `HLT_e60_lhmedium` OR `HLT_e120_lhloose`
  2016 data: `HLT_e26_lhtight_nod0_ivarloose` OR `HLT_e60_lhmedium_nod0` OR `HLT_e140_lhloose_nod0`
- $\not{E}_T$(no e) > 250 GeV (electron term is subtracted from the $\sum E_T$),
- no baseline muon as defined in Chap. 6 is reconstructed,
- exactly one baseline and signal electron is reconstructed with $p_T > 30$ GeV and $|\eta| < 1.37$ or $|\eta| > 1.52$,
- the signal electron is required to pass `FixedCutTight` isolation criteria,
- $m_T(W)$ as defined in Eq. 7.7 has to fulfil: 30 GeV$< m_T(W) <$ 100 GeV,
- $\not{E}_T/\sqrt{H_T} > 5.0$ GeV$^{1/2}$, where H_T is the sum of all good jets' transverse momenta.

This region is defined similar to the CR1m applying the same transverse mass cut and $\not{E}_T$ cut, which treats electrons as invisible. The additional cut on $\not{E}_T/\sqrt{H_T}$ (genuine $\not{E}_T$) suppresses a background from multijet events in this region. This is also the reason for requiring a tight isolation as defined in Sec. 6.3.

Dimuon Control Region

The dimuon control region is called CR2m and is a region enriched with $Z(\rightarrow \mu\mu)$+jets processes. The additional requirements are:

- $\not{E}_T > 250$ GeV (muons invisible),
- no baseline electrons are reconstructed,
- exactly two baseline muons that fulfil good muon definitions,
- the invariant mass of the two muons is 66 GeV$< m_{\mu\mu} <$ 116 GeV.

The cut on the invariant mass is placed around the Z-boson mass and leads to a high purity of the $Z(\rightarrow \mu\mu)$+jets sample selection ($\sim 90\%$).

Apart from the here mentioned regions, also studies employing a **γ+jets** control region have been performed. The kinematic proximity to Z+jets production at large boson-p_T and the high statistical precision of a γ+jets sample in principle provides the means to estimate the dominant $Z(\nu\nu)$+jets background.
In order to do so, the available MC+theory modelling of the γ+jets production and the W/Z+jets production need to be consistent. The available MC simulation for γ+jets processes is done by Sherpa 2.1.1 at LO with up to four additional jets. The theory reweighting scheme can be applied to this background to get a consistent modelling at NLO in QCD and NNLO in EW calculation. In this respect, the isolation definition of the photon plays an important role: the photon needs to be isolated to avoid that QCD effects lead to collinear singularities. This is not needed for W- and Z-bosons, whose masses regulate the singularities. As described in Sec. 6.4, the isolation prescription at analysis level requires the energy/track momenta deposited in a cone of fixed size R around the photon to fall below a certain threshold. The theory description on the other hand uses a dynamic cone size R, which is E_T dependent. This is done to ensure a consistent treatment of γ+jets and W/Z+jets processes. However, the intrinsic isolation cut applied in Sherpa is tighter than the dynamic prescription. Therefore, the denominator in Eq. 7.2 cannot be calculated properly and the theory correction factor will not be reliable. Due to this inconsistency, the analysis strategy cannot make use of a γ+jets control region. More details and studies on the impact of a γ+jets control region on the analysis sensitivity are given in the appendix in Sec. A.3.

7.6.3 Multijet Background Estimation

The multijet background is assumed to originate mainly from mismeasurements of energetic jets. The modelling of this background including non-Gaussian detector effects is difficult and therefore a data-driven method is devised: the so-called *jet smearing method*. This method follows the steps:

1. Select 'seed events' in data with a low $\not{E}_T$-significance, defined as $(\not{E}_T - 8)/\sqrt{\sum E_T}$.
2. Measure the jet response function in MC and match them to *smeared* seed events from data (step 1):
   The jet response function describes the measurement of reconstructed particles as a function of truth level particles. They can only be obtained in MC simulation where the truth level is generated and compared to the reconstructed level. These functions are constrained

by data: control regions sensitive to jet measurements like dijet events and three-jet events are used. The MC jet response functions are modified to match the data events.

3. The modified jet response functions are used to smear the seed events and to obtain the distributions for kinematic variables relevant for the analysis.

Seed events in step 1 are selected by requiring single jet triggers and applying event cleaning cuts as used in the analysis. Additionally, a low $\not\!\!E_T$-significance is required to use only events in which the jets are well measured (low $\not\!\!E_T$ in events). At the same time, this cut should not bias the variables that will be examined later. Therefore, the following cut is applied:

$$\frac{\not\!\!E_T - 8}{\sqrt{\sum E_T}} < 0.5 + 0.1 \cdot N_{b\text{-jet}}\sqrt{\text{GeV}},$$

where $N_{b\text{-jet}}$ is the number of b-tagged jets (the response functions differ for b- and non b-jets). Applying the obtained jet response functions to the seed events is called smearing and enables to generate multijet pseudo-data. The normalisation of the smeared events is obtained in a multijet control region: it is defined like the SR, except the $\Delta\phi(\not\!\!E_T$,jet)-cut is reversed: $\Delta\phi(\not\!\!E_T$, any jet) < 0.4 is applied in order to select events from the smeared pseudo-data where jet momenta are most likely mismeasured, producing fake $\not\!\!E_T$ in the event. In this control region, a normalisation factor k_{QCD} is obtained via

$$k_{QCD} = \frac{N_{QCD}^{\text{data}} - N_{QCD}^{\text{otherMC}}}{N_{QCD}^{\text{smeared}}},$$

where N_{QCD}^{data} denotes the number of data events in the multijet control region and N_{QCD}^{otherMC} the other background events present in this region. N_{QCD}^{smeared} is the number of smeared events that pass the multijet control region cuts. The normalisation is applied on $N_{\text{SR}}^{\text{smeared}}$ to obtain the final event yield in the SR. The factor k_{QCD} is obtained in the inclusive $\not\!\!E_T$-region and therefore is the same in all $\not\!\!E_T$-bins.

7.6.4 Non-Collision Background Estimation

The introduced jet cleaning cuts in Sec. 7.3 reduce the number of events stemming from non-collision backgrounds (NCB) by a factor of $\mathcal{O}(10^3)$. The residual contamination that survives the leading jet cleaning cuts can be estimated with the use of jet timing information, t_{jet}. The time of a jet is determined as the energy weighted average time of the corresponding energy deposit in the calorimeter w. r. t. the event time recorded by the trigger. If $|t_{\text{jet}}| > 5$ ns then the jet is most likely a 'NCB jet'. This timing behaviour is used to tag non-collision background jets where the efficiency is determined in a NCB enriched region. This region is defined like the SR but with reversed tight-cleaning cuts. Then the NCB tagging efficiency is determined as:

$$\varepsilon_{\text{NCB}} = \frac{N_{t_{\text{jet}}<-5\text{ ns}}^{\text{CR}}}{N^{\text{CR}}},$$

where $N_{t_{\text{jet}}<-5\text{ ns}}^{\text{CR}}$ is the number of events in the NCB enriched region with $t_{\text{jet}} < -5$ ns and N^{CR} is the total number of events in this region. Applying this efficiency to the number of events in

the SR with $t_{\text{jet}} < -5$ ns yields the final estimate of non-collision background events in the SR:

$$N_{\text{NCB}}^{\text{SR}} = \frac{N_{t_{\text{jet}}<-5\text{ ns}}^{\text{SR}}}{\varepsilon_{\text{NCB}}}.$$

The jets tagged as NCB jets are positively out-of-time w. r. t. to the pp collision event (before the event), which are more likely than negatively out-of-time events. The kinematics of jets with $t_{\text{jet}} > 5$ ns are different. Nevertheless, a cross-check of the NCB estimate can be done by tagging these jets. This shows agreement with the estimate from the positively out-of-time jets. This estimate is done in the various $\not{E}_T$-regions.

7.7 Statistical Analysis

The following section introduces the statistical model to obtain the background prediction in the various defined signal regions. It also discusses the derivation of exclusion limits on specific signal hypotheses and, in general, model-independent upper cross section limits. The model includes information from the control regions and incorporates systematic uncertainties.

7.7.1 Maximum Likelihood Method

The maximum likelihood method is a way to estimate unknown parameters from a certain dataset and to perform hypothesis testing. The method is ascribed to R. A. Fisher, 1912 [153, 154]. Assume a dataset with $\boldsymbol{x} = \{x_1, x_2, \dots x_N\}$ from N measurements is given. The set of the unknown parameters to be estimated is denoted by $\boldsymbol{\theta} = \{\theta_1, \theta_2 \dots\}$. The different x_i are statistically independent and distributed according to a parent distribution (probability density function, pdf) $P(x_i|\boldsymbol{\theta})$. The likelihood $\mathcal{P}$ is then defined as the product of the pdfs of each x_i:

$$\mathcal{P}(\boldsymbol{x}|\boldsymbol{\theta}) = \prod_{i=1}^{N} P(x_i|\boldsymbol{\theta}). \tag{7.8}$$

Thus, Eq. 7.8 represents the probability for a certain set of $\boldsymbol{\theta}$ to explain the measured data $\boldsymbol{x}$. The best estimate for $\boldsymbol{\theta}$ is given by $\hat{\boldsymbol{\theta}}$ which maximises the likelihood $\mathcal{P}$. In complex cases, the expression in Eq. 7.8 may be difficult to handle in computations and therefore often the negative logarithm of the likelihood is used, that contains sums rather than products:

$$-\ln \mathcal{P}(\boldsymbol{x}|\boldsymbol{\theta}) = -\sum_{i=1}^{N} \ln P(x_i|\boldsymbol{\theta}). \tag{7.9}$$

Here, the expression in 7.9 needs to be minimised to find the best parameter estimate $\hat{\boldsymbol{\theta}}$. The minimisation is often carried out numerically by tools like MINUIT [155].

7.7.2 Monojet Analysis Fit Model

In a dataset where the number of measurements N is large, it is more efficient to bin the data rather than to provide single measurements of x_i as input to the likelihood. This is done without losing essential information and at the same time facilitating the computation. The monojet analysis utilises the $\not{E}_T$ distribution with a binning as introduced in Tab. 7.3. One can then construct the multinomial likelihood for M bins (where $M = 10$ holds here) as:

$$\mathcal{P} = N! \prod_{j=1}^{M} \frac{P_j(\boldsymbol{\theta})^{n_j}}{n_j!}, \tag{7.10}$$

where n_j is the observed number of entries in bin j and $P_j(\boldsymbol{\theta}) = \int_{x_j^{\text{low}}}^{x_j^{\text{high}}} P_j(x|\boldsymbol{\theta})\mathrm{d}x$. The bin limits in $x(= \not{E}_T)$ of bin j are denoted by x_j^{low} and x_j^{high}. For each number of entries in a bin j the expected number of entries is given by ν_j. The overall expected number in all bins shall be ν and this leads to $\nu_j = P_j(\boldsymbol{\theta})\nu_j$ with $\sum \nu_j = \nu$. Likewise applies: $\sum n_j = N$. The probability of

observing N events overall is then given by a Poisson distribution:

$$\frac{\nu^N}{N!}\mathrm{e}^{-\nu}. \tag{7.11}$$

The Poisson term in Eq. 7.11 is multiplied to the likelihood in Eq. 7.10 and consequently leads to

$$\mathcal{P} = \prod_{j=1}^{M} \frac{\nu_j^{n_j}}{n_j!}\mathrm{e}^{-\nu_j}, \tag{7.12}$$

and thereby it is clear that the Poissonian probability holds for the individual bin entries. The likelihood in Eq. 7.12 represents only a single region with M bins in $\not\!\!E_T$. In the monojet analysis control regions are included in a combined fit to constrain the various backgrounds. Therefore, a likelihood like in Eq. 7.12 is constructed for all control regions, with C as the number of CRs. The likelihoods are multiplied with each other:

$$\mathcal{P} = \prod_{l=1}^{C}\prod_{j=1}^{M} \frac{\nu_{lj}^{n_{lj}}}{n_{lj}!}\mathrm{e}^{-\nu_{lj}}. \tag{7.13}$$

Here, n_{lj} denotes the number of observed events in region l and bin j and ν_{lj} is the number of expected events in region l and bin j. This number is composed of a signal expectation and a background expectation:

$$\nu_{lj} = \mu_{\mathrm{sig}} N_{lj}^{\mathrm{sig}} + N_{lj}^{\mathrm{BKG}}, \tag{7.14}$$

where the predicted event number of a certain signal is given by N_{lj}^{sig}. It is multiplied by the *signal strength* μ_{sig}, which is a free parameter of the fit. The background prediction is given by the number of expected events in a control region modified by the respective *transfer factors* κ_j^{bkg} (bkg as index over all background contributions):

$$\begin{aligned} N_{lj}^{\mathrm{BKG}} &= \sum_{\mathrm{bkg}} \kappa^{\mathrm{bkg}} N_{lj}^{\mathrm{MC,bkg}} + N_{lj}^{\mathrm{multijet}} + N_{lj}^{\mathrm{NCB}} \\ &= \kappa^{V}\left[N_{lj}^{\mathrm{MC},W(\ell\nu)+\mathrm{jets}} + N_{lj}^{\mathrm{MC},Z(\nu\nu)+\mathrm{jets}} + N_{lj}^{\mathrm{MC},Z(\ell\ell)+\mathrm{jets}}\right] \\ &+ \kappa^{\mathrm{Top}} N_{lj}^{\mathrm{MC},t\bar{t}+\mathrm{single}\ t} \\ &+ N_{lj}^{\mathrm{MC,diboson}} + N_{lj}^{\mathrm{multijet}} + N_{lj}^{\mathrm{NCB}}. \end{aligned} \tag{7.15}$$

As outlined above and summarised in Tab. 7.4, different background sources are scaled differently, using different information. The diboson, multijet and NCB background are either data-driven (latter two) or do not employ transfer factors $\kappa^{\mathrm{bkg}}(=1)$ but rely on the MC prediction only. In total, two different factors are defined to normalise the MC background prediction by the observed data in the control regions. The backgrounds that are normalised by κ^{bkg}-factors according to Eq. 7.15 are also listed in Tab. 7.5. Together with the signal strength μ_{sig} they are free parameters of the fit. The transfer factor κ^{Top} normalises the $t\bar{t}$ and single top-quark backgrounds correlated over all $\not\!\!E_T$-bins. Likewise, the single transfer factor κ^{V} normalises all $W(\ell\nu)$+jets and $Z(\ell\ell)$+jets processes correlated over all $\not\!\!E_T$-bins. This factor also normalises the $Z(\nu\nu)$+jets prediction that does not significantly contribute to any defined control region. The choice of normalising all V+jets, including $Z(\nu\nu)$+jets, backgrounds via one single κ^{V} ensures

Parameter	Meaning	Constraint
μ_{sig}	signal strength	free in fit
κ^{V}	transfer factor for W+jets and Z+jets	free in fit
κ^{Top}	transfer factor for $t\bar{t}$ and single top	free in fit

Tab. 7.5: Free parameters of the fit model and associated backgrounds and signal.

a low statistical uncertainty on the transfer factor which is propagated into the signal region via the normalisation of the dominant $Z(\nu\nu)$+jets background. Differences between the processes are taken into account via the mentioned theoretical uncertainties in Sec. 7.6.1.

7.7.3 Inclusion of Uncertainties

The likelihood function of Eq. 7.13 is not complete yet: it does not include uncertainties on the measurements. These are commonly included via the addition of so-called *nuisance parameters*. A nuisance parameter α_p describes how ν_{lj} changes if a certain systematic source is varied. The nominal ν_{lj} is obtained for $\alpha_p = 0$. The variations corresponding to $\pm 1\sigma$ of that source on ν_{lj} correspond to $\alpha_p = \pm 1$ (see Fig. 7.6 for illustration). The standard deviations are determined in auxiliary measurements. Systematic sources with this impact are usually included via Gaussian constraints with mean of 0 and standard deviation of 1:

$$G(\alpha_p) = \mathrm{e}^{\alpha_p^2}. \tag{7.16}$$

In a maximum likelihood fit the nuisance parameter α_p is allowed to vary continuously between ± 1 and beyond. This is possible by interpolating between ± 1, where $\alpha_p = 0$ is fixed to ν_{lj}, using a higher-order polynomial function. Beyond ± 1 the behaviour of $\nu_{lj}(\alpha_p)$ is obtained by performing a linear extrapolation. Figure 7.6 illustrates the effect of α_p on ν_{lj} along with a sketched interpolation (black) curve. Furthermore, the green histograms show a potential effect on the shape of the fitted distribution if ν_{lj} varies differently for different bins j as a function of α_p.
Finally, the likelihood is multiplied by terms of Eq. 7.16 for each systematic source p. Statistical uncertainties stemming from finite MC statistics are included by Poissonian nuisance terms with parameter γ_s. The final likelihood takes the following form:

$$\mathcal{P}(\mu_{\text{sig}}, \boldsymbol{\kappa}, \boldsymbol{\alpha}) = \prod_{l}^{C} \prod_{j}^{M} \frac{\nu_{lj}(\boldsymbol{\kappa}, \boldsymbol{\alpha})^{n_{lj}}}{n_{lj}!} \mathrm{e}^{-\nu_{lj}} \prod_{p,s} f(\boldsymbol{\alpha}). \tag{7.17}$$

The nuisance parameters have been summarised as $\boldsymbol{\alpha}$. The terms $f(\boldsymbol{\alpha})$ are the Gaussian terms in Eq. 7.16 in case of systematic uncertainties and Poisson functions for γ_s. The transfer factors are consequently functions of $\boldsymbol{\alpha}$. The set of systematic uncertainties considered for this analysis will be discussed in Sec. 7.8 and is predefined, prior to performing the analysis. The uncertainties associated to γ_s are included only for samples whose MC statistical uncertainty is above a certain threshold. In this analysis, this threshold is set to 5%.

7.7.4 Different Fit Configurations

The maximisation of the likelihood in Eq. 7.17 is performed to obtain the background transfer factors, determine the nuisance parameters and to finally predict the background contribution

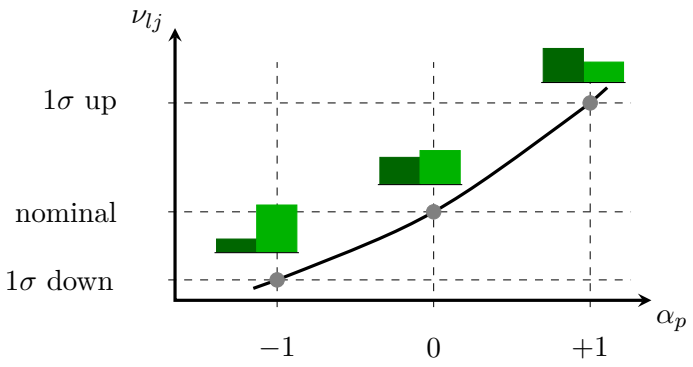

Fig. 7.6: Illustration of the impact of a nuisance parameter α_p on the event yield ν_{lj}. An interpolation is sketched as well as a histogram (green) showing the potential effect on the shape (in different bins j). Adapted from Ref. [156].

in the signal regions along with its uncertainty. The fit performed is referred to as *global fit*, simultaneously using information from all control regions and signal regions. However, the fit can be configured in different ways:

Background-only fit: The background-only fit is performed in order to obtain the background prediction in the signal regions assuming the absence of any BSM signal. Therefore, this configuration takes into account only the control region information. The obtained transfer factors are then applied to the signal region pre-fit prediction of the backgrounds. Thereby the control region fit is extrapolated to the signal region and one can obtain the background yields and their uncertainties.

Model-independent signal fit: In this setup the control regions and signal regions are fitted simultaneously. A 'dummy' signal contribution is assumed in the signal region only, no contribution in the control regions. This signal is model-independent and therefore no assumptions on the $\not{E}_T$-shape or uncertainty can be made. Therefore, the fit setup changes to an inclusive setup: the $\not{E}_T$-shape analysis is transformed to a cut-and-count analysis. The events are counted in inclusive $\not{E}_T$-regions, whose lower cuts are defined in Tab. 7.3. The model-independent signal fit is performed in these inclusive regions to obtain upper limits on the cross section of any BSM signal. This is useful to test the analysis outcome against a multitude of signal hypotheses that cannot be all investigated here.

Model-dependent signal fit: Like the model-independent setup, here, control regions and signal regions are simultaneously fitted. The power of the fit is based on the different $\not{E}_T$-shapes in the background model and signal models. The specific signal models tested here provide a $\not{E}_T$-shape prediction and a corresponding uncertainty. Signals may also contribute to the control regions, which is taken into account here as well. Finally, this configuration aims at excluding[d] specific model-dependent signal hypotheses.

The results of the background prediction will be obtained from the background-only fit. The quoted uncertainties in the signal region will be the errors extrapolated from the control region pdfs to the signal region pdfs. They depend on the fit outcome of the free parameters $(\mu_{\text{sig}}, \kappa_j^{\text{bkg}})$

[d] If an excess in data is found, p-values are computed for the signal models, to access a potential discovery.

and the nuisance parameters α_p. They are summarised as variables η_i and the uncertainty on them and their correlation is taken into account in the error propagation:

$$\sigma^2_{\mathrm{BKG}} = \sum_i \left(\frac{\partial \mathrm{BKG}}{\partial \eta_i}\right)^2 \sigma^2_{\eta_i} + \sum_i \sum_{h \neq i} \varrho_{ih} \left(\frac{\partial \mathrm{BKG}}{\partial \eta_i}\right) \left(\frac{\partial \mathrm{BKG}}{\partial \eta_h}\right) \sigma_{\eta_i} \sigma_{\eta_h}. \tag{7.18}$$

The correlation coefficient between η_i and η_h is called ϱ_{ih}, the standard deviation of η_i is σ_{η_i}. The total background uncertainty is σ_{BKG}.

7.7.5 Hypothesis Testing

In order to quantify the agreement of the data with a background-only prediction or a prediction that includes a signal as well, hypothesis test are performed: in the case of an exclusion of signals the so-called null-hypothesis H_0 is defined as the model including background+signal with the purpose of falsifying this hypothesis. In case of discovery, the null-hypothesis includes only the background known from the SM. Again, the purpose is to falsify this hypothesis. The alternative hypothesis is called H_1, in case of exclusion it contains the background-only model, in case of discovery it includes background+signal models. The background-only hypothesis will always assume $\mu_{\mathrm{sig}} = 0$, while the background+signal hypothesis assumes $\mu_{\mathrm{sig}} > 0$. The *profile likelihood ratio* is employed for hypothesis testing:

$$\lambda(\mu_{\mathrm{sig}}) = \frac{\mathcal{P}\left(\mu_{\mathrm{sig}}, \hat{\hat{\boldsymbol{\theta}}}\right)}{\mathcal{P}\left(\hat{\mu}_{\mathrm{sig}}, \hat{\boldsymbol{\theta}}\right)}, \tag{7.19}$$

where $\hat{\boldsymbol{\theta}}$ and $\hat{\mu}_{\mathrm{sig}}$ maximise the likelihood in Eq. 7.17, whereas $\hat{\hat{\boldsymbol{\theta}}}$ maximises the likelihood for a fixed μ_{sig} as included by a certain background+signal hypothesis. That means, for each μ_{sig} all other parameters have to be refitted to maximise the likelihood and the likelihood is profiled. This is exactly what is done when incorporating nuisance parameters that are not a parameter of interest but profiled to obtain the total uncertainties. The profile likelihood ratio in Eq. 7.19 will be close to one in case the data is background+signal-like, it will be a small number if the data is more background-only-like since then the likelihood corresponding to a non-zero μ_{sig} will be small. The *test statistic* is constructed to quantify the terms 'background+signal-like' and 'background-only-like':

$$q_\mu = -2 \ln \lambda(\mu_{\mathrm{sig}}). \tag{7.20}$$

For large data samples this test statistic follows a χ^2 distribution. For sensitive analyses the distribution of the test statistic q_μ is well separated for H_0 and H_1. With the help of q_μ one can calculate how probable a certain measurement is for H_0 or H_1 to be true. This probability is called p-value and is determined as

$$\begin{aligned} p_b &= \int_{-\infty}^{q_{\mu,\mathrm{obs}}} f(q_\mu, \mu') \mathrm{d}q_\mu \qquad \text{for} \qquad \mu' = 0, \\ p_{s+b} &= \int_{q_{\mu,\mathrm{obs}}}^{\infty} f(q_\mu, \mu') \mathrm{d}q_\mu \qquad \text{for} \qquad \mu' > 0. \end{aligned} \tag{7.21}$$

The data observation is $q_{\mu,\mathrm{obs}}$. The distribution of q_μ with different assumptions μ' is given by $f(q_\mu, \mu')$. The pdf of q_μ can be either obtained by MC sampling or by asymptotic functions

invoking the mentioned χ^2 distributions. The integral limits in Eq. 7.21 hold, if $f(q_\mu, \mu' = 0)$ is shifted to higher values w. r. t. $f(q_\mu, \mu' > 0)$, which is the case for the defined test statistic in Eq. 7.20. The probability p_b (background-only) is then the probability to find a q_μ as small as $q_{\mu,\text{obs}}$ or smaller. The probability p_{s+b} is the probability to find a q_μ as large as $q_{\mu,\text{obs}}$ or larger. Fig. 7.7 illustrates the subject by drawing the two pdfs corresponding to the two hypotheses. The

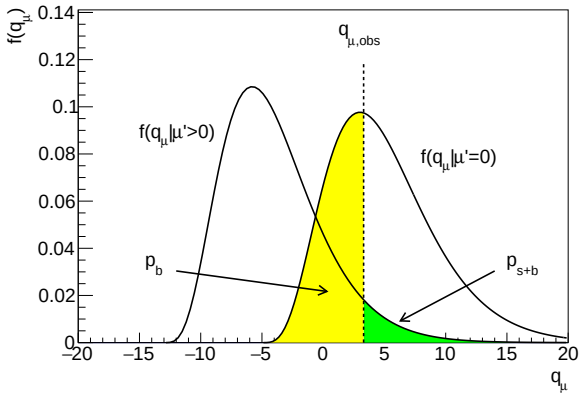

Fig. 7.7: Distribution of q_μ for the background-only and background+signal hypotheses. An observed $q_{\mu,\text{obs}}$ is drawn as a vertical line. The corresponding p-values p_b and p_{s+b} are indicated as coloured areas below the corresponding pdfs.

coloured areas indicate the p-values. In this example, the measured $q_{\mu,\text{obs}}$ corresponds rather to a background scenario with $p_{s+b} \ll p_b$. The decision on when to accept H_0 and when to reject H_0 is fixed before. In most ATLAS analysis exclusion statements are made at '95% confidence level (CL)'. This implies that if $p_{s+b} < 0.05$ the background+signal hypothesis is rejected. In fact, another quantity is defined to make that statement:

$$\text{CL}_s = \frac{p_{s+b}}{1 - p_b}. \tag{7.22}$$

Requiring that $\text{CL}_s < 0.05$ to make an exclusion statement is called CL_s-method [157]. In the case of a downward fluctuation in the data, likely to happen in low statistics regions, the exclusion power is artificially improved, although the analysis is not sensitive enough prior to the measurement. Therefore, p_{s+b} is normalised by $1 - p_b$(the background-only probability). Thus, the CL_s-method also takes the p-value of the background-only model into account. The CL_s-method is used in the monojet analysis to set 95% CL limits on BSM signal hypotheses and model-independent upper cross section limits for inclusive $\not{E}_T$-regions.

7.8 Systematics Uncertainties

This section is devoted to the systematic uncertainties that are taken into account in the monojet analysis. As seen in Eq. 7.17, systematic uncertainties are included in the fit-model via Gaussian distributed nuisance parameters with an initial value for the mean of 0 and the standard deviation of 1. In the global fit, the nuisance parameters can be adjusted in order to maximise the likelihood. If the fitted mean value deviates significantly from 0 and the standard deviation is reduced below 1σ it means that the model is sensitive to shape/normalisation variations induced by the nuisance parameters and the fit to data is able to constrain the uncertainty stemming from this particular nuisance parameter. First, experimental uncertainties are intro-

duced followed by theoretical uncertainties of the MC modelling and higher order theoretical corrections. If not stated otherwise, the uncertainties are correlated across all $\not{E}_T$-bins and all regions and background processes. All nuisance parameters corresponding to considered sources of systematic uncertainties are listed in Tab. 7.6.

7.8.1 Experimental Uncertainties

In the following, the experimental uncertainties are listed and briefly described along with their pre-fit uncertainty on the total background prediction in the signal region.

Jet Energy Scale
The jet energy scale (JES) is a-priori one of the dominant uncertainties in the monojet analysis. It originates from uncertainties related to the jet calibration procedure as outlined in Sec. 6.6.2. The uncertainties are p_T and η-dependent. It is fairly flat in η, while it amounts to $\sim 6\%$ for low p_T jets (20 GeV), $\sim 1\%$ for 200 GeV jets and about 2% for high energetic jets (2 TeV) [125]. The JES uncertainty is in total derived from 80 different nuisance parameters. Most of them (67) are related to uncertainties on the in-situ calibration. Other uncertainties stem from η-intercalibration, pileup-suppression (the JVT cut is varied to assess the uncertainty), punch-through corrections, uncertainties related to the flavour composition and response (MC studies to model response of calorimeter) and single particle response studies to asses the uncertainty for high-p_T jets. Since analyses usually cannot include 80 individual nuisance parameters into their analysis, the set of parameters is strongly reduced via eigenvalue decomposition techniques (see Ref. [158]). This facilitates the analysis, albeit information on correlations among the different systematic sources is lost. However, most analyses are not sensitive to these correlations. To assess the sensitivity, four different sets of nuisance parameters, with 3 parameters each, are provided. Studies performed with the monojet analysis have shown no significant difference between these sets. Therefore, 3 nuisance parameters are associated to the JES and used in the analysis. The impact of one of these is shown as an example for the $W(\mu\nu)$+jets background (CR1m) and the $Z(\nu\nu)$+jets background (SR) $\not{E}_T$-distributions in Fig. 7.8. The variation is very small for the lowest $\not{E}_T$-bin and for higher $\not{E}_T$-bins clearly above the statistical uncertainty of the MC prediction. Its pre-fit impact on the total background uncertainty in the signal region amounts to $\sim 3\%$.

Jet Energy Resolution
One nuisance parameter is associated to the jet energy resolution (JER). This systematic is one-sided and obtained by smearing the jets with the uncertainty corresponding to the JER. In the fit, this uncertainty is symmetrised. Its pre-fit impact amounts to 0.4% in the signal region. Figure 7.9(a) presents the impact of the JER for the $W(e\nu)$+jets sample in the CR1e, which shows shape effects. However, the uncertainty is similar to the statistical uncertainty.

$\not{E}_T$ Soft Track Uncertainties
All variations associated to objects like electrons, photons, muons and jets are propagated to the $\not{E}_T$-calculation. The remaining uncertainty of the $\not{E}_T$-scale and resolution is governed by the knowledge of the soft energy term that is not related to any physics object. In the analysis, the soft track term as measured in the ID is used. One nuisance parameter for the scale variation and two parameters for the resolution perpendicular and parallel to the hadronic recoil system (or $\not{E}_T$ itself) are taken into account. The pre-fit uncertainty in the signal region is about 0.3%.

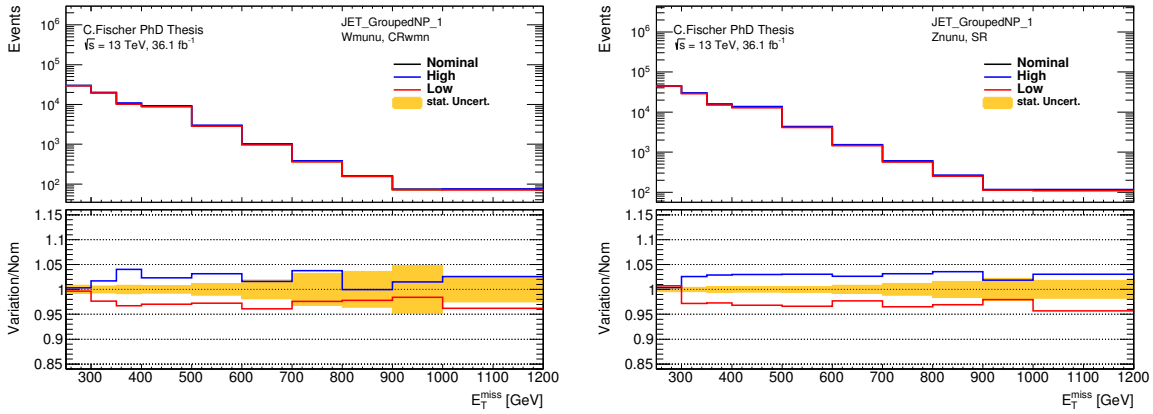

(a) $W(\mu\nu)$+jets, CR1m (b) $Z(\nu\nu)$+jets, SR

Fig. 7.8: Impact of one JES nuisance parameter on the $\not{E}_T$-distribution in (a) CR1m ($W(\mu\nu)$+jets sample) and (b) signal region ($Z(\nu\nu)$+jets sample). The bins in $\not{E}_T$ correspond to the exclusive regions defined in Tab. 7.3.

b-tagging

The CRtop and CR1m are defined with requirements on the number of b-jets. Therefore, for these regions only, uncertainties on the b-tag efficiency have to be taken into account. Four nuisance parameters are added: the uncertainty on the b-tag efficiency, the c-tag, the mistag rate of light flavour jets and an extrapolation uncertainty to high p_T jets. The total pre-fit impact on the CRtop yields is 6.4%, for the CR1m it amounts to 0.8%. The impact of the b-tag efficiency component can bee seen in Fig. 7.9(b) for the top-quark background in the CRtop, being more dominant for low $\not{E}_T$-values.

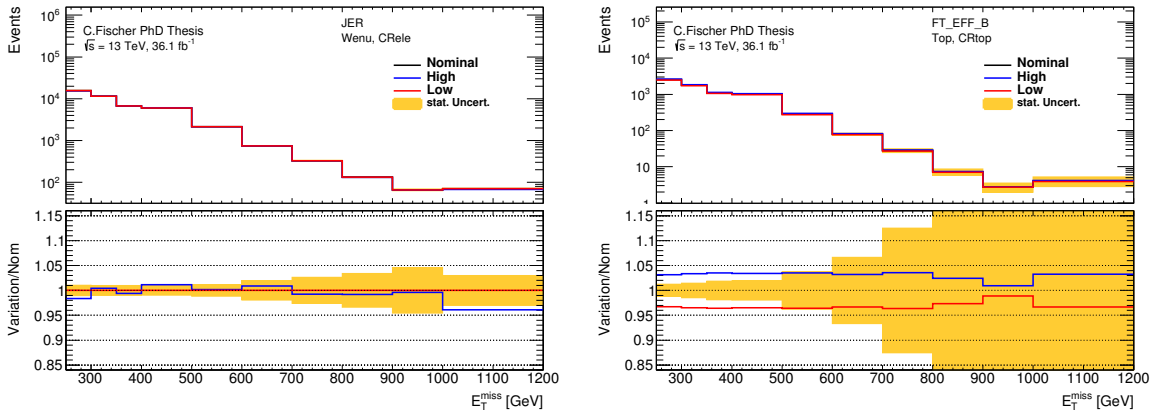

(a) $W(e\nu)$+jets, CR1e (b) $t\bar{t}$+single top, CRtop

Fig. 7.9: (a): Impact of JER uncertainty on the $\not{E}_T$-distribution in SR ($W(\tau\nu)$+jets sample): this uncertainty is one-sided (high variation), the low variation coincides with the nominal prediction. (b): Impact of uncertainty on b-tagging efficiency in CRtop ($t\bar{t}$+single top sample). The bins in $\not{E}_T$ correspond to the exclusive regions defined in Tab. 7.3.

Electron(Photon) Related Uncertainties
There is a nuisance parameter for the electron/photon energy scale and one for the energy resolution. Uncertainties on the identification, reconstruction, trigger and isolation efficiency of electrons are included in the fit model via three additional nuisance parameters. The $W(e\nu)$+jets prediction is changed by about 1% flat in $\not{E}_T$ in CR1e according to Fig. 7.10(a) via the identification efficiency uncertainty alone. The respective uncertainties on the scale facors are propagated to the SR by the use of inefficiency scale factors when applying electron vetoes. The total impact of electron related uncertainties amounts to $\sim 0.6\%$ in the signal region.

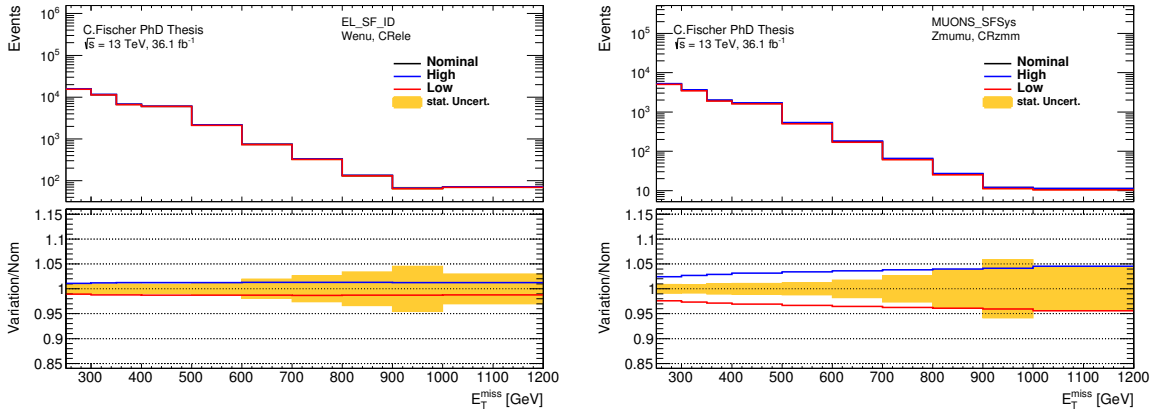

(a) $W(e\nu)$+jets, SR

(b) $Z(\mu\mu)$+jets, CR2m

Fig. 7.10: Impact of uncertainty on lepton SFs on $\not{E}_T$-distribution: (a) Variation of reconstruction efficiency for $W(e\nu)$+jets in the SR. (b) Variation of systematic component of the muon SF for $Z(\mu\mu)$+jets in CR2m. The bins in $\not{E}_T$ correspond to the exclusive regions defined in Tab. 7.3.

Muon Related Uncertainties
The muon track is measured in both inner detector and muon spectrometer. There are two nuisance parameters assigned to the muon energy resolution as measured in the ID and the MS. Furthermore, there is one nuisance parameter for the muon energy scale and four nuisance parameters related to the statistical and systematic components of the identification efficiency and low-p_T efficiency scale factors. The variation of the systematic component of the muon SF on the $\not{E}_T$-distribution of $Z(\mu\mu)$+jets in CR2m leads to a yield variation of about 2% for low $\not{E}_T$ and 5% for high $\not{E}_T$ (Fig. 7.10(b)). As for the electron scale factors, inefficiency scale factors are applied in case of a muon veto. For the signal region, the induced variation from muon related uncertainties is as high as 1.2%.

Pileup Reweighting
The analysis applies a pileup reweighting to the MC distributions in order to correct $\langle\mu\rangle$ to match the data. For each MC sample a profile is obtained by dividing the number of events of a certain $\langle\mu\rangle$ in data by the generated events in MC with an a-priori $\langle\mu\rangle$. This profile is used to correct the MC. The uncertainty on this correction is included in a single nuisance parameter and its pre-fit impact in the SR amounts to 0.3%.

Luminosity
The uncertainty on the luminosity measurement for the total 2015+2016 dataset amounts to 3.2% and is included as an individual nuisance parameter in the fit for all MC driven back-

grounds. The uncertainty is derived following a methodology similar to the one explained in Ref. [120], from a preliminary calibration of the luminosity scale using x-y beam-separation scans performed in August 2015 and May 2016.

Data-driven Backgrounds
A conservative estimate of 100% uncertainty on the multijet and non-collision backgrounds is applied. Two nuisance parameters are added, respectively. The pre-fit impact on the signal region yield for both background variations is 0.4%.

7.8.2 Modelling/Theoretical Uncertainties

Modelling uncertainties depend on the used MC generators and differ for specific background processes (signal uncertainties will be discussed in Chap. 9). The components taken into account are listed in the following.

Diboson Modelling
The nominal generator simulating diboson events is Sherpa. The uncertainty on the NLO cross section is assumed to be 6%. The uncertainty on the renormalisation/factorisation and resummation scale choice is evaluated by varying the corresponding scales by factors of 2 and 1/2 independently (this is called *7-point variation* in terms of μ_F and μ_R). Different samples with a varying CKKW-L matching scale are used to obtain the corresponding uncertainty from this scale choice. The nominal CKKW scale is 20 GeV, the variations are 15 GeV and 30 GeV. Uncertainties due the parton shower model are evaluated by comparing the prediction from Sherpa with the PowhegBox generator prediction. The full difference of these predictions is considered as systematic uncertainty. The variations from these uncertainty sources are normalised to the nominal event yield in order to avoid double counting of normalisation uncertainties. The different sources of uncertainties are added up in quadrature and a single nuisance parameter for the diboson modelling uncertainty is added. The pre-fit impact in the signal region is 0.2%. The impact on the $\not{E}_T$-shape of the diboson sample in the CR1e of high and low variations can be seen in Fig. 7.11(a) and reaches from 6% for low $\not{E}_T$ to $\sim$ 23% for high $\not{E}_T$.

Top-Quark Production Modelling
Dedicated samples with varying settings for the $t\bar{t}$ and single top production are generated. The uncertainty considering the hard scattering process is evaluated by comparing the nominal prediction to the one inferred from aMC@NLO+Herwig++. Different scale settings controlling initial and final state radiation are varied: the resummation damping factor[e] is set to $2 \times m_t$ and m_t . The two generated samples are then compared with the nominal sample. Half the difference is considered as the corresponding uncertainty. PDF related uncertainties are evaluated by reweighting the events with a weight corresponding to different PDF sets and PDF error sets (NNPDF, CT14, PDF4LHC, MMHT). These weights are included and calculated during the event generation. Uncertainties related to the fragmentation and hadronisation modelling are obtained by comparing the nominal generator with the prediction from Powheg +Herwig++. All variations are added up in quadrature and the resulting systematic uncertainty is included in one nuisance parameter. The pre-fit impact on the top-quark background from the modelling uncertainty varies from 25% in the lowest $\not{E}_T$-bins to 72% in the highest $\not{E}_T$ bins in all regions. This is illustrated in the CRtop in Fig. 7.11(b). The pre-fit impact of this uncertainty on the signal region yield amounts to 1.3%.

[e] See Ref. [159] for reference on damping scale factors settings.

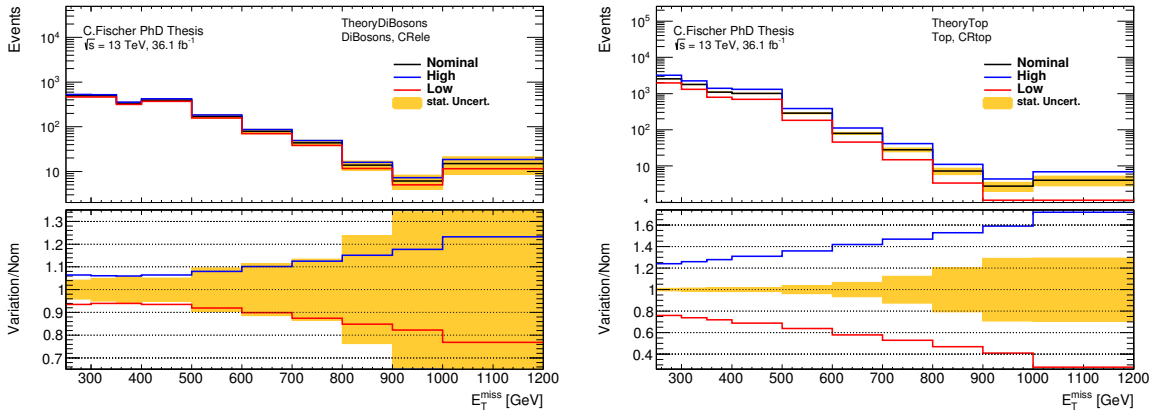

(a) Diboson, CR1m

(b) Top-quark, CRtop

Fig. 7.11: Impact of diboson modelling uncertainty on $\not{E}_T$-distribution (CR1e, diboson sample) and top-quark modelling uncertainty on $\not{E}_T$-distribution (CRtop, $t\bar{t}$+single top sample). The bins in $\not{E}_T$ correspond to the exclusive regions defined in Tab. 7.3.

V+jets Modelling

The reweighting of the MC to NLO QCD and NNLO EW corrections as introduced in Sec. 7.6.1 leads to additional systematic uncertainties: There are seven additional nuisance parameters included: three for QCD higher-order corrections, three for EW higher-order corrections and one for mixed EW-QCD higher-order corrections. The QCD uncertainties are: one uncertainty due to scale variations is obtained by 7-point scale variations of μ_F and μ_R (as convention for background modelling uncertainties, at NLO the factors are 1/4 and 4). Half the difference of $K_{\text{NLO}}^{\text{max}} - K_{\text{NLO}}^{\text{min}}$ is used as an uncertainty. The second component accounts for shape variations of $p_T(V)$ by varying the scales differently in different $p_T(V)$ regions. The key feature of the higher order corrections, as implemented in the analysis, is to understand correlations among different processes when fitting the $Z(\nu\nu)$+jets background. Therefore, uncertainties on the correlation between different processes make up the third component. All QCD uncertainties are correlated across all $p_T(V)$ bins and processes. The three nuisance parameters are independent.
Also three uncertainties are associated with EW corrections: one uncertainty accounts for unknown higher order Sudakov logarithms ($\mathcal{O}(\alpha^3)$) at high p_T. The estimated effect on the correction is $\pm 5\%$ for the multi-TeV range. The second uncertainty is defined as 5% of the full EW correction $K_{\text{EW}}(x)$. It is a conservative estimate to cover effects of photon Bremsstrahlung and for NNLO effects on the hard process. The third uncertainty is introduced as a difference between rigorous NLL Sudakov approximation and naive exponentiation of the NLO EW correction. The three uncertainties are incorporated as three nuisance parameters that are correlated across all $p_T(V)$. The first component is correlated for all processes while the correlation for the latter two is unknown and therefore uncorrelated across W+jets and Z+jets processes.
An uncertainty is applied to account for non-factorised mixed EW-QCD effects and is 10% of the difference between the multiplicative correction (Eq. 7.6) and the additive correction ($K_{\text{th}} = K_{\text{NLO}}(x,\vec{\mu})+K_{\text{EW}}(x)K_{\text{LO}}(x,\vec{\mu})/K_{\text{LO}}(x,\vec{\mu}_0)$). The uncertainty is correlated across $p_T(V)$ and all processes.
The impact on the reweighted $p_T(V)$ distribution can be seen in the lower panels of the plots in Fig. 7.5: they show the relative uncertainty on the higher order corrections. Most of the nuisance parameters have a similar impact among the different processes. This reflects on the fact that

W/Z+jets processes are rather similar at high boson-p_T. The biggest impacts stem from the three nuisance parameters assigned to the QCD correction. The first two nuisance parameters (see alpha_vjets_d1K_NLO and alpha_vjets_d2K_NLO in Tab. 7.6) influence the total signal region yield by 7.3% and 4.5%, while the third component (alpha_vjets_d3K_NLO) only has an impact of 0.5%. The numbers refer to pre-fit uncertainties. All other theory nuisance parameters have much lower impacts in the signal region.
In addition to these seven nuisance parameters provided by theorists one also has to apply an uncertainty based on the *smoothing* performed for the NLO QCD corrections: the QCD corrections are a correction NLO(MC)→NLO(theory). The correction is close to unity, slightly below. There are fluctuations observed in the correction factor that stem from limited MC statistics in the high $p_T(V)$-regions. A fit-function to this correction factor dependent on $p_T(V)$ was obtained in order to smooth these fluctuations out. An uncertainty is applied corresponding to the quadratic sum of the fit-parameter uncertainties. In the region beyond $p_T(V) \sim 1$ TeV, the uncertainty grows out to 10% due to a lack of knowledge of the exact correction behaviour from limited MC statistics. This is taken into account as an individual nuisance parameter. Its pre-fit impact amounts to 0.4% for the whole signal region.
The PDF uncertainties are not provided within the theory uncertainties. They are evaluated similar to other processes: Differences between the nominal set NNPDF3.0nlo and the sets MMHT2014nnlo68cl and CT14nnlo with two variations of α_s in addition are combined into a single uncertainty adding one additional nuisance parameter. The pre-fit impact in the SR is 1.7%.
The uncertainties related to parton shower modelling are added as the relative uncertainty on the transfer factors (extrapolation from control regions to signal regions) of the backgrounds from comparing different matching scales in CKKW (nominal 20 GeV, variations 15 GeV and 30 GeV). This means that the associated uncertainty is not constrained in a background-only fit, because the technical evaluation of this uncertainty is not suited for profiling[f]. The pre-fit impact amounts to 0.83% in the inclusive SR.

[f] Different versions of Sherpa were used for the estimation, which is not supporting continuous interpolations between variations, as needed for profiling

Name of Systematic	Description
	Experimental Uncertainties
alpha_JET_GroupedNP_1	Uncertainty on the jet energy scale
alpha_JET_GroupedNP_2	Uncertainty on the jet energy scale
alpha_JET_GroupedNP_3	Uncertainty on the jet energy scale
alpha_JER	Uncertainty on the jet energy resolution
alpha_EtaIntercalibration	Uncertainty on the jet η intercalibration
alpha_MET_SoftTrk_ResoPara	Uncertainty on the $\not{E}_T$-resolution (parallel to hadronic recoil system)
alpha_MET_SoftTrk_ResoPerp	Uncertainty on the $\not{E}_T$-resolution (perpendicular to hadronic recoil system)
alpha_MET_SoftTrk_Scale	Uncertainty on soft track energy scale
alpha_EG_RESOLUTION_ALL	Uncertainty on e/γ energy resolution
alpha_EG_SCALE_ALL	Uncertainty on e/γ energy scale
alpha_EL_SF_Reco	Uncertainty on reconstruction efficiency of electrons
alpha_EL_SF_Iso	Uncertainty on isolation efficiency of electrons
alpha_EL_SF_ID	Uncertainty on identification efficiency of electrons
alpha_EL_SF_Trig	Uncertainty on electron trigger efficiency scale factor
alpha_MUONS_ID	Uncertainty on muon momentum resolution inner detector
alpha_MUONS_MS	Uncertainty on muon momentum resolution muon spectrometer
alpha_MUONS_SCALE	Uncertainty on muon momentum scale
alpha_MUONS_SFstat	Uncertainty on muon identification efficiency (statistical component)
alpha_MUONS_SFsys	Uncertainty on muon identification efficiency (systematic component)
alpha_MUONS_SFstatLowPt	Uncertainty on muon identification efficiency (statistical component low p_T)
alpha_MUONS_SFsysLowPt	Uncertainty on muon identification efficiency (systematic component low p_T)
alpha_FT_EFF_B	Uncertainty on b-tagging efficiency
alpha_FT_EFF_C	Uncertainty on c-tagging efficiency
alpha_FT_EFF_L	Uncertainty on light flavour mistag-rate efficiency
alpha_FT_EFF_Extr	Uncertainty on b-tagging efficiency (extrapolation to high p_T)
alpha_PRW_SF	Uncertainty on pileup reweighting/data scale factor
alpha_Luminosity	Uncertainty on integrated luminosity
alpha_qcd	Uncertainty on multijet background
alpha_ncb	Uncertainty on non-collision background
	Theoretical Uncertainties
alpha_theory_dib	Modelling uncertainty of diboson background
alpha_theory_top	Modelling uncertainty of top-quark background
alpha_vjets_d1K_NLO	Theory uncertainty on NLO QCD correction (scale uncertainty)
alpha_vjets_d2K_NLO	Theory uncertainty on NLO QCD correction (shape uncertainty)
alpha_vjets_d3K_NLO	Theory uncertainty on NLO QCD correction (process uncertainty)
alpha_vjets_d1kappa_EW	Theory uncertainty on NNLO EW correction (unknown Sudakov)
alpha_vjets_d2kappa_EW_lnu	Theory uncertainty on NNLO EW correction on W+jets (higher order)
alpha_vjets_d2kappa_EW_zll	Theory uncertainty on NNLO EW correction on Z+jets (higher order)
alpha_vjets_d3kappa_EW_lnu	Theory uncertainty on NNLO EW correction on W+jets (Sudakov approx)
alpha_vjets_d3kappa_EW_zll	Theory uncertainty on NNLO EW correction on Z+jets (Sudakov approx)
alpha_vjets_dK_NLO_mix	Theory uncertainty on combination of EW and QCD corrections
alpha_QCDSmoothing	Uncertainty on smoothing of NLO QCD correction
alpha_PDF	PDF uncertainty for V+jets processes
alpha_Vjets_ckkw	shower modelling uncertainty for V+jets processes

Tab. 7.6: List of nuisance parameters included in the fit and the corresponding source of systematic uncertainty.

7.9 Pre-Fit Distributions

In the following, pre-fit distributions for different kinematic variables of all employed control regions are shown. They compare the MC prediction after the higher order theory reweighting with the data. Uncertainties on the background prediction are shown as hashed areas. They include the statistical uncertainty and the systematic uncertainties introduced in Sec. 7.8.

For the regions CR1e, CR1m and CR2m, dominated by V+jets processes, we can observe a normalisation discrepancy of ∼20-25%, where the MC predictions undershoot the data. This originates from the higher-order theory corrections. They reduce the background prediction by $p_T(V)$-dependent factors between 0.9 and 0.7 (see Fig. 7.5). On the other hand, the shapes of the measured distributions are well described. The normalisation will be obtained by the fit to the data. The origin of this normalisation offset might be explained with the non-inclusive monojet selection of boson+jets events: at least one jet and at most four jets per event are required, which can be considered as a small part of the phase space. The theory higher-order corrections were derived in inclusive boson+jets processes with no restriction on the jet multiplicity. We can also observe that the offset is mostly stemming from events with one or two jets (see Fig. 7.13(d), Fig. 7.16(d) and Fig. 7.19(d)). These events are dominating the monojet phase space. A consistent data description among the V+jets control regions can be observed. The top-quark processes dominate the CRtop, where a good agreement between data and MC prediction can be observed. The applied uncertainties are able to cover most of the differences between data and MC. There is a small deficit of predicted events with low H_T, one jet and high minimum $\Delta\phi(\not{E}_T,\text{jets})$, namely events with one b-tagged jet back-to-back with the $\not{E}_T$. This region of 1-jet events is dominated by $W(\mu\nu)$+jets processes rather than top-quark processes. This deficit is thus likely related to the normalisation offset observed among V+jets processes. Another observation is an asymmetry in the description of the lepton η distribution in CR1e, CR1m and CR2m. This is a mismodelling at the truth level in Sherpa and is not observed in other generators like MadGraph. This mismodelling seems to only affect low jet-multiplicity bins and thus is pronounced in the phase space of the monojet selection. The overall normalisation however is unaffected by this asymmetry. Studies of the relevant distributions for $\eta(\ell) > 0$ and $\eta(\ell) < 0$ have shown no other deviations. Therefore, the asymmetry is not considered to be a serious problem which needs correction.
Table 7.7 shows the total pre-fit background prediction for exclusive signal regions as defined in Tab. 7.3. The observed event yields in data are shown as well. The pre-fit uncertainties on the total background event yield grow from ∼ 9.6% for EM1 to 17.4% for IM10. The latter region exhibits 245 data events for $\not{E}_T > 1$ TeV underlining the sensible choice of the $\not{E}_T$-binning preserving an acceptable statistical accuracy at high $\not{E}_T$.
The individual contributions of the different background processes in the inclusive region IM1 are shown in Tab. 7.8 for the signal region as well as the control regions before the fit. As anticipated, the dominant backgrounds in the signal region are $Z \to \nu\nu$+jets production, making up ∼ 50% of the total background prediction, followed by $W \to \tau\nu$+jets and $W \to \mu\nu$+jets production, which contribute ∼ 20% and 9%, respectively. The top-quark and diboson production contribute 4.3% and ∼ 2.5%, respectively. The multijet and non-collision background contribute only at the level of 0.5%. The $Z \to \ell\ell$+jets processes have virtually no contribution to the background.
The control regions are dominated by the processes they were designed to be enriched in. The purities for CR1e, CR1m, CR2m and CRtop amount to ∼77%($W(e\nu)$+jets) , ∼84%($W(\mu\nu)$+jets), ∼93%($Z(\mu\mu)$+jets) and ∼75% (top), respectively. The control regions were also designed such

that there is no contribution from multijet and non-collision background, hence the respective fields in Tab. 7.8 are not filled.
The signal contamination in the control regions is negligible, lying well below 1%, and at most contributing 0.2% to any region.

Signal region	EM1	EM2	EM3	EM4	EM5
Observed	111203	67475	35285	27843	8583
SM expected	86300 ± 8300	52400 ± 5300	26000 ± 2600	21500 ± 2200	6550 ± 660
Data/SM	1.29	1.29	1.35	1.29	1.31
Signal region	EM6	EM7	EM8	EM9	IM10
Observed	2975	1142	512	223	245
SM expected	2190 ± 220	847 ± 93	352 ± 38	161 ± 19	161 ± 28
Data/SM	1.36	1.35	1.46	1.38	1.52

Tab. 7.7: Data event yields in the exclusive signal regions compared to the total expected pre-fit yield of all considered background contributions. The uncertainty on the background prediction includes all systematic and statistical uncertainties pre-fit. The ratio Data/MC denotes the ratio of observed events over predicted events pre-fit.

Region	SR	CR1e	CR1m	CR2m	CRtop
Observed	255486	68973	110938	17372	9729
Exp. Background	196000 ± 19000	56600 ± 5600	87400 ± 8700	14100 ± 1400	9200 ± 2000
$Z/\gamma^* \to \nu\nu$+jets	109000 ± 11000	1.5 ± 0.3	30 ± 5	0 ± 0	5 ± 1
$W \to \tau\nu$+jets	39400 ± 4200	3260 ± 350	4600 ± 480	2.2 ± 0.5	148 ± 37
$W \to \mu\nu$+jets	16500 ± 1800	4 ± 3	73600 ± 7900	24 ± 3	1960 ± 580
$W \to e\nu$+jets	15900 ± 1700	43300 ± 4600	5 ± 2	0 ± 0	$0.15^{+0.18}_{-0.15}$
$Z/\gamma^* \to \tau\tau$+jets	646 ± 65	175 ± 20	226 ± 29	13 ± 3	10 ± 2
$Z/\gamma^* \to \mu\mu$+jets	463 ± 50	0.5 ± 0.2	1420 ± 170	13100 ± 1400	53 ± 11
$Z/\gamma^* \to ee$+jets	0.09 ± 0.04	6 ± 4	0 ± 0	0 ± 0	0 ± 0
$t\bar{t}$+single top	8100 ± 2200	7800 ± 2200	4300 ± 1200	460 ± 120	6900 ± 1900
Dibosons	5220 ± 420	2050 ± 170	3180 ± 230	541 ± 40	128 ± 44
multijet	700 ± 700	-	-	-	-
non-collision	360 ± 360	-	-	-	-

Tab. 7.8: Event yields for data and background prediction pre-fit for the inclusive region IM1. The background uncertainty includes all systematic sources and statistical uncertainties.

7.9.1 Distributions in CR1e

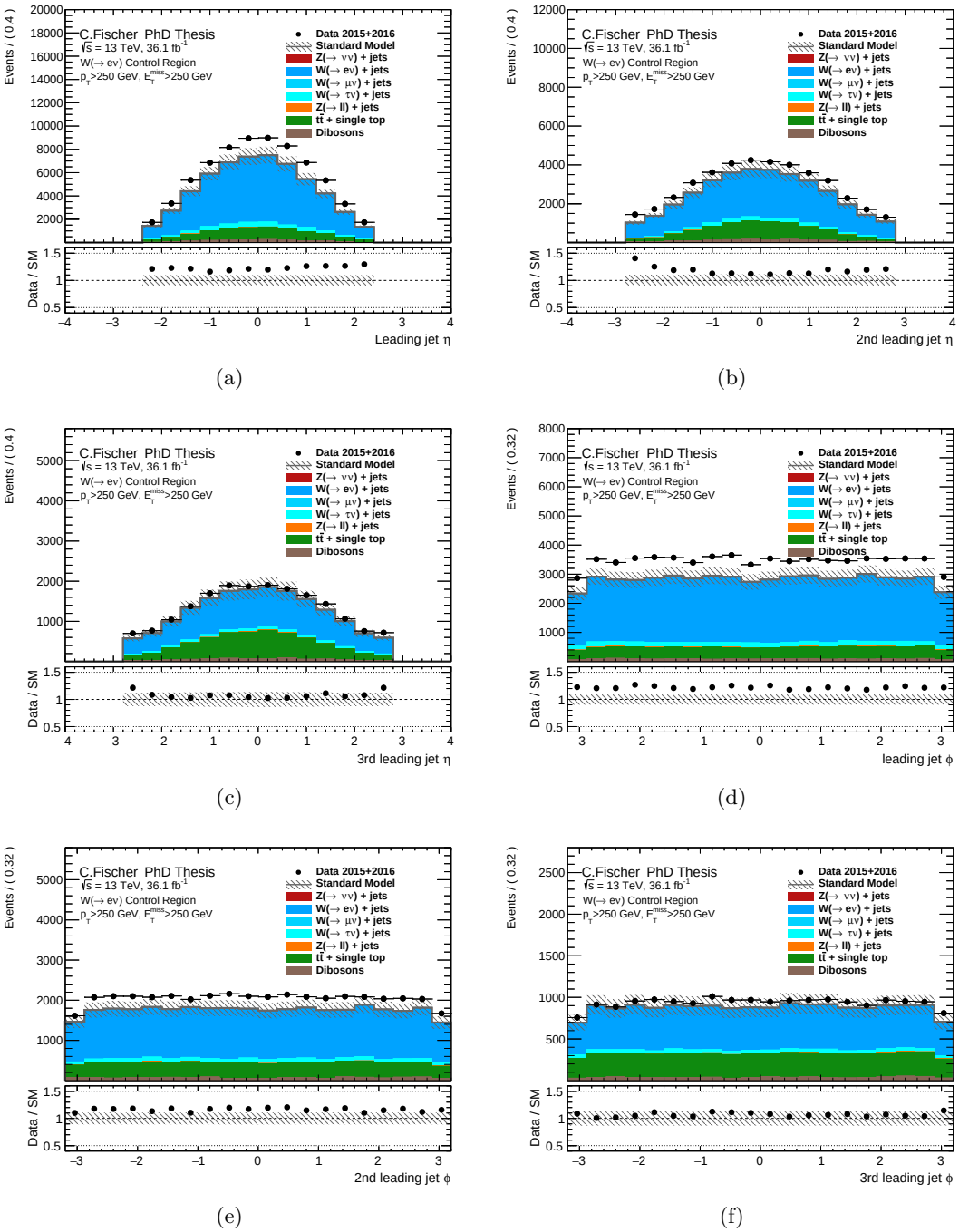

Fig. 7.12: Pre-fit distributions in CR1e for IM1. The data is shown as black dots, the total background prediction as the grey histogram. The hashed uncertainty band includes all experimental and theoretical uncertainties before the fit. The lower panels show the ratio of data over pre-fit MC prediction.

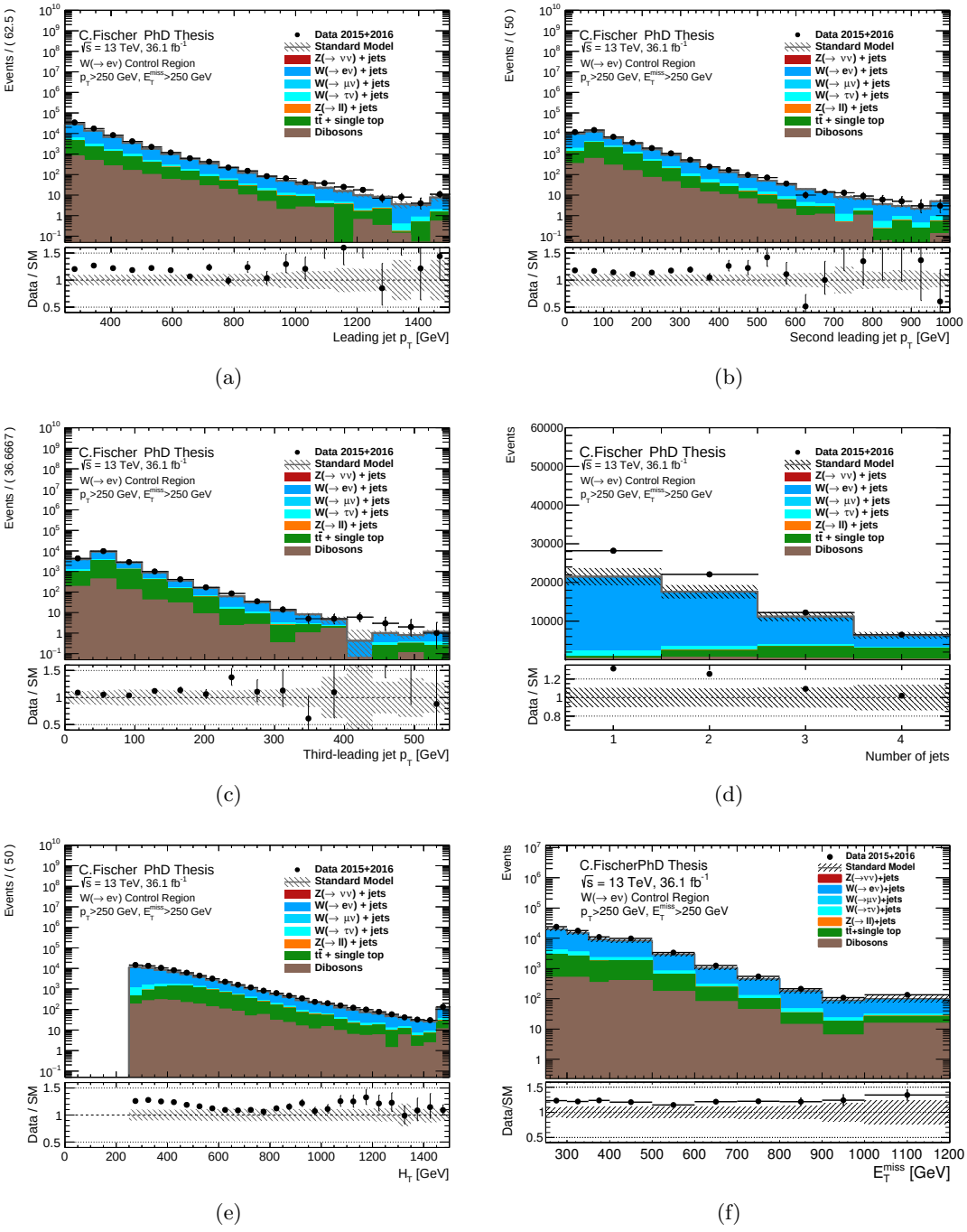

Fig. 7.13: Pre-fit distributions in CR1e for IM1. The data is shown as black dots, the total background prediction as the grey histogram. The hashed uncertainty band includes all experimental and theoretical uncertainties before the fit. The lower panels show the ratio of data over pre-fit MC prediction.

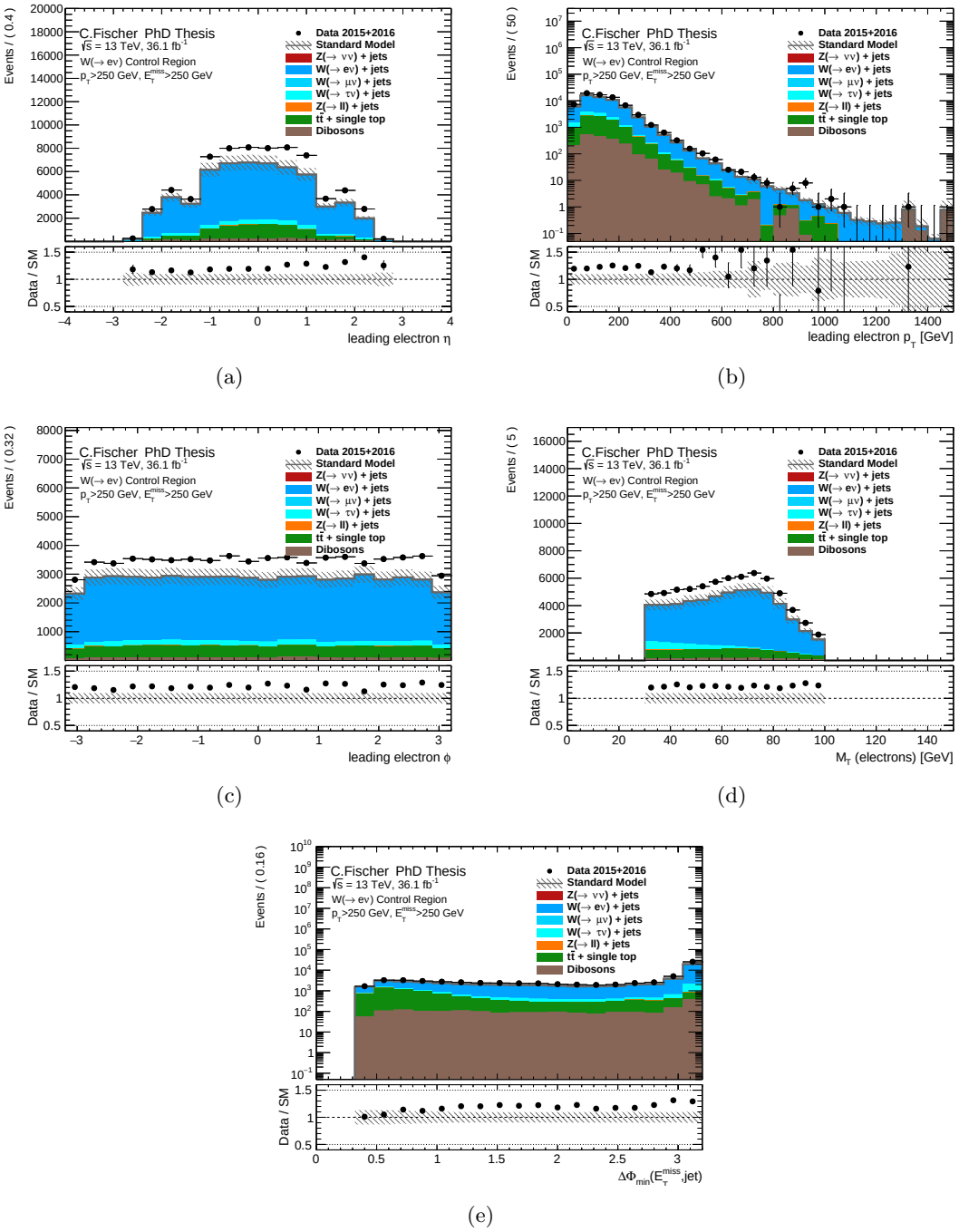

Fig. 7.14: Pre-fit distributions in CR1e for IM1. The data is shown as black dots, the total background prediction as the grey histogram. The hashed uncertainty band includes all experimental and theoretical uncertainties before the fit. The lower panels show the ratio of data over pre-fit MC prediction.

7.9.2 Distributions in CR1m

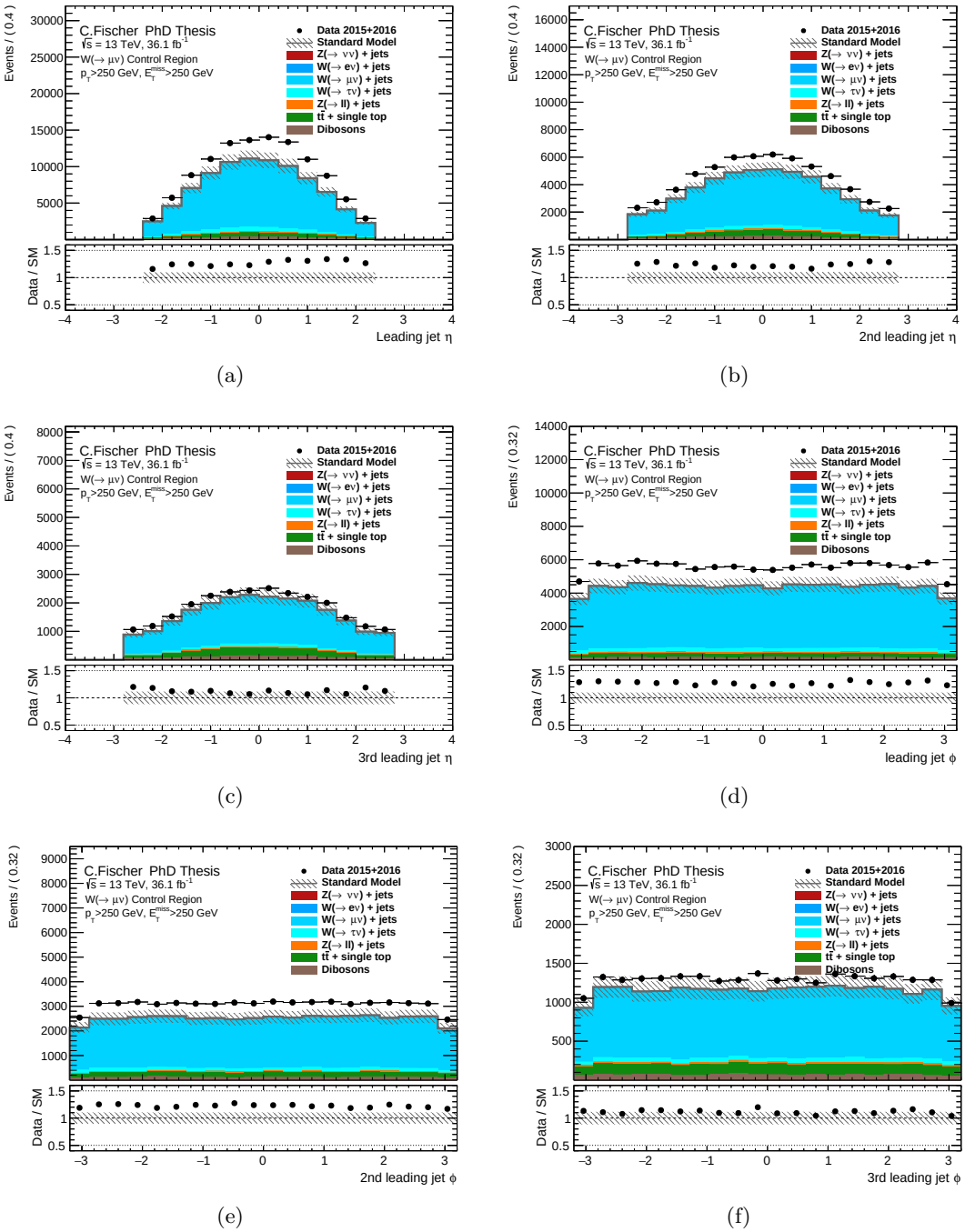

Fig. 7.15: Pre-fit distributions in CR1m for IM1. The data is shown as black dots, the total background prediction as the grey histogram. The hashed uncertainty band includes all experimental and theoretical uncertainties before the fit. The lower panels show the ratio of data over pre-fit MC prediction.

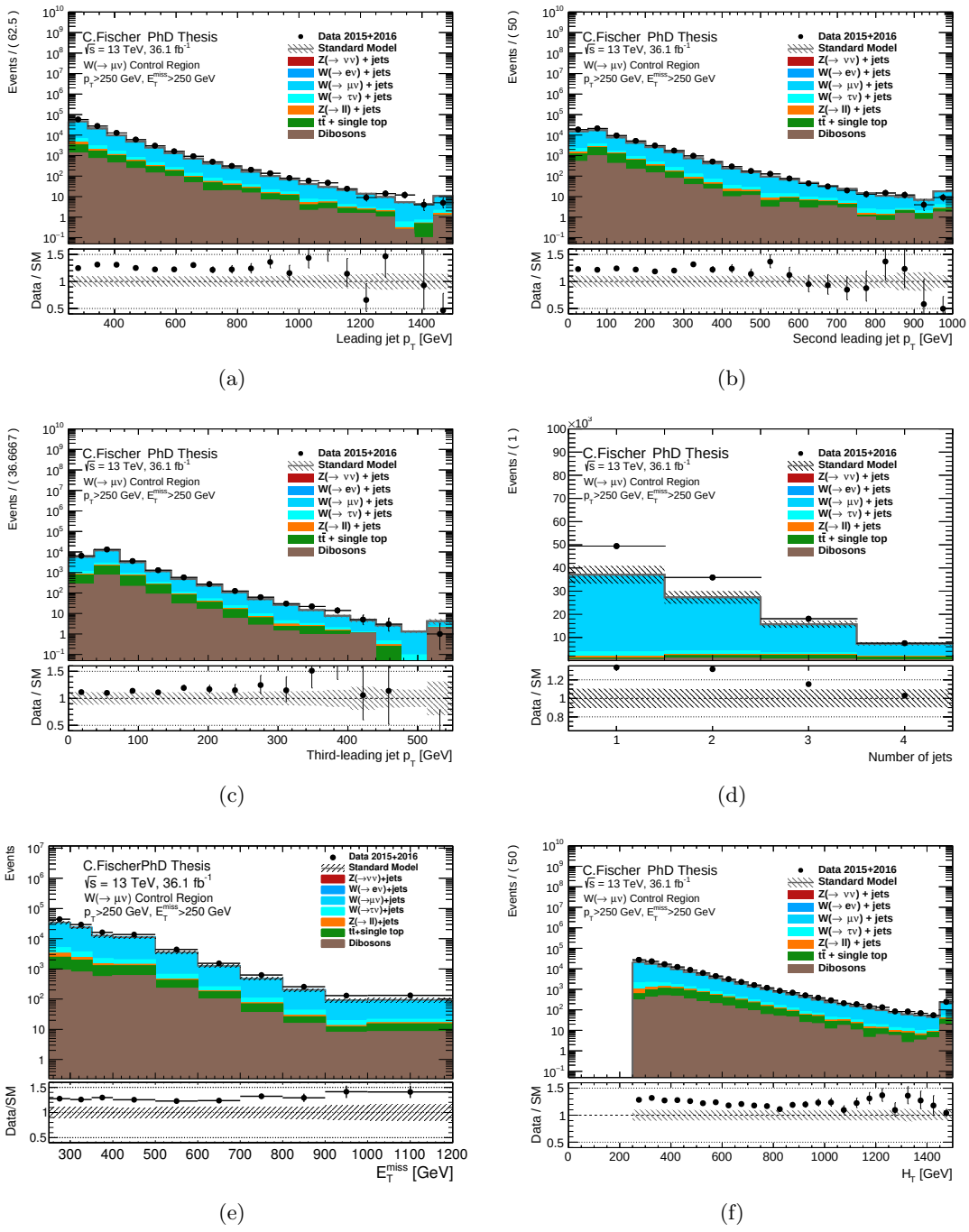

Fig. 7.16: Pre-fit distributions in CR1m for IM1. The data is shown as black dots, the total background prediction as the grey histogram. The hashed uncertainty band includes all experimental and theoretical uncertainties before the fit. The lower panels show the ratio of data over pre-fit MC prediction.

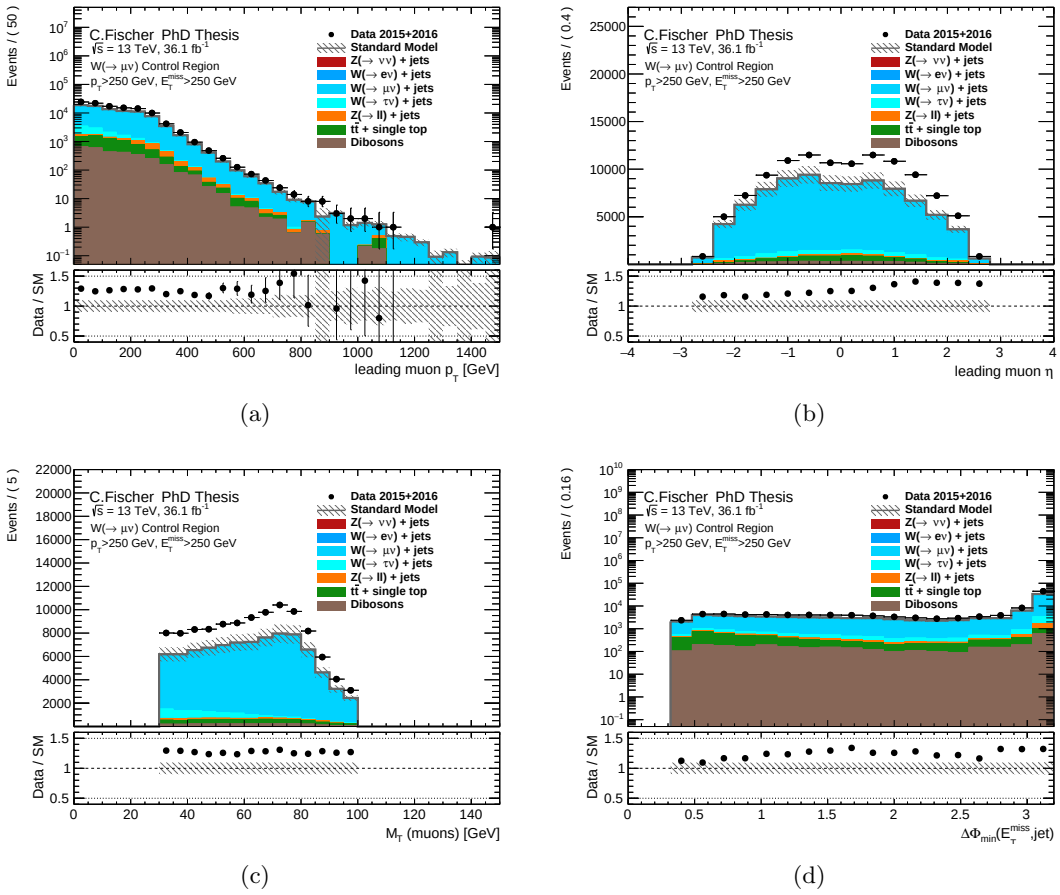

Fig. 7.17: Pre-fit distributions in CR1m for IM1. The data is shown as black dots, the total background prediction as the grey histogram. The hashed uncertainty band includes all experimental and theoretical uncertainties before the fit. The lower panels show the ratio of data over pre-fit MC prediction.

7.9.3 Distributions in CR2m

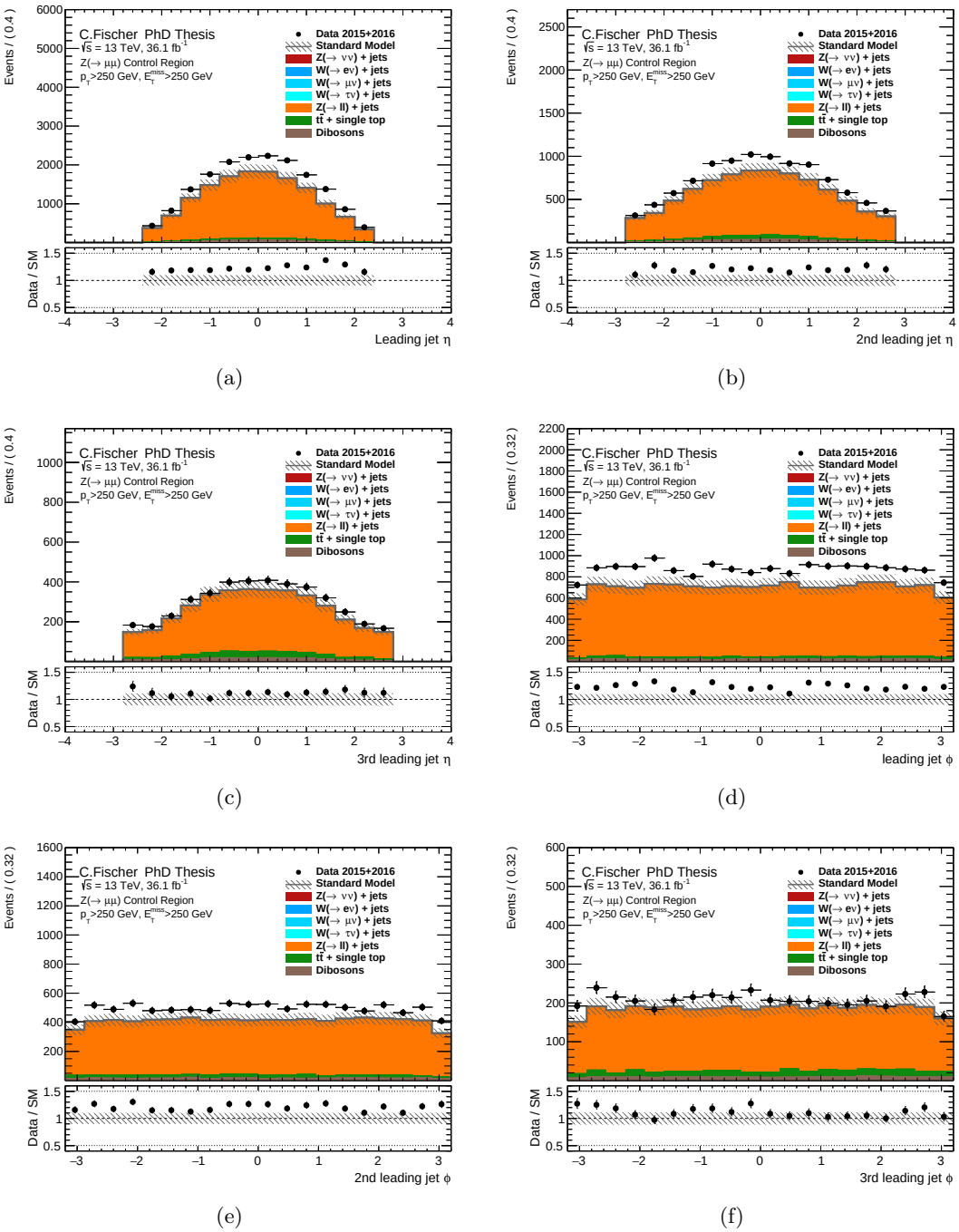

Fig. 7.18: Pre-fit distributions in CR2m for IM1. The data is shown as black dots, the total background prediction as the grey histogram. The hashed uncertainty band includes all experimental and theoretical uncertainties before the fit. The lower panels show the ratio of data over pre-fit MC prediction.

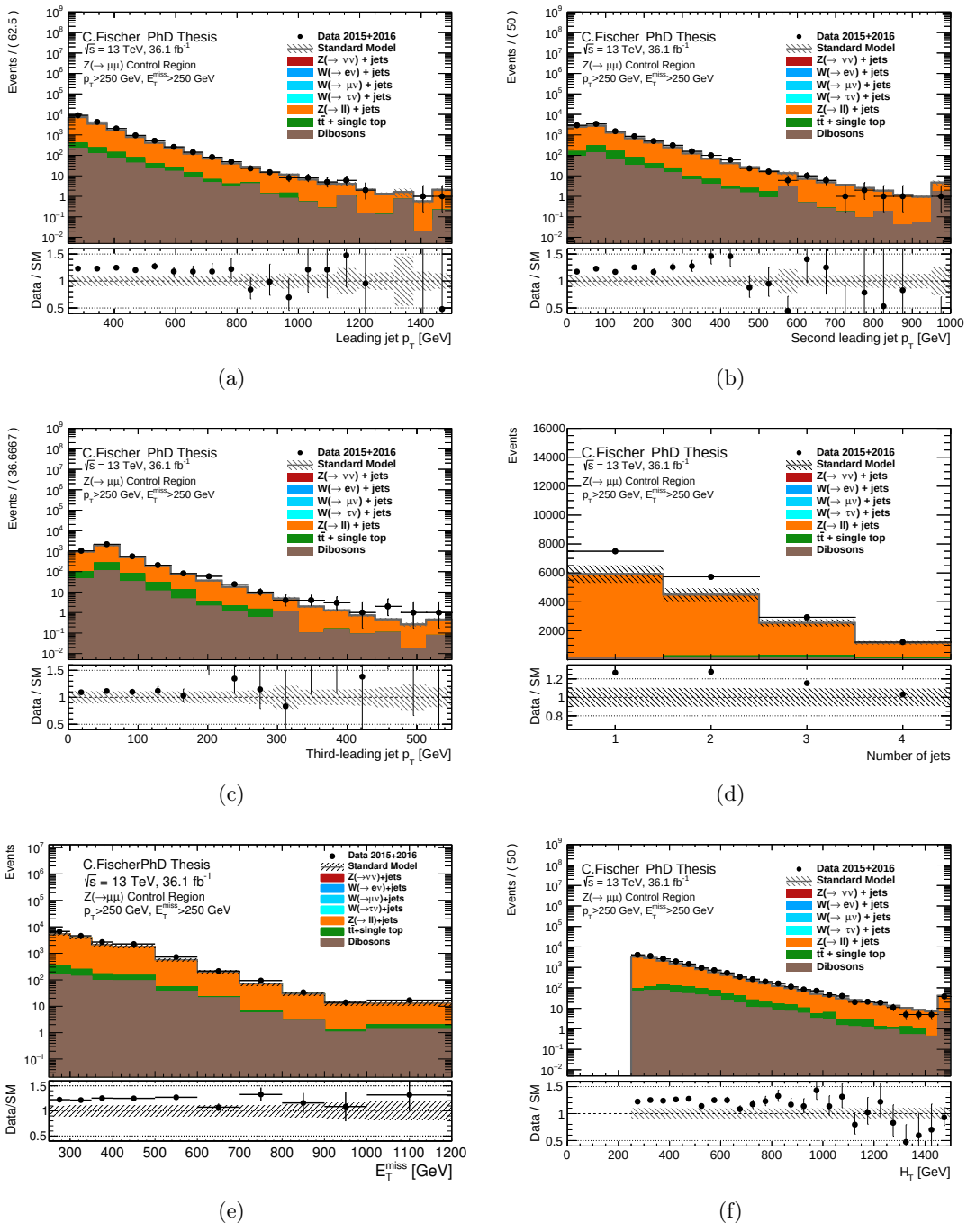

Fig. 7.19: Pre-fit distributions in CR2m for IM1. The data is shown as black dots, the total background prediction as the grey histogram. The hashed uncertainty band includes all experimental and theoretical uncertainties before the fit. The lower panels show the ratio of data over pre-fit MC prediction.

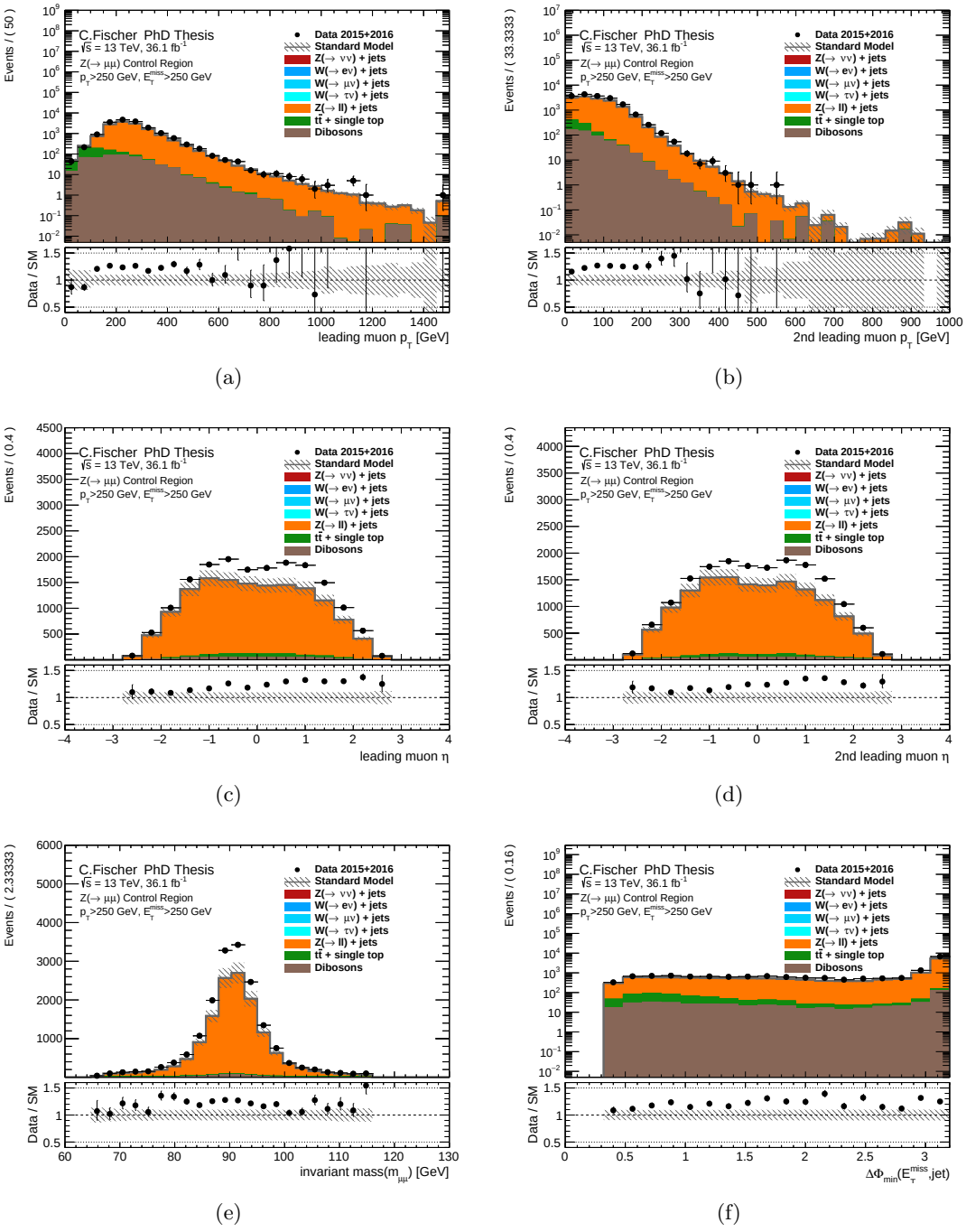

Fig. 7.20: Pre-fit distributions in CR2m for IM1. The data is shown as black dots, the total background prediction as the grey histogram. The hashed uncertainty band includes all experimental and theoretical uncertainties before the fit. The lower panels show the ratio of data over pre-fit MC prediction.

7.9.4 Distributions in CRtop

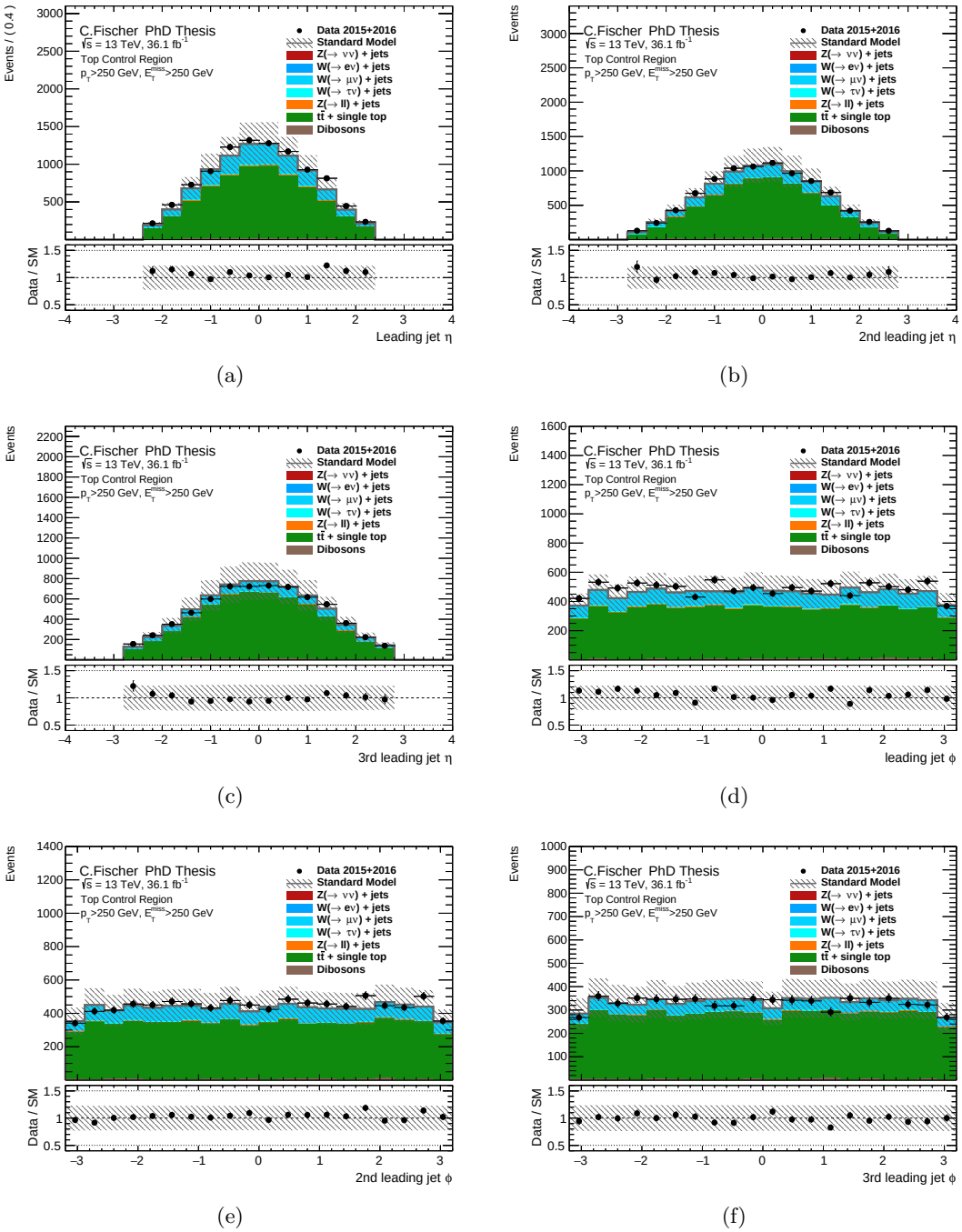

Fig. 7.21: Pre-fit distributions in CRtop for IM1. The data is shown as black dots, the total background prediction as the grey histogram. The hashed uncertainty band includes all experimental and theoretical uncertainties before the fit. The lower panels show the ratio of data over pre-fit MC prediction.

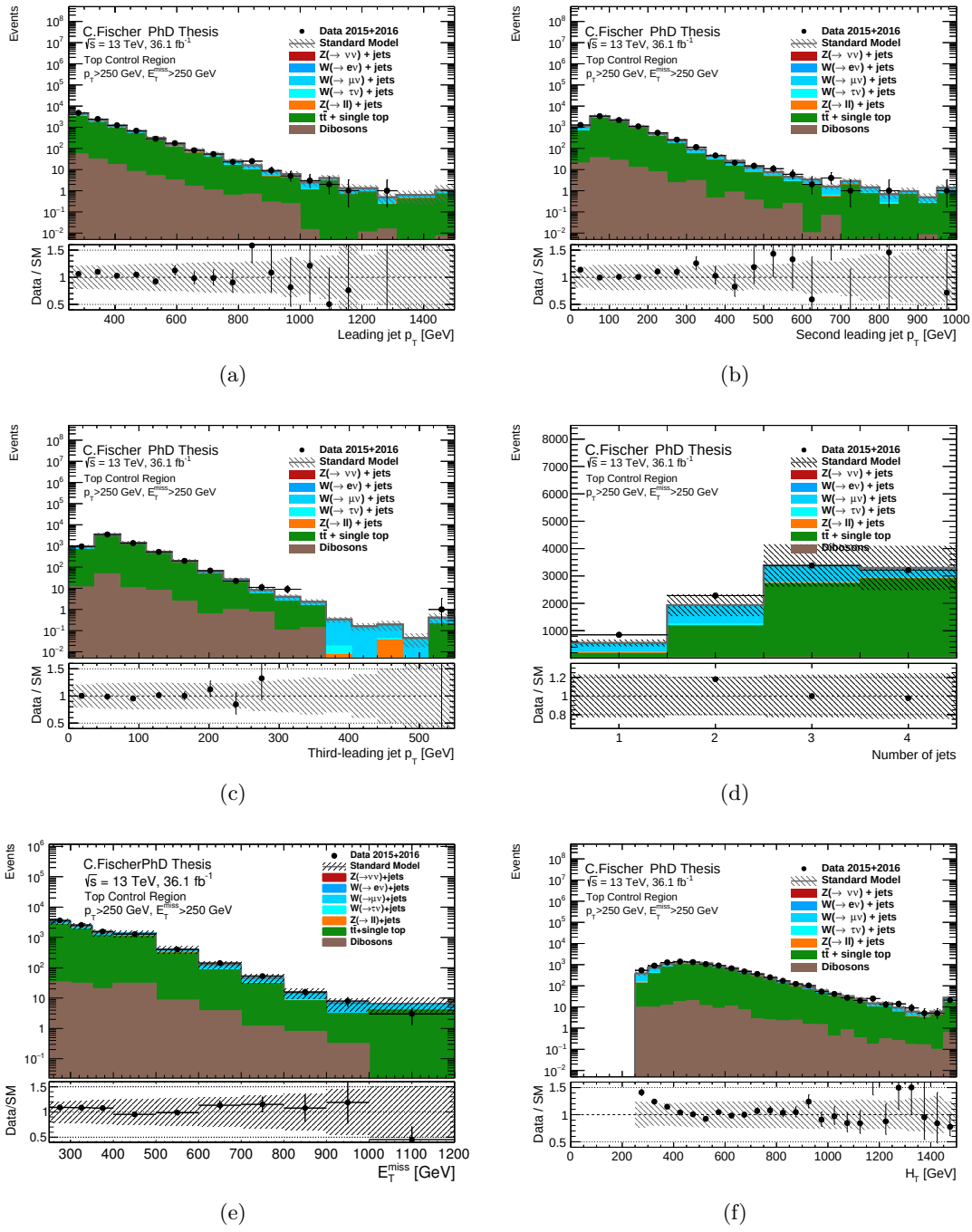

Fig. 7.22: Pre-fit distributions in CRtop for IM1. The data is shown as black dots, the total background prediction as the grey histogram. The hashed uncertainty band includes all experimental and theoretical uncertainties before the fit. The lower panels show the ratio of data over pre-fit MC prediction.

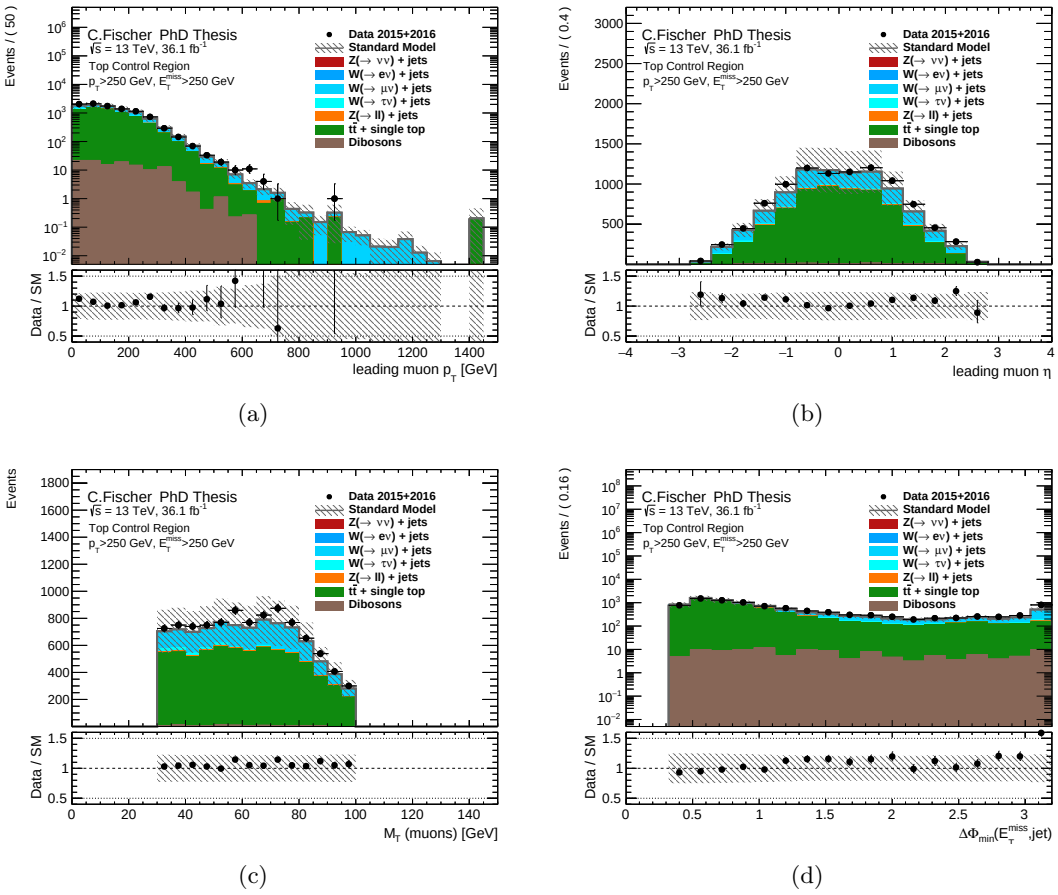

Fig. 7.23: Pre-fit distributions in CRtop for IM1. The data is shown as black dots, the total background prediction as the grey histogram. The hashed uncertainty band includes all experimental and theoretical uncertainties before the fit. The lower panels show the ratio of data over pre-fit MC prediction.

Chapter 8

Results

The following chapter presents the results after performing the background-only fit in all control regions using the statistical model as introduced in Sec. 7.7. All the discussed systematic sources are taken into account as nuisance parameters allowed to be constrained by the shape-fit to the $\not{E}_T$ distributions. The fit parameters and the final background estimation will be presented. The goodness of the fit is evaluated in Sec. 8.2. Limits are extracted by comparing the background prediction with the data yields. The model-independent upper cross section limits are presented in Sec. 8.3, where the signal region is included in the fit as well. Model specific interpretations are presented in Chap. 9.

8.1 Background-Only Fit

The backgrounds are normalised by process specific scale factors via the $\not{E}_T$-shape fit performed in all control regions simultaneously. Thereby the nuisance parameters influencing the $\not{E}_T$-shape and normalisation are adjusted such that the likelihood is maximised. The obtained scale factors are multiplied to the SM signal region prediction. These yields are the final background estimations in the signal region.
First, the behaviour of the free parameters and the nuisance parameters in the fit and their correlations are discussed. The final prediction after performing the background-only fit in the CRs, including event yields and kinematic distributions of these is presented in Sec. 8.1.2, prior to discussing the final SM prediction in the signal region.

8.1.1 Fit Parameters

The fitted scale factors for the two processes are listed in Tab. 8.1. As anticipated in Sec. 7.9, the normalisation factor for κ^V is fitted to 1.26. This resolves the normalisation discrepancy observed, which was introduced by the higher order theory corrections. The normalisation factor assigned to the top-quark background is fitted to 1.31. This high value might not have been expected from the pre-fit agreement that was close to 1. This value is attributed to the interplay between κ^{Top} and the top theory uncertainty nuisance parameter, which is fitted to a value of -0.78, which means that the total yield is scaled down by a factor of almost 1σ of this uncertainty which goes from 25% in the low $\not{E}_T$ region up to 72% for the highest $\not{E}_T$-bin. This compensates the high scale factor κ^{Top} and therefore the agreement of data and MC in the top control region after the fit is still close to 1. The fitted nuisance parameters as introduced in Tab. 7.6 are shown in Fig. 8.1. The exact values and uncertainties are listed in Tab. 8.2. Nuisance parameters fitted close to their initial values (value of 0 and uncertainty of 1) do not influence the fit significantly. The two parameters corresponding to the multijet and non-collision background uncertainty are not adjusted at all, since these backgrounds only appear in the SR and the uncertainties play no role in the background-only fit. There is a number of nuisance parameters that are 'pulled',

Scale Factor	Value	Uncertainty
κ^V	1.26	0.13
κ^{Top}	1.31	0.17

Tab. 8.1: Fitted scale factors for the normalisation of W/Z+jets processes (κ^V) and for the $t\bar{t}$+single top background normalization (κ^{Top}).

which means their fitted value is not close to 0. All of these pulls lie within $\pm 1.4\sigma$. These parameters also exhibit an uncertainty below 1σ. This means that they are constrained in the fit. From the experimental uncertainties, the nuisance parameters mostly constrained are the JES parameters and JER. Also pulled are electron scale factor (ID) and muon identification scale factor (SYS) uncertainties as well as the uncertainty related to the c-jet rejection in b-tagging and the soft track term influencing the $\not{E}_T$-resolution and scale. The uncertainties on the e/γ energy resolution and scale are constrained as well and the e/γ energy scale is pulled slightly up to about 0.5. One can also note that the nuisance parameter associated to the uncertainty on the pileup reweighting is pulled up to about 0.96 and its uncertainty is constrained to about 0.5σ. This indicates a sensitivity of the analysis to the exact description of the pileup activity.

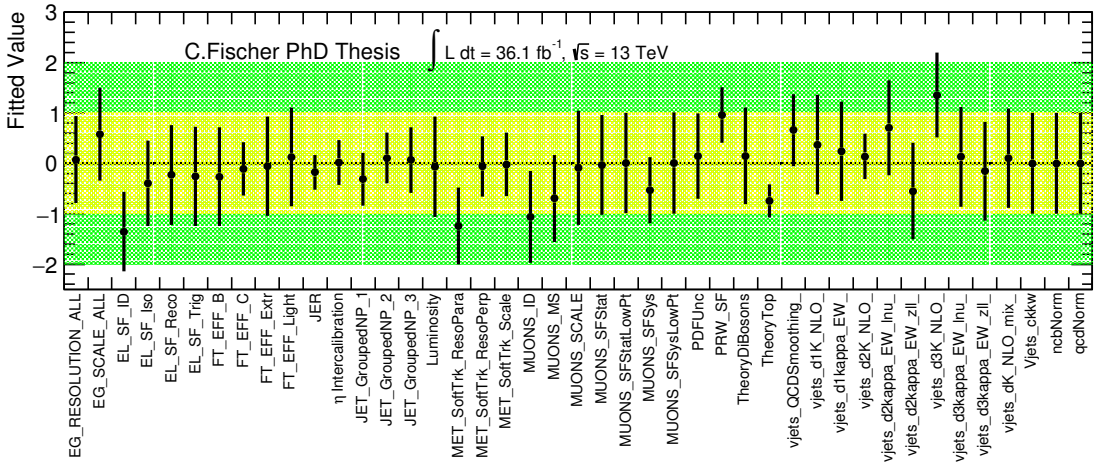

Fig. 8.1: Fitted nuisance parameters in the background-only shape fit.

From the theory uncertainties, the already mentioned top theory uncertainty is constrained and pulled. The nuisance parameters related to the higher order QCD corrections are also constrained and fitted to values between 0.3 and 1.3. This behaviour was also anticipated, since these uncertainties influenced the boson-p_T distribution the most, as can be seen in Fig. 7.5. The parameter called vjets_d1K_NLO mostly influences the normalisation. Its value is shifted from 0 but the uncertainty remains close to 1σ. The parameter associated to the uncertainty on the correlation between different processes (vjets_d3K_NLO) is fitted to a value of ~ 1.4 and therefore is the nuisance parameter pulled the most among all parameters. The nuisance parameters related to the EW correction are slightly less constrained and pulled. The parameter related to mixed QDC-EW correction is only slightly influenced. The parameter accounting for differences in the NLO prediction between theory and MC (vjets_QCDSmoothing) is adjusted by the fit to take a value of 0.66 with an uncertainty of 0.7σ.

Nuisance Parameter	Value	Uncertainty
alpha_EG_RESOLUTION_ALL	+0.076030	0.864230
alpha_EG_SCALE_ALL	+0.582369	0.923061
alpha_EL_SF_ID	-1.355003	0.789108
alpha_EL_SF_Iso	-0.398170	0.846024
alpha_EL_SF_Reco	-0.231114	0.988729
alpha_EL_SF_Trig	-0.255249	0.987325
alpha_FT_EFF_B	-0.261874	0.976856
alpha_FT_EFF_C	-0.109966	0.527047
alpha_FT_EFF_Extr	-0.053133	0.985919
alpha_FT_EFF_Light	+0.128828	0.978844
alpha_JER	-0.177534	0.345123
alpha_JET_EtaIntercalibration	+0.018766	0.448532
alpha_JET_GroupedNP_1	-0.312989	0.524485
alpha_JET_GroupedNP_2	+0.104758	0.501961
alpha_JET_GroupedNP_3	+0.068282	0.649932
alpha_Luminosity	-0.067208	0.993089
alpha_MET_SoftTrk_ResoPara	-1.243165	0.762650
alpha_MET_SoftTrk_ResoPerp	-0.060015	0.601086
alpha_MET_SoftTrk_Scale	-0.022499	0.629192
alpha_MUONS_ID	-1.063601	0.911018
alpha_MUONS_MS	-0.694722	0.864380
alpha_MUONS_SCALE	-0.086509	1.134998
alpha_MUONS_SFStat	-0.029625	0.986768
alpha_MUONS_SFStatLowPt	+0.006628	0.991866
alpha_MUONS_SFSys	-0.528345	0.659882
alpha_MUONS_SFSysLowPt	+0.007090	1.002172
alpha_PDFUnc	+0.147641	0.848037
alpha_PRW_SF	+0.957667	0.550488
alpha_TheoryDiBosons	+0.149997	0.954086
alpha_TheoryTop	-0.745247	0.323906
alpha_vjets_QCDSmoothing	+0.660294	0.717661
alpha_vjets_d1K_NLO	+0.371463	0.995187
alpha_vjets_d1kappa_EW	+0.239125	0.986015
alpha_vjets_d2K_NLO	+0.136636	0.451931
alpha_vjets_d2kappa_EW_lnu	+0.705355	0.945423
alpha_vjets_d2kappa_EW_zll	-0.548028	0.960150
alpha_vjets_d3K_NLO	+1.353176	0.843160
alpha_vjets_d3kappa_EW_lnu	+0.133666	0.990078
alpha_vjets_d3kappa_EW_zll	-0.153391	0.981546
alpha_vjets_dK_NLO_mix	+0.103332	0.989085
alpha_vjets_ckkw	+0.000000	1.000000
alpha_ncbNorm	+0.000000	1.000000
alpha_qcdNorm	+0.000000	1.000000

Tab. 8.2: Values and uncertainties of the fitted nuisance parameters in the background-only fit.

Figure 8.2 shows the correlations among the free fit parameters and the nuisance parameters in the fit (that exhibit any correlation coefficient above $|0.15|$). The top scale factor κ^{Top} is anti-correlated with the theory uncertainty on top-quark production. It is also anti-correlated with the uncertainty regarding the c-jet rejection, which is due to the applied b-tag requirement. There is also a slight anti-correlation with the luminosity nuisance parameter. The

κ^V scale factor is anti-correlated with alpha_vjets_d1K_NLO, while it is correlated with alpha_vjets_d2K_NLO. The former influences mainly the normalisation of the boson-p_T distribution. Thus an up variation of κ^V requires a compensation of alpha_vjets_d1K_NLO in the opposite direction. On the other hand, alpha_vjets_d2K_NLO influences the boson-p_T shape such that an up variation below $\not{E}_T \sim 600$ GeV induces a reduction of events in that region. The opposite is the case for $\not{E}_T > 600$ GeV (see Fig. 7.5). Since the statistical power of the fit is governed by the low $\not{E}_T$-bins this implies a correlation for κ^V and alpha_vjets_d2K_NLO. Furthermore, there are slight anti-correlations between κ^V and the luminosity nuisance parameter, one of the muon scale factor uncertainties (SYS) and the nuisance parameter related to the PDF uncertainty of the V+jets processes. The PDF uncertainty parameter is in turn anti-correlated with alpha_vjets_d2K_NLO. Also displayed are parameters named `gamma_CRbin` that are added for statistical uncertainties exceeding 5% (parameters called γ_s in Sec. 7.7.3). Overall, the fit behaves as expected: the shape-fit constrains some of the dominant pre-fit uncertainties by using the information from exclusive bins in $\not{E}_T$. This leads to a strongly decreased background uncertainty in all regions after the fit.

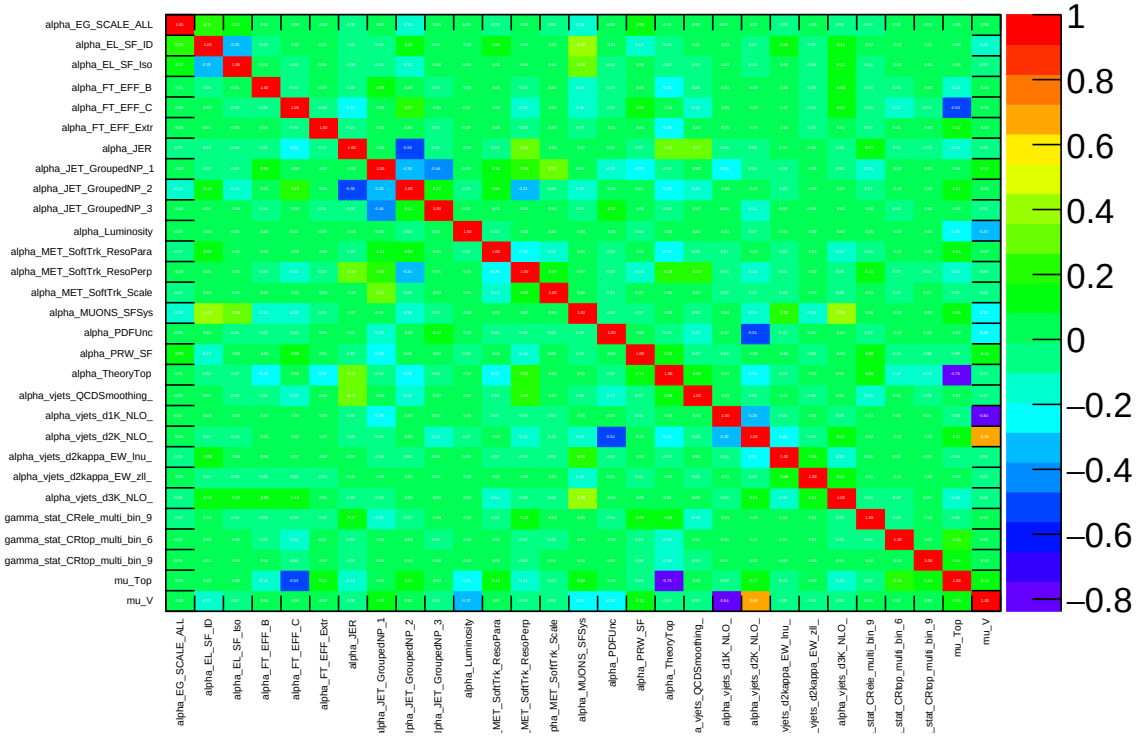

Fig. 8.2: Correlation matrix of nuisance parameters and free parameters in the background-only fit. Only parameters with any correlation coefficient above |0.15| are shown.

8.1.2 Post-Fit Distributions: Control Regions

The fitted $\not{E}_T$ distributions in the four control regions are shown in Fig. 8.3. The ratio of data over final background prediction is displayed in the lower panels. An adequate description of the data is reflected in a ratio of data/SM prediction that is close to unity. This is fulfilled and can be observed in Fig. 8.3. Almost all data points lie within 1σ of the final background estimate. The actual fitted event yields for each considered background are presented for the

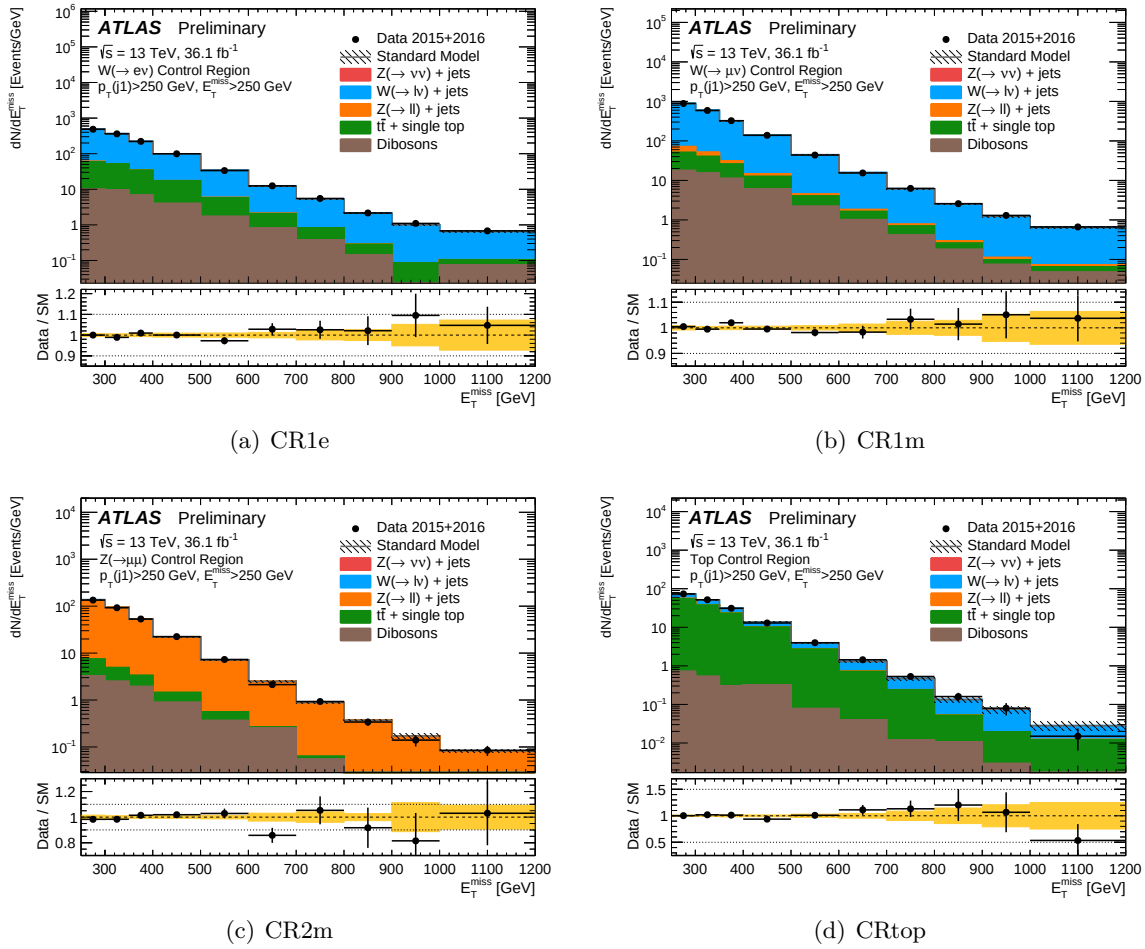

(a) CR1e (b) CR1m

(c) CR2m (d) CRtop

Fig. 8.3: Fitted $\not{E}_T$-distributions in the four control regions. The data is shown as black dots, the uncertainty is the hashed area including statistical and systematic uncertainties. The ratio of data/SM expectation is displayed in the lower panels, where the uncertainty is indicated in yellow.

regions EM1, EM5, EM9 and IM10 in Tab. 8.3, Tab. 8.4, Tab. 8.5 and Tab. 8.6, respectively. The tables corresponding to regions EM2, EM3, EM4, EM6, EM7 and EM8 are included in the appendix in Sec. A.1.

The quoted background uncertainties include all systematic uncertainties in addition to the statistical uncertainty after the fit. The uncertainties have been reduced, in particular the top-quark background uncertainty has been reduced significantly down to $\sim 7\%$ via the definition of a dedicated CRtop which constrains the theory uncertainty on the top-quark production. In Fig. 8.4 to Fig. 8.11, post-fit distributions are shown for the control regions for other kinematic variables not included in the global fit. The description of the jet multiplicity remains slightly imperfect. There is a trend that the MC simulation overestimates the jet multiplicity predicting on average slightly more jets per event than actually observed. This points to a mismodelling of the physics involved in the jet fragmentation and parton shower evolution, the non-perturbative part of the event simulation. This is a mismodelling in SHERPA that has been observed in various measurements, see e. g. the cross section measurement of Z+jets production in Ref. [160]. Apart from this feature, all distributions of the CR1e are well described. The asymmetry in the electron η distribution remains. The same statement holds for the CR1m distributions, where the muon

η is slightly asymmetric in the MC prediction. Distributions in CR2m are also well described within the overall uncertainty bands. A small discrepancy remains for the CRtop: the first bin of the jet multiplicity is not well described. Here the MC prediction undershoots the data by about 35%. The same is true for the first bin of the H_T distribution and a slightly higher discrepancy remains for $\Delta\phi(\not{E}_T,\text{jets}) \sim \pi$. This discrepancy is decreased w. r. t. the pre-fit distribution. However, since the jet multiplicity is not perfectly modelled, a slight discrepancy remains in that region, dominated by $W(\mu\nu)$+jets production rather than top-quark production. Another explanation is an imperfect b-tag calibration with an underestimated scale factor that has been derived in a different phase space than the analysis' one. These distributions however have no impact on the background-only fit and the derived background estimation in the signal region.

Region	CR1e	CR1m	CR2m	CRtop
Observed events	24280	44295	6733	3670
Post-fit SM prediction	24280 ± 150	44120 ± 210	6847 ± 71	3661 ± 49
$Z \to \nu\nu$+jets	0.3 ± 0.1	20 ± 3	0 ± 0	2.7 ± 0.4
$W \to \tau\nu$+jets	1501 ± 29	2293 ± 63	0.9 ± 0.2	66 ± 13
$W \to \mu\nu$+jets	$0.3^{+0.6}_{-0.3}$	38250 ± 290	14 ± 1	850 ± 150
$W \to e\nu$+jets	19770 ± 240	1 ± 1	0 ± 0	0 ± 0
$Z/\gamma^* \to \tau\tau$+jets	89 ± 7	129 ± 6	8 ± 2	6 ± 1
$Z/\gamma^* \to \mu\mu$+jets	0.4 ± 0.1	910 ± 24	6461 ± 71	29 ± 3
$Z/\gamma^* \to ee$+jets	2 ± 2	0 ± 0	0 ± 0	0 ± 0
$t\bar{t}$ +single top	2420 ± 200	1630 ± 200	202 ± 17	2670 ± 180
Dibosons	495 ± 38	887 ± 60	162 ± 11	35 ± 8

Tab. 8.3: Event yields after the fit in all control regions for 250 GeV $< \not{E}_T <$ 300 GeV corresponding to 36.1 fb^{-1}. The uncertainties include statistical and systematic uncertainties after the fit. Multijet and non-collision background are omitted since they are negligible in the CRs.

Region	CR1e	CR1m	CR2m	CRtop
Observed events	3353	4384	731	398
Post-fit SM prediction	3466 ± 32	4485 ± 36	713 ± 9	394 ± 13
$Z \to \nu\nu$+jets	0.4 ± 0.1	1.6 ± 0.2	0 ± 0	0.2 ± 0
$W \to \tau\nu$+jets	210 ± 5	270 ± 7	0.1 ± 0	10 ± 1
$W \to \mu\nu$+jets	0.4 ± 0.1	3769 ± 47	1.4 ± 0.1	120 ± 12
$W \to e\nu$+jets	2673 ± 51	$-0.2^{+0.0}_{-0.2}$	0 ± 0	0 ± 0
$Z/\gamma^* \to \tau\tau$+jets	11 ± 1	11 ± 1	0.9 ± 0.1	0.5 ± 0.2
$Z/\gamma^* \to \mu\mu$+jets	0.1 ± 0	35 ± 5	656 ± 9	1.8 ± 0.2
$Z/\gamma^* \to ee$+jets	0.2 ± 0.1	0 ± 0	0 ± 0	0 ± 0
$t\bar{t}$ +single top	399 ± 40	176 ± 26	19 ± 3	254 ± 21
Dibosons	172 ± 17	223 ± 17	36 ± 3	8 ± 4

Tab. 8.4: Event yields after the fit in all control regions for 500 GeV $< \not{E}_T <$ 600 TeV corresponding to 36.1 fb^{-1}. The uncertainties include statistical and systematic uncertainties after the fit. Multijet and non-collision background are omitted since they are negligible in the CRs.

Region	CR1e	CR1m	CR2m	CRtop
Observed events	110	130	14	8
Post-fit SM prediction	101 ± 5	122 ± 6	17 ± 2	8 ± 1
$Z \to \nu\nu$+jets	0 ± 0	0 ± 0	0 ± 0	0 ± 0
$W \to \tau\nu$+jets	7 ± 1	8 ± 1	0 ± 0	$0.0^{+0.0}_{-0.0}$
$W \to \mu\nu$+jets	0 ± 0	102 ± 6	0 ± 0	6 ± 1
$W \to e\nu$+jets	85 ± 3	0 ± 0	0 ± 0	0 ± 0
$Z/\gamma^* \to \tau\tau$+jets	$0.1^{+0.1}_{-0.1}$	0.4 ± 0.1	0 ± 0	$0.0^{+0.0}_{-0.0}$
$Z/\gamma^* \to \mu\mu$+jets	0 ± 0	1.1 ± 0.1	15 ± 1	0 ± 0
$Z/\gamma^* \to ee$+jets	0 ± 0	0 ± 0	0 ± 0	0 ± 0
$t\bar{t}$ +single top	6 ± 2	2 ± 1	0.1 ± 0	2 ± 1
Dibosons	$2.5^{+4.2}_{-2.5}$	7 ± 2	1.4 ± 0.3	0.3 ± 0.1

Tab. 8.5: Event yields after the fit in all control regions for 900 GeV $< \not{E}_T <$ 1000 GeV corresponding to 36.1 fb^{-1}. The uncertainties include statistical and systematic uncertainties after the fit. Multijet and non-collision background are omitted since they are negligible in the CRs.

Region	CR1e	CR1m	CR2m	CRtop
Observed events	136	133	17	3
Post-fit SM prediction	128 ± 9	127 ± 7	17 ± 1	6 ± 1
$Z \to \nu\nu$+jets	0 ± 0	0 ± 0	0 ± 0	0 ± 0
$W \to \tau\nu$+jets	8 ± 1	8 ± 1	0 ± 0	0.3 ± 0.1
$W \to \mu\nu$+jets	0 ± 0	105 ± 7	0 ± 0	3 ± 1
$W \to e\nu$+jets	102 ± 8	0 ± 0	0 ± 0	0 ± 0
$Z/\gamma^* \to \tau\tau$+jets	0.2 ± 0	0.1 ± 0	0 ± 0	0 ± 0
$Z/\gamma^* \to \mu\mu$+jets	0 ± 0	1.7 ± 0.2	15 ± 1	0.0 ± 0.0
$Z/\gamma^* \to ee$+jets	0 ± 0	0 ± 0	0 ± 0	0 ± 0
$t\bar{t}$ +single top	6 ± 2	3 ± 2	0.6 ± 0.3	2 ± 1
Dibosons	13 ± 6	9 ± 1	1.2 ± 0.2	$-0.1^{+0.0}_{--0.1}$

Tab. 8.6: Event yields after the fit in all control regions for $\not{E}_T >$ 1 TeV corresponding to 36.1 fb^{-1}. The uncertainties include statistical and systematic uncertainties after the fit. Multijet and non-collision background are omitted since they are negligible in the CRs.

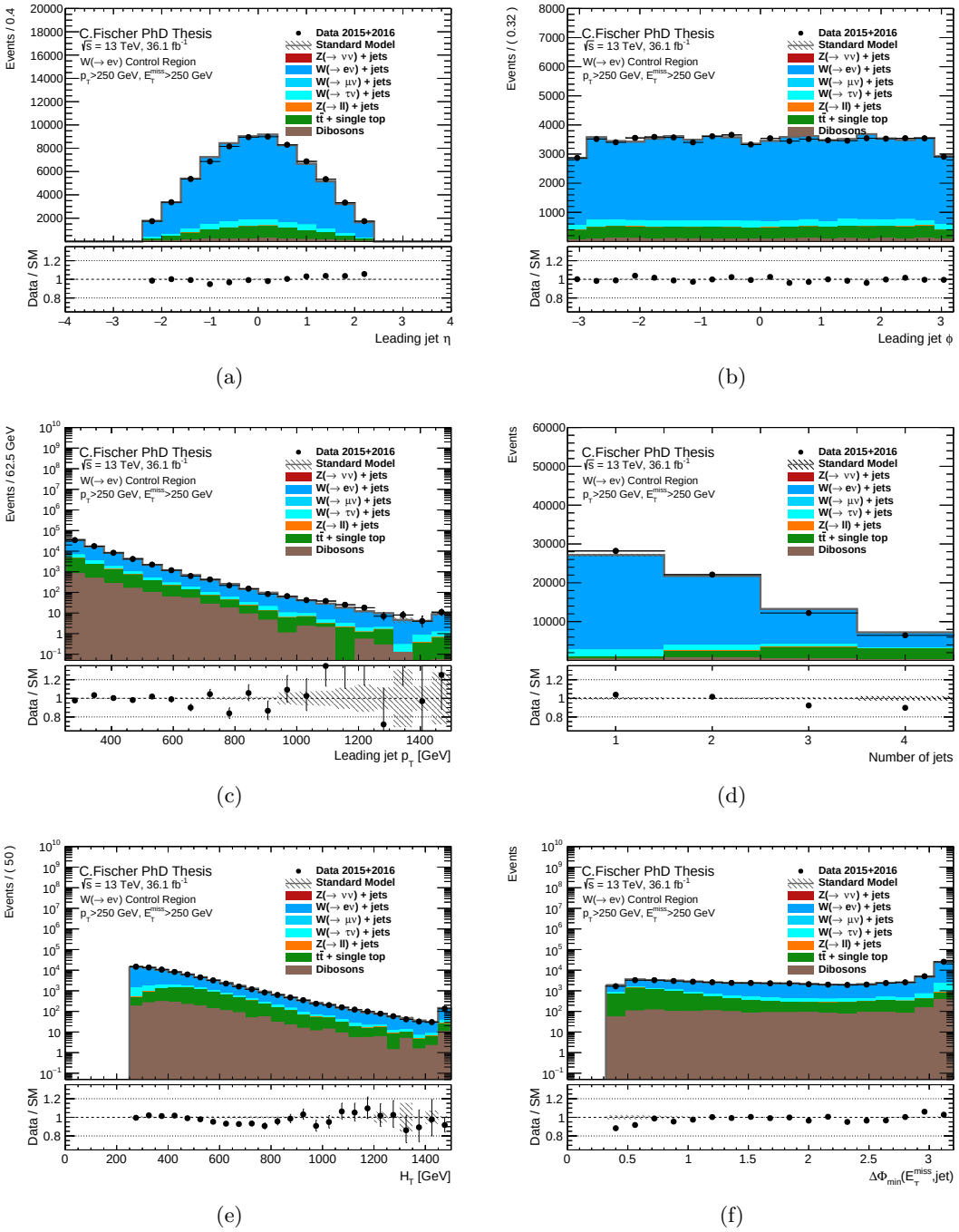

Fig. 8.4: Post-fit distributions in CR1e for IM1. The data is shown as black dots, the total background prediction as the grey histogram. The hashed uncertainty band includes all experimental and theoretical uncertainties after the fit. The lower panels show the ratio of data over SM prediction after the fit.

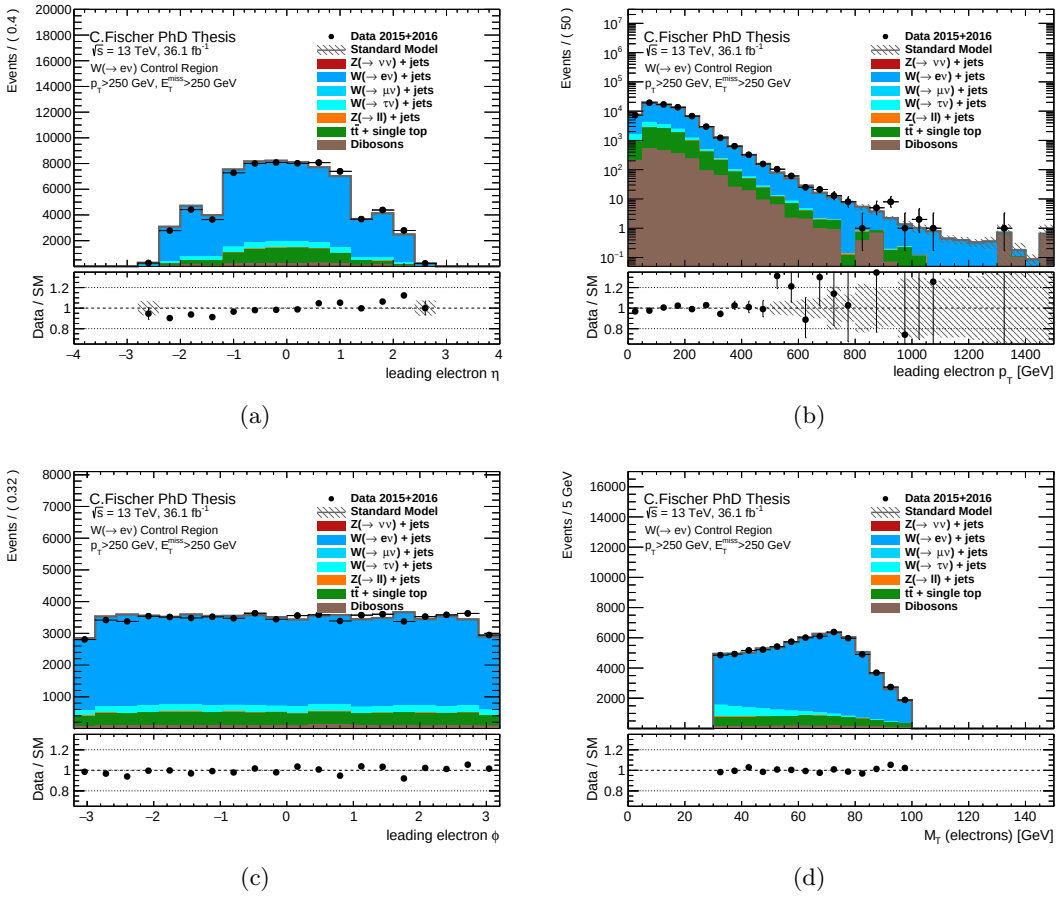

Fig. 8.5: Post-fit distributions in CR1e for IM1. The data is shown as black dots, the total background prediction as the grey histogram. The hashed uncertainty band includes all experimental and theoretical uncertainties after the fit. The lower panels show the ratio of data over SM prediction after the fit.

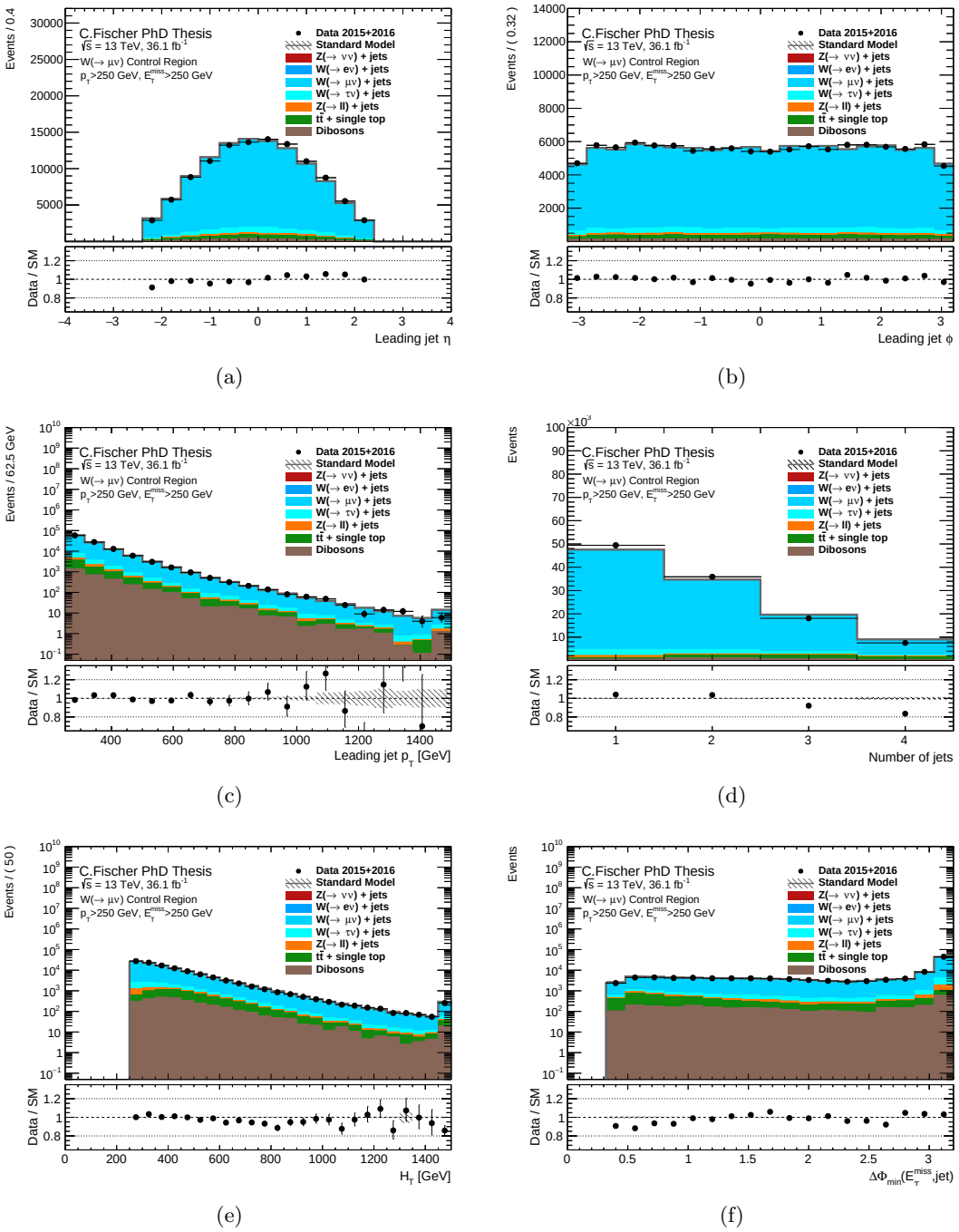

Fig. 8.6: Post-fit distributions in CR1m for IM1. The data is shown as black dots, the total background prediction as the grey histogram. The hashed uncertainty band includes all experimental and theoretical uncertainties after the fit. The lower panels show the ratio of data over SM prediction after the fit.

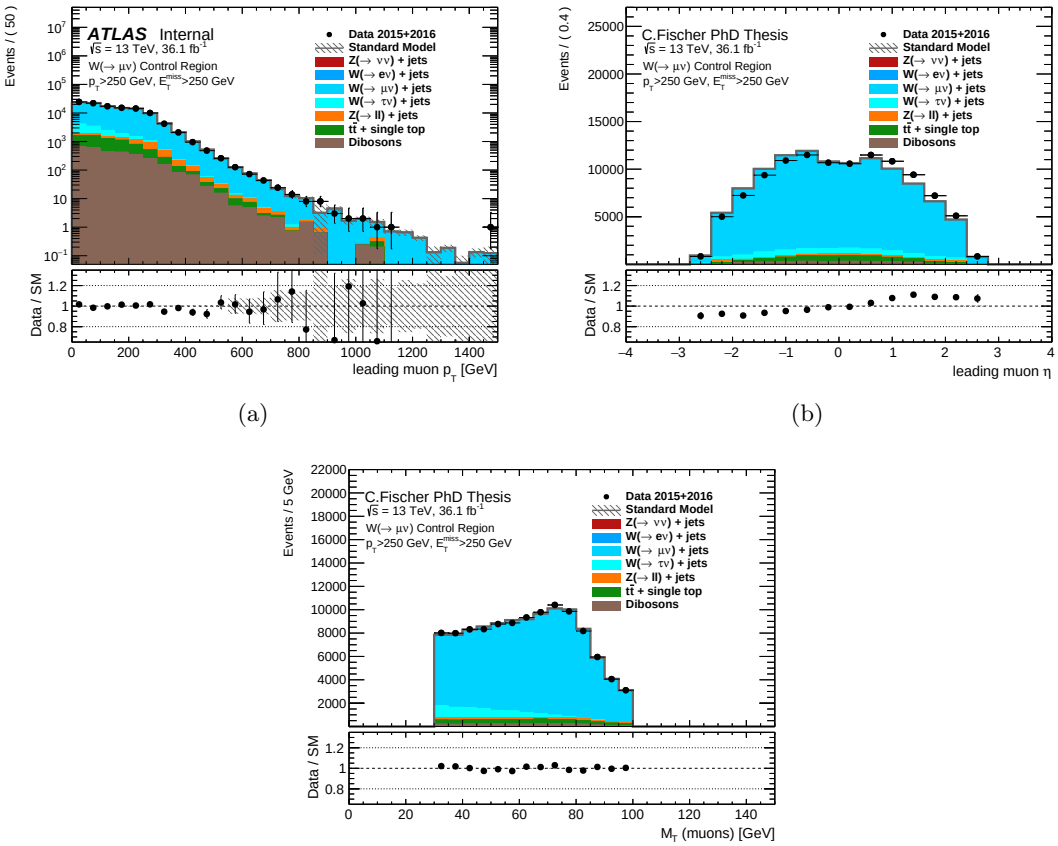

Fig. 8.7: Post-fit distributions in CR1m for IM1. The data is shown as black dots, the total background prediction as the grey histogram. The hashed uncertainty band includes all experimental and theoretical uncertainties after the fit. The lower panels show the ratio of data over SM prediction after the fit.

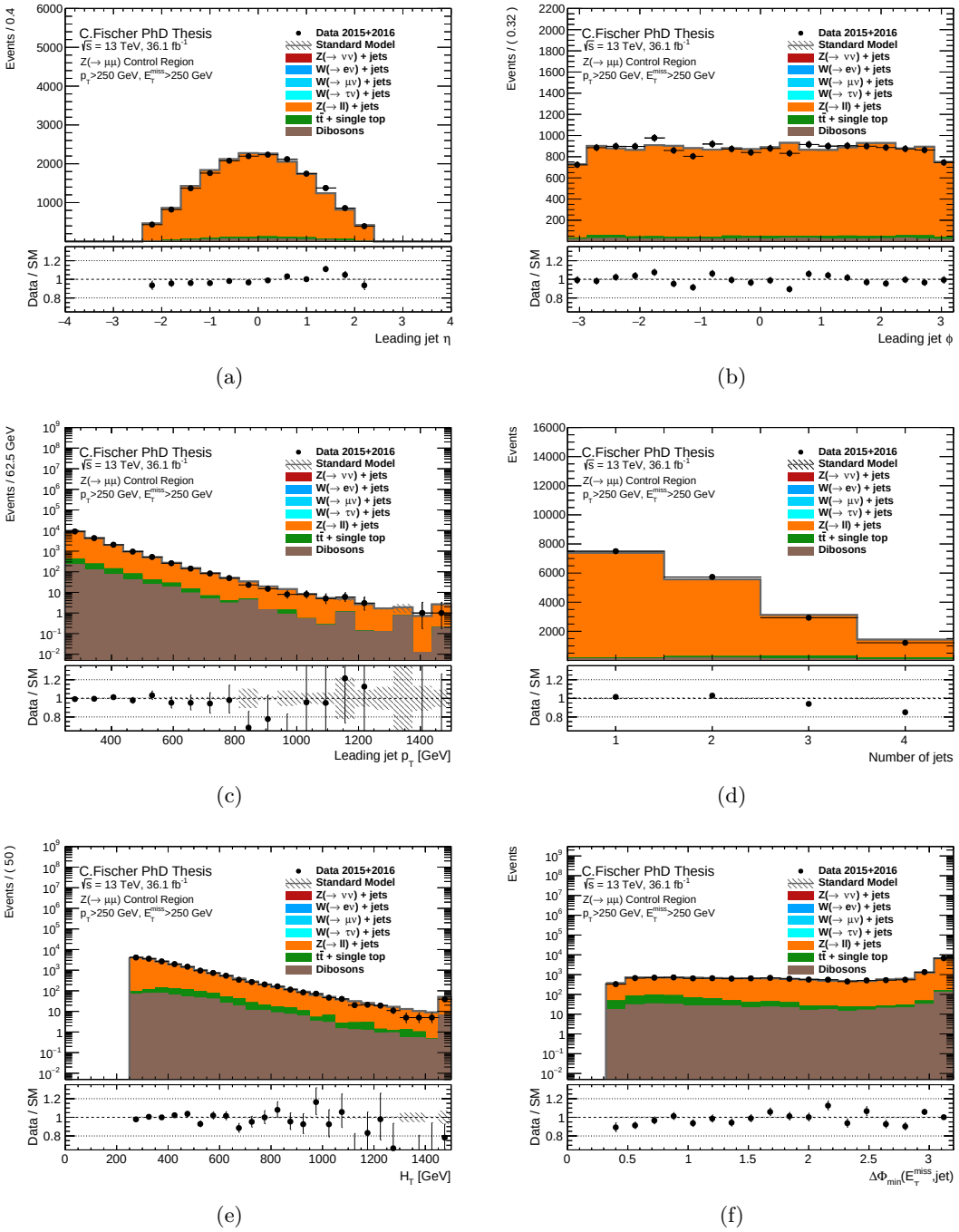

Fig. 8.8: Post-fit distributions in CR2m for IM1. The data is shown as black dots, the total background prediction as the grey histogram. The hashed uncertainty band includes all experimental and theoretical uncertainties after the fit. The lower panels show the ratio of data over SM prediction after the fit.

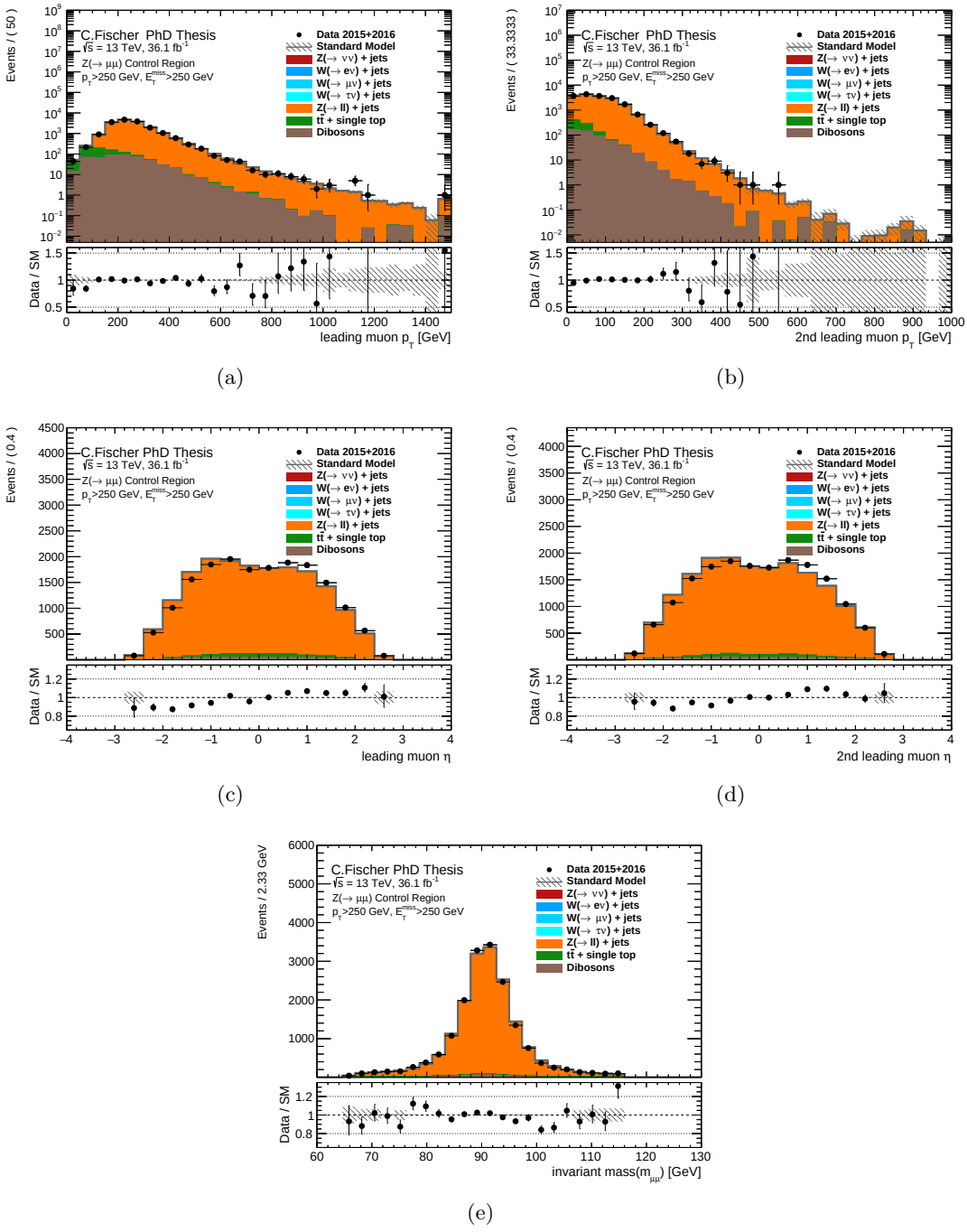

Fig. 8.9: Post-fit distributions in CR2m for IM1. The data is shown as black dots, the total background prediction as the grey histogram. The hashed uncertainty band includes all experimental and theoretical uncertainties after the fit. The lower panels show the ratio of data over SM prediction after the fit.

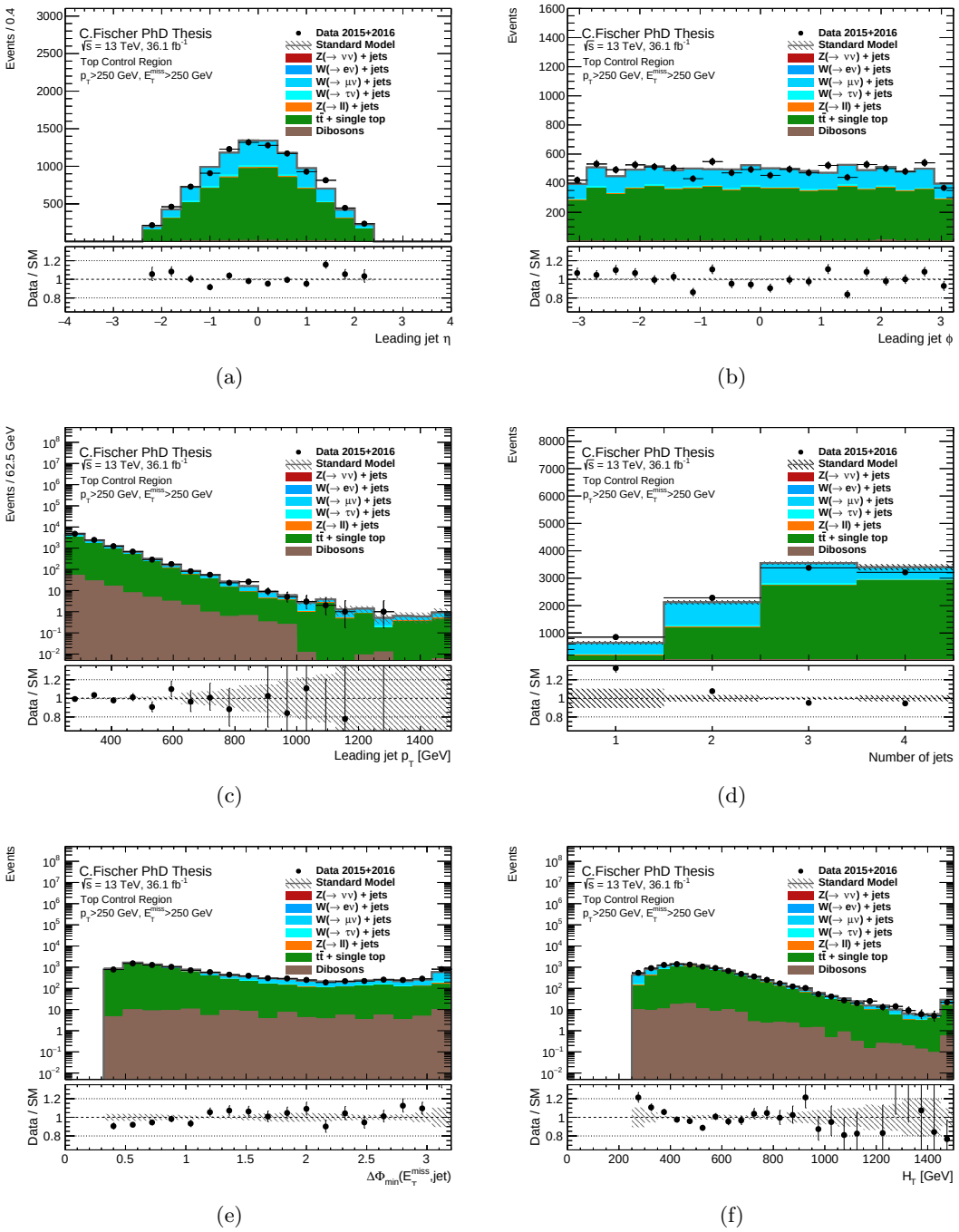

Fig. 8.10: Post-fit distributions in CRtop for IM1. The data is shown as black dots, the total background prediction as the grey histogram. The hashed uncertainty band includes all experimental and theoretical uncertainties after the fit. The lower panels show the ratio of data over SM prediction after the fit.

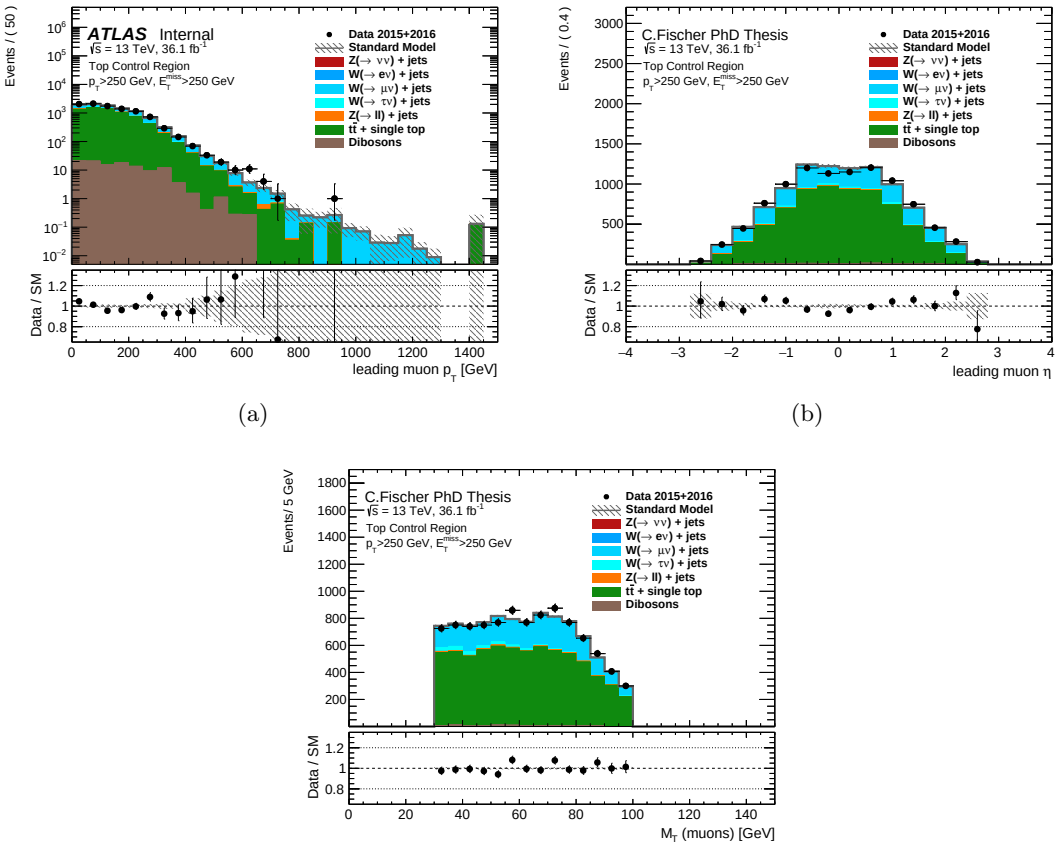

Fig. 8.11: Post-fit distributions in CRtop for IM1. The data is shown as black dots, the total background prediction as the grey histogram. The hashed uncertainty band includes all experimental and theoretical uncertainties after the fit. The lower panels show the ratio of data over SM prediction after the fit.

8.1.3 Background Estimation in the Signal Region

The final prediction of the total background from the CR-only fit is shown for the inclusive signal region in Fig. 8.12 and is compared to the data. The actual numbers of the fitted background processes in all bins of the signal region are shown in Tab. 8.7. The corresponding total background prediction before the fit can be found in Tab. 7.7. As already anticipated by the fitted scale factors, the yields have grown by about 25%. The uncertainty has been reduced significantly: for the region EM1 the total background uncertainty amounts to 2.1%, for region IM10 it is ∼7%. The overall uncertainty for the inclusive signal region is dominated by the precision of the lowest $\not{E}_T$-bins and amounts to 2.1%. In Fig. 8.12 (and Tab. 8.7), one can observe that the total background is dominated by $Z(\nu\nu)$+jets production. Its contribution varies from $\sim$ 51% in EM1 to $\sim$ 72% in IM10. The second largest background contribution stems from $W(\tau\nu)$+jets production and varies from $\sim$ 24% (EM1) to $\sim$ 11% (IM10). The third largest background is $W(\mu\nu)$+jets production with $\sim$ 9% contribution in EM1 and $\sim$ 8% in IM10. While the diboson background increases from $\sim$ 1.5% (EM1) to $\sim$ 5.8% (IM10), the $W(e\nu)$+jets contribution decreases from $\sim$ 9.6% (EM1) down to 3.1% (IM10). The contribution from top-quark production varies from $\sim$ 3.7% (EM1) down to $\sim$ 0.4% (IM10). All other

background contributions remain at less than 1% level. For illustration purposes, three signal hypotheses are overlayed on the $\not{E}_T$-distribution in Fig. 8.12. They are specific models of ADD, DM and SUSY sbottom production in compressed scenarios. The chosen hypotheses all exhibit an enhanced tail for high $\not{E}_T$. These models will be discussed further in Chap. 9.
Before discussing the agreement between the data and the SM prediction after the fit, the uncertainties and the individual systematic sources that contribute to the total background uncertainties will be discussed next.

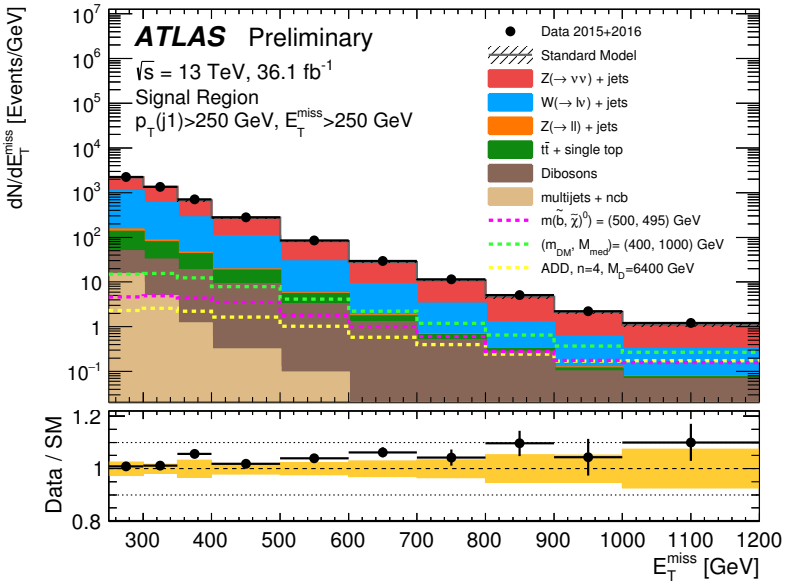

Fig. 8.12: Fitted $\not{E}_T$-distribution in the signal region after performing the background-only fit. The black dots are the data. The yellow area corresponds to the total background uncertainty. For illustration, three signal hypotheses are drawn on top: sbottom production with $(m_{\tilde{b}}, m_{\tilde{\chi}^0}) = (500, 495)$ GeV, DM production with $(m_\chi, M_{\text{med}}) = (400, 1000)$ GeV and ADD extra dimensions with $n = 4$ and $M_D = 6400$ GeV.

8.1.4 Impact of Individual Uncertainties

The total systematic uncertainty on the background is evaluated via the employment of the various nuisance parameters which are included as penalty terms as described in Eq. 7.17. The fitted values have been already presented in Tab. 8.2 and discussed. In order to determine the actual impact of individual uncertainties on the total background uncertainty, the background-only fit is repeated as follows: one nuisance parameter at a time is shifted by its initial standard deviation 1σ up and 1σ down and is then fixed, i.e. it is not fitted. All other nuisance parameters are fitted. The final impact is obtained by evaluating the difference in the total background yield in the SR between the different configurations. The impact on the yields in the fully inclusive region IM1 are illustrated in Fig. 8.13. It shows the pre-fit impacts along with the post-fit impacts evaluated as outlined above. The systematic sources are ranked in order of their post-fit impact where the largest impact is displayed in the far left. The pre-fit lines are centered around 0, the post-fit values can be shifted due to the pull of the respective nuisance parameter. The largest pre-fit impacts stem from the theory uncertainty vjets_d1K_NLO accounting for uniform QCD scale variations (7.3%) and the one accounting for non-uniform scale variations (4.5%, vjets_d2K_NLO). The luminosity has an impact of 3.2% pre-fit. Further

Signal region	EM1	EM2	EM3	EM4	EM5
Observed	111203	67475	35285	27843	8583
Fitted Background	111100 ± 2300	67100 ± 1400	33820 ± 940	27640 ± 610	8360 ± 190
$Z \to \nu\nu$+jets	56600 ± 1400	37600 ± 970	19940 ± 510	17070 ± 460	5450 ± 140
$W \to \tau\nu$+jets	25990 ± 590	13680 ± 310	6060 ± 490	4900 ± 110	1303 ± 35
$W \to \mu\nu$+jets	10420 ± 270	6120 ± 200	2940 ± 120	2021 ± 82	534 ± 22
$W \to e\nu$+jets	10710 ± 280	5510 ± 140	2656 ± 97	1789 ± 59	532 ± 23
$Z/\gamma^* \to \tau\tau$+jets	475 ± 20	185 ± 6	95 ± 4	68 ± 4	16 ± 1
$Z/\gamma^* \to \mu\mu$+jets	329 ± 12	167 ± 8	71 ± 4	35 ± 2	6.9 ± 0.5
$Z/\gamma^* \to ee$+jets	0.06 ± 0.02	0.03 ± 0	0 ± 0	0 ± 0	0 ± 0
$t\bar{t}$+single top	4100 ± 380	2230 ± 200	1140 ± 110	848 ± 86	203 ± 23
Dibosons	1700 ± 130	1327 ± 90	859 ± 57	874 ± 46	306 ± 29
multijet	490 ± 490	170 ± 160	30 ± 30	13 ± 13	5 ± 5
non-collision	240 ± 240	71 ± 71	29 ± 29	18 ± 18	4 ± 4
Data/SM	1.0	1.01	1.04	1.01	1.03

Signal region	EM6	EM7	EM8	EM9	IM10
Observed	2975	1142	512	223	245
Fitted Background	2825 ± 78	1094 ± 33	463 ± 19	213 ± 9	226 ± 16
$Z \to \nu\nu$+jets	1933 ± 57	773 ± 26	337 ± 12	153 ± 7	162 ± 12
$W \to \tau\nu$+jets	397 ± 11	149 ± 5	55 ± 5	29 ± 2	24 ± 2
$W \to \mu\nu$+jets	173 ± 9	79 ± 8	21 ± 5	11 ± 1	18 ± 2
$W \to e\nu$+jets	147 ± 9	25 ± 4	18 ± 1	8 ± 1	7 ± 1
$Z/\gamma^* \to \tau\tau$+jets	5.1 ± 0.3	2.5 ± 0.3	0.3 ± 0.1	0.31 ± 0.04	0.5 ± 0.1
$Z/\gamma^* \to \mu\mu$+jets	2.0 ± 0.2	0.8 ± 0.2	0.4 ± 0.1	0.5 ± 0.1	0.2 ± 0.1
$Z/\gamma^* \to ee$+jets	0 ± 0	0 ± 0	0 ± 0	0 ± 0	0 ± 0
$t\bar{t}$+single top	43 ± 6	15 ± 3	4 ± 1	1.3 ± 0.4	1 ± 1
Dibosons	124 ± 16	49 ± 8	26 ± 5	10 ± 2	13 ± 4
multijet	1 ± 1	1 ± 1	1 ± 1	0.1 ± 0.1	0.1 ± 0.1
non-collision	0 ± 0	0 ± 0	0 ± 0	0 ± 0	0 ± 0
Data/SM	1.05	1.04	1.11	1.05	1.08

Tab. 8.7: Data event yields in the exclusive signal regions compared to the total fitted yield of all considered background contributions. The uncertainty on the background prediction includes all systematic and statistical uncertainties after the background-only fit. The ratio Data/SM denotes the ratio of observed events over predicted events post-fit.

notable pre-fit influences stem from the PDF uncertainty, the JES uncertainty and the theoretical uncertainty on the top-quark production. After the fit, all these uncertainties are reduced significantly. Instead, the muon ID efficiency uncertainty becomes the dominant uncertainty with an overall impact of ∼2%. The following uncertainty is the electron ID efficiency uncertainty with a post-fit impact of 1.2%. Other major uncertainties are contributed by the pileup reweighting uncertainty, the uncertainties on parton shower modelling, the c-jet rejection efficiency, $\not{E}_T$ soft-track resolution and scale and the theory uncertainty on non-uniform QCD scale variations. The contributions of the systematic uncertainties can be examined in exclusive regions of $\not{E}_T$, which are looked at in some detail in the following. The tables in Tab. 8.8, 8.9 and 8.10 show the resulting impact of each nuisance parameter on the SR yield for EM1, EM5 and IM10, respectively. The dominant impacts in EM1 stem from the uncertainty on the muon

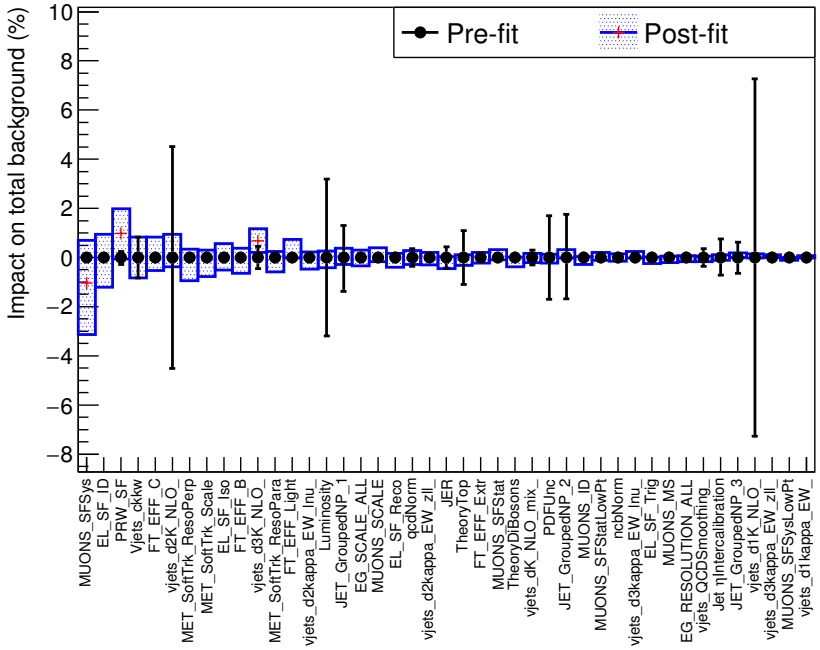

Fig. 8.13: Impact of individual systematic sources on the total background yield in the IM1 SR from a CR-only shape fit. The impacts are ranked in order of the largest post-fit impact (blue boxes). The pre-fit impacts are displayed as black data points centered at 0 and an error corresponding to the impact.

(2%) and electron identification ($\sim$ 1%), pileup reweighting ($\sim$ 1.3%) and $\not{E}_T$ soft term measurement ($\sim$ 0.86%). The impact of the V+jets theory uncertainties is largely reduced after the fit, amounting in total to about 1.1%. All other individual nuisance parameters exhibit an impact on the EM1 SR yield of less than 0.5%. Amongst them are the JES nuisance parameters and the luminosity nuisance parameter which are constrained by the background-only fit. In the region EM5 ($500 < \not{E}_T < 600$ GeV), the impact of the V+jets theory uncertainties reaches up to $\sim$ 1.6%, while the impact of the electron identification uncertainty increases slightly to 1.2%. The dominant individual uncertainty remains the muon identification (2.6%). Uncertainties related to b-tagging are also propagated into the signal region amounting to $\sim$ 0.9% in EM5. The impact of the individual sources on the highest region in $\not{E}_T$ is shown in Tab. 8.10. Here, the dominant impact stems from the `QCDSmoothing` uncertainty, which was assigned after correcting the MC to the theory NLO prediction suffering from limited MC statistics in the region above $\not{E}_T \sim 1$ TeV. Its pre-fit impact in this region was 9% and is reduced to around 6% after the fit. The muon ID efficiency uncertainty is at the level of 3.9%. Further major impacts are attributed to the JER, pileup reweighting, JES, PDF, $\not{E}_T$-resolution uncertainties and uncertainties on the EW theory correction, whose impacts range from 2%-3%. Those exhibited a considerable pre-fit impact in this region as well. The total uncertainty on the yields in IM10 is about 7%. Thus we can note, that the total uncertainty in the high $\not{E}_T$-regions is increased w. r. t. the low $\not{E}_T$-regions not only due to the increased statistical uncertainty but also due to theoretical and experimental uncertainties. Since, as seen in Fig. 8.2, various nuisance parameters are correlated among each other we can not simply add the individual contributions to obtain the total background uncertainty. The uncertainties related to lepton identification

and energy measurements remain a dominant component after the fit since these do not cancel out in the signal region. Furthermore, the pileup reweighting uncertainty and $\not{E}_T$ soft term uncertainty play an important role in an environment of multiple parton interactions producing dominantly jets that can enter the SR selection. However, with the chosen analysis strategy we are able to obtain total uncertainties on the background in the range of 2%-7% with increasing $\not{E}_T$.

In Fig. 8.12, the mentioned total uncertainties on the background are displayed as the yellow band in the ratio panel. In five of the 10 regions defined in $\not{E}_T$, the data agrees with the background prediction within one standard deviation of the background. The data lies always slightly above the predicted background, which is evident by looking at the ratio of Data/SM prediction after the fit which is also shown in Tab. 8.2. In the regions EM6 and EM8 the data even overshoots the prediction by about 1.9σ (EM6) and 2.6σ (EM8). The deviation is calculated via (data−SM fitted background)/total background uncertainty. In all other cases the deviation is below 1.9σ, mostly around 1σ. A good agreement is observed for the first two bins EM1 (0.04σ) and EM2 (0.27σ), where prediction and data agree well within 1σ . The goodness of the background-only fit when compared to data will be discussed in the next section.

Systematic Source	SR EM1 impact [%]
Total background uncertainty	2.1%
alpha_EG_RESOLUTION_ALL	(+0.04, +0.18)
alpha_EG_SCALE_ALL	(+0.41, −0.26)
alpha_EL_SF_ID	(−1.09, +1.13)
alpha_EL_SF_Iso	(−0.04, +0.03)
alpha_EL_SF_Reco	(−0.13, +0.16)
alpha_EL_SF_Trig	(−0.08, +0.10)
alpha_FT_EFF_B	(+0.08, −0.26)
alpha_FT_EFF_C	(+0.23, −0.28)
alpha_FT_EFF_Extr	(+0.02, −0.03)
alpha_FT_EFF_Light	(+0.02, −0.07)
alpha_JER	(+0.30, −0.38)
alpha_JET_EtaIntercalibration	(−0.01, +0.25)
alpha_JET_GroupedNP_1	(−0.44, +0.62)
alpha_JET_GroupedNP_2	(+0.48, −0.09)
alpha_JET_GroupedNP_3	(+0.50, +0.09)
alpha_Luminosity	(+0.19, −0.24)
alpha_MET_SoftTrk_ResoPara	(−0.58, +0.46)
alpha_MET_SoftTrk_ResoPerp	(−0.50, +0.36)
alpha_MET_SoftTrk_Scale	(−0.38, +0.58)
alpha_MUON_ID	(−0.15, −0.45)
alpha_MUON_MS	(−0.23, +0.19)
alpha_MUON_SCALE	(+0.04, −0.11)
alpha_MUON_SFStat	(−0.14, +0.26)
alpha_MUON_SFStatLowPt	(+0.01, −0.00)
alpha_MUON_SFSys	(−1.75, +1.98)
alpha_MUON_SFSysLowPt	(+0.01, +0.03)
alpha_PDFUnc	(+0.15, −0.45)
alpha_PRW_SF	(+1.27, −1.33)
alpha_TheoryDiBosons	(−0.09, +0.48)
alpha_TheoryTop	(+0.49, −0.44)
alpha_vjets_ckkw	(−0.75, +0.75)
alpha_vjets_QCDSmoothing	(−0.48, +0.30)
alpha_vjets_d1K_NLO	(−0.01, −0.06)
alpha_vjets_d1kappa_EW	(−0.21, −0.01)
alpha_vjets_d2K_NLO	(+0.61, −0.21)
alpha_vjets_d2kappa_EW_lnu	(−0.09, +0.02)
alpha_vjets_d2kappa_EW_zll	(+0.20, −0.23)
alpha_vjets_d3K_NLO	(−1.07, +0.01)
alpha_vjets_d3kappa_EW_lnu	(+0.15, −0.19)
alpha_vjets_d3kappa_EW_zll	(+0.15, −0.21)
alpha_vjets_dK_NLO_mix	(−0.07, −0.24)
alpha_qcdNorm	(−0.44, +0.44)
alpha_ncbNorm	(−0.22, +0.22)

Tab. 8.8: Impact on the signal region yield in region EM1 ($250 < \not{E}_T < 300$ GeV) from the various systematic sources included as nuisance parameters in the fit. The first value is the relative variation of the SR yield implied by a -1σ variation of the source, the second the one from a $+1\sigma$ variation. A negative value implies a downward variation of the SR yield.

Systematic Source	SR EM5 impact [%]
Total background uncertainty	2.24%
alpha_EG_RESOLUTION_ALL	(+0.04, +0.02)
alpha_EG_SCALE_ALL	(+0.35, −0.28)
alpha_EL_SF_ID	(−1.33, +1.33)
alpha_EL_SF_Iso	(−0.50, +0.76)
alpha_EL_SF_Reco	(−0.21, +0.12)
alpha_EL_SF_Trig	(−0.03, +0.03)
alpha_FT_EFF_B	(+0.72, −0.56)
alpha_FT_EFF_C	(+0.81, −0.53)
alpha_FT_EFF_Extr	(+0.14, −0.17)
alpha_FT_EFF_Light	(+0.08, −0.17)
alpha_JER	(+0.17, +0.07)
alpha_JET_EtaIntercalibration	(+0.56, +0.16)
alpha_JET_GroupedNP_1	(+0.28, +0.21)
alpha_JET_GroupedNP_2	(+0.52, +0.30)
alpha_JET_GroupedNP_3	(+0.12, +0.30)
alpha_Luminosity	(+0.19, +0.15)
alpha_MET_SoftTrk_ResoPara	(−0.03, +0.34)
alpha_MET_SoftTrk_ResoPerp	(−0.25, +0.51)
alpha_MET_SoftTrk_Scale	(−0.19, +0.35)
alpha_MUON_ID	(+0.47, +0.03)
alpha_MUON_MS	(+0.28, +0.06)
alpha_MUON_SCALE	(−0.02, −0.07)
alpha_MUON_SFStat	(−0.19, +0.29)
alpha_MUON_SFStatLowPt	(−0.03, +0.00)
alpha_MUON_SFSys	(−2.40, +2.63)
alpha_MUON_SFSysLowPt	(+0.06, +0.07)
alpha_PDFUnc	(+0.03, −0.01)
alpha_PRW_SF	(+0.47, −0.18)
alpha_TheoryDiBosons	(−0.03, +0.50)
alpha_TheoryTop	(+0.01, +0.33)
alpha_vjets_ckkw	(−0.55, +0.55)
alpha_vjets_QCDSmoothing	(−0.29, +0.55)
alpha_vjets_d1K_NLO	(+0.13, +0.18)
alpha_vjets_d1kappa_EW	(+0.15, +0.08)
alpha_vjets_d2K_NLO	(+1.24, −0.28)
alpha_vjets_d2kappa_EW_lnu	(−0.56, +0.92)
alpha_vjets_d2kappa_EW_zll	(+0.53, −0.66)
alpha_vjets_d3K_NLO	(−0.61, −0.03)
alpha_vjets_d3kappa_EW_lnu	(+0.13, +0.09)
alpha_vjets_d3kappa_EW_zll	(+0.54, −0.55)
alpha_vjets_dK_NLO_mix	(−0.03, +0.17)
alpha_qcdNorm	(−0.06, +0.06)
alpha_ncbNorm	(−0.05, +0.05)

Tab. 8.9: Impact on the signal region yield in region EM5 ($500 < \not{E}_T < 600$ GeV) from the various systematic sources included as nuisance parameters in the fit. The first value is the relative variation of the SR yield implied by a -1σ variation of the source, the second the one from a $+1\sigma$ variation. A negative value implies a downward variation of the SR yield.

Systematic Source	SR IM10 impact [%]
Total background uncertainty	7%
alpha_EG_RESOLUTION_ALL	(−0.03, +0.02)
alpha_EG_SCALE_ALL	(+0.47, −0.41)
alpha_EL_SF_ID	(−1.74, +0.76)
alpha_EL_SF_Iso	(−1.65, +0.15)
alpha_EL_SF_Reco	(−0.17, +0.08)
alpha_EL_SF_Trig	(−0.12, +0.14)
alpha_FT_EFF_B	(−1.02, −0.90)
alpha_FT_EFF_C	(−1.43, −0.30)
alpha_FT_EFF_Extr	(+0.48, −0.62)
alpha_FT_EFF_Light	(+0.18, −0.35)
alpha_JER	(+1.81, −3.74)
alpha_JET_EtaIntercalibration	(−1.72, −0.06)
alpha_JET_GroupedNP_1	(−2.46, +1.55)
alpha_JET_GroupedNP_2	(+0.89, −1.23)
alpha_JET_GroupedNP_3	(+1.07, −1.64)
alpha_Luminosity	(+0.24, −1.19)
alpha_MET_SoftTrk_ResoPara	(−1.95, +0.14)
alpha_MET_SoftTrk_ResoPerp	(−0.51, −0.56)
alpha_MET_SoftTrk_Scale	(−0.54, +0.79)
alpha_MUON_ID	(−0.29, −1.86)
alpha_MUON_MS	(−1.41, +0.03)
alpha_MUON_SCALE	(+0.15, −0.02)
alpha_MUON_SFStat	(−0.19, +0.22)
alpha_MUON_SFStatLowPt	(+0.15, −0.06)
alpha_MUON_SFSys	(−3.58, +3.97)
alpha_MUON_SFSysLowPt	(+0.05, −0.06)
alpha_PDFUnc	(+1.29, −2.92)
alpha_PRW_SF	(+1.46, −2.78)
alpha_TheoryDiBosons	(+1.02, −0.89)
alpha_TheoryTop	(−0.62, −1.86)
alpha_vjets_ckkw	(−0.65, +0.65)
alpha_vjets_QCDSmoothing	(+5.02, −6.14)
alpha_vjets_d1K_NLO	(−0.05, −1.29)
alpha_vjets_d1kappa_EW	(−1.53, −0.04)
alpha_vjets_d2K_NLO	(−0.05, −0.21)
alpha_vjets_d2kappa_EW_lnu	(−1.04, +0.38)
alpha_vjets_d2kappa_EW_zll	(+1.15, −1.42)
alpha_vjets_d3K_NLO	(−1.53, +0.03)
alpha_vjets_d3kappa_EW_lnu	(−1.52, +0.08)
alpha_vjets_d3kappa_EW_zll	(+1.34, −1.28)
alpha_vjets_dK_NLO_mix	(−0.08, −1.27)
alpha_qcdNorm	(−0.05, +0.05)
alpha_ncbNorm	(+0.00, +0.00)

Tab. 8.10: Impact on the signal region yield in region IM10 ($\not{E}_T > 1$ TeV) from the various systematic sources included as nuisance parameters in the fit. The first value is the relative variation of the SR yield implied by a -1σ variation of the source, the second the one from a $+1\sigma$ variation. A negative value implies a downward variation of the SR yield.

8.2 Goodness of Fit

The data yields in the signal region have been compared with the background prediction following the background-only fit in Sec. 8.1.3. Table 8.7 and Fig. 8.12 show the results. We want to focus on the ratio data/SM: Figure 8.14 shows the ratio where both statistical uncertainty of the data and the total uncertainty of the SM prediction are taken into account when drawing the data points in the ratio. We observe three bins in which the agreement between data and SM prediction is not reached within the uncertainties. Overall, there seems to be an upward trend in this ratio. We want to quantify the agreement or disagreement between data and SM

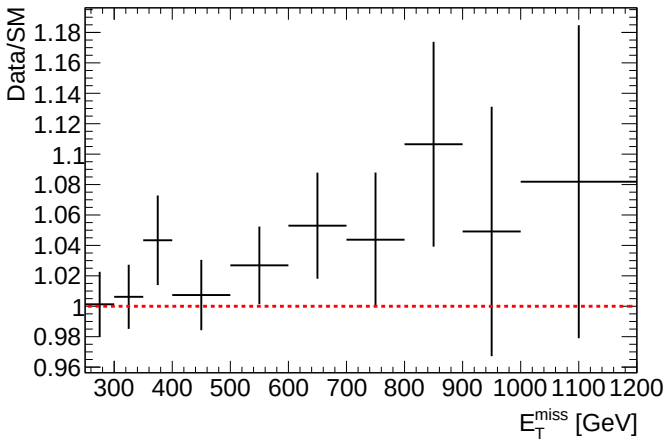

Fig. 8.14: Ratio of data events over predicted background in the inclusive signal region after the background-only fit has been performed.

by computing the probability that a background fluctuation is capable of explaining the data, meaning we set a null hypothesis that assumes the background-only model is true. In Sec. 7.7.5, the statistical procedure for the hypothesis testing has been described in cases where one seeks to falsify the background+signal hypothesis in order to set exclusion limits. This requires a signal strength μ_{sig} to be present in the profile likelihood (see Eq. 7.19). Thus, the computation of p_b always requires a signal hypothesis. If we want to calculate a background-only probability without a signal hypothesis we can compute a χ^2 probability. The χ^2 in that case is calculated via:

$$\chi^2 = \sum_{j=1}^{M} \frac{(d_j - t_j(\alpha))^2}{\Delta d_j^2 + \Delta t_j(\alpha)^2} + \sum_{p=1}^{A} \alpha_p^2, \tag{8.1}$$

where d_j denotes the measured data in bins j ($M = 10$) and $t_j(\alpha)$ the background prediction post-fit, after minimising the negative log-likelihood taking uncertainties as nuisance parameters α into account The uncertainties on the data and the background prediction are expressed as Δd_j and $\Delta t_j(\alpha)$, respectively. The second term in Eq. 8.1 sums over all nuisance parameters with their fitted values α_p (A =number of nuisance parameters). The underlying assumption is that these are independent and correlated across all bins in $\not{E}_T$. This formula takes into account the adjustment of nuisance parameters to better describe the data and is derived from the penalty term in the likelihood (Eq. 7.17). With the inputs from Tab. 8.7 and Tab. 8.2 the computed χ^2 is ≈ 22. Considering the SR with 10 bins, the number of degrees of freedom is 9.

This implies a probability to measure a χ^2 at least as high as the computed value of $p = 0.88\%$. We can consider this number as a simplified background probability without the assumption of a certain μ_{sig}. This probability can be transformed into a significance z:

$$z = \Phi^{-1}(1 - p), \tag{8.2}$$

where Φ^{-1} is the inverse of the cumulative distribution of the Gaussian with mean 0 and $\sigma = 1$. The observed significance of the data excess in this fit configuration is thus 2.37σ. This level of disagreement is not significant enough to falsify the background-only hypothesis and therefore it can be concluded that there is no significant excess and the data is in agreement with the background prediction. A more sophisticated discussion of the background probability employing the full profile likelihood in a SR+CR fit is presented in Sec. 9.4.

8.2.1 Post-Fit Distributions: Signal Region

A further check of the compatibility of the data in the signal region and the background predictions is the comparison of other distributions than the fitted $\not{E}_T$. In Fig. 8.15 and Fig. 8.16, post-fit distributions for the signal region are shown. Overall good agreement between data and background prediction can be observed. There is a slight asymmetry in the leading jet η distribution (Fig. 8.15(a)). This is likely to be connected with the lepton η mismodelling in the CRs. Furthermore, there is a slight deficit of data for high H_T at around 1.4 TeV (Fig. 8.15(f)). There are around 1100 events measured in this region, which have a higher jet multiplicity than the bulk of the data. The deficit appears for low $\not{E}_T$-events and events containing four jets. Thus, this deficit is likely related to the jet multiplicity mismodelling, which has already been discussed and is also apparent from Fig. 8.15(d).
To illustrate the sensitivity to the considered BSM models, three example signal predictions are drawn as dashed lines. They are one dark matter signal with a mediator mass of 1 TeV and a DM mass of $m_\chi = 400$ GeV. Another signal hypothesis shown is for ADD extra dimensions with $n = 4$ and $M_D = 6400$ GeV. The third signal sample displayed corresponds to sbottom pair production with $m_{\tilde{b}} = 500$ GeV and $m_{\tilde{\chi}} = 495$ GeV. These samples show a similar behaviour in all distributions and are particularly enhanced over the background for high values of $\not{E}_T$, i. e. the distributions do not fall as steeply with increasing $\not{E}_T$ as the background does (see Fig. 8.12). The monojet analysis is potentially sensitive to these signal hypothesis that will be discussed in Chap. 9.

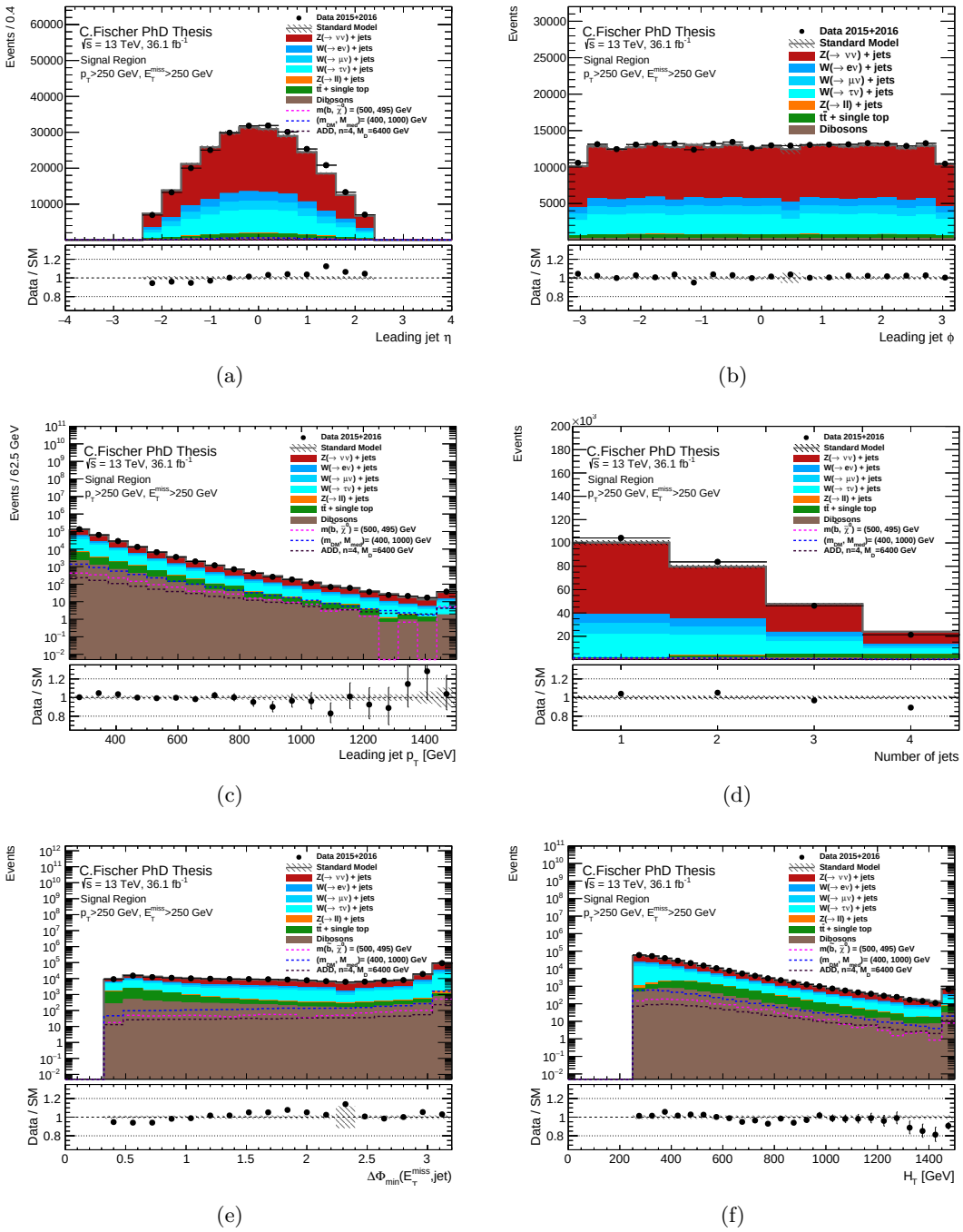

Fig. 8.15: Post-fit distributions in the signal region for IM1. The data is shown as black dots, the total background prediction as the grey histogram. The hashed uncertainty band includes all experimental and theoretical uncertainties after the fit. The lower panels show the ratio of data over SM prediction after the fit. Three examples of signal distributions are drawn on top as dashed lines.

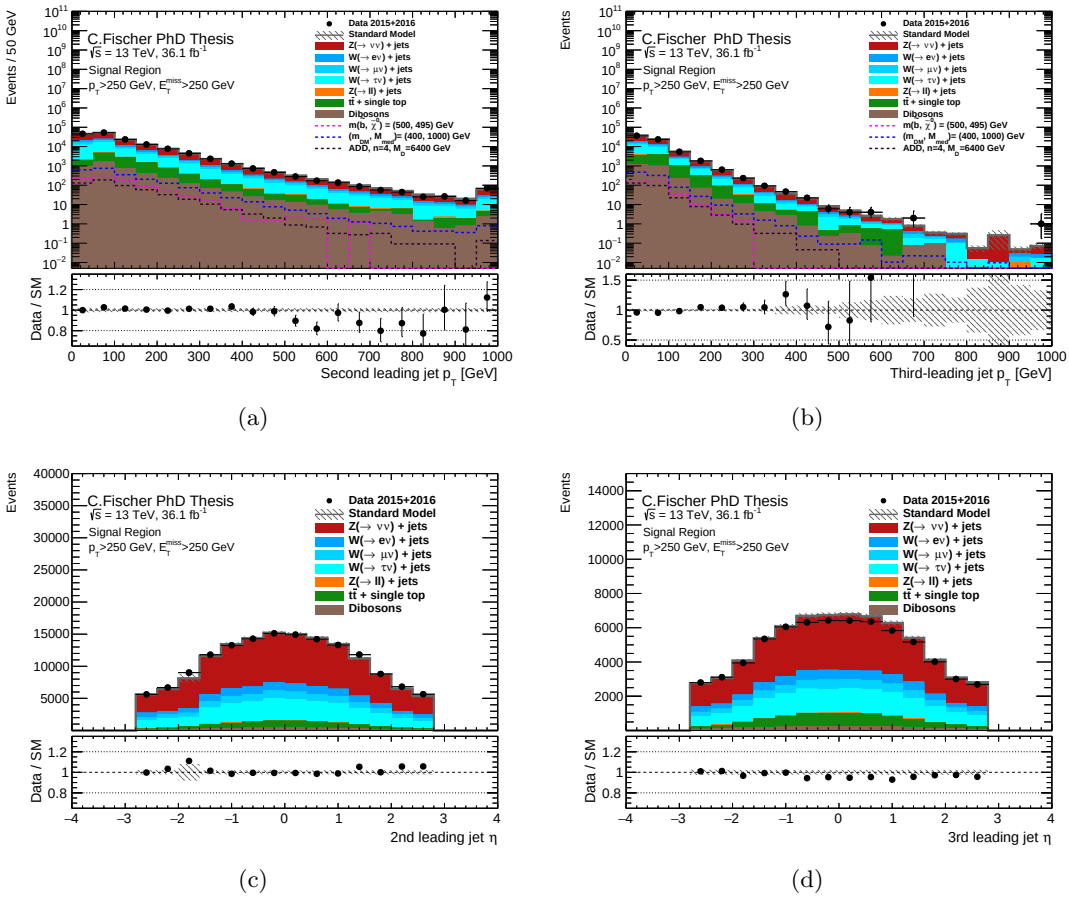

Fig. 8.16: Post-fit distributions in the signal region for IM1. The data is shown as black dots, the total background prediction as the grey histogram. The hashed uncertainty band includes all experimental and theoretical uncertainties after the fit. The lower panels show the ratio of data over SM prediction after the fit.

8.3 Model-Independent Limits

As explained in Sec. 7.7.4, the fit configuration has to be changed to an inclusive setup in order to obtain model-independent upper limits on the cross section. This means that the fit is performed simultaneously in all control regions and the signal region for the regions IM1-IM10. For each of these regions, a signal with 1 event[a] and 0 uncertainty is injected into the signal region and its signal strength μ_{sig} is fitted. The obtained 95% CL limit on μ_{sig} gives the maximum amount of events in addition to the background allowed. This number is denoted as S^{95}_{exp} for expected and S^{95}_{obs} for the observed limit. These numbers can be translated into a cross section limit: $\langle\sigma^{95}_{\text{obs}}\rangle = \sigma \times \mathcal{A} \times \varepsilon$ is called the visible cross section limit and is obtained by dividing S^{95} by the corresponding luminosity of the dataset. The acceptance of the signal in our signal regions IM1-IM10 is denoted as $\mathcal{A}$, the efficiency is called ε. The corresponding limits are presented in Tab. 8.11. As the lower cut on $\not{E}_T$ increases the visible cross section decreases naturally due to lower acceptance and efficiencies. While a visible cross section above 531 fb can be excluded in

[a] For regions with high event numbers such as IM1-IM4, the signal event number is chosen as 5000 events, for IM5-IM7 it is chosen to be 100, for IM8 and IM9 it is indeed 1 event and for IM10 it is 0.1 events. The fitted upper limits are consequently multiplied by these numbers.

region IM1, region IM10 only allows for visible cross sections below 1.6 fb to be compatible with the observation.

Region	$\langle\sigma^{95}_{\text{obs}}\rangle$ [fb]	S^{95}_{obs}	S^{95}_{exp}
IM1	531	19 135	$11\,737^{+4352}_{-3280}$
IM2	330	11 903	$6\,964.^{+2599}_{-1558}$
IM3	188	6 771	$3\,953^{+1407}_{-1104}$
IM4	93	3 344	$2\,099^{+771}_{-586}$
IM5	43	1 546	774^{+282}_{-216}
IM6	19	696	360^{+132}_{-101}
IM7	7.7	276	204^{+74}_{-57}
IM8	4.9	178	126^{+47}_{-35}
IM9	2.2	79	76^{+29}_{-21}
IM10	1.6	59	56^{+21}_{-16}

Tab. 8.11: Model-independent upper cross section limits at 95% CL: Ten inclusive regions are used and the limit is extracted in a control region and signal region fit taking all background systematics into account. The luminosity used is 36.1 fb^{-1}. The upper limit on the number of signal events is given by the third and fourth column for the observed and expected scenario.

Chapter 9

Interpretation

Chapter 8 presented the results from the simultaneous $\not{E}_T$-shape fit. In Sec. 8.2 it was concluded that the background model describes the data well and no significant excess has been observed. The procedure following is the interpretation of this agreement in terms of limits on various signal hypotheses. In Sec. 8.3, model-independent limits were presented for the results in the various inclusive regions IM1-IM10. Here, the result of the shape-fit is interpreted for specific models, namely ADD extra spatial dimensions, SUSY compressed scenarios and WIMP dark matter production via a light mediator (simplified model). For all the interpretations, a simultaneous fit in all control regions and signal regions is performed. The same background uncertainties are applied as nuisance parameters as for the model-independent fit. In addition, signal systematic uncertainties are applied as nuisance parameters to the signal prediction. They include experimental uncertainties as for the backgrounds plus theoretical uncertainties stemming from uncertainties related to the scale choice (renormalisation/factorisation), PDF sets used and parton shower modelling. The exclusion fit is performed where contours are drawn in the relevant parameter spaces corresponding to 95% CL limits for the signal strengths $\mu_{\text{sig}} = 1$. The specific models and relevant parameters will be introduced and the resulting limits are presented.

For all three signal scenarios, the event generation is briefly described followed by the signal specific systematic uncertainties taken into account in the analysis. The MC generation of all signal models utilises the ATLFAST II tool to perform the detector simulation.

First, the ADD model of large extra dimensions is discussed, followed by various types of SUSY compressed scenarios and closing with the search for dark matter in simplified models.

9.1 Extra Dimensions

9.1.1 Signal Modelling

Large extra spatial dimension processes are modelled in the ADD scenario. Events are generated with PYTHIA8 at LO. The PDF set used is NNPDF2.3, the underlying event and parton shower tune is A14. The renormalisation scale is set to $\mu_R^2 = (p_{T,G}^2 + m_G^2)(p_{T,p}^2 + m_p^2)$ and the factorisation scale is $\mu_F^2 = \min(p_{T,G}^2 + m_G^2, p_{T,p}^2 + m_p^2)$, where the subscript G denotes the graviton and the subscript p the parton produced in association (see Fig. 3.1 for LO graviton production diagrams). Five different samples have been generated: one sample for each number of extra dimensions from $n = 2$ to $n = 6$ and different M_D values. The values were chosen close to the exclusion limit in the Run 1 monojet analysis ($M_D = 5.25$ TeV for $n = 2$, $M_D = 3.06$ TeV for $n = 6$ [133]). The chosen values are listed in Tab. 9.1 along with two other parameters: the approximated central mass m_0 and the width Γ of the distribution of the KK graviton mass states. More details on the samples can be found in Ref. [161] and Ref. [162]. To ensure efficient

sampling of the phase space with high $\not{E}_T$, a cut on $\hat{p}_T > 150$ GeV is introduced at generator level, where $\hat{p}_T$ denotes the minimum transverse energy of graviton and parton. This implies a fully efficient sampling for $\not{E}_T \gtrsim 350$ GeV.

n	M_D [GeV]	m_0 [GeV]	Γ [GeV]
2	5300	800	750
3	4100	1500	1000
4	3600	2200	1100
5	3200	2200	1100
6	3000	3300	1300

Tab. 9.1: The five generated ADD signal samples with the parameters n, M_D, m_0 and Γ.

9.1.2 Signal Uncertainties

Besides the experimental uncertainties, theoretical uncertainties on the ADD signal samples are included as nuisance parameters in the model-dependent signal fit. The uncertainties are related to PDF uncertainties, scale choices and parton shower modelling.
The PDF uncertainties were evaluated for each of the five ADD signal samples for each region EM1-IM10. The intra-PDF uncertainty of the PDF sets NNPDF2.3, CT10 and MHT2014lo68cl as well as the inter-PDF uncertainties between those were evaluated following the PDF4LHC prescription [163]. The final PDF uncertainty is the envelope of the three PDF sets variations considered. The uncertainty ranges from 8% up to 32%, increasing for increasing $\not{E}_T$-regions.
The impact of a scale variation of renormalisation and factorisation scales is obtained by varying these by factors of 2 and 0.5. The result influences the overall cross section of the ADD samples. Therefore, an uncertainty in the range between 23% and 36% is considered, increasing with increasing n.
The parton shower settings controlling the underlying event, internal jet structure and emission of additional jets (ISR/FSR) are varied in ten different samples. A common envelope for all ADD samples constitutes the corresponding uncertainty that is evaluated as a function of the $\not{E}_T$-requirement. The uncertainty varies from 8% to 18%, independent of n.
In addition to these theoretical uncertainties, experimental uncertainties on the signal samples are considered. Their main constitution stems from JER, JES, pileup reweighting uncertainty and $\not{E}_T$ soft term related uncertainties. Depending on n the experimental uncertainty ranges from 0.6% to 1% in IM4 ($\not{E}_T > 400$ GeV). The luminosity uncertainty of 3.2% has to be added to this number. Since the phase space cut on $\hat{p}_T$ implies a fully efficient sampling above $\not{E}_T \approx 350$ GeV, only regions above $\not{E}_T = 400$ GeV are considered further on. This sampling cut has been chosen since the sensitivity to ADD samples is only given in the region with $\not{E}_T > 400$ GeV. The typical acceptance×efficiency ($\mathcal{A} \times \varepsilon$) in the signal region with $\not{E}_T > 400$ GeV is of the order of 13% ($n = 2$) to 17% ($n = 6$). For the highest inclusive region with $\not{E}_T > 1$ TeV, $\mathcal{A} \times \varepsilon$ is reduced to about 0.7%-1.4%.

9.1.3 Exclusion Limits

The 95% CL limits on the ADD models are extracted using a model-dependent signal fit as explained in Sec. 7.7.4. The regions below $\not{E}_T = 400$ GeV , namely EM1, EM2 and EM3, are excluded from the fit. The signal uncertainties are included as nuisance parameters in the fit.

The fitted signal strength μ_{sig} for each n is used to calculate the highest M_D value that can be excluded. According to Eq. 3.6 and demanding $\mu_{\text{sig}} < 1$ for exclusion the excluded $M_{D,\text{excl}}$ can be calculated as follows:

$$M_{D,\text{excl}} = \frac{M_D}{\mu_{\text{sig}}^{\frac{1}{n+2}}}, \tag{9.1}$$

where μ_{sig} is the fitted signal strength of the samples with input parameters n and M_D. The validity of the EFT model is evaluated by performing a *truncation* of the obtained limit on $M_{D,\text{excl}}$ for a given n. Therefore a truncation factor is derived depending on the transferred momentum $\hat{s}$ of the event:

$$k(M_D) = \begin{cases} 1 & \text{if} \quad \hat{s} < M_D^2, \\ M_D^4/\hat{s}^2 & \text{if} \quad \hat{s} \geq M_D^2. \end{cases}$$

This means, that events with $\hat{s} \geq M_D^2$ are still retained but weighed down by a factor of $M_D^4/\hat{s}^2$, which reduces the event yield of the EFT ADD prediction. The impact of the limited EFT validity is evaluated in an iterative truncation procedure, which is carried out in three distinct steps:

- step 1: production of a limit without truncation,
- step 2: truncation of signal yield in each $\not{E}_T$-bin according to $M_{D,\text{excl}}$ and repetition of limit setting,
- step 3: comparison of new $M_{D,\text{excl, new}}$ with previous limit:
  if $M_{D,\text{excl}} - M_{D,\text{excl,new}} > 0.1 \cdot \sigma_{\text{exp}}$: set $M_{D,\text{excl}} = M_{D,\text{excl,new}}$ and repeat step 2;
  if $M_{D,\text{excl}} - M_{D,\text{excl,new}} < 0.1 \cdot \sigma_{\text{exp}}$: stop, $M_{D,\text{excl, new}}$ is final truncated limit,

where σ_{exp} is the uncertainty on the expected limit. Following this procedure, a repetition of at most two times is needed for the convergence on the final $M_{D,\text{excl}}$. The procedure has converged after only one step for $n = 2$-5, and has to be repeated twice only for the case with $n = 6$. For the former, the truncated limit is identical to the untruncated limit. There is a reduction of the limit on $M_{D,\text{excl}}$ for $n = 6$ of about 2%. This implies a reasonable validity of the EFT in the probed phase space of the analysis. The final, truncated limit on M_D as a function of n is shown in Fig. 9.1 at the 95% CL. The dashed blue line indicates the expected limit, while the green band indicates the corresponding uncertainty of $\pm 1\sigma$, and the yellow band indicates the experimental uncertainty of $\pm 2\sigma$. The solid black line represents the observed limit. The dotted black lines around the observed limit are obtained by repeating the limit setting with the nominal cross section varied by its theoretical uncertainty, i.e. $\pm 1\sigma_{\text{theory}}$, that includes normalisation impacts of the scale and PDF variations. Values of up to 7.74 TeV can be excluded for $n = 2$. The limit on M_D decreases with increasing n due to the cross section scaling with $1/M_D^{n+2}$ (Eq. 3.6). At $n = 6$, values for M_D of below 4.77 TeV can be excluded. For reference, the limit obtained for the full 2015 dataset (Ref. [131]) is shown as well. A significant improvement w. r. t. the past analysis by increasing the limits by around $\sim$ 16%-17% is established. The exact values for the M_D limits are listed in Tab. 9.2. It can be noted that the central observed limit does not lie within the 1σ uncertainty band of the expected limit and is less strict than the expected limit. This behaviour is due to the fact that there are slightly more events observed in the SR than are predicted for the background yield. The observed limit is compatible within the 2σ uncertainty band of the expected limit.

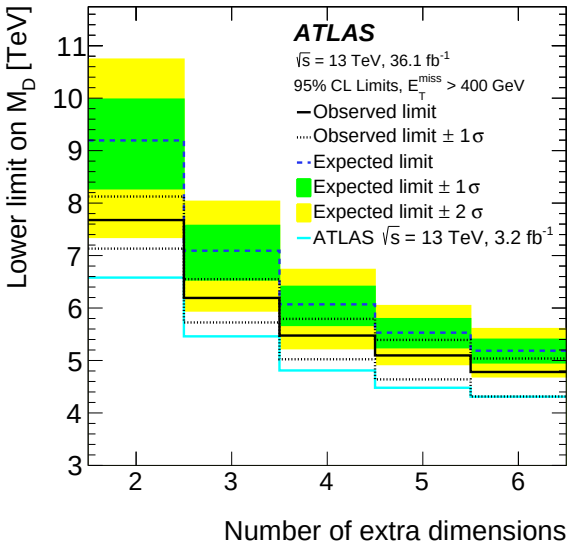

Fig. 9.1: Extracted 95% CL limit on M_D as a function of n. The truncated limit is shown. The dashed blue line corresponds to the expected limit, the solid black line to the observed limit. The dotted black lines show the impact on the observed limit if the cross section is varied by its theoretical uncertainty to $\pm 1\sigma$. The $\pm 1\sigma$ uncertainty on the measurement is shown as a green band around the expected limit, the yellow band represents the $\pm 2\sigma$ uncertainty. For comparison, the limit obtained with the full 2015 dataset is shown as well.

ADD Model	Expected [TeV]	Observed (truncated) [TeV]
$n = 2$	$9.27^{+0.79}_{-0.96}$	$7.74^{+0.45}_{-0.55}$ (7.74)
$n = 3$	$7.12^{+0.48}_{-0.59}$	$6.22^{+0.36}_{-0.47}$ (6.22)
$n = 4$	$6.09^{+0.34}_{-0.43}$	$5.49^{+0.32}_{-0.45}$ (5.49)
$n = 5$	$5.54^{+0.27}_{-0.32}$	$5.11^{+0.30}_{-0.46}$ (5.11)
$n = 6$	$5.20^{+0.22}_{-0.26}$	$4.79^{+0.26}_{-0.47}$ (4.77)

Tab. 9.2: Expected and observed 95% CL lower limits on the fundamental Planck scale M_D in $4+n$ dimensions as a function of the number of extra dimensions n. The impact of the $\pm 1\sigma$ uncertainty from the theory on the observed limits and the expected $\pm 1\sigma$ range of limits in absence of a signal is reported. The 95% CL observed limits after truncating the signal cross section for $\hat{s} > M_D^2$ are reported in parentheses.

9.2 Squark Production in Compressed Scenarios

9.2.1 Signal Modelling

Four different SUSY scenarios are considered in the analysis: (1) The production of light-flavour squarks and the subsequent decay: $\tilde{q} \to q + \tilde{\chi}_1^0$ with a 100% branching ratio and $q = u, d, s, c$. (2) The production of sbottom quarks with the subsequent decay $\tilde{b} \to b + \tilde{\chi}_1^0$ with a 100% branching ratio. (3) The production of stop quarks, where $\tilde{t} \to c + \tilde{\chi}_1^0$ with 100% BR is considered and (4) the decay $\tilde{t} \to b + ff' + \tilde{\chi}_1^0$ with 100% branching ratio is considered. The latter is called four-body decay.

All signal scenarios are generated with MadGraph+Pythia8. The CKKW-L scheme is employed for matching of different parton generations with the matching scale set to 1/4 of the squark mass. Simplified scenarios with tree-level diagrams are considered where diagrams including internal gluino lines are not accounted for in the ME calculation. The samples are generated with the A14 set of tuned parameters and with NNPDF2.3 as the PDF set. A $\not{E}_T$-filter was applied with a cut at 100 GeV. The cross sections are normalised to NLO accuracy in α_s and NLL accuracy for soft gluon resummation. The MEs contain up to 2 additional partons, depending on the process. The mass splitting between squark and neutralino is defined as $\Delta m = m_{\tilde{q}} - m_{\tilde{\chi}}$. Signal samples according to $\tilde{q} \to q + \tilde{\chi}_1^0$ are generated for squark masses ranging from 400 GeV up to 1 TeV and mass splittings of $\Delta m = 5, 15, 25$ GeV. The process $\tilde{b} \to b + \tilde{\chi}_1^0$ is simulated with sbottom masses between 250 GeV and 600 GeV with different mass splittings of which the smallest mass splitting is $\Delta m = 5$ GeV and the smallest neutralino mass considered is 1 GeV. The stop-pair production with $\tilde{t} \to c + \tilde{\chi}_1^0$ is generated with stop masses between 250 GeV and 600 GeV and neutralino masses between 195 GeV and 595 GeV where Δm always obeys the kinematic requirement for the stop-to-charm decay: $m_c < \Delta m < m_b + m_W$. The smallest mass splitting is $\Delta m = 5$ GeV. Finally, the decay $\tilde{t} \to b + ff' + \tilde{\chi}_1^0$ is generated with stop masses ranging from 250 GeV to 550 GeV and neutralino masses ranging from 200 GeV to 543 GeV, where the lowest Δm is 7 GeV and the highest Δm is 80 GeV. The corresponding Feynman diagrams have been introduced in Chap. 3, in Fig. 3.4.

9.2.2 Signal Uncertainties

Theoretical signal uncertainties on the squark production are evaluated similarly to the ADD samples. In this case, the theoretical uncertainties corresponding to PDF uncertainties, uncertainties on the scale choice and parton shower modelling are included in a single additional nuisance parameter. The theoretical uncertainty is evaluated as a function of the $\not{E}_T$ requirement. It yields very similar impacts for all considered signal points and thus exhibits a rather mild dependence on the squark and neutralino mass. The theoretical signal uncertainty ranges from 13% in the low $\not{E}_T$-region up to 23% at very high $\not{E}_T$. The experimental uncertainties stem from JES, JER, pileup reweighting and $\not{E}_T$ related uncertainties. For light squark production the impact is about 2% on the signal yield. For sbottom and stop production the impact ranges from 1% to 3% depending on the squark mass. Samples of the four-body decay mode show uncertainties up to at most 6%.
The typical $\mathcal{A} \times \varepsilon$ of the various SUSY models range from 3% up to 45% in the SR IM1. The highest acceptances being reached for the case of sbottom pair production with high $m_{\tilde{b}}$ and high mass splitting. The acceptance decreases with increasing $\not{E}_T$-cut to 1%-8% for $\not{E}_T > 700$ GeV down to 0.002%-1.3% for IM10 with $\not{E}_T >1$ TeV, dependent on the squark flavour and mass.

9.2.3 Exclusion Limits

The 95% CL limits on SUSY squark pair production is obtained from the control region and signal region shape fit in all ten bins of $\not{E}_T$. For each available signal point, μ_{sig} is computed. Via interpolation between signal strengths for different mass points the contour corresponding to $\mu_{\text{sig}} = 1$ is extracted in a plane of $m_{\tilde{\chi}_1^0}$ versus $m_{\tilde{b}/\tilde{t}}$. This contour is the 95% CL limit. In the case of light squark production, the exclusion contour is drawn in the plane of Δm versus $m_{\tilde{q}}$. For all scenarios, the uncertainty on the cross section is indicated as a $\pm 1\sigma$ band around the observed limit (dotted black lines). These $\pm 1\sigma$ observed contours are obtained by re-performing the signal fit with varied cross sections by $\pm 1\sigma^{\text{theory}}$, respectively. The theoretical cross section uncertainties are around 13%. The limits on Δm vs. $m_{\tilde{q}}$ are shown in Fig. 9.2 at 95% CL limit.

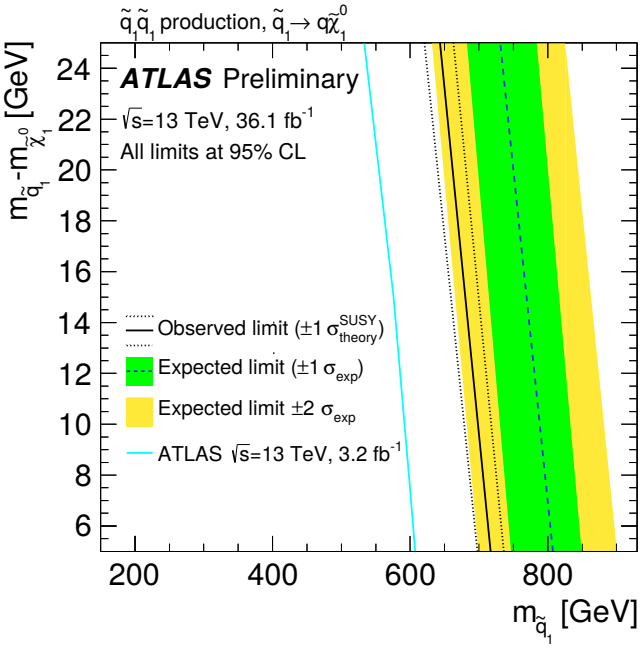

Fig. 9.2: 95% CL limit on squark-pair production with $\tilde{q} \to q + \tilde{\chi}_1^0$ 100% BR and $q = u, d, s, c$. The area left of the dashed blue (solid black) line is excluded by the expected (observed) limit. The green and yellow bands represent the $\pm 1\sigma$ and $\pm 2\sigma$ uncertainties on the measurement. The dotted black lines correspond to the theoretical cross section uncertainties drawn around the observed value. The limit obtained with a dataset of 3.2 fb^{-1} is displayed as well [131].

The blue dashed line corresponds to the expected limit with the green band indicating the $\pm 1\sigma$ experimental uncertainty. The $\pm 2\sigma$ band is shown in yellow as well. The black solid line shows the observed limit. For $\Delta m = 5$ GeV values of up to $m_{\tilde{q}} \sim 710$ GeV can be excluded. In the case of $\Delta m = 25$ GeV the exclusion reaches up to masses of 640 GeV. For comparison, the results presented in [131] for 3.2 fb^{-1} are shown as well (light blue) and the limits could be extended by about 100 GeV for both $\Delta m = 5$ GeV and $\Delta m = 25$ GeV. Also here we observe that the observed limit is weaker than the expected limit, in this case by about 90 GeV in $m_{\tilde{q}}$. Thus, the central observed value is not contained in the 1σ band of the expected value, rather it is contained within 2σ, due to the underprediction of the SR event yields.
The sbottom pair production limit is presented in the plane $m_{\tilde{\chi}_1^0}$ versus $m_{\tilde{b}}$ in Fig. 9.3. The region enclosed by the contours is excluded at 95% CL. Close to the diagonal ($m_{\tilde{\chi}_1^0} = m_{\tilde{b}}$) the excluded sbottom mass reaches up to around 430 GeV. It thus superseeds former results by about 100 GeV. The monojet analysis is also able to exclude mass points up to 610 GeV for low neutralino masses around several GeV where the mass splitting Δm is large. The sensitivity to these signal hypotheses far away from the diagonal (i. e. no compressed scenario given) can be explained in the following way: samples with low $m_{\tilde{\chi}_1^0}$ tend to produce more jets than can be reconstructed in the detector (many low energetic jets). These jets recoil against the neutralinos and therefore produce larger $\not{E}_T$. Such events with a higher jet multiplicity are selected in the monojet analysis since up to four jets are allowed. This region with large Δm is however already excluded by the dedicated sbottom search analysis [164]. Again, we can observe that the observed limits are less strict than the expected by a margin of about 70-80 GeV. The observed contour is contained within 2σ of the expected exclusion limit.

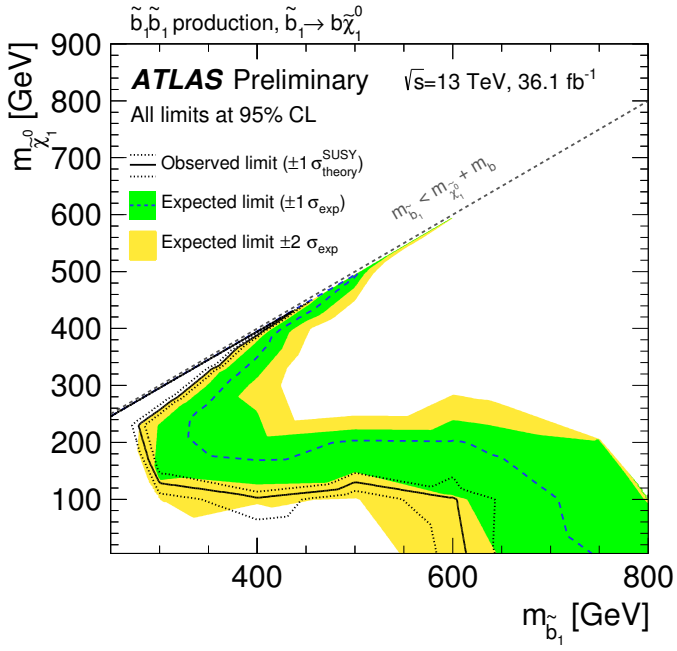

Fig. 9.3: 95% CL limit on sbottom-pair production with $\tilde{b} \rightarrow b + \tilde{\chi}_1^0$ 100% BR. The area enclosed by the dashed blue (solid black) line is excluded by the expected (observed) limit. Experimental uncertainties corresponding to $\pm 1\sigma$ and $\pm 2\sigma$ are shown as the green and yellow bands, respectively. The impact of the theoretical cross section uncertainty is shown as the dotted curves around the observed limit.

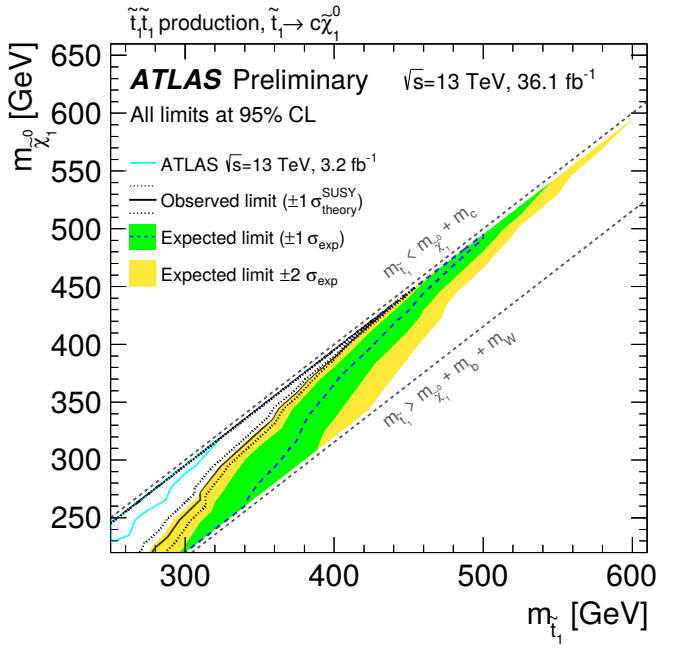

Fig. 9.4: 95% CL limit on stop-pair production with a 100% BR to $\tilde{t} \rightarrow c + \tilde{\chi}_1^0$. The area enclosed by the dashed blue (solid black) line is excluded by the expected (observed) limit. Experimental uncertainties corresponding to $\pm 1\sigma$ and $\pm 2\sigma$ are shown as the green and yellow bands, respectively. The impact of the theoretical cross section uncertainty is shown as the dotted curves around the observed limit. The limit obtained with 3.2 fb^{-1} of data is shown as well [131].

The exclusion contour for stop pair production with $\tilde{t} \to c + \tilde{\chi}_1^0$ is shown in Fig. 9.4. The allowed region for these decays is indicated by the grey dashed lines. The enclosed region is excluded at 95% CL limit. Similarly to the sbottom sensitivity, the observed limit reaches up to about 430 GeV in stop mass at the diagonal with $\Delta m = 5$ GeV. The exclusion achieved by the 2015 analysis is displayed in light blue. A significant extension of these limits has been achieved with this analysis extending the reach by about 100 GeV. The same observations regarding the relation of observed and expected limit is obtained here.

Limits on stop pair production and a subsequent decay to $\tilde{t} \to bff' + \tilde{\chi}_1^0$ are presented in

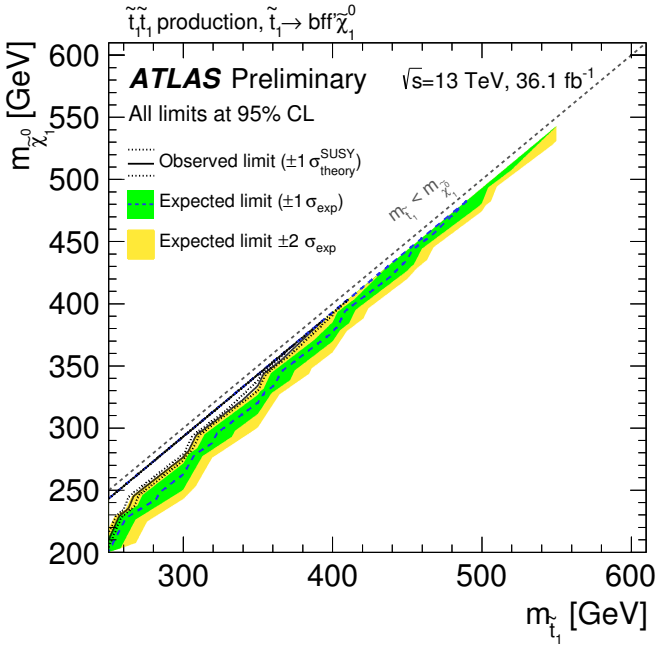

Fig. 9.5: 95% CL limit on stop-pair production with a 100% BR to $\tilde{t} \to bff' + \tilde{\chi}_1^0$. The area enclosed by the dashed blue (solid black) line is excluded by the expected (observed) limit. Experimental uncertainties corresponding to $\pm 1\sigma$ and $\pm 2\sigma$ are shown as the green and yellow bands, respectively. The impact of the theoretical cross section uncertainty is shown as the dotted curves around the observed limit.

Fig. 9.5 at 95% CL. As expected, the exclusion power close to the diagonal is similar to the stop-to-charm and sbottom-to-bottom scenarios, albeit slightly reduced due to higher experimental uncertainties, reaching $m_{\tilde{t}} \approx 390$ GeV. The exclusion power decreases rapidly for higher mass splittings. A previous limit on this scenario was set using Run 1 data and reached up to 280 GeV close to the diagonal [131]. Thus, the presented limit extends the reach by more than 100 GeV close to the diagonal. The observed limit is contained within the 2σ uncertainty of the expected limit.

9.3 Dark Matter Production

9.3.1 Signal Modelling

We focus on the dark matter production via an s-channel mediator exchange in the context of simplified models. A corresponding Feynman diagram has been introduced in Sec. 3.3, Fig. 3.7(b). WIMP production with an additional parton in the ME is generated with POWHEG-

BOXv2 [165] at NLO precision. The PDF set is NNPDF30nlo. PYTHIA8 and the A14 tune are used for the parton shower with the NNPDF23lo. The mediator has an axial-vector coupling to SM and DM particles with spin-1. The mediator width is modelled with a Breit-Wigner distribution. At generation level, a phase space cut is applied which leads to fully efficient sampling for $\not{E}_T > 250$ GeV. The renormalisation and factorisation scales are set to $H_T/2$ on an event-by-event basis, where H_T is defined as $H_T = \sqrt{m^2_{\chi\chi} + p^2_{T,j1}} + p_{T,1}$. The transverse momentum of the leading jet is $p_{T,j1}$ and the invariant mass of the WIMP pair is $m_{\chi\chi}$. The couplings chosen are $g_q = 0.25$ and $g_\chi = 1$. These values ensure the validity of the narrow width approximation and suppress a strong interplay between monojet and dijet constraints. WIMP masses are generated between 1 GeV and 1 TeV. Mediator masses range from 10 GeV to 10 TeV (the latter being useful for EFT interpretation). The different mass points in the m_χ-m_A grid generated are mostly in the off-shell regime ($m_A < 2m_\chi$). Further signal points in the on-shell regime are generated at truth level for the cross section calculation. The acceptance of the monojet analysis has been verified to be constant for a given mediator mass. The acceptances range for different dark matter and mediator mass combinations between $\sim 6\%$ and $\sim 30\%$ for $\not{E}_T > 250$ GeV. For higher $\not{E}_T$-cuts of up to 1 TeV the $\mathcal{A} \times \varepsilon$ decreases to 0.03-1.1%, depending on the particle masses.

9.3.2 Signal Uncertainties

The same uncertainties as for ADD and SUSY production are considered here and evaluated in a similar manner. Additional theory uncertainties enter the signal fit as individual nuisance parameters. To account for the uncertainty on the renormalisation and factorisation scale choice a flat 3% uncertainty is applied in all regions for all samples. The PDF uncertainty amounts to 20% for samples with $m_\chi < 100$ GeV or $m_\chi > 1$ TeV. All other samples assume a PDF uncertainty of 10%. Uncertainties on parton shower modelling are taken into account as a flat 20% uncertainty for all signal points. The usual experimental uncertainties are relevant for the signals: JER, JES, pileup reweighting and $\not{E}_T$-uncertainties have an impact of around 1-3% on the signal region yields.

9.3.3 Exclusion Limits

The exclusion contour is obtained in a plane of m_χ vs. m_A. The on-shell signal strength limits are obtained by rescaling the fitted μ_{sig} of the points with $m_\chi = 1$ GeV and different mediator masses. The rescaling uses the cross sections provided by the truth MC samples: $\mu_{\text{rescaled}} = \mu_{\text{sig}} \cdot \sigma_1/\sigma_X$, where σ_1 denotes the cross section for $m_\chi = 1$ GeV samples to which μ_{sig} corresponds and σ_X denotes the cross section with a varied WIMP mass $m_\chi = X$ GeV, but same mediator mass m_A. The final result in terms of 95% CL limits is shown in Fig. 9.6. As usual, expected and observed exclusion contours are drawn along with their uncertainties. The grey hashed area indicates the phase space that violates perturbative unitary ($m_\chi > \sqrt{\pi/2} m_A$ [166]). In addition, the line corresponding to models predicting the correct relic dark matter density as measured by the WMAP and Planck satellites [48, 167] is shown as the red curve. Models above this curve would predict an under-production of dark matter, and likewise an overproduction is expected below this curve. The observed exclusion crosses the red line at about $m_A \sim 1.1$ TeV and $m_\chi \sim 400$ GeV. For low dark matter masses, mediator masses up to 1.55 TeV can be excluded. Most of the excluded area lies in the on-shell regime. The limit extends slightly into the off-shell regime for low mediator masses below 200 GeV. The monojet analysis loses sensitivity to off-shell scenarios due to the kinematically suppressed decay. The maximum

excluded WIMP mass is about 440 GeV, corresponding to a mediator mass of around 1.2 TeV. This is also where the relic density curve crosses the observed limit. These limits extend the 2015 limits obtained by ATLAS by about 500 GeV in mediator mass at low m_χ and about 150 GeV in dark matter mass for mediator masses of ∼1 TeV. As in all other discussed limit plots, the observed limit is weaker than the expected by more than 1σ, but within 2σ reach. The limit in

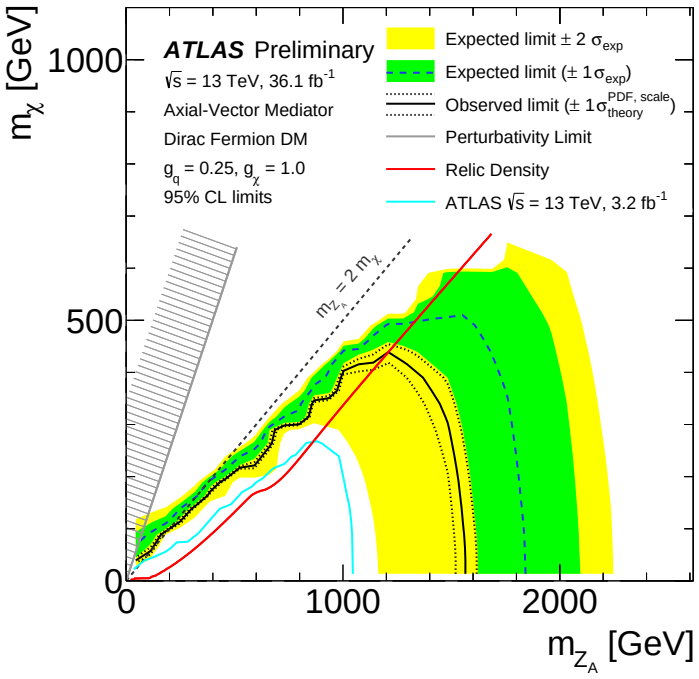

Fig. 9.6: 95% CL limit on WIMP pair production via an axial-vector mediator. The couplings $g_q = 0.25$ and $g_\chi = 1$ are used. The area below the dashed blue (solid black) line is excluded by the expected (observed) limit. Experimental uncertainties corresponding to $\pm 1\sigma$ and $\pm 2\sigma$ are shown as the green and yellow bands, respectively. The impact of the theoretical cross section uncertainty is shown as the dotted curves around the observed limit. Additionally, the red curve corresponds to the models predicting the correct relic dark matter density [168]. The hashed area indicates the perturbativity violating phase space. The light blue curve shows the limit obtained with 3.2 fb^{-1} data [131].

the m_χ-m_A plane can be translated into a WIMP-nucleon scattering cross section limit. This is done by using the relation as discussed in Ref. [169]:

$$\sigma_{\text{SD}} = 2.4 \cdot 10^{-41}\ \text{cm}^2 \cdot \left(\frac{g_\chi g_q}{0.25}\right)^2 \cdot \left(\frac{1\ \text{TeV}}{m_A}\right)^4 \cdot \left(\frac{\mu_{n\chi}}{1\ \text{GeV}}\right)^2, \tag{9.2}$$

where σ_{SD} denotes the spin dependent WIMP-nucleon scattering cross section and $\mu_{n\chi}$ is the reduced WIMP-nucleon mass $\mu_{n\chi} = \frac{m_\chi m_n}{m_\chi + m_n}$, where m_n is either the mass of the proton or neutron. The derivation of the WIMP-nucleon scattering cross section limit as a function of the WIMP mass allows for a comparison of the collider sensitivity to WIMP production with the ones from dedicated direct detection search experiments. Therefore, the limits are derived at 90% CL as is conveniently done in direct detection search results. The results are compared in Fig. 9.7 for scattering with neutrons (a) and protons (b). The limit obtained by the monojet analysis excludes scattering cross sections above 2.9×10^{-43} cm^2 (3.3×10^{-43} cm^2) for WIMP masses

below 10 GeV (400 GeV), identically in both interactions with protons and neutrons (given the assumption that the mediator nucleon coupling is the same for all quarks). Beyond 400 GeV, this analysis is not able to establish lower limits on the scattering cross sections. In this regime of WIMP masses, the direct detection experiments are more sensitive. Below 400 GeV however, the monojet analysis shows stronger sensitivity. It is important to note that the results obtained here are vastly model-dependent, while the direct detection searches are rather model-independent.

Alternative interpretations for WIMP dark matter models with a t-channel mediator or an s-channel pseudo-scalar mediator are briefly discussed in the Appendix, in Sec. A.2.

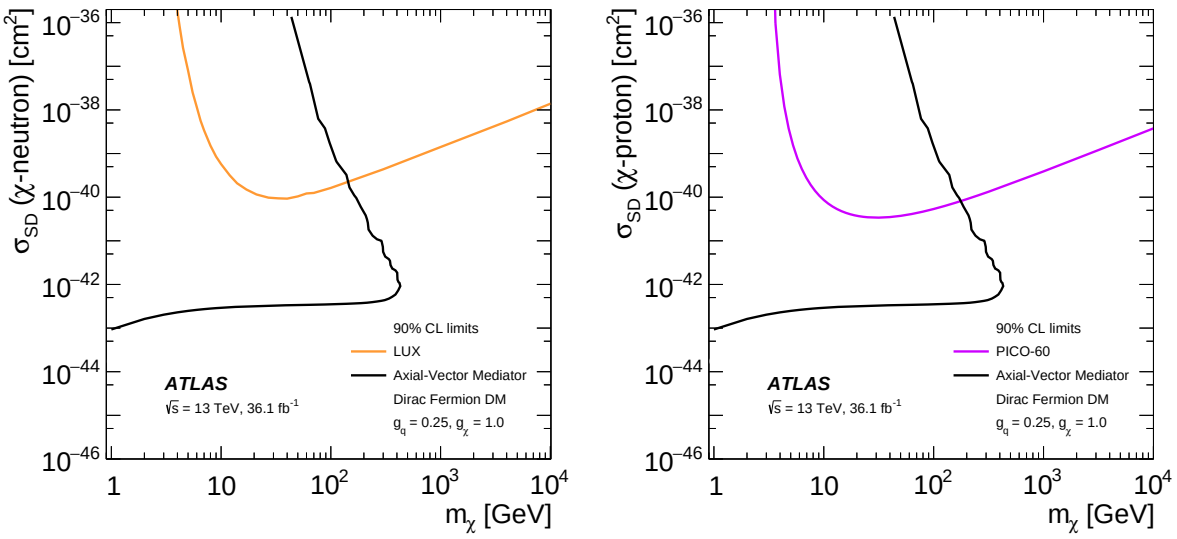

(a) (b)

Fig. 9.7: Observed 90% CL limit exclusion contour in the plane of WIMP-nucleon scattering cross section versus WIMP mass: (a) the nucleon is a neutron, (b) the nucleon is a proton. The regions above the curves are excluded. A comparison is shown with direct detection experiments: PICO [137] for the scattering with protons and Lux [52] for the scattering with neutrons.

9.4 Background Probability and Discovery Potential

In Sec. 8.2, it was anticipated that the background probability p_b can only be calculated under an alternative hypothesis of a specific model, since $\not{E}_T$-shape information is used. In this chapter, exclusion limits on several BSM models were presented with the notion that the observed limits are not within 1σ of the expected limits. To quantify the actual probability that the background-only hypothesis explains the data, the p_b is calculated using the profile likelihood and a μ_{sig} as predicted by a subset of the analysed models. The convention in high-energy physics searches is to claim evidence for new particles/processes if the significance (as calculated in Eq. 8.2) exceeds 3σ, corresponding to a background probability of $\sim 0.135\%$. If the background probability falls below 3×10^{-7} then a discovery is claimed, corresponding to a significance of 5σ. Table 9.3 lists the computed probabilities and significances for various models of WIMP production and SUSY squark production. Various different mass points were chosen that cover a wide phase space of

the respective models. While the probabilities computed from the full profile likelihood often fall below 5% we see that the significances vary mostly between 1σ and 2σ, at most 2.4σ. Thus, there is no evidence yet for the existence of new particles that could explain the data overshoot.

Signal	p_b	$z_b[\sigma]$
Dark Matter (axial-vector mediator)		
$(m_\chi, m_A) = (1, 10\,000)$ GeV	0.062	1.54
$(m_\chi, m_A) = (1, 1\,000)$ GeV	0.042	1.73
$(m_\chi, m_A) = (1, 2\,000)$ GeV	0.086	1.37
$(m_\chi, m_A) = (1, 2\,250)$ GeV	0.077	1.42
$(m_\chi, m_A) = (1, 1\,750)$ GeV	0.031	1.86
$(m_\chi, m_A) = (200, 10\,000)$ GeV	0.068	1.49
$(m_\chi, m_A) = (250, 10\,000)$ GeV	0.068	1.49
$(m_\chi, m_A) = (250, 10)$ GeV	0.040	1.75
$(m_\chi, m_A) = (250, 400)$ GeV	0.042	1.73
$(m_\chi, m_A) = (255, 500)$ GeV	0.035	1.81
$(m_\chi, m_A) = (300, 10\,000)$ GeV	0.072	1.46
$(m_\chi, m_A) = (500, 700)$ GeV	0.071	1.47
$(m_\chi, m_A) = (50, 10\,000)$ GeV	0.071	1.47
$(m_\chi, m_A) = (50, 10)$ GeV	0.043	1.71
$(m_\chi, m_A) = (50, 20)$ GeV	0.047	1.67
Sbottom Pair-Production		
$(m_{\tilde{b}}, m_{\tilde{\chi}^0}) = (300, 295)$ GeV	0.014	2.20
$(m_{\tilde{b}}, m_{\tilde{\chi}^0}) = (300, 280)$ GeV	0.013	2.21
$(m_{\tilde{b}}, m_{\tilde{\chi}^0}) = (800, 1)$ GeV	0.049	1.64
$(m_{\tilde{b}}, m_{\tilde{\chi}^0}) = (600, 300)$ GeV	0.043	1.71
$(m_{\tilde{b}}, m_{\tilde{\chi}^0}) = (600, 595)$ GeV	0.042	1.73
$(m_{\tilde{b}}, m_{\tilde{\chi}^0}) = (500, 400)$ GeV	0.012	2.25
$(m_{\tilde{b}}, m_{\tilde{\chi}^0}) = (400, 1)$ GeV	0.023	1.99
$(m_{\tilde{b}}, m_{\tilde{\chi}^0}) = (300, 150)$ GeV	0.103	1.27
$(m_{\tilde{b}}, m_{\tilde{\chi}^0}) = (300, 100)$ GeV	0.219	0.78
$(m_{\tilde{b}}, m_{\tilde{\chi}^0}) = (450, 400)$ GeV	0.008	2.43
$(m_{\tilde{b}}, m_{\tilde{\chi}^0}) = (450, 430)$ GeV	0.023	2.00
$(m_{\tilde{b}}, m_{\tilde{\chi}^0}) = (450, 445)$ GeV	0.020	2.05
$(m_{\tilde{b}}, m_{\tilde{\chi}^0}) = (500, 495)$ GeV	0.038	1.77
$(m_{\tilde{b}}, m_{\tilde{\chi}^0}) = (550, 545)$ GeV	0.026	1.94
Light-flavour Squark Pair-Production		
$(m_{\tilde{q}}, m_{\tilde{\chi}^0}) = (600, 575)$ GeV	0.019	2.09
$(m_{\tilde{q}}, m_{\tilde{\chi}^0}) = (600, 585)$ GeV	0.033	1.84
$(m_{\tilde{q}}, m_{\tilde{\chi}^0}) = (600, 595)$ GeV	0.026	1.94
$(m_{\tilde{q}}, m_{\tilde{\chi}^0}) = (650, 625)$ GeV	0.027	1.92
$(m_{\tilde{q}}, m_{\tilde{\chi}^0}) = (650, 635)$ GeV	0.036	1.80
$(m_{\tilde{q}}, m_{\tilde{\chi}^0}) = (650, 645)$ GeV	0.042	1.73
$(m_{\tilde{q}}, m_{\tilde{\chi}^0}) = (700, 675)$ GeV	0.034	1.83
$(m_{\tilde{q}}, m_{\tilde{\chi}^0}) = (700, 685)$ GeV	0.031	1.86
$(m_{\tilde{q}}, m_{\tilde{\chi}^0}) = (700, 695)$ GeV	0.042	1.73
$(m_{\tilde{q}}, m_{\tilde{\chi}^0}) = (780, 795)$ GeV	0.050	1.65

Tab. 9.3: Results for p_b and z_b for some of the signal models used for model-dependent interpretations. Dark matter production, compressed sbottom pair production and light-flavour squark production signal points with given masses are considered as benchmarks.

Signal	p_b	$z_b[\sigma]$
$(m_{\tilde{b}}, m_{\tilde{\chi}^0}) = (500, 495)$ GeV	0.011	2.29
$(m_{\tilde{t}}, m_{\tilde{\chi}^0}) = (450, 425)$ GeV $(\tilde{t} \to c + \tilde{\chi}_1^0)$	0.049	1.65
$(m_{\tilde{q}}, m_{\tilde{\chi}^0}) = (800, 795)$ GeV	0.012	2.25
$(m_{\tilde{t}}, m_{\tilde{\chi}^0}) = (400, 393)$ GeV $(\tilde{t} \to b + f f' + \tilde{\chi}_1^0)$	0.028	1.91

Tab. 9.4: Expected p_b and z_b for four different signal hypotheses using pseudo-data, where the respective signal prediction has been added to the background-only prediction post-fit to form the pseudo-data.

To determine the discovery potential of the monojet analysis, a test with pseudo-data can be performed, where the pseudo-data is constructed by adding a certain signal prediction to the background prediction post-fit. The background probabilities are then calculated as was done before with the actual data. Signal hypotheses have been chosen that are not yet excluded by the observations presented in this chapter. Table 9.4 shows the corresponding results for four different scenarios of compressed SUSY squark pair-production. The computed background probabilities lie in a similar range as the results for the real data fit. In conclusion, we can say that the analysis is not yet sensitive to the four models tested here where the expected significance of at most 2.3σ lies well below the 3σ-threshold to claim an evidence, even if the signal was actually present. With the dataset at hand we are not able to falsify the background-only hypothesis nor the signal+background hypothesis.

Chapter 10

Summary and Conclusion

The monojet analysis carried out with the full 2015 and 2016 datasets as recorded by ATLAS with a centre-of-mass energy of $\sqrt{s} = 13$ TeV corresponding to an integrated luminosity of 36.1 fb^{-1} has been presented in this thesis. The monojet search is aimed at a variety of theories beyond the SM predicting additional particles. The monojet search is interpreted in terms of models of ADD large extra spatial dimensions, SUSY production in compressed scenarios and WIMP dark matter production via the exchange of an s-channel axial-vector mediator. The analysis strategy is based on a simultaneous shape fit to the $\not{E}_T$-distribution in control regions and signal region via the profile likelihood method. Four control regions are defined and aimed at constraining the dominant backgrounds and their uncertainties stemming from V+jets production and top-quark production. The $\not{E}_T$-distribution is divided into ten bins, where the lowest $\not{E}_T$ requirement is $\not{E}_T > 250$ GeV and the highest requirement is $\not{E}_T > 1$ TeV. The control regions are defined utilising a $\not{E}_T$-definition including either muons or electrons as invisible in order to resemble the boson-p_T distribution of the respective backgrounds. All V+jets backgrounds are reweighted in boson-p_T to NLO precision in QCD and NNLO precision in EW prediction. Correlations between different processes are thereby taken into account as well as theoretical uncertainties. This benefits the understanding of the dominant $Z(\nu\nu)$+jets background that can be thus estimated via the other V+jets backgrounds that are fitted in the control regions. The observed data is in agreement with the SM background prediction after the fit. Model-independent limits are presented for ten inclusive regions and exclude visible cross sections from 531 fb ($\not{E}_T > 250$ GeV) down to 1.6 fb ($\not{E}_T > 1$ TeV). The agreement between data and SM prediction is translated into model-dependent limits on ADD extra dimension, SUSY compressed scenarios and WIMP dark matter production for simplified models. Existing limits from previous ATLAS analyses have been improved by 15% to 30%. The limits on ADD extra dimensions reach up to 7.74 TeV for $n = 2$ and 4.77 TeV for $n = 6$. Limits on light squark production reach up to 710 GeV for the lowest mass splitting between squark mass and neutralino mass. The sbottom and stop production reaches limits in this compressed scenario of around 430 GeV (sbottom production, stop production with subsequent decay to a charm quark and a neutralino) and 390 GeV (stop production with four-body decay mode). These limits improve pre-existing ATLAS limits by about 100 GeV in the squark mass. Finally, the limits on the mediator vs. dark matter mass-plane for the s-channel axial-vector mediator exchange extends the reach to $m_A \approx 1.55$ TeV for low dark matter mass. The maximal dark matter mass that can be excluded is $m_\chi \sim 440$ GeV for mediator masses of around 1.2 TeV. The limits can be translated into cross section limits on WIMP-nucleon scattering to provide a complementary sensitivity to direct detection searches. The monojet search provides a unique exclusion power for dark matter masses below 400 GeV in a spin-dependent WIMP-nucleon interaction.

In context with other ATLAS SUSY searches the monojet search offers a unique sensitivity in cases where the squark and neutralino mass are almost degenerate. The current limit on sbottom pair production set by ATLAS [164] exhibits a gap close to the diagonal that can be partly filled by the results of this analysis.

At the moment of concluding this thesis, the results are about to be submitted for publication in the Journal of High Energy Physics (JHEP).

The monojet analysis continues to be a powerful search for BSM physics for a large variety of models. The analysis sensitivity has not only improved due to the increased dataset. A major improvement stems from including higher-order theory predictions in QCD and EW calculation which allow a good understanding of the correlation between V+jets involving charged-leptonic decays and the dominant $Z(\nu\nu)$+jets process. Further possible optimisations include NNLO QCD predictions and the inclusion of a γ+jets control region and higher MC statistical precision. With more data accumulated over the next years, the analysis will be able to explore higher $\not{E}_T$-regions. In this regime, the inclusion of a γ+jets background will decrease the uncertainty on the background prediction due to its statistical power.
An increased dataset and a further refined analysis strategy promise to give further insights on the existence of new particles at the TeV-scale.

Appendix A

Additional Material/Studies

A.1 Event Yields After CR-only Fit

The following tables show the event yields in the regions EM2, EM3, EM4, EM6, EM7 and EM8 after the fit for all control regions.

Region	CR1e	CR1m	CR2m	CRtop
Observed events	18047	29454	4627	2587
Post-fit SM prediction	18209 ± 98	29540 ± 130	4694 ± 43	2543 ± 31
$Z \to \nu\nu$+jets	0.3 ± 0	12 ± 1	0 ± 0	1.9 ± 0.3
$W \to \tau\nu$+jets	1147 ± 28	1640 ± 31	1 ± 0.2	49 ± 7
$W \to \mu\nu$+jets	1 ± 1	25330 ± 210	6 ± 1	630 ± 110
$W \to e\nu$+jets	14480 ± 180	3 ± 1	0 ± 0	0.2 ± 0.1
$Z/\gamma^* \to \tau\tau$+jets	49 ± 3	76 ± 4	7 ± 3	4 ± 1
$Z/\gamma^* \to \mu\mu$+jets	0 ± 0	481 ± 11	4435 ± 45	20 ± 3
$Z/\gamma^* \to ee$+jets	3 ± 1	0 ± 0	0 ± 0	0 ± 0
$t\bar{t}$ +single top	2050 ± 170	1230 ± 150	120 ± 10	1810 ± 120
Dibosons	487 ± 34	770 ± 58	125 ± 9	27 ± 4

Tab. A.1: Event yields after the fit in all control regions for 300 GeV $< \not{E}_T <$ 350 GeV corresponding to 36.1 fb^{-1}. The uncertainties include statistical and systematic uncertainties after the fit.

Region	CR1e	CR1m	CR2m	CRtop
Observed events	11079	16249	2664	1556
Post-fit SM prediction	10946 ± 73	15927 ± 93	2624 ± 23	1536 ± 27
$Z \to \nu\nu$+jets	0.2 ± 0.1	4 ± 0.2	0 ± 0	0.2 ± 0.2
$W \to \tau\nu$+jets	631 ± 19	856 ± 19	$0.3^{+0.4}_{-0.3}$	28 ± 4
$W \to \mu\nu$+jets	2.5 ± 0.4	13520 ± 120	2.7 ± 0.4	371 ± 48
$W \to e\nu$+jets	8590 ± 130	1 ± 1	0 ± 0	0 ± 0
$Z/\gamma^* \to \tau\tau$+jets	44 ± 3	34 ± 2	0.9 ± 0.3	2 ± 0.3
$Z/\gamma^* \to \mu\mu$+jets	0.1 ± 0	233 ± 6	2456 ± 25	10 ± 1
$Z/\gamma^* \to ee$+jets	0.5 ± 0.5	0 ± 0	0 ± 0	0 ± 0
$t\bar{t}$ +single top	1340 ± 110	717 ± 94	69 ± 6	1109 ± 72
Dibosons	345 ± 24	559 ± 39	95 ± 7	16 ± 3

Tab. A.2: Event yields after the fit in all control regions for 350 GeV $< \not{E}_T <$ 400 GeV corresponding to 36.1 fb^{-1}. The uncertainties include statistical and systematic uncertainties after the fit.

Region	CR1e	CR1m	CR2m	CRtop
Observed events	9947	13859	2246	1293
Post-fit SM prediction	9980 ± 68	13955 ± 81	2212 ± 21	1377 ± 23
$Z \to \nu\nu$+jets	0.2 ± 0	4.3 ± 0.3	0 ± 0	0.3 ± 0.1
$W \to \tau\nu$+jets	580 ± 15	785 ± 23	0.0 ± 0.0	35 ± 5
$W \to \mu\nu$+jets	0.3 ± 0.2	11730 ± 120	4 ± 0.4	354 ± 52
$W \to e\nu$+jets	7680 ± 110	0.3 ± 0	0 ± 0	0 ± 0
$Z/\gamma^* \to \tau\tau$+jets	35 ± 2	29 ± 2	1.7 ± 0.1	1 ± 0.3
$Z/\gamma^* \to \mu\mu$+jets	0.2 ± 0	163 ± 4	2064 ± 22	7 ± 1
$Z/\gamma^* \to ee$+jets	$0.2^{+0.2}_{-0.2}$	0 ± 0	0 ± 0	0 ± 0
$t\bar{t}$ +single top	1290 ± 110	639 ± 84	54 ± 5	949 ± 66
Dibosons	391 ± 29	603 ± 42	88 ± 6	30 ± 8

Tab. A.3: Event yields after the fit in all control regions for 400 GeV $< \not{E}_T <$ 500 GeV corresponding to 36.1 fb^{-1}. The uncertainties include statistical and systematic uncertainties after the fit.

Region	CR1e	CR1m	CR2m	CRtop
Observed events	1251	1543	213	144
Post-fit SM prediction	1219 ± 17	1564 ± 20	247 ± 6	128 ± 6
$Z \to \nu\nu$+jets	0.1 ± 0	0.2 ± 0.1	0 ± 0	0 ± 0
$W \to \tau\nu$+jets	79 ± 3	80 ± 5	0 ± 0	5 ± 1
$W \to \mu\nu$+jets	$-0.2^{+0.1}_{-0.2}$	1305 ± 23	0 ± 0	54 ± 7
$W \to e\nu$+jets	935 ± 19	0 ± 0	0 ± 0	0 ± 0
$Z/\gamma^* \to \tau\tau$+jets	2.8 ± 0.3	4.9 ± 0.3	0.1 ± 0	0 ± 0
$Z/\gamma^* \to \mu\mu$+jets	0 ± 0	15 ± 1	222 ± 5	0.7 ± 0.1
$Z/\gamma^* \to ee$+jets	0 ± 0	0 ± 0	0 ± 0	0 ± 0
$t\bar{t}$ +single top	122 ± 15	60 ± 10	1 ± 1	65 ± 7
Dibosons	80 ± 8	99 ± 10	24 ± 3	4 ± 1

Tab. A.4: Event yields after the fit in all control regions for 600 GeV $< \not{E}_T <$ 700 GeV corresponding to 36.1 fb^{-1}. The uncertainties include statistical and systematic uncertainties after the fit.

Region	CR1e	CR1m	CR2m	CRtop
Observed events	553	629	93	53
Post-fit SM prediction	535 ± 10	607 ± 11	89 ± 2	47 ± 4
$Z \to \nu\nu$+jets	0 ± 0	0.1 ± 0	0 ± 0	0 ± 0
$W \to \tau\nu$+jets	33 ± 1	45 ± 2	0 ± 0	2 ± 1
$W \to \mu\nu$+jets	0 ± 0	485 ± 10	0.1 ± 0	21 ± 3
$W \to e\nu$+jets	419 ± 11	0 ± 0	0 ± 0	0 ± 0
$Z/\gamma^* \to \tau\tau$+jets	1.6 ± 0.2	2.7 ± 0.2	0.2 ± 0.1	0.3 ± 0.3
$Z/\gamma^* \to \mu\mu$+jets	0 ± 0	5.2 ± 0.3	82 ± 2	0.2 ± 0.1
$Z/\gamma^* \to ee$+jets	0 ± 0	0 ± 0	0 ± 0	0 ± 0
$t\bar{t}$ +single top	44 ± 7	27 ± 5	0.6 ± 0.2	22 ± 3
Dibosons	38 ± 5	41 ± 4	6 ± 1	1.1 ± 0.3

Tab. A.5: Event yields after the fit in all control regions for 700 GeV $< \not{E}_T <$ 800 GeV corresponding to 36.1 fb^{-1}. The uncertainties include statistical and systematic uncertainties after the fit.

Region	CR1e	CR1m	CR2m	CRtop
Observed events	216	258	34	16
Post-fit SM prediction	212 ± 6	253 ± 5	37 ± 1	14 ± 2
$Z \to \nu\nu$+jets	0 ± 0	0.1 ± 0	0 ± 0	0 ± 0
$W \to \tau\nu$+jets	14 ± 1	18 ± 1	0 ± 0	0.7 ± 0.2
$W \to \mu\nu$+jets	0.1 ± 0	206 ± 5	0.2 ± 0	8 ± 1
$W \to e\nu$+jets	168 ± 7	0 ± 0	0 ± 0	0 ± 0
$Z/\gamma^* \to \tau\tau$+jets	0.6 ± 0.1	0.7 ± 0.1	0.1 ± 0	0 ± 0
$Z/\gamma^* \to \mu\mu$+jets	0 ± 0	3 ± 0.3	34 ± 1	0.1 ± 0.1
$Z/\gamma^* \to ee$+jets	0 ± 0	0 ± 0	0 ± 0	0 ± 0
$t\bar{t}$ +single top	14 ± 3	8 ± 2	0 ± 0	4 ± 1
Dibosons	15 ± 2	17 ± 3	2.8 ± 0.2	1.1 ± 0.4

Tab. A.6: Event yields after the fit in all control regions for 800 GeV $< \not{E}_T <$ 900 GeV corresponding to 36.1 fb^{-1}. The uncertainties include statistical and systematic uncertainties after the fit.

A.2 Limits on Alternative Dark Matter Models

Apart from the axial-vector mediated WIMP production, also alternative WIMP models have been regarded in the analysis. One of these is the already discussed t-channel production (see Sec. 3.3.3) with a hypothetical coloured scalar mediator. In this case, there is only one coupling g defined as the coupling of the mediator to both SM particles and WIMP particles (see Fig. 3.8 for interaction vertex). The respective signals were generated with $g = 1$. The 95% CL limit is shown in Fig. A.1 in the plane of dark matter mass vs. mediator mass, m_η. The mediator width becomes 0 for cases where the WIMP mass is higher than the mediator mass. The observed limit reaches up to 620 GeV in the case of $m_\chi = m_\eta$. For low WIMP masses, mediator masses of up to 1.67 TeV can be excluded.

Another model that has been studied is the pseudo-scalar mediated WIMP production. The analysis is not yet sensitive to this model in the sense that none of the space of the mass plane m_χ vs. M_P can be excluded (M_P =mediator mass). Therefore, only upper limits on the signal strength can be set. Figure A.2 shows the 95% CL upper limit on μ_{sig} as a function of the WIMP mass ((a), mediator mass fixed to 10 GeV) and the mediator mass M_P ((b), WIMP mass fixed to 1 GeV). Since these limits are above 1, no mass points can be excluded. The observed upper limit reaches down to $\mu_{\text{sig}} \sim 2$ for low WIMP and mediator masses. It remains flat as a function of M_P up to 300 GeV before the sensitivity decreases rapidly with increasing M_P. The sensitivity is monotonically decreasing as a function of m_χ.

A.3 Inclusion of a γ+jets Control Region in the Likelihood Model

This appendix shows an alternative analysis strategy including a γ+jets control region that has been studied in the course of the analysis optimisation. The intention behind using such a control region, the analysis setup it implies and the outcome w. r. t. the background estimation will be discussed.

The production of photons in association with jets is not a background of the monojet analysis. However, its kinematics at high boson-p_T resemble those of W/Z+jets production. Thus, a study of the γ+jets process offers the opportunity to constrain W/Z+jets production by us-

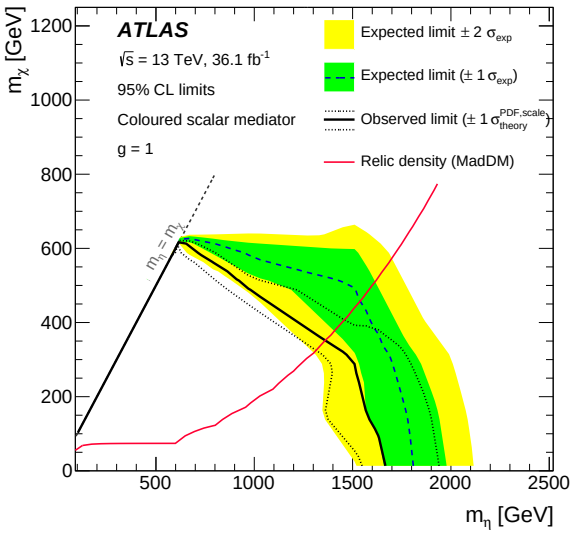

Fig. A.1: 95% CL limit on WIMP production via a scalar coloured t-channel mediator. The coupling involved is $g = 1$. The area below the dashed blue (solid black) line is excluded by the expected (observed) limit. Experimental uncertainties corresponding to $\pm 1\sigma$ and $\pm 2\sigma$ are shown as the green and yellow bands, respectively. The impact of the theoretical cross section uncertainty is shown as the dotted curves around the observed limit. Additionally, the red curve corresponds to the models predicting the correct relic dark matter density [168]. Above the diagonal with equal WIMP and mediator masses the mediator width becomes 0.

ing its statistical power: in pp-collision events, one can select a sample of γ+jets events with high purity (low background contamination) and high statistical accuracy. This high statistical accuracy may help to reduce uncertainties on the dominant $Z(\nu\nu)$+jets background for high boson-p_T, i. e. $\not{E}_T$. The available γ+jets MC simulation is done with Sherpa 2.1.1. at LO (unlike all other background samples) with up to four additional jets. The renormalisation and factorisation scale used is E_γ, the energy of the photon. The CT10 PDF set is used. The γ+jets samples are produced in exclusive boson-p_T slices and exclusive heavy-flavour quark content.

Photon Control Region

The photon control region is denoted as CR1ph. Single-photon triggers are employed to select the events. The criteria below have to be fulfilled:

- the trigger `HLT_g120` (2015 data) or the `HLT_g140` (2016 data) trigger has fired,
- $p_T(\gamma) > 250$ GeV,
- no baseline muons or electrons,
- exactly one baseline and signal photon,
- the photon fulfils the `FixedCutTight` isolation.

In contrast to the regions aiming at W/Z+jets events, here no cut on the $\not{E}_T$ is applied. Instead, the boson-p_T itself is cut on, namely $p_T(\gamma)$. The region exhibits a high purity of γ+jets events

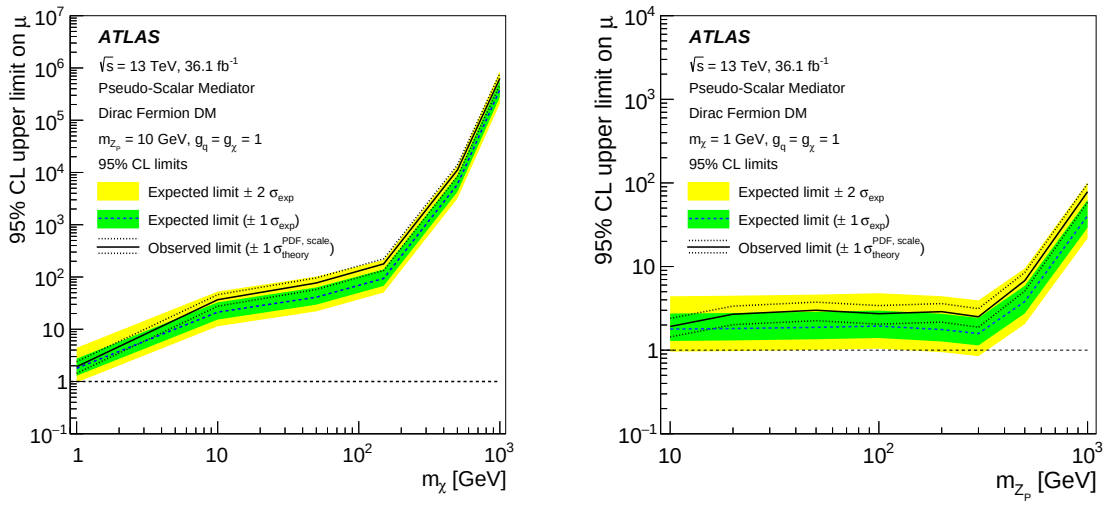

(a) (b)

Fig. A.2: 95% CL limit upper limit on the signal strength of WIMP production via a pseudo-scalar s-channel mediator. The couplings involved are $g_q = g_\chi = 1$. The limit is presented for a fixed mediator mass $M_P = 10$ GeV as a function of m_χ (a) or or fixed $m_\chi = 1$ GeV as a function of M_P (b). Experimental uncertainties corresponding to $\pm 1\sigma$ and $\pm 2\sigma$ are shown as the green and yellow bands, respectively. The impact of the theoretical cross section uncertainty is shown as the dotted curves around the observed limits.

with a high number of total events of the order 3×10^5 for region IM1, which is $3\times$ more than for CR1m. If this region is introduced, all other regions defined in Sec. 7.6.2 and employed in the main analysis have to add the requirement of a photon-veto in order to maintain the orthogonality among all control regions and signal regions.

The γ+jets control region can be included in the likelihood model applying the same scale factor κ^V for γ+jets processes, and thus Eq. 7.15 turns to

$$\begin{aligned} N_{lj}^{\mathrm{BKG}} =& \kappa^V \left[N_{lj}^{\mathrm{MC},W+\mathrm{jets}} + N_{lj}^{\mathrm{MC},Z+\mathrm{jets}} + N_{lj}^{\mathrm{MC},\gamma+\mathrm{jets}} \right] \\ &+ \kappa_j^{\mathrm{Top}} N_{lj}^{\mathrm{MC},t\bar{t}+\text{single } t} \\ &+ N_{lj}^{\mathrm{MC,diboson}} + N_{lj}^{\mathrm{multijet}} + N_{lj}^{\mathrm{NCB}}. \end{aligned} \tag{A.1}$$

In this likelihood model, the $Z(\nu\nu)$+jets background is normalised by the combined scale factor κ^V normalising all V+jets processes ($V = W, Z, \gamma$). This requires two conditions: the processes for W/Z+jets and γ+jets are modelled consistently and the considered kinematic region lies well above the Z-mass. The latter condition is fulfilled by requiring boson-$p_T > 250$ GeV as is done in the analysis. The former condition requires a consistent theory correction to the γ+jets process as discussed for W/Z+jets in Sec. 7.6.1. Since the MC model is only at LO in QCD, a correction to NLO is expected to affect the normalisation of the LO γ+jets by factors of about 1.3-1.4 [150]. These correction factors are provided for a theory LO to theory NLO transition. Special care is needed for the photon isolation prescription: QCD effects lead to collinear singularities in γ+jets production, whereas the masses of W/Z regulate those singularities. This problem can be solved

by defining the photon isolation in a way that it mimics the W/Z+jets processes. Therefore, a dynamic cone variable is defined such that the invariant mass of a γ-jet pair corresponds to the Z-mass, which makes the cone size R dependent on E_T [150]. The maximum cone size is $R = 1.0$. This isolation prescription differs from the standard "Frixione" isolation [170] with a fixed cone used at the analysis level. This is in principle not a problem but the difference between these prescriptions is added as a nuisance parameter since this can influence the cross sections in different boson-p_T regions quite significantly. When computing the denominator of Eq. 7.2 we encounter a problem: the SHERPA samples have an intrinsic Frixione isolation (fixed size for R) implemented that is tighter than the dynamic cone isolation prescription. The result is that the MC LO cross section is $\sim 40\%$ below the theoretical prediction. This can also be due to the fact that SHERPA is not a pure LO generator but employs multi-leg merging. When applying the NLO QCD correction to the SHERPA MC we find the correction factors shown in Fig. A.3(a). This correction is around 1 for the phase space of our interest. The shape and normalisation impact of the nuisance parameter labelled with `vjets_dK_NLO_fix` is shown in Fig. A.3(b) and can be as high as 15% for the lowest region EM1. Applying the overall theory

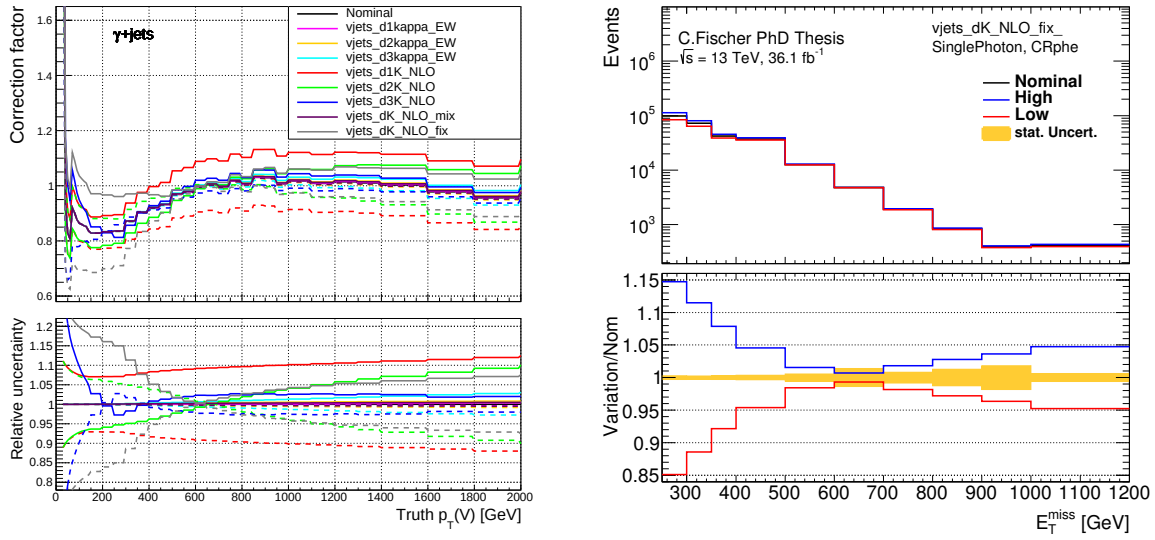

(a) Higher-order QCD-EW correction

(b) Isolation impact on $p_T(\gamma)$

Fig. A.3: (a): Higher-order theory QCD-EW correction as a function of $p_T(V = \gamma)$ (black line). In addition, the impact of the associated theory uncertainties is shown. An additional uncertainty due to the different isolation prescriptions is included as the component `vjets_dK_NLO_fix`. The impact of this nuisance parameter on the reconstructed photon p_T in bins as employed in the analysis in CR1ph is shown in (b). The upper panel shows the distribution itself and the lower panel the ratio of the variation over the nominal prediction. The yellow band displays the statistical uncertainty.

correction should result in a consistent description of the backgrounds with W/Z+jets. However, from Fig. A.4 we observe a stronger mismodelling. The normalisation of the LO MC modelling is roughly unchanged, the γ+jets prediction does not describe the data well, neither before the theory correction nor after applying it. Also, the shape of $p_T(\gamma)$ is not well described showing a clear downward slope. These discrepancies are due to the afore mentioned problems with the isolation prescription. This inconsistent behaviour disqualifies the use of γ+jets to normalise the $Z(\nu\nu)$+jets process using the recommended theory correction which cannot be carried out

properly. A correct implementation requires further work which is beyond the scope of this thesis.

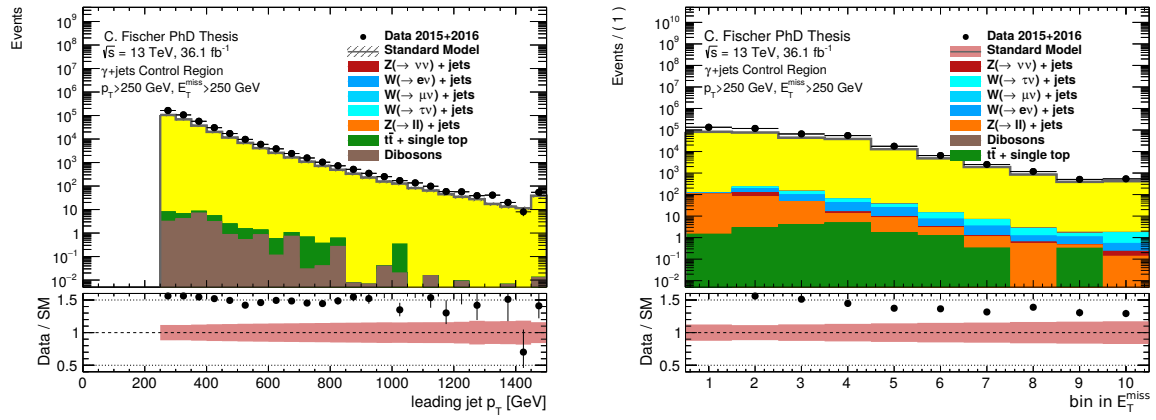

(a) (b)

Fig. A.4: Pre-fit plot of the leading jet p_T and photon p_T in CR1ph after theory reweighting. The γ+jets background is displayed as the yellow histogram on top of other minor background contributions. The bins in $\not{E}_T$ shown in (b) correspond to the binning of the analysis as introduced in Tab. 7.3 and $\not{E}_T \equiv p_T(\gamma)$ holds. The data is shown as black dots. The uncertainty band includes all systematic uncertainties.

In order to estimate the potential of the CR1ph in the fit with a consistent background modelling, we approximately correct the γ+jets process using the W+jets and Z+jets control regions: we can apply a correction factor C to the γ+jets prediction:

$$C = \frac{N^{\text{data}}_{\text{CR1ph}}}{N^{\text{Th}}_{\text{CR1ph}}} \Big/ \frac{N^{\text{data}}_{\text{CR1e+CR1m+CR2m}}}{N^{\text{Th}}_{\text{CR1e+CR1m+CR2m}}}, \tag{A.2}$$

where $N^{\text{data}}_{\text{CR1ph}}(N^{\text{Th}}_{\text{CR1ph}})$ is the number of events observed (predicted) in the CR1ph and $N^{\text{data}}_{\text{CR1e+CR1m+CR2m}}(N^{\text{Th}}_{\text{CR1e+CR1m+CR2m}})$ is the total number of events in the regions CR1e, CR1m and CR2m combined as observed (predicted). By applying C to the theory prediction of γ+jets the same agreement between data and prediction is established as for W/Z+jets. We have to assign a 100% uncertainty on the correction factor C and include this as an additional nuisance parameter in the fit. To assess the final impact of employing such a CR1ph the expected background uncertainties in the SR for two strategies is compared: the baseline strategy used in the analysis of this thesis without CR1ph and the strategy with CR1ph and κ^V containing information from CR1ph. The result is shown in Fig. A.5[a]. The observation (including the additional modelling uncertainty in the form of C) is that the additional statistics from the CR1ph have the potential to reduce the uncertainty of the background in the highest $\not{E}_T$-bins by 0.5% and about 0.2% in the lowest $\not{E}_T$-regions. This improvement is sizable, yet not capable to improve the actual sensitivity to BSM signals. This underlines the power of the chosen final strategy of the thesis' analysis which already exhibits a high statistical accuracy. However, for future iterations with even more integrated luminosity available, higher bins in $\not{E}_T$ are going to be explored and therefore it is worth revisiting the γ+jets background strategy with an improved

[a] Note that these studies were conducted before the additional assignment of a QCD smoothing uncertainty, which increases the total uncertainty significantly in the highest $\not{E}_T$-regions.

theory modelling on the generator site which is in progress. This will enable to omit a 100% uncertainty associated to the ad-hoc correction C, which also drives the improvement to only marginal gains.

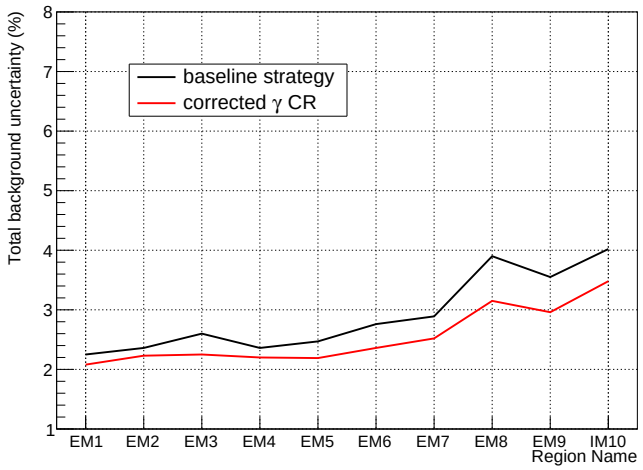

Fig. A.5: Comparison of relative uncertainty on the total background estimate in the various signal regions EM1-IM10 for two different strategies. The black line corresponds to the uncertainty evaluated with the baseline strategy of the thesis. The red line is the uncertainty associated to the strategy that includes the γ+jets control region into the likelihood model.

A.4 TileCal Correction Tool

During 2015 and 2016 data taking, several modules of the tile calorimeter were partly masked and not used for jet reconstruction and calibration. In 2015, two modules were completely masked: LBA10 and EBC21, where LBA10 is a long barrel module that covers $0 < \eta < 0.85$ and $0.89 < \phi < 0.99$ and EBC21 an extended barrel module covering $-1.7 < \eta < -0.8$ and $1.96 < \eta < 2.06$. These module failures have occurred before the start of the data taking. Therefore, the MC samples used in 2015 analyses have been simulated with the same two dead modules in the detector simulation. In 2016, the failure of the modules LBC05 ($-0.9 < \eta < 0.$ and $0.39 < \phi < 0.49$) and LBA52 ($0 < \eta < 0.9$ and $-1.27 < \phi < -1.17$) occurred during data taking. The MC events were generated with all modules functional (LBA10 and EBC21 were repaired during the shut-down). Therefore, the 2016 data might show a deficit in jet observables compared to the MC prediction due to these 'holes'. In order to recover the jet energy lost in the dead modules a tool has been developed within ATLAS: the `JetTileCorrectionTool`. The intention behind this tool is to recover the true energy of a jet whose cone overlaps with the η-ϕ region of the dead modules rather than to veto events containing such jets entirely.
The jet energy is recovered by employing the 'numerical inversion technique' [171]: first, a response function $\mathcal{R}(p_T^{\text{good}}) = \langle p_T^{\text{bad}}/p_T^{\text{good}} \rangle$ is calculated. The transverse momenta p_T^{good} and p_T^{bad} denote the momenta of a jet not affected by dead readout channels and a jet affected by dead readout channels in the calorimeter, respectively. The response function can be numerically inverted in order to obtain p_T^{good} when only p_T^{bad} is known. The response function is obtained via MC simulation. Dijet events have been generated with POWHEG +PYTHIA8 with two different configurations: one *ideal* setup with all calorimeter modules functional and one *real* setup with two dead modules as present in the actual data. The ideal jets are compared to the real jets affected by the dead modules. The response function is then parameterised as a function of the jet p_T and the relative direction w. r. t. the dead module centre ($\Delta\eta, \Delta\phi$ correspond to distances between the jet axis and the centre of the dead module). The response functions are calculated separately for long barrel and extended barrel in bins of p_T^{good}. For the core affected jets (jet axis lies within $\Delta\eta < 0.45$ and $\Delta\phi < 0.05$) the parametrisation function is an exponential function. For edge-affected jets (jet axis lies within $0.45 < \Delta\eta < 0.85$ and $0.05 < \Delta\phi < 0.45$) the function is a linear function. The free parameters of these functions are obtained via a fit to the MC data points. Via the inverse response function the JetTileCorrectionTool corrects the p_T^{bad}. The uncertainty related to this correction is obtained by doing a closure test of corrected jet momenta vs. good jet momenta and assigning a systematic uncertainty that covers any residual differences.

To check if the two holes in the tile calorimeter have an impact on the events selected in the monojet analysis, the 2016 distributions are compared before and after this jet correction is applied. This is done for several distributions in the inclusive CR1e and inclusive SR. Figure A.6 and Fig. A.7 show the leading jet η, ϕ, p_T, sub-leading jet p_T, jet multiplicity and $\not{E}_T$ distributions for CR1e and SR, respectively. The uncorrected data is drawn in red, the corrected data in blue. The distributions agree very well with each other. In fact, the effect of the holes is only visible in the leading jet ϕ distributions, where the corrected data see more events in the affected ϕ regions. There is a slight discrepancy visible in Fig. A.6(d) in the highest p_T-bin of the sub-leading jet of about 10%. The high-p_T jets are the ones mostly affected by dead modules: since their shape is comparatively narrow it may occur that a jet is not reconstructed at all if the axis points to the centre of the dead module. To cover for any kind of overcorrection the systematic uncertainty that comes with the tool needs to be added. In the case at hand,

the statistical uncertainty already covers the potential effect. All other distributions are vastly unaffected and therefore the jet correction is not applied.

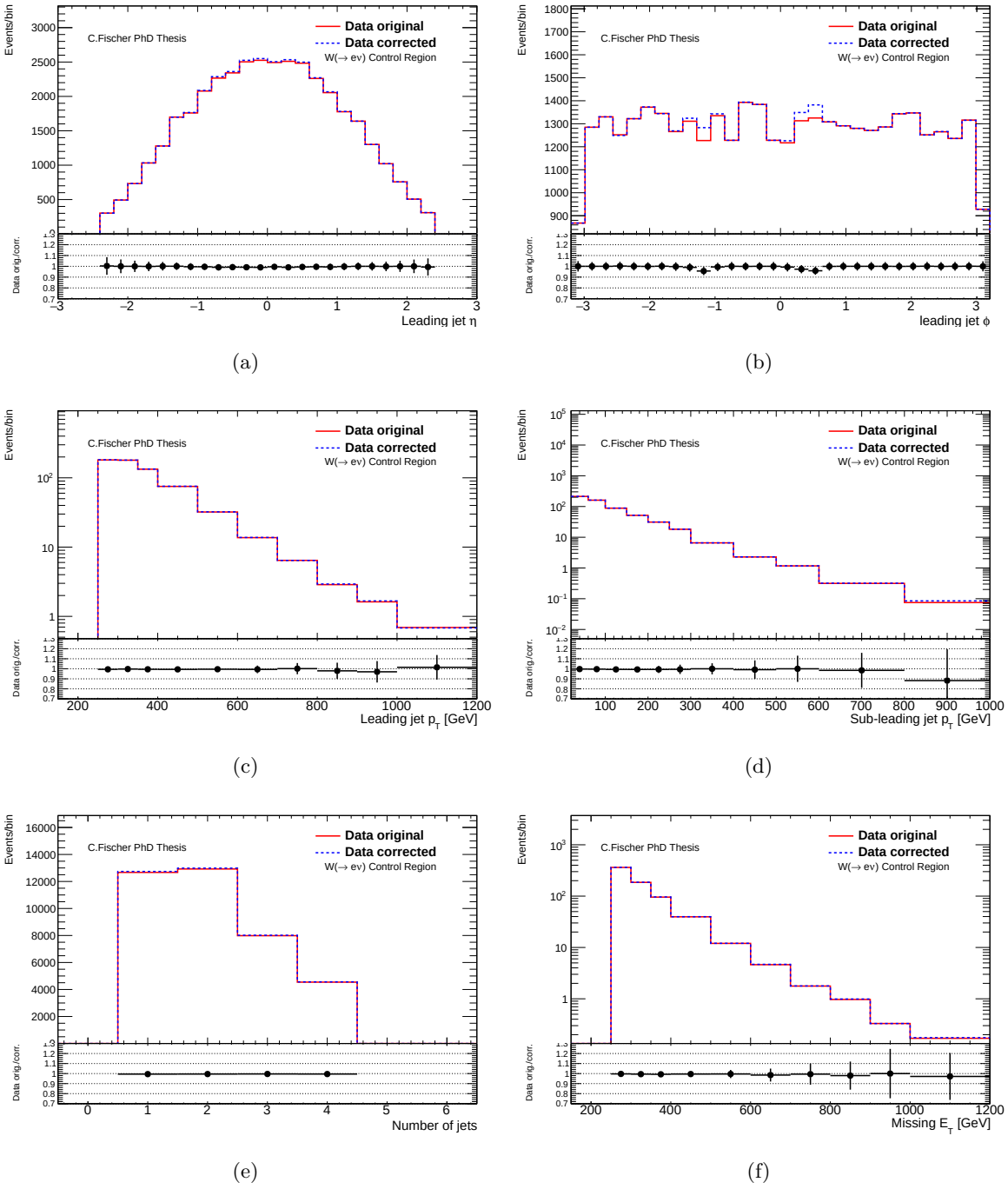

Fig. A.6: Comparison of jet distributions and real $\not{E}_T$ of original data and corrected data via the JetTileCorrectionTool in CR1e.

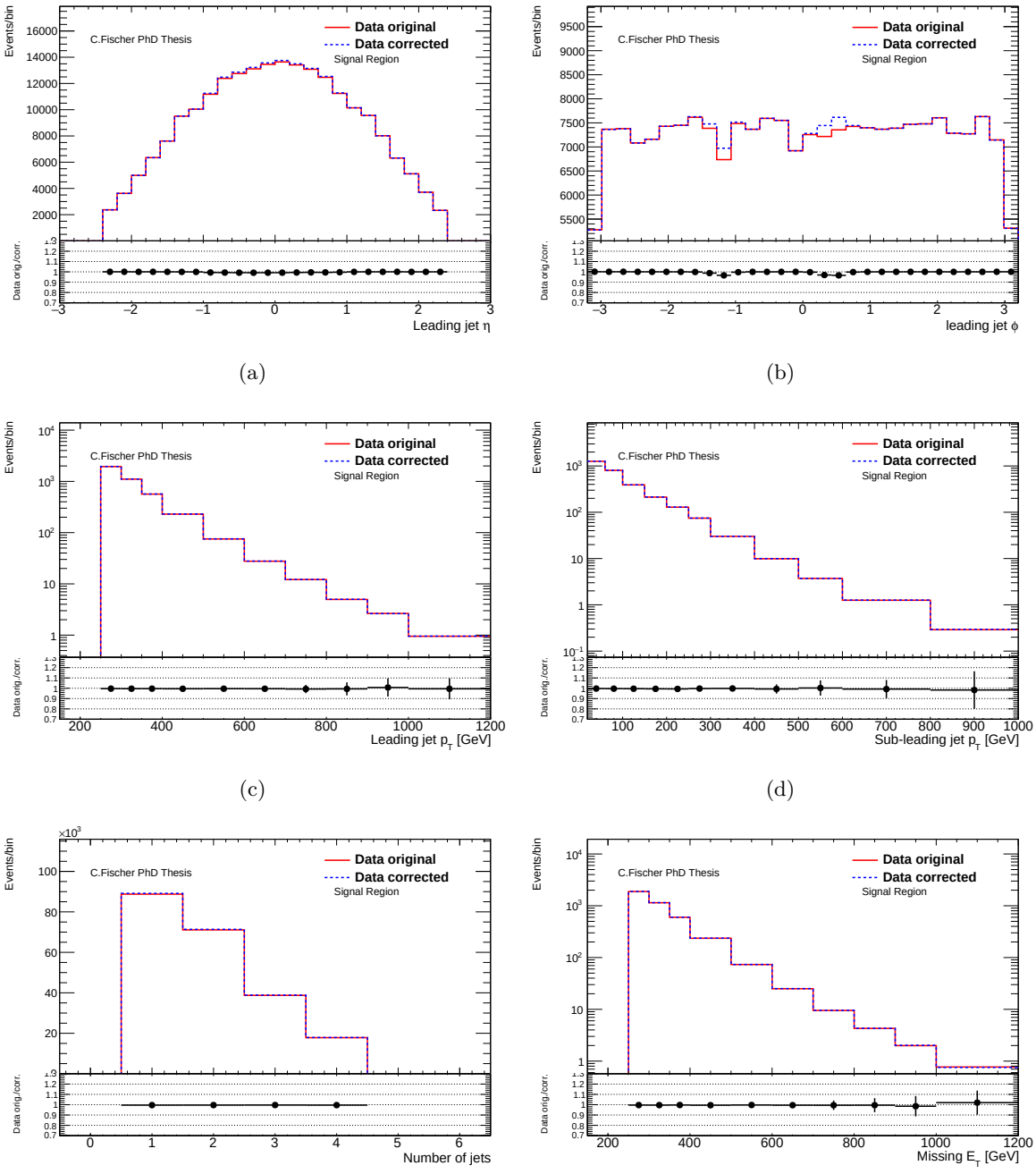

Fig. A.7: Comparison of jet distributions and real $\not{E}_T$ of original data and corrected data via the JetTileCorrectionTool in SR.

Appendix B

The 2015 Monojet Analysis

The main analysis presented in this thesis is the natural continuation of an analysis carried out and published with the 2015 data corresponding to 3.2 fb^{-1} of integrated luminosity. This appendix introduces the strategy used at the time of the 2015 analysis, pointing out differences to the current analysis, and revisits the main physics results that were published in Ref. [131].

B.1 Strategy

The 2015 analysis used a dataset with ∼10 times less events than the full 2015+2016 analysis. The main differences w. r. t. the 2015 analysis is the employment of a dedicated top control region, an increased number of bins in $\not{E}_T$ and most importantly the strategy concerning the $Z(\nu\nu)$+jets background normalisation including higher-order QCD and electroweak calculations. The main difference concerns the V+jets background normalisation procedure in the global fit. There were no EW+QCD corrections applied. Instead, individual κ-factors were retrieved for each bin in $\not{E}_T$ in order to allow the fit to adjust the shape without pulling systematic nuisance parameters to compensate for shape mismodelling. The corresponding background prediction in the likelihood function was:

$$\begin{aligned} N_{lj}^{\text{BKG}} =& \sum_{\text{bkg}} \kappa_j^{\text{bkg}} N_{lj}^{\text{MC,bkg}} + N_{lj}^{\text{multijet}} + N_{lj}^{\text{NCB}} \\ =& \kappa_j^W \left[N_{lj}^{\text{MC},Z(\nu\nu)\text{+jets}} + N_{lj}^{\text{MC},W(\mu\nu)\text{+jets}} \right] \\ &+ \kappa_j^e \left[N_{lj}^{\text{MC},W(e\nu)\text{+jets}} + N_{lj}^{\text{MC},W(\tau\nu)\text{+jets}} + N_{lj}^{\text{MC},Z(\tau\tau)\text{+jets}} \right] \\ &+ \kappa_j^Z N_{lj}^{\text{MC},Z(\mu\mu)\text{+jets}} \\ &+ N_{lj}^{\text{MC},Z(ee)\text{+jets}} + N_{lj}^{\text{MC,diboson}} + N_{lj}^{\text{MC},t\bar{t}\text{+single } t} \\ &+ N_{lj}^{\text{multijet}} + N_{lj}^{\text{NCB}}. \end{aligned} \tag{B.1}$$

The index j goes from bin 1 to bin 7 in $\not{E}_T$, while the index l denotes the regions CR1m, CR1e and CR2m. The binning was the same as shown in Tab. 7.3 with the exception that the 7th bin (IM7≡EM7) was an inclusive bin with $\not{E}_T > 700$ GeV. This binning was chosen to accommodate the statistics available in the 2015 data. There was no CRtop. This means, no b-tagging was employed and there was no b-veto in the CR1m. The top-quark background normalisation was taken from MC prediction and allowed to float around its nominal value by its uncertainty. The uncertainty on the top background ranged from 30% in the lower $\not{E}_T$-bins to 40% for the highest $\not{E}_T$-bin.

The likelihood was otherwise identical to the one in Eq. 7.17. The free parameters of the fit were $\mu_{\text{sig}}, \kappa_j^W, \kappa_j^e$ and κ_j^Z. We can see in Eq. B.1 that the $Z(\nu\nu)$+jets background was normalised by the κ_j^W-factors, dominantly determined in the CR1m. This strategy was chosen in order to re-

duce the uncertainty on the $Z(\nu\nu)$+jets background by cancellation of systematic uncertainties in SR and CRs. Uncertainties on the $W(\mu\nu)$+jets estimation could be reduced in the fit and propagated to the $Z(\nu\nu)$+jets process that only (significantly) contributes to the SR background. The statistics available in the CR1m exceeded the one from the CR2m by about 7 times. This favoured the use of κ_j^W over the use of κ_j^Z to normalise the dominant background, despite the closer kinematic relation between the $Z(\mu\mu)$+jets and $Z(\nu\nu)$+jets production. The remaining differences in $W(\mu\nu)$+jets and $Z(\nu\nu)$+jets production were included via an additional uncertainty called `WZtransfer` with two components. One component was attributed to differences in modelling (PDFs, renormalisation/factorisation scales, PS, hadronisation model, lepton reconstruction and acceptance) between the $W(\ell\nu)$+jets and $Z(\nu\nu)$+jets/$Z(\tau\tau)$+jets production. This uncertainty was 3% in all $\not{E}_T$ bins. The second component accounted for different NLO electroweak corrections to the W+jets/Z+jets production ratio [172, 173]. The corrections were derived from parton level studies applying the same cuts as in the analysis. The uncertainty of these correction factors was governed at that time by the uncertainty on the photon PDF of the proton (photons can initiate V+jets production). Since these were of the order of the correction itself, they were not applied to the $Z(\nu\nu)$+jets normalisation. Instead, the `WZtransfer` uncertainty included the correction plus its uncertainty as an additional uncertainty. The total `WZtransfer` uncertainty (modelling$\oplus$electroweak corrections) ranged between 3% in the lowest $\not{E}_T$-bin and 6% in the highest $\not{E}_T$-bin ($\not{E}_T > 700$ GeV). This uncertainty was not constrained in the global fit to data.

The control region cuts were vastly the same as in the current analysis. An exception is the definition of the CR1e: here, the $\not{E}_T$ that was used was not corrected for the electron p_T. Therefore, the $\not{E}_T$ did not model the W-boson p_T. Furthermore, there was no additional cut applied on the transverse W-mass. The reason behind this was to control the $W(\tau\nu)$+jets background, whose fractional contribution was enhanced. At the same time this definition simplified the selection in terms of trigger requirements . The distributions shown in Fig. B.1 and Fig. B.2 show the agreement between data and MC prediction in the control regions after the global background-only fit. The uncertainties displayed as hatched areas include statistical and systematic uncertainties after the fit. By construction, the normalisation agreed well between the data and the background prediction. The shapes were also mostly in agreement. The shape of the invariant Z-mass in Fig. B.2(e) was not well modelled. The distribution in MC was broader compared to the data. Since the cuts on this variable were not tight this had no impact on the normalisation. The transverse mass shown in Fig. B.2(c) in the CR1e shows nicely the contribution of $W(\tau\nu)$+jets events for low values.

The non-collision and multijet backgrounds did not contribute to the control regions and are thus not included in the plots. Their contribution to the signal region was estimated with data-driven techniques. The non-collision background was estimated with the help of the beam-induced-background tagger in contrast to using jet timing information. There were no contributions above 500 GeV. The multijet background was estimated employing the same jet smearing method. The multijet control region was defined the same way: the $\Delta\phi(\not{E}_T$,jets)-cut is reversed. The $\not{E}_T$ and the jet multiplicity distributions for this control region are shown in Fig. B.3. The uncertainty on the background in this region included a 100% uncertainty assigned to the multijet background estimation. Within this uncertainty, the background prediction and data agreed well. A dedicated *validation region* was also employed in the 2015 analysis: it was defined as the signal region with 150 GeV$< \not{E}_T <$ 250 GeV. The multijet contribution to this validation region was found to be of the order of 7% and the total background prediction was in agreement with the data within the uncertainty. The $\not{E}_T$-distribution in the validation region can be seen in Fig. B.4. The background prediction after the fit was slightly above the data but compatible

within the uncertainties. It is clearly visible that the multijet background mainly contributed at low $\not{E}_T$, close to 150 GeV and rapidly decreased towards higher values. The contribution of multijet events in the signal region IM1 was found to be ∼0.2%.

B.2 Systematic Uncertainties

The luminosity uncertainty on the 2015 dataset was determined to be of the order of 5%. The impact of the luminosity uncertainty on the analysis was reduced to 0.4% after constraining the SM predictions via the data in the control regions. The dominant uncertainties in the background-only fit stemmed from the JES uncertainty, the uncertainty on the top-quark background normalisation and the uncertainty on the `WZtransfer`. The added JES+JER uncertainty led to an impact of 1.1% in the overall signal region after the $\not{E}_T$-shape fit. The uncertainty from the `WZtransfer` amounted to 2.1%. The uncertainty on the top-quark background normalisation led to an overall contribution of 2.7%. Lepton reconstruction and identification efficiencies, energy/momentum scale and resolution altogether contributed 1.8%. The modelling uncertainty on the V+jets background (PDFs, scale choices, PS) amounted to 1.1%. Multijet and non-collision background uncertainties lead to an impact of 0.5%.

B.3 Results

The final event yields in the different inclusive and exclusive signal regions are summarised in Tab. B.1. The total background prediction after the fit had a statistical uncertainty ranging from 2.5% (IM1) to 10% for the highest $\not{E}_T$-region IM7. The total background uncertainties ranged between 4% (IM1) and 12% (IM7) taking correlations between different sources of uncertainties into account. The data and background prediction were in good agreement. In the regions EM5 and IM7 the data overshot the background no more than 1σ, in region EM6 the background prediction exceeded the data by no more than 1.2σ. The individual background contributions and number of events measured in the control regions are illustrated in Fig. B.5 for the regions IM1 (a), IM7 (b), EM1 (c) and EM4 (d). The ratio of data/SM was exactly at 1 in the control regions after the fit. This was by construction since individual κ-factors per $\not{E}_T$-bin were applied in the global fit. The uncertainty in the plots includes the total background uncertainty after

Signal Region	IM1	IM2	IM3	IM4	IM5	IM6	IM7
Observed events	21 447	11 975	6 433	3 494	1 170	423	185
SM prediction	21 730±940	12 340±570	6 570±340	3 390±200	1 125±77	441±39	167±20
	EM1	EM2	EM3	EM4	EM5	EM6	EM7
Observed events	9 472	5 542	2 939	2 324	747	238	
SM prediction	9 400±410	5 770±260	3 210±170	2 260±140	686±50	271±28	

Tab. B.1: Comparison of events observed in data and total SM background prediction after the global fit for each inclusive and exclusive region. The uncertainty on the background prediction includes statistical and systematic uncertainties.

the fit. The $Z(\nu\nu)$+jets background makes up about half of the background contribution in the SR for the lowest $\not{E}_T$-bin. It clearly dominates in high $\not{E}_T$-regions, making up about 65% of the total background. Some kinematic distributions as measured in the IM1 signal region after the $\not{E}_T$-shape fit are shown in Fig. B.6. All distributions in data were well described by the fitted SM background. For illustration purposes, three examples of signal distributions are shown on

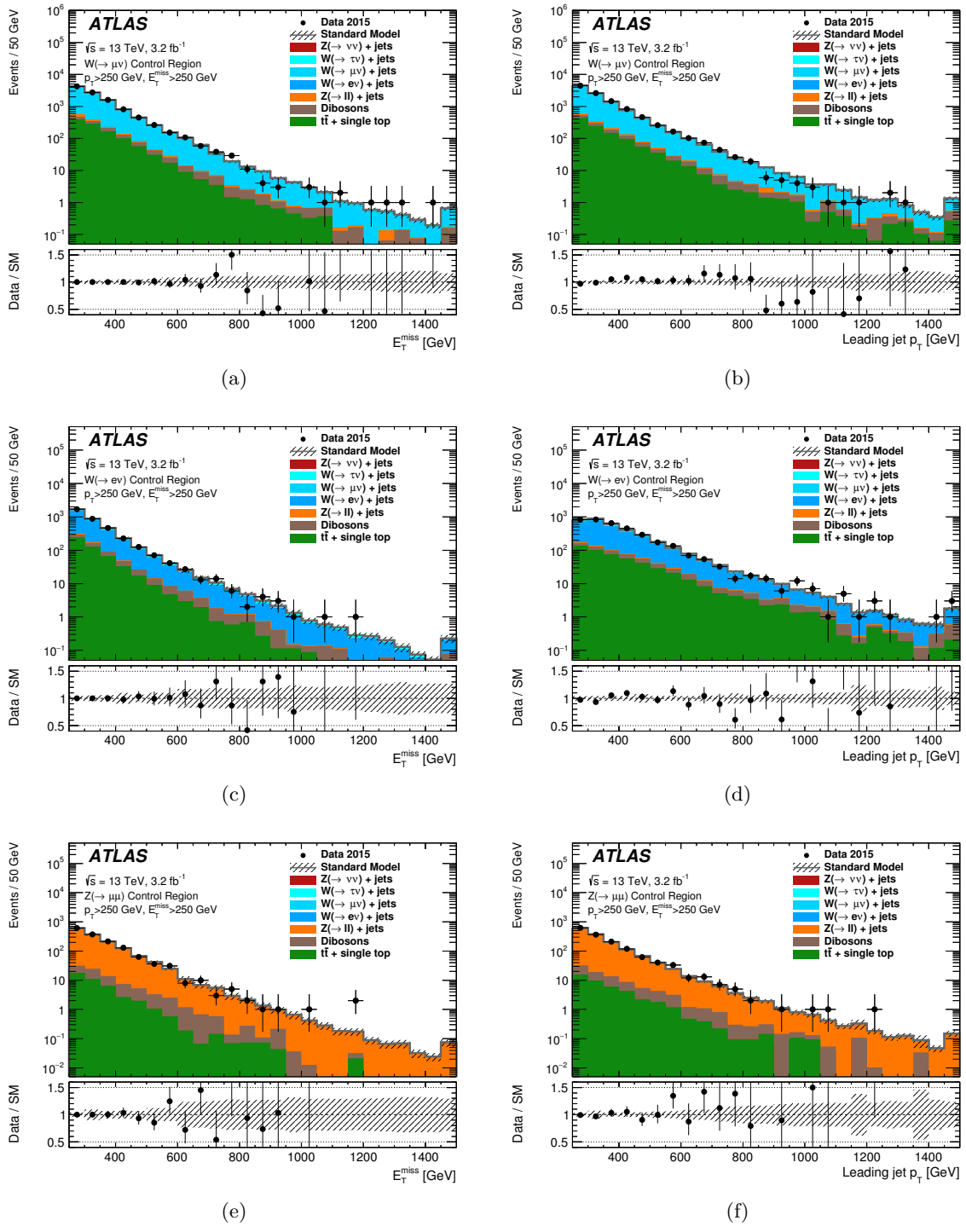

Fig. B.1: Leading jet p_T and $\not{E}_T$ distributions in the CRs for the IM1 selection after the background-only fit: (a)+(b): $W(\mu\nu)$+jets CR distributions, (c)+(d): $W(e\nu)$+jets CR distributions, (e)+(f): $Z(\mu\mu)$+jets CR distributions. Data points are shown as black dots, the total fitted background is shown as the grey line. The hatched area represents the uncertainty band including all systematic uncertainties after the fit. Taken from Ref. [131].

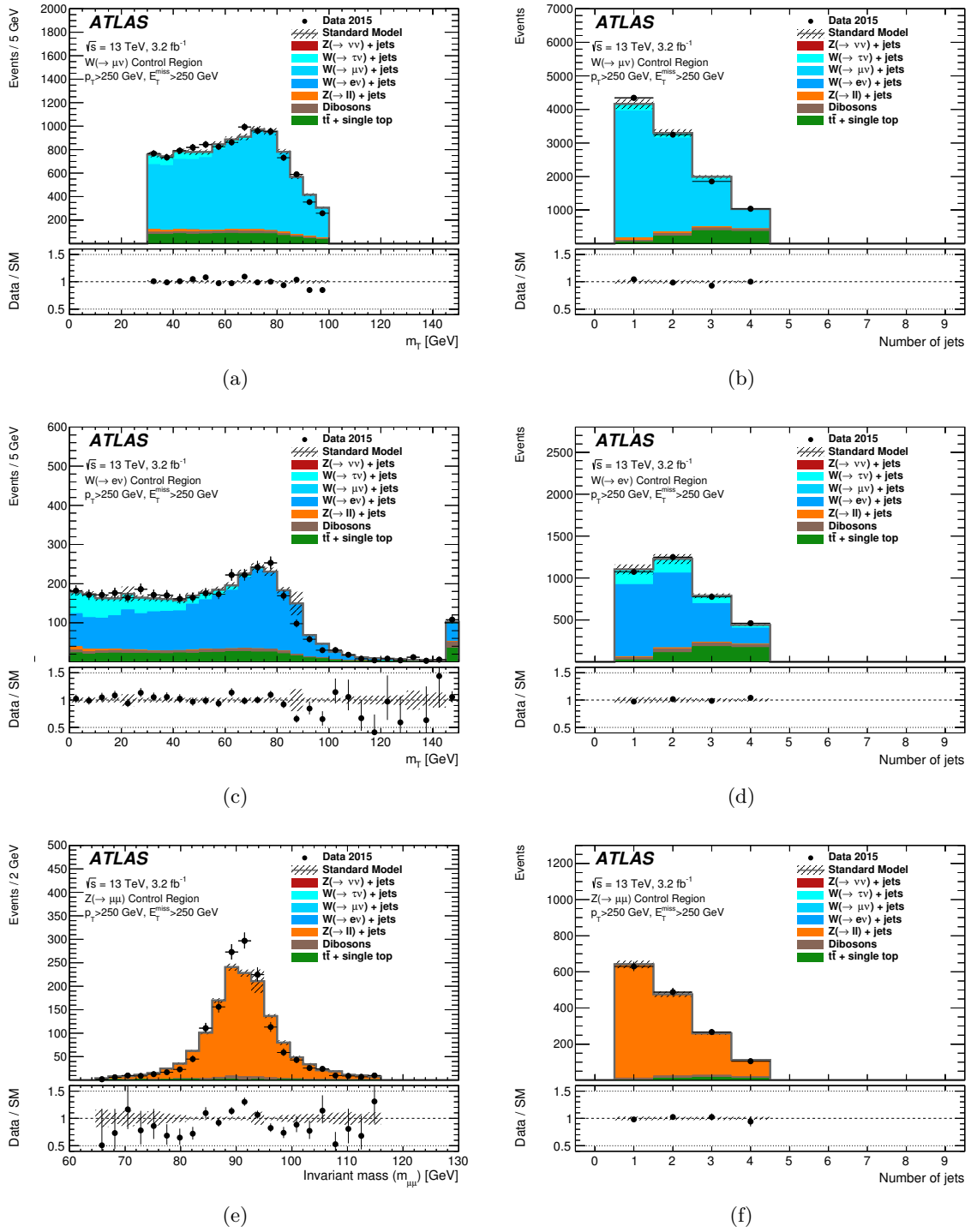

Fig. B.2: Transverse mass, invariant mass and jet multiplicity distributions in the CRs for the IM1 selection after the background-only fit: (a)+(b): $W(\mu\nu)$+jets CR distributions, (c)+(d): $W(e\nu)$+jets CR distributions, (e)+(f): $Z(\mu\mu)$+jets CR distributions. Data points are shown as black dots, the total fitted background is shown as the grey line. The hatched area represents the uncertainty band including all systematic uncertainties after the fit. Taken from Ref. [131].

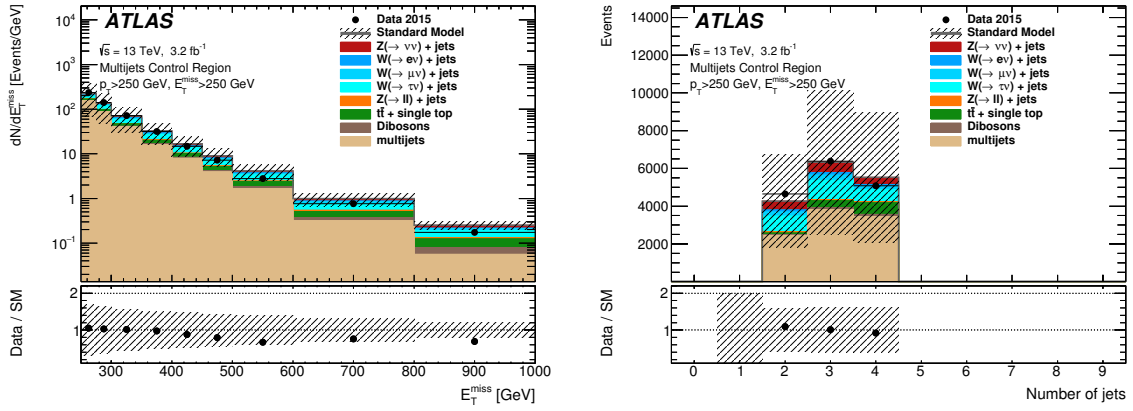

(a) (b)

Fig. B.3: (a) $\not{E}_T$-distribution and (b) jet multiplicity distribution in the multijet control region. The multijet contribution is estimated via the jet smearing method. The data is shown as black points, the hatched areas include a 100% systematic uncertainty assigned to the multijet background estimation. Taken from Ref. [131].

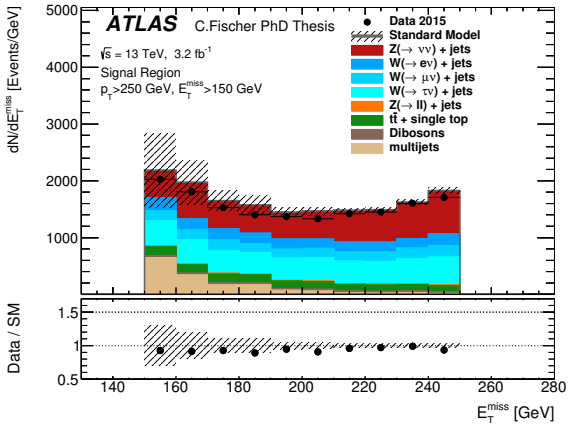

Fig. B.4: $\not{E}_T$-distribution in the validation region with 150 GeV$< \not{E}_T <$ 250 GeV and all other signal region cuts applied. The multijet background shape is obtained from the jet smearing method, the normalisation from a dedicated multijet control region. The uncertainty band only includes statistical uncertainties and the 100% uncertainty assigned to the multijet contribution.

top of the background prediction: an ADD signal with $M_D = 5600$ GeV and $n = 3$, a DM signal with an axial-vector mediator of mass $M_{\text{med}} = 1$ TeV and a WIMP mass of $m_\chi = 150$ GeV and a SUSY signal with sbottom pair production and $m_{\tilde{b}} = 350$ GeV and $m_{\tilde{\chi}^0} = 345$ GeV. These are signals to which the monojet analysis is sensitive as it is displayed in Fig. B.6(a).

B.4 Interpretations

Following the background-only fit in the control regions, limits were set on the upper visible cross section $\langle\sigma\rangle^{95}$, defined as $\langle\sigma\rangle^{95} = \mathcal{A} \cdot \varepsilon \cdot \sigma$, and on specific signal models at 95% CL. This is done in a control region+signal region fit. The model-independent upper cross section limits can only be derived in inclusive $\not{E}_T$-regions, since no shape assumption can be made for a $\not{E}_T$-binned

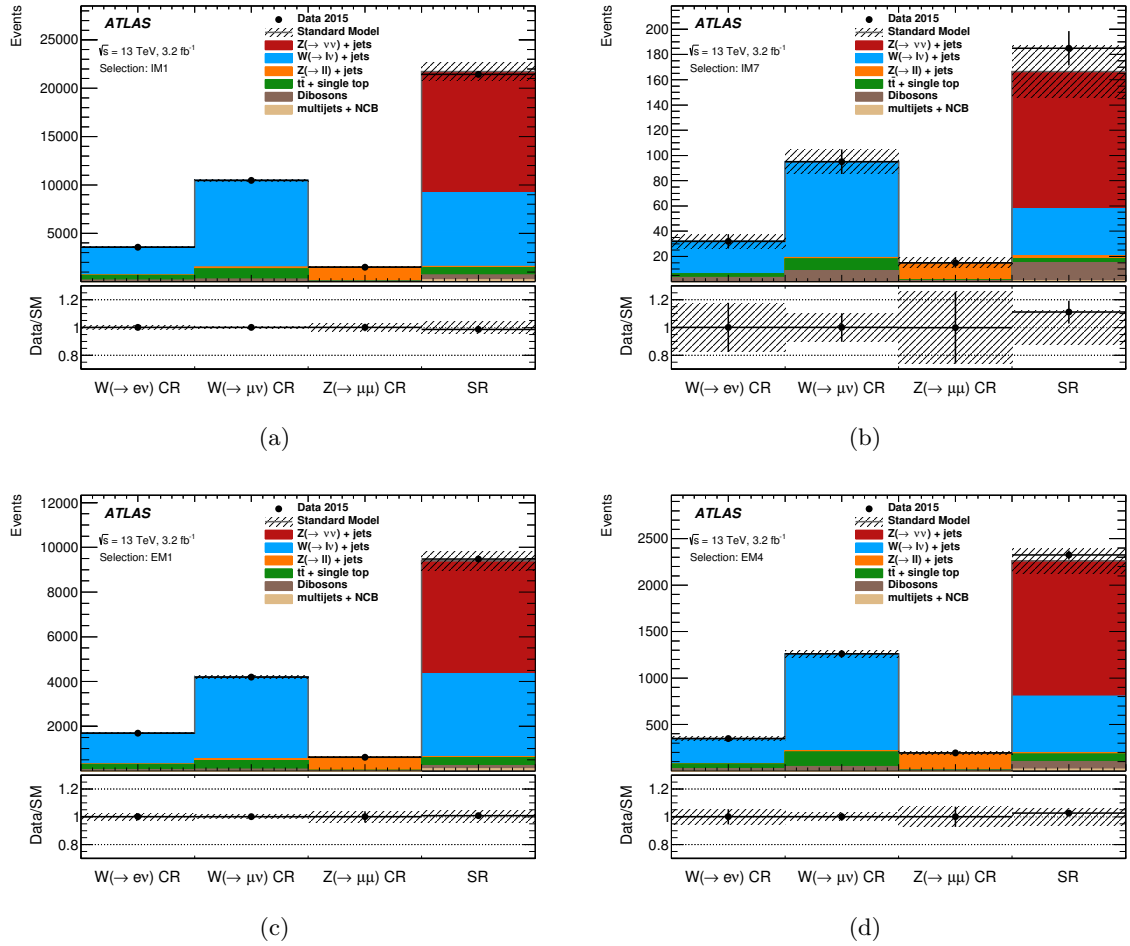

Fig. B.5: Region composition for different event selections after the global fit. (a) shows the region IM1 ($\not{E}_T > 250$ GeV), (b) the region IM7 ($\not{E}_T > 700$ GeV), (c) the region EM1 ($250 < \not{E}_T < 300$ GeV) and (d) the region EM4 ($400 < \not{E}_T < 500$ GeV). The different background processes are indicated for the different regions. The observed data is shown as black dots. The hatched area indicates the total background uncertainty after the fit.

fit. The model-independent fit led to upper limits on S^{95}, the number of events in addition to the SM prediction that is allowed by the observed events in the data. Dividing this number by the luminosity leads to the limit on the visible cross section. For each of the inclusive signal regions, $\langle\sigma\rangle^{95}_{\text{obs}}$, S^{95}_{obs} and S^{95}_{exp} are given in Tab. B.2. The expected limits were derived from the SM prediction in the signal regions after the fit. The numbers decrease with increasing $\not{E}_T$-cut due to the decreasing acceptance. The efficiency of selecting $Z(\nu\nu)$+jets events in the SRs varied between 100% (IM1) and 96% (IM7).

B.4.1 Signal Models

The absence of a signal was interpreted as limits on the three main models of ADD extra dimensions, compressed SUSY scenarios and WIMP dark matter production.
In context of the ADD models, limits were set on the reduced Planck-mass M_D as a function of the number of extra dimensions n. Only bins from 400 GeV onwards have been considered for the limit setting, since studies were performed that showed no sensitivity to the ADD model in

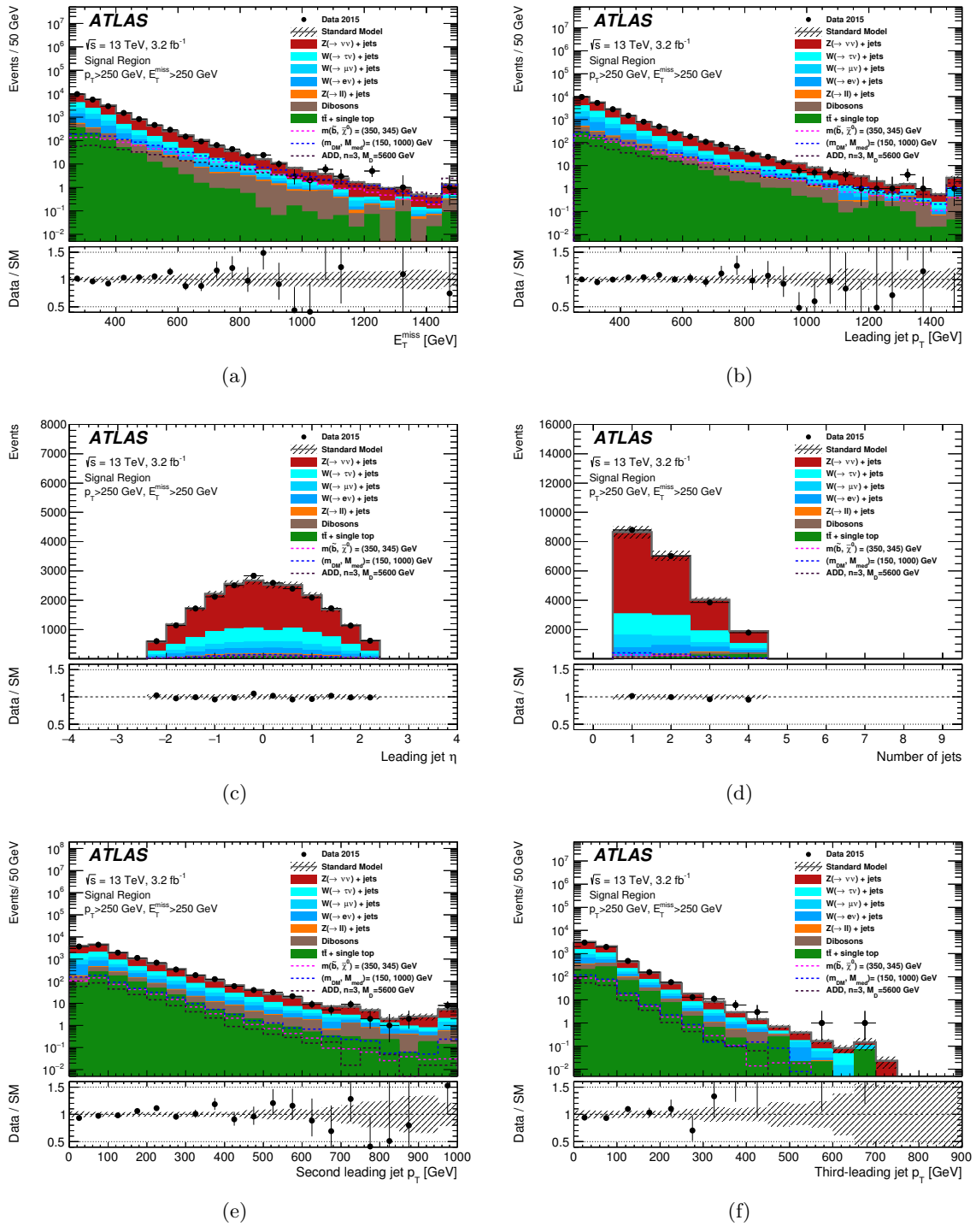

(a) (b) (c) (d) (e) (f)

Fig. B.6: Kinematic distributions in the SR for the IM1 selection after the background-only fit: (a) $\not{E}_T$ (the binning is not the one used in the shape fit), (b) leading jet p_T, (c) leading jet η, (d) jet multiplicity, (e) sub-leading jet p_T and (f) third leading jet p_T. The data is shown as black dots, the total fitted background as the grey line. The hatched area represents the uncertainty band including all systematic uncertainties after the fit. For illustration, three different signal model predictions are shown as coloured dashed lines for ADD, SUSY and WIMP scenarios. Taken from Ref. [131].

Signal Region	$\langle\sigma\rangle^{95}_{\text{obs}}$ [fb]	S^{95}_{obs}	S^{95}_{exp}
IM1	553	1 773	$1\,864^{+829}_{-548}$
IM2	308	988	$1\,178^{+541}_{-348}$
IM3	196	630	694^{308}_{-204}
IM4	153	491	401^{+168}_{-113}
IM5	61	196	164^{+63}_{-45}
IM6	23	75	84^{+32}_{-13}
IM7	19	61	48^{+18}_{-13}

Tab. B.2: Model-independent upper limits on the visible cross section $\langle\sigma\rangle^{95}_{\text{obs}}$ in the different inclusive signal regions. The upper limits on the number of signal events are also shown for the observed and expected numbers. All limits are given at 95% CL.

lower regions in $\not{E}_T$. Here, both the untruncated and the truncated limit are shown together in Fig. B.7. The impact of the cross section truncation or *damping* (further details in Sec. 9.1.3) is only visible for higher numbers of extra dimensions and is about 5% for $n = 6$. The uncertainty on the expected limit includes all signal uncertainties, both experimental and theoretical. Theory uncertainties included uncertainties on the modelling of initial and final state radiation, PDFs, renormalisation and factorisation scales. The observed value was obtained by using the nominal signal cross section reduced by 1σ of the cross section uncertainty (reduced the nominal limit by about 6%). Values of $M_D < 6.58$ TeV at $n = 2$ were excluded as well as a value of $M_D < 4.31$ TeV at $n = 6$. Also shown in Fig. B.7 is the limit from the Run 1 monojet analysis at 8 TeV that is significantly exceeded.

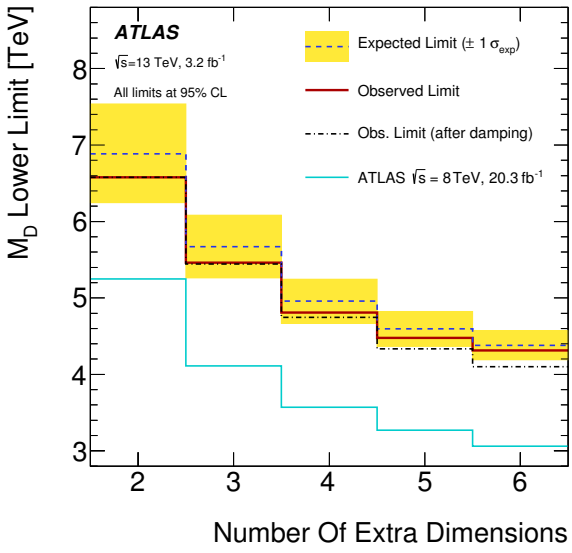

Fig. B.7: 95% CL lower limit on M_D vs. number of extra dimensions in ADD models. The observed limit after damping is derived by depleting the signal cross section for $\hat{s} > M_D^2$ by a factor of $M_D^4/\hat{s}^2$. The yellow bands are the $\pm 1\sigma$ contours including all uncertainties. The limit obtained in Run 1 at 8 TeV is shown for comparison [133].

Limits were derived for three different scenarios of SUSY squark production: the pair production of stop-quarks, where the branching ratio $\tilde{t} \to c + \tilde{\chi}_1^0$ is assumed to be 100%; the pair production of sbottom-quarks, where the branching ratio $\tilde{b} \to b + \tilde{\chi}_1^0$ is assumed to be 100%; and the pair production of light squark-flavours, where the branching ratio $\tilde{q} \to q + \tilde{\chi}_1^0$ is assumed to be 100% and $q = u, d, s, c$. In all cases, the mass difference Δm between the produced squark and the neutralino is small, going down to $\Delta m = 5$ GeV. Smaller splittings were not considered since those may imply long lived squarks. The theoretical uncertainties on the signal yields include the same components as for the ADD model.

Exclusion limits on SUSY compressed scenarios are shown for the nominal SUSY NLO cross section as the observed limit, as well as for the $\pm 1\sigma$ variations of the signal cross section as dotted lines around the observed limit. The whole $\not{E}_T$-spectrum is fitted. Figure B.8 shows the 95% CL exclusion contours on stop-quark production with a decay into charm-quarks and neutralinos. Also here the Run 1 limit is shown for comparison. It could be extended close to the diagonal to masses of about $m_{\tilde{t}} = 323$ GeV where the stop and neutralino are almost degenerate. The observed limit was weaker than the expected limit by no more than 1σ. This is due to the fact that more data than the SM background prediction was observed corresponding to about 1σ in two of the last three $\not{E}_T$-bins, where the analysis is sensitive to SUSY signals.

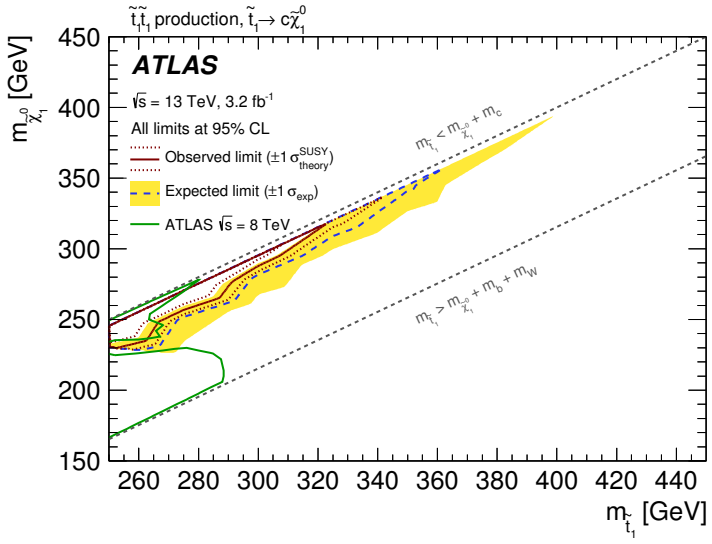

Fig. B.8: 95% CL exclusion contour in the plane $m_{\tilde{t}} - m_{\tilde{\chi}_1^0}$ for the decay channel $\tilde{t} \to c + \tilde{\chi}_1^0$. The grey lines indicate the kinematically allowed region. The region enclosed by the red line indicates the excluded region. The dotted lines around the observed contour indicate the limits derived by varying the NLO SUSY cross section by $\pm 1\sigma$. The yellow bands are the $\pm 1\sigma$ contours including all other uncertainties. Also shown is the Run 1 limit at 8 TeV from the dedicated stop-to-charm analysis combining monojet search regions and charm-tagged search regions [134].

The limits for sbottom and light squark production are presented in a slightly different way in Fig. B.9: Since the analysis is only sensitive to low Δm, the exclusion is presented in the plane of Δm vs. $m_{\tilde{b}}/m_{\tilde{q}}$, respectively. Similar to the stop exclusion, the sbottom exclusion was extended to 323 GeV for $\Delta m \sim m_b$. The same limits are shown for the production of light-flavour squarks. Since they include all flavours of u, d, c, s the production cross section is higher and the analysis is more sensitive. Therefore, masses below $m_{\tilde{q}} = 608$ GeV could be excluded for low Δm.

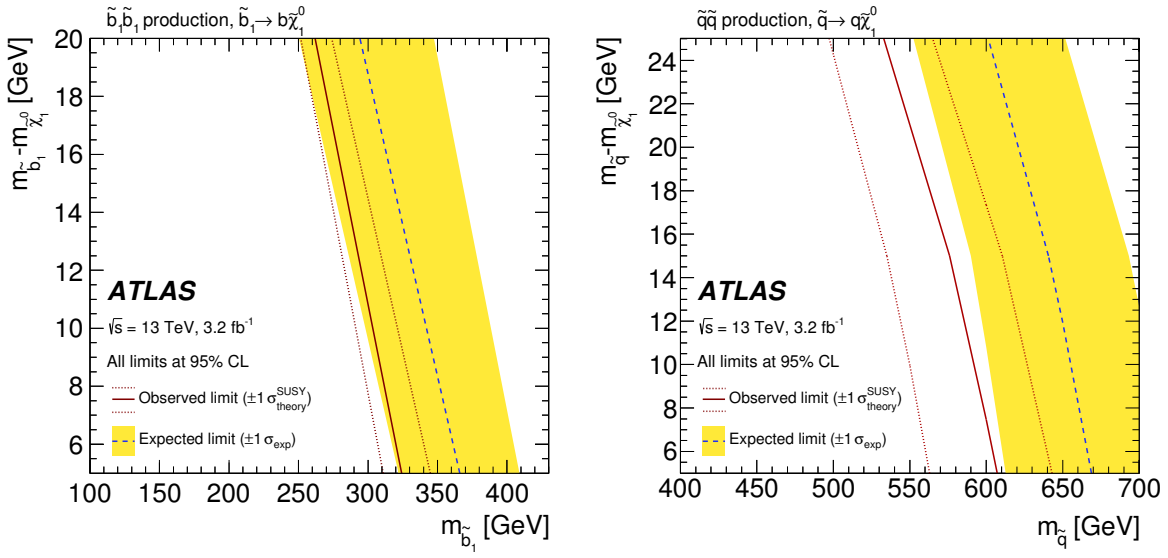

(a) (b)

Fig. B.9: Exclusion contours derived at 95% CL in the Δm-$m_{\tilde{q}}$ plane for (a) $\tilde{b} \to b + \tilde{\chi}_1^0$ and (b) $\tilde{q} \to q + \tilde{\chi}_1^0, q = u, d, c, s$ SUSY scenarios. The area left of the observed contour is excluded. The dotted lines around the observed contour indicate the limits derived by varying the NLO SUSY cross section by $\pm 1\sigma$. The yellow bands are the $\pm 1\sigma$ contours including all other uncertainties.

The results were finally expressed in terms of upper limits on the WIMP pair production in an s-channel model with an axial-vector mediator with mass m_A in the plane m_χ vs. m_A. The couplings are $g_q = 0.25$ and $g_\chi = 1$ and a minimal width is assumed following the prescription of the LHC Dark Matter forum [169]. The limit was again obtained from the global fit in control regions and signal regions of the whole $\not{E}_T$-spectrum. The limits are presented in the same way as the SUSY limits with dotted lines corresponding to $\pm 1\sigma$ variations of the nominal WIMP production cross section around the observed limit. The mass limits are shown in Fig. B.10(a). The on-shell regime is the area left to the dashed line, where $2m_\chi < m_A$ holds. For low WIMP masses mediator masses below 1 TeV can be excluded. The monojet search is not sensitive to off-shell production of WIMP pairs, which is suppressed. The phase space indicated by the grey area is forbidden due to non-perturbativity of the theory (for $m_\chi > \sqrt{\pi/2}m_A$ [166]). The limit in the m_χ-m_A plane can be translated into a WIMP-nucleon scattering cross section limit as a function of the WIMP mass. This is done in order to compare the LHC WIMP sensitivity to direct-detection experiments. They quote their results as 90% CL limits. Therefore, the ATLAS limit in Fig. B.10(b) is also shown as a 90% CL contour. The parameter space above this curve is excluded. Compared are the results on WIMP-proton scattering (spin-dependent interaction) from XENON100 [136], LUX [135] and PICO [137, 138]. It has to be noted that the ATLAS limit is still model-dependent, assuming the Z'-like axial vector mediator exchange. The monojet search is able to exclude cross sections above 10^{-42} cm^2 for WIMP masses up to 300 GeV. In the range of WIMP masses up to 10 GeV the ATLAS limit complements the direct-detection search results adding sensitivity. For higher WIMP masses the ATLAS limit degrades quickly due to the suppressed production mode, whereas the direct-detection searches gain in sensitivity.

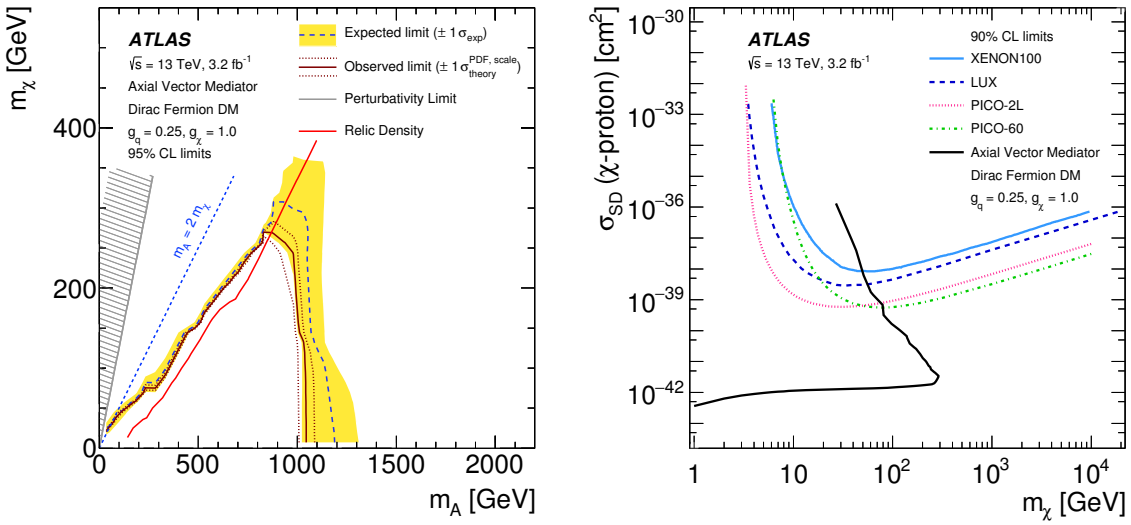

(a) (b)

Fig. B.10: (a): Observed and expected limits at 95% CL for dark matter production in the m_χ-m_A parameter space. The dotted lines around the observed contour indicate the limits derived by varying the signal prediction by $\pm 1\sigma$ of the theory uncertainty. The yellow bands are the $\pm 1\sigma$ contours including all other uncertainties. The expected relic density is indicated in red (bright). The hatched area corresponds to $m_\chi > \sqrt{\pi/2} m_A$ and represents the non-perturbative regime. (b): Derived 90% CL limit in the plane of the WIMP-proton scattering cross section vs. the WIMP mass (spin dependent). The ATLAS limit is compared to direct-detection limits from XENON100 [136], LUX [135] and PICO [137, 138]. The ATLAS limit is model-dependent assuming minimal mediator width and couplings of $g_q = 0.25$ and $g_\chi = 1$.

B.5 Conclusion

As already pointed out, the 2015 analysis based on 3.2 fb^{-1} of data, constituted the initial baseline for the main analysis subject of this thesis, with the full 2015+2016 datasets and a total of 36.1 fb^{-1} luminosity. The increase by an order of magnitude of the dataset and the revisited method for the determination of the background contributions supersede the 2015 results significantly.

Appendix C

On the WIMP Signal Interpretation using EFT

In Chap. 3 the model of effective field theories (EFTs) as an approach to search for dark matter at the LHC has been discussed. These models played a major role in the monojet analyses carried out with Run 1 data with lower centre-of-mass energies of 7 and 8 TeV. However, since the EFTs are not valid for high momentum transfers, as probed in Run 2 searches, and not UV complete models they are not used anymore for WIMP interpretations. This appendix focuses on these EFT models and how they need to be interpreted and in which cases they resemble simplified models used for WIMP interpretations throughout Run 2 analyses.

C.1 Effective Field Theory and Truncation

The EFT model introduces three new parameters into the theory: the suppression scale M_*, the mass of the dark matter particle m_χ and the coupling $g_q g_\chi$. Figure 7.2(a) shows a limit on an EFT model with an effective vector coupling for M_* vs. m_χ. The coloured dashed lines are labelled with 'truncated'. This *truncation* is applied to take the valid phase space of the EFT into account. The term truncation refers to the reduction of the actual dark matter production cross section. Generated events with a momentum transfer $\hat{s}(\equiv Q_{\mathrm{tr}})$ above a certain threshold are simply disregarded.
The EFT can be connected to an existing UV complete simplified model as already discussed in Eq. 3.17 of Chap. 3:

$$M_{\mathrm{med}} = \sqrt{g_q g_\chi} M_*.$$

As a minimum requirement[a] for the EFT to be valid we can ask that

$$Q_{\mathrm{tr}} < M_{\mathrm{med}} = \sqrt{g_q g_\chi} M_*, \tag{C.1}$$

where Q_{tr} denotes the momentum transferred to the WIMP pair system:

$$Q_{\mathrm{tr}} = \sqrt{(p(\mathrm{DM1}) + p(\mathrm{DM2}))^2},$$

where $p(\mathrm{DM1})$ and $p(\mathrm{DM2})$ are the four-momenta of the two DM particles. If we assume a coupling of $\sqrt{g_q g_\chi} = 1$ the condition turns to $Q_{\mathrm{tr}} < M_*$. This is what has been used to obtain the truncated limit in Fig. 7.2(a) (blue dashed line). The maximal coupling is 4π which weakens the requirement significantly to a point where the cross section is not truncated at all. A more conservative approach than introduced in Eq. C.1, but more model independent requirement is

[a] This means it is not the strictest requirement but a convenient approach to asses a more reliable sensitivity of EFTs.

the following [174]:

$$E_{\mathrm{cm}} < M_{\mathrm{med}}. \tag{C.2}$$

E_{cm} denotes the centre-of-mass energy in monojet processes:

$$E_{\mathrm{cm}} = \sqrt{(p(\mathrm{DM1}) + p(\mathrm{DM2}) + p(\text{1st jet}))^2}.$$

It includes the jet produced in association with the WIMP pair system (neglecting additional jets whose momenta are much smaller than the one of the leading jet). Since $E_{\mathrm{cm}} > Q_{\mathrm{tr}}$ holds for a given event this approach is stricter. However, it is also valid for different sorts of WIMP pair production like a t-channel production, where the transferred momentum is different than for the s-channel production that is assumed for Q_{tr}. The shape of E_{cm} depends on the selection cuts applied that require an ISR jet with a certain p_T. Further, the lower end point for Q_{tr} and E_{cm} depend on the dark matter mass. MC studies at truth level have been performed to access the impact of truncation and quantify the fraction of valid events for a given M_* and m_χ. Figure C.1 shows the distributions of Q_{tr} and E_{cm} for an EFT signal sample with $m_\chi = 150$ GeV (a) and $m_\chi = 500$ GeV (b) simulated at a centre-of-mass energy of 14 TeV. A monojet selection with the following cuts has been applied (all truth level):

- jet $p_T > 50$ GeV, at most two jets, with the leading jet fulfilling: $p_T > 250$ GeV,
- $\not{E}_T > 250$ GeV and $\Delta\phi(\not{E}_T, \mathrm{jets}) > 0.5$.

The lower endpoint for Q_{tr} ($\hat{s}$ in the figure) is $2 \cdot m_\chi$, while it is shifted to higher values by the p_T of the leading jet for E_{cm}. The requirements in Eq. C.1 and Eq. C.2 mean to cut on

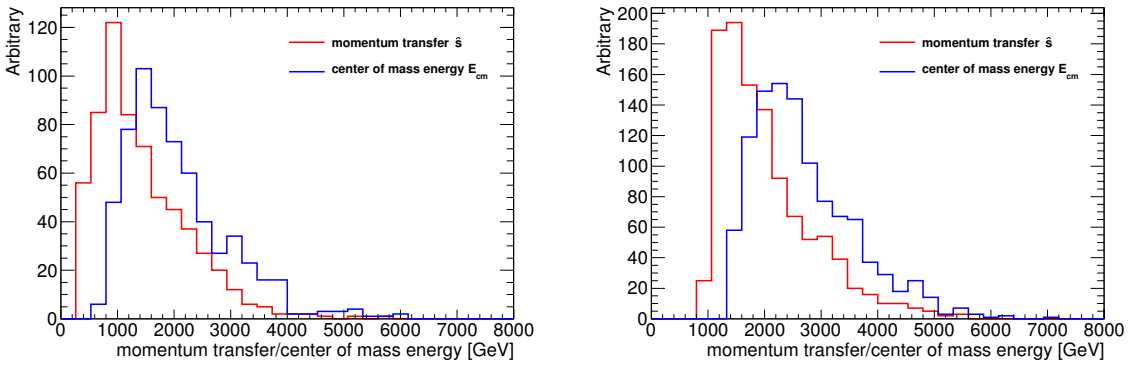

(a) $m_\chi = 150$ GeV (b) $m_\chi = 500$ GeV

Fig. C.1: MC studies at truth level: EFT samples with $m_\chi = 150$ GeV (a) and $m_\chi = 500$ GeV (b) have been produced an the Q_{tr} and E_{cm} have been calculated, whose distributions are shown.

these distributions at $\sqrt{g_q g_\chi} M_*$ and disregard any event above $\sqrt{g_q g_\chi} M_*$. The fraction of events surviving this cut, the 'valid' fraction of events, is further on denoted as R_{M^*} and goes from 0 to 1. Figure C.2 shows how R_{M^*} evolves for different dark matter masses for the two cuts on Q_{tr} (a) and E_{cm} (b) if the couplings are assumed to be 1 ($\sqrt{g_q g_\chi} = 1$). R_{M^*} reaches values of 1 for high M_*. The higher the dark matter mass, the higher the value of M_* before R_{M^*} reaches to 1. All curves are shifted to higher values for the E_{cm}-cuts w. r. t. the Q_{tr}-cuts. For both requirements in Eq. C.1 and Eq. C.2 the procedure to obtain the truncated limits is the same:

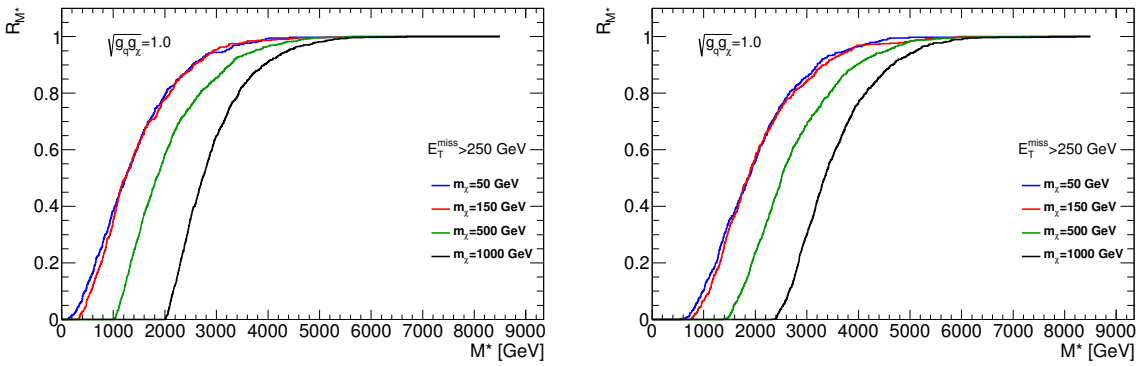

(a) $Q_{\mathrm{tr}} < M_*$ (b) $E_{\mathrm{cm}} < M_*$

Fig. C.2: Validity fraction R_{M^*} vs. the cut value M^* applied to Q_{tr} (a) and E_{cm} (b) for different dark matter masses m_χ. The couplings are set to 1.

The nominal signal sample is produced with a certain $M_{*,0}$. From Eq. 3.16 we know that the cross section simply scales as:

$$\sigma(M_*) \propto \left(\frac{M_{*,0}}{M_*}\right)^k. \tag{C.3}$$

For a vector coupling, that is considered in the following, $k = 4$ is used. This allows to perform a scan in M_* to obtain different signal predictions. The cross section is truncated by either of the requirements in Eq. C.1 or Eq. C.2 with the corresponding R_{M^*} as illustrated in Fig. C.2. At the same time the cross section is rescaled. This leads to an effective cross section as depicted in Fig. C.3. It shows an example for a WIMP mass of 500 GeV. The red line shows the behaviour corresponding to Eq. C.3. The blue and green curves are obtained via truncation. A new limit

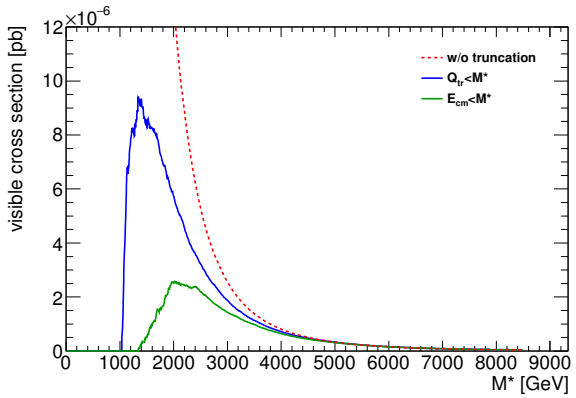

Fig. C.3: Visible WIMP pair production cross section as a function of M_* if truncation is applied and couplings are assumed to be 1.

on M_* is derived by comparing the signal prediction with the upper limit on the visible cross section. By looking at Fig. C.3 it is apparent that there will be a lower limit as well as an upper limit on M_*. In general, the visible cross section is a function of the chosen couplings and the WIMP mass m_χ. To illustrate the impact of the choice of couplings on the validity fraction a

value of 1.6 TeV has been chosen for M^*[b]. The corresponding R_{M^*} is drawn as a function of $\sqrt{g_q g_\chi}$ for both truncation approaches and a given WIMP mass in Fig. C.4. The selection on $\not{E}_T$ has been tightened to 600 GeV, where the monojet analysis is more sensitive to WIMP signals. For $\sqrt{g_q g_\chi} > 3$ all generated events are valid and the limit on M_* is unchanged. The lower the couplings the lower the validity fraction. It decreases more rapidly for the E_{cm}-cut approach. These lower couplings will lead to lower limits on M_*. The final truncated limits on M_* as a

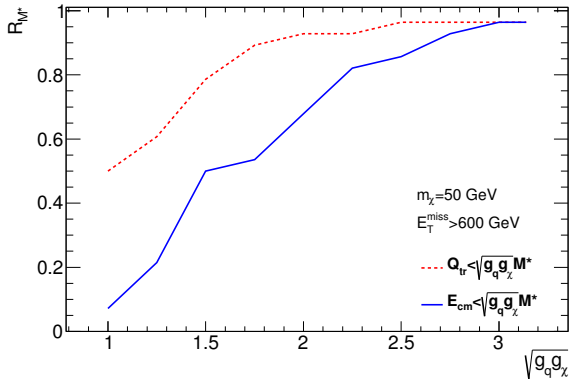

Fig. C.4: Fraction of valid events for $M^* = 1.6$ TeV vs. the coupling constants for $m_\chi = 50$ GeV and $\not{E}_T > 600$ GeV as selection cut.

function of the couplings $\sqrt{g_q g_\chi}$ are shown in Fig. C.5 for the same setup as used in Fig. C.4 with a WIMP mass of 50 GeV. The untruncated limit of $M_* = 1.6$ TeV has been used as an input. Below a coupling of $\sqrt{g_q g_\chi} \sim 1.8$ (where the blue curves eventually meet) the second approach that cuts on E_{cm} is not able to exclude any M_* values. As anticipated and illustrated in Fig. C.3, there are two curves that indicate upper limits from below and lower limits from above on M_*, for both approaches. For couplings of unity and the Q_{tr} approach, the limit of 1.6 TeV is reduced to a lower limit of 1.2 TeV, while values of $M_* < 200$ GeV cannot be excluded in this example. These 'truncated limits' are an ad-hoc solution to perform a sensible EFT

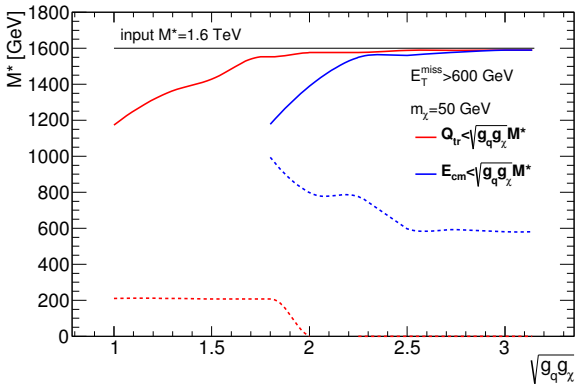

Fig. C.5: Truncated limit for M_* as a function of couplings $\sqrt{g_q g_\chi}$ [59]. The untruncated limit used as input is indicated by the horizontal line at $M_* = 1.6$ TeV. The WIMP mass is $m_\chi = 50$ GeV.

model interpretation and clearly indicate the limited power depending on choices of couplings.

[b] Value taken from early Run 2 sensitivity studies.

C.2 Simplified Models in Comparison with EFT

Consequently, the interpretation of dark matter searches in terms of EFT models has been abandoned in favour of simplified models for all Run 2 analyses. If the Z' mediator mass is high, beyond the reach of Run 2 momentum transfers, the simplified model is expected to converge to the EFT model. The following studies focus on comparisons of simplified models and EFTs for a vector coupling interaction (D5 operator in EFT language). Different mediator masses are tested as well as the impact of different WIMP masses on the event kinematics.
Similar to the truncation studies before, signal samples for simplified models have been generated with a centre-of-mass energy of 14 TeV and truth variables are used in these studies. Different mediator masses of 5 TeV, 10 TeV and 20 TeV have been simulated with a width of $\Gamma = M_{\text{med}}/10$ (narrow width) for an s-channel mediator. Figure C.6 shows the transverse momenta of the two DM particles, the truth $\not{E}_T$ and leading jet p_T and the centre-of-mass energy E_{cm} for three simplified models and one EFT model with $m_\chi = 150$ GeV after applying a monojet selection as discussed above. All distributions are normalized to unity and shapes are compared. The shapes of 10 TeV and 20 TeV mediator mass signals are similar to the EFT model prediction, while a distinct peak at 5 TeV is visible in the E_{cm} distribution for a mediator mass of 5 TeV. In Fig. C.7 EFT and simplified model kinematic distributions are compared for different WIMP masses: the truth $\not{E}_T$ and the $m_{\chi\chi}$ are plotted for the EFT model (first row) and simplified model (second row) for masses of $m_\chi = 50, 150, 500$ and 1000 GeV. The mediator mass is 10 TeV and a narrower width of $\Gamma = M_{\text{med}}/20$ was chosen for comparison. Figure C.8 shows how this signal (magenta line) compares to the one chosen for the comparisons in Fig. C.6 (black line) for the $m_{\chi\chi}$ distribution. They are very similar and comparable to the EFT distribution. A slightly enhanced tail for high $m_{\chi\chi}$ for the simplified models compared to the EFT model can be observed both in Fig. C.8 and Fig. C.7.

The ultimate conclusion from the here presented studies is that the EFT model can be reproduced by using simplified models with mediator masses of 10 TeV and more for a centre-of-mass energy of around 14 TeV. In cases, where no UV completion is available to replace the EFT interpretation the limits on M_* should be truncated via the here described procedure using the variable E_{cm} since it is more general and applicable to most models leading to a monojet signature (or mono-X, where the transverse momentum of X is used to calculate E_{cm}).

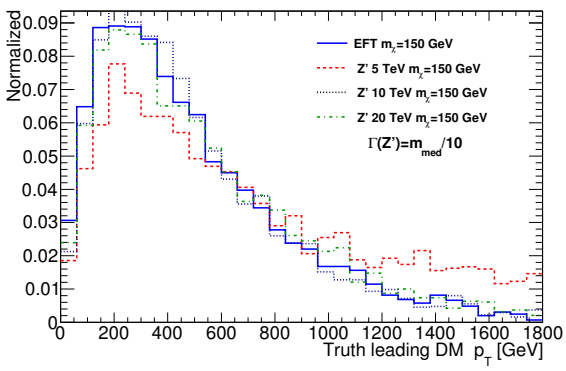

(a) Leading DM p_T

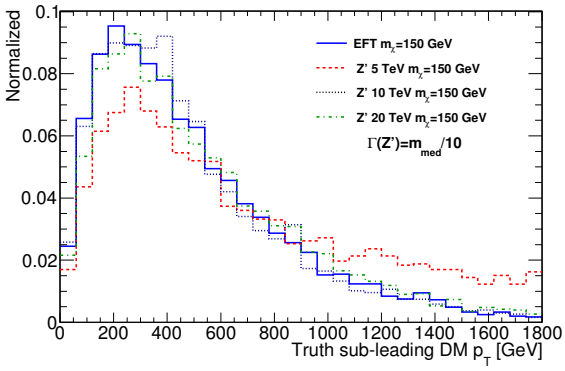

(b) Sub-leading DM p_T

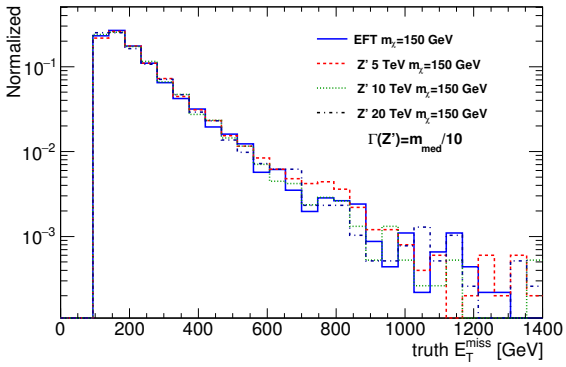

(c) Truth $\not{E}_T$

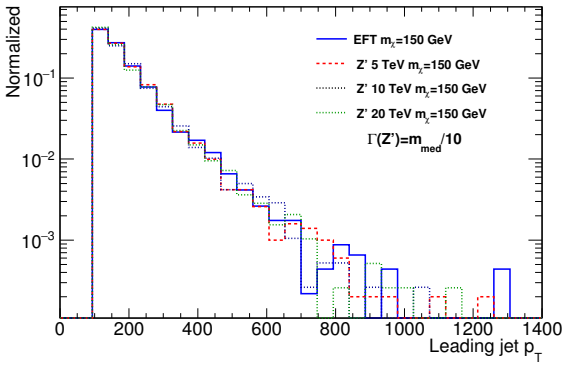

(d) Truth p_T(1st jet)

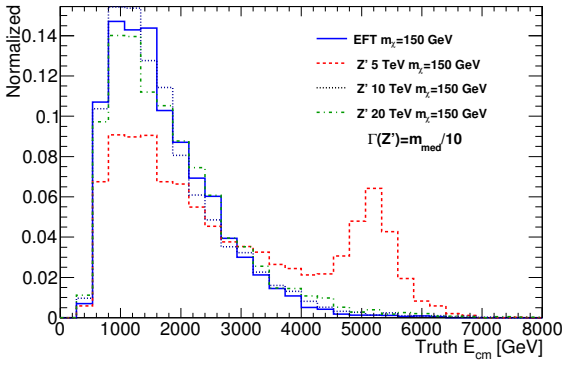

(e) Truth E_{cm}

Fig. C.6: Comparison of kinematic distributions of EFT samples with simplified models with different mediator masses [59]. The WIMP mass is always $m_\chi = 150$ GeV, the couplings are vector couplings. A monojet selection has been applied.

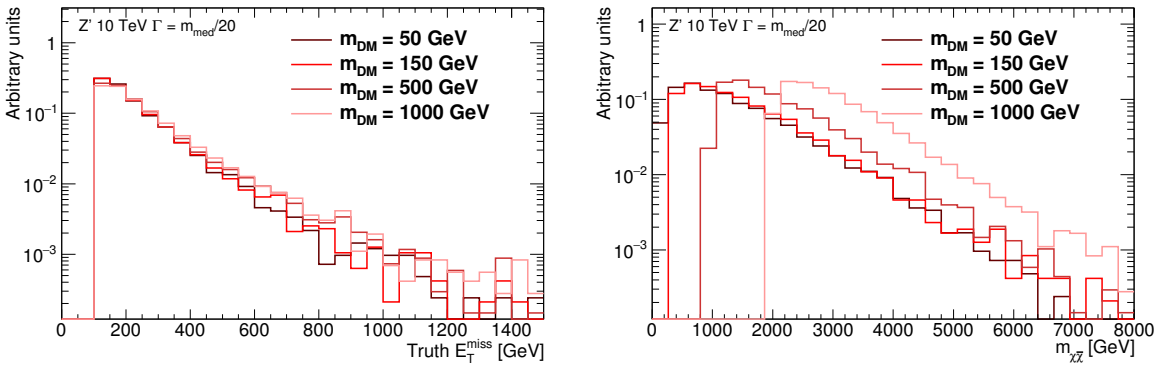

(a) EFT, D5 operator

(b) EFT, D5 operator

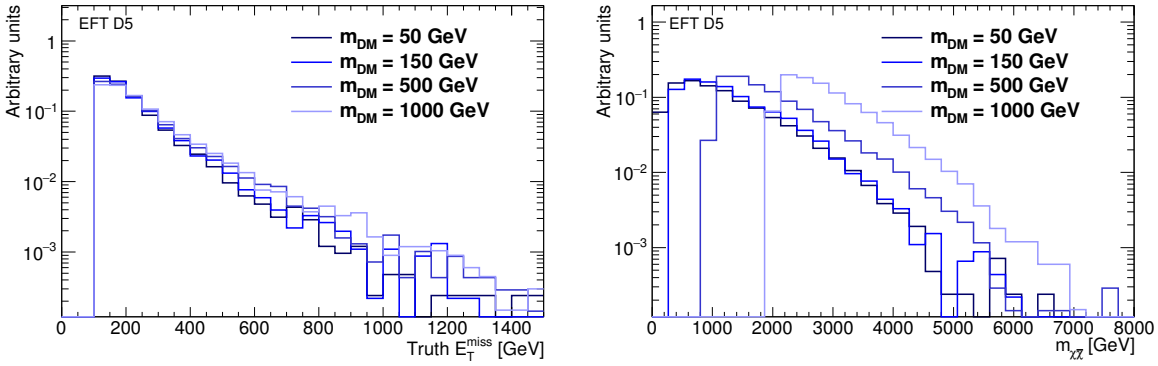

(c) Simplified Model

(d) Simplified Model

Fig. C.7: $\not{E}_T$ distributions for EFT (a) and simplified models (b) and invariant dark matter mass $m_{\chi\chi}$ ($= \hat{s}$) for EFT (b) and simplified models (d) for different dark matter masses [59].

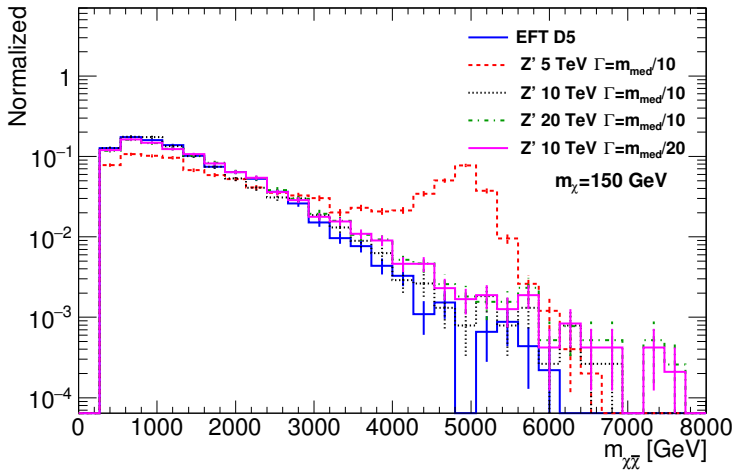

Fig. C.8: Comparison of EFT and simplified model predictions for $m_{\chi\chi}$ for a vector coupling and monojet selection [59].

Appendix D

The ATLAS Tile Calorimeter

The Atlas calorimeters including the hadronic tile calorimeter (TileCal) have been described in some detail in Sec. 5.2.3. More detailed information of the TileCal is given in Ref. [175]. This section focuses on the monitoring of the luminosity and the response of the TileCal modules with the help of *minimum bias currents*.
The layout of the TileCal cells is shown schematically in Fig. D.1. The TileCal consists of a Long Barrel (LB) covering the region of $0.0 < |\eta| < 1.0$ and two Extended Barrels (EB) that cover $0.75 < |\eta| < 1.65$ in pseudo-rapidity. The so-called A-side denotes the part that covers positive pseudo-rapidities, while the C-side denotes the part that covers negative pseudo-rapidities. Within LB and EB the cells are arranged in three layers: the one closest to the beam axis is called A-layer, the one furthest away is called D-layer. In between is the B(C)-layer. Special cells are the E-cells, that are marked in yellow in Fig. D.1. They cover the so-called gap/crack region with $1.0 < |\eta| < 1.6$ and are partly closer to the beam axis than the A-layer. Given their location and varying protection inside the TileCal, different cells experience different exposures during Lhc collisions.

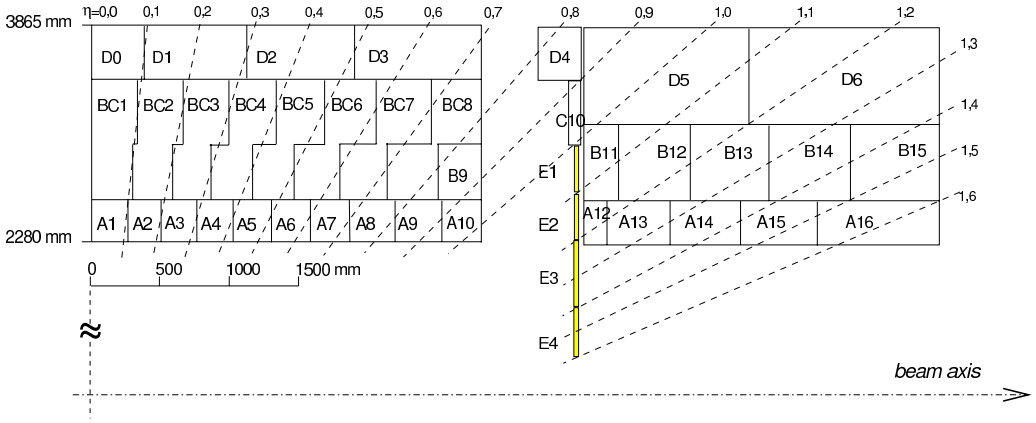

Fig. D.1: Longitudinal view of the Atlas tile calorimeter cell geometry [176]. The Long Barrel and Extended Barrel parts are shown for positive pseudo-rapidity and positive z (one quarter of longitudinal plane). The layers and cells are shown and their corresponding η-coverage is indicated.

D.1 Minimum Bias Data

During Lhc collisions the majority of the events taking place are low-momentum scattering events. These events can be triggered by requiring a minimum number of hits in the MBTS cells. The corresponding data sample is called 'minimum bias' (MB) data, where the term refers to the minimum requirement on the data selection. The MB currents are those measured by the photo multiplier tubes (PMTs) of the TileCal for the MB data. The MB system that uses

this data is one of four systems within the TileCal that are responsible for the monitoring and calibration of the detector. The calibration chain scheme is shown in Fig. D.2. The cesium system relies on a ^{137}Cs source that is moved through the detector via hydraulic tubes. Thereby it tests the whole readout chain from scintillators to fibers and PMTs. The laser system uses laser light to measure gain variations of the PMTs. The charge injection system monitors the front-end electronics of the readout. The blue part highlighted in Fig. D.2 shows the path of minimum bias and cesium signals. The corresponding signals are processed with the slow integrator readout (fast readout is used in physics analyses). Integrator currents are recorded for all (∼10 000) readout channels. The currents are measured about 20-25 times per lumiblock time interval and averaged over when stored. This data can be used to (1) monitor the instantaneous luminosity and to (2) detect response variations of the detector cells due to irradiation. These are two important measurements that will be described in more detail in the next sections.

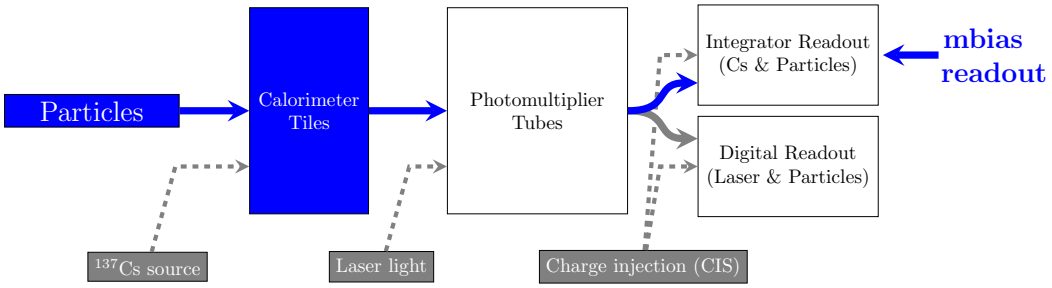

Fig. D.2: Scheme of the TileCal signal path [177]. Different calibration systems are indicated that monitor the various TileCal components at different stages in the signal development.

D.2 Luminosity Monitoring

MB currents that are readout by the integrator system during collisions are linearly dependent on the instantaneous luminosity. The more particles produced at a time, the higher the currents. Figure D.3 confirms this behaviour for the currents of cell D5 (C-side) as measured during the 2015 data taking period. The currents are drawn versus the instantaneous luminosity as measured by LUCID [178]. LUCID is a Cherenkov detector located upstream of the ATLAS detector dedicated to the luminosity measurement. The profile can be fitted with a linear function and the function and the data show a good agreement, which can be seen in the ratio plot of Fig. D.3. The shown cell D5 lies in the region of $0.9 < |\eta| < 1.1$ and is protected from irradiation by the other two layers. The response of this cell is thus rather stable in time during the 2015 data taking. This is a prerequisite for a linear behaviour. Figure D.4 shows the same relation for the same cell during 2016 data taking for the A-side. The luminosity range is wider, starting at $2{\cdot}10^{33}$ cm^{-2}s^{-1} going up to more than $11{\cdot}10^{33}$ cm^{-2}s^{-1}. This shows that the linear behaviour can be recovered for a larger span, about an order of magnitude, in $\mathcal{L}$. The fitted slope of the linear function is called *luminosity coefficient*. This coefficient simply denotes current/instantaneous luminosity and can be also obtained in single runs. Since in general the response of TileCal cells can vary over time (discussion in next section), the luminosity coefficient can vary as well. The luminosity coefficient extracted from an early run, without response degradation, is assumed to be constant and can be used to estimate the total collected charge of the PMTs over a given time. The plots in Fig. D.5 show the luminosity coefficients obtained in early runs during 2012 and 2016 data taking. It is shown for all TileCal cells and drawn against

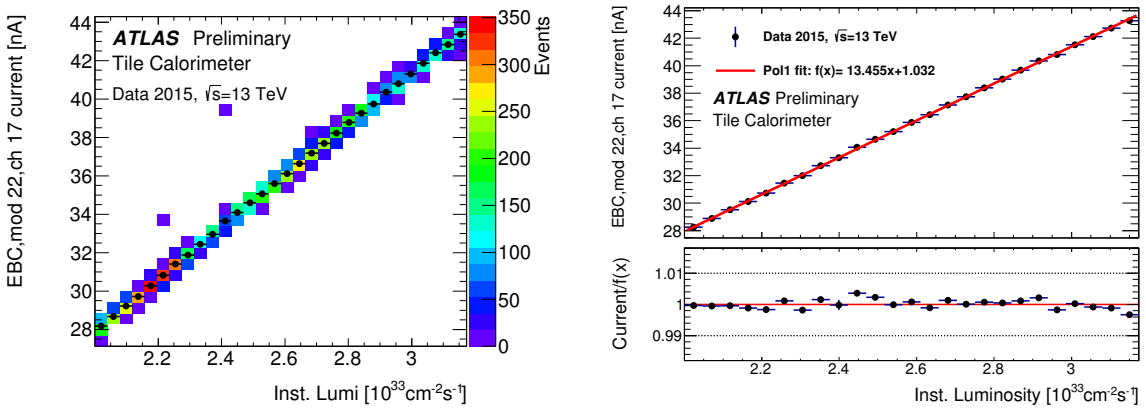

Fig. D.3: MB current vs. instantaneous luminosity for cell D5 (C-side) during 2015 data taking period [179, 180]. The left side shows the 2d-map of (current, luminosity) pairs with the profile drawn on top as black points. The right side shows the same profile, this time fitted with a linear function. The fit-parameters are displayed in the upper panel, while the ratio of data/fitted function is shown in the lower panel.

the corresponding η_{cell}. The currents of the E-cells are only shown in the 2016 data since they were not read-out in Run 1 (2011-2012 data periods). It is expected that the coefficients measured during data periods with $\sqrt{s} = 13$ TeV are related to the $\sqrt{s} = 8$ TeV coefficients via coefficient($\sqrt{s} = 13$ TeV)= 13/8×coefficient($\sqrt{s} = 8$ TeV) because the MB currents also depend linearly on the centre-of-mass energy of the collisions. This is exactly what can be observed from these plots, where the relation is about 1.6. Apart from that the curves are similar between the two data periods. They show distinctive behaviour which results from the position of the individual TileCal cells within the calorimeter. The highest currents are measured for the A-cells which are closest to the beam line. Consequently, the lowest currents are measured for the D-layer cells. The special E-cells exhibit even larger currents than any A-cells because they are even closer to the beam line. The curves also show distinctive maxima at around $|\eta| \sim 1.2$: This is partly due to the nature of pp-collisions producing mostly particles that are scattered into a forward region (proton PDFs) but also due to less material in front of the TileCal in this region. Cells that measure the highest currents are the ones that are most irradiated. Apart from the E-cells, the cell A13 is the most irradiated cell which measures the highest currents.

D.3 Irradiation Studies

Besides luminosity monitoring, MB currents also allow to monitor the detector response in time. This is only possible by having a reference cell which is stable in time. Such a reference cell should be protected by inner TileCal layers and measure significant currents in order to reduce uncertainties on the measurement due to statistical fluctuations. Such a reference cell can then be used for luminosity monitoring over the whole data taking period. Here, the cells D5 (2015) and D6 (2016) are used as references. They both lie in the D-layer of the EB. In order to assess the response variation of a given TileCal cell one builds the ratio of MB currents: current(probe cell)/current(reference cell). Since there is one current measurement for each lumiblock, a single run has to be averaged over the number of lumiblock measurements. Figure D.6 shows these currents for an example run taken in 2015: the ratio of current(A13)/current(D5) is shown where A13 is the probe cell and D5 the reference cell. The number of measurements (lumiblock

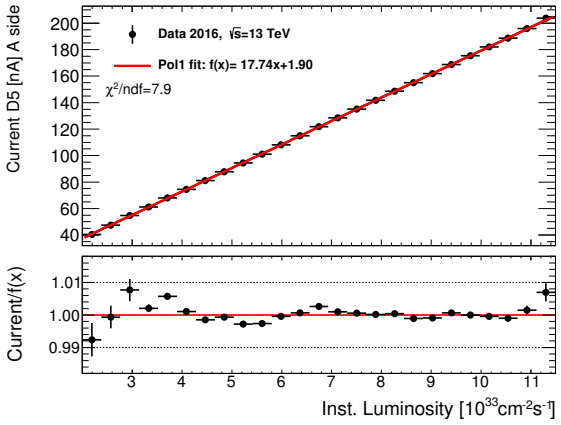

Fig. D.4: MB currents vs. instantaneous luminosity during 2016 data taking for cell D5, A-side. The data is fitted by a linear function. The fit-parameters are displayed in the upper panels, while the ratios data/fitted function are shown in the lower panels.

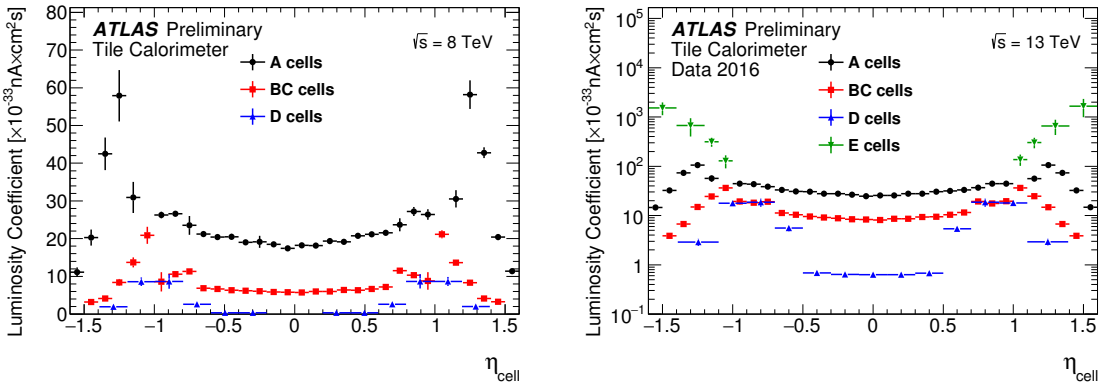

(a) 2012 data

(b) 2016 data

Fig. D.5: Luminosity coefficient vs. η for run 207046 taken during 2012 data period (a) and for run 298633 taken during 2016 data period (b) [179, 180]. Both runs were recorded at the beginning of the corresponding data taking period.

entries) follows a normal distribution. Consequently a Gaussian is fitted to the distribution in order to obtain one single mean value plus its uncertainty. In this way, the mean can be build for all runs in a given data period. The runs correspond to certain times. The variation of the obtained mean values per run w. r. t. a start run is the response variation as measured by the MB system. This is done for each PMT channel individually. In order to obtain a single expression for a given cell, all variations of individual channels($\times$64 modules) belonging to a cell are averaged over. The runs taken into account for the MB measurement must satisfy the GRL used for physics analyses and certain quality criteria (long runs with enough statistics and removal of outliers from the current's ratio).

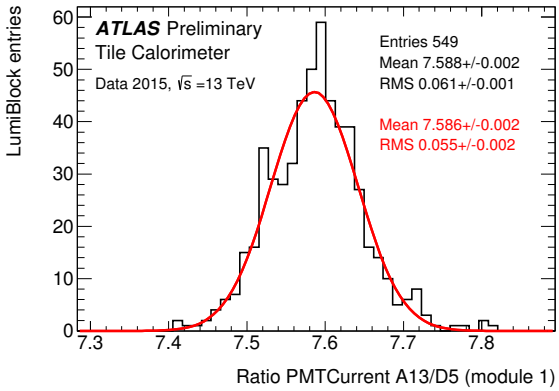

Fig. D.6: Current of probe cell A13 over current of reference cell D5 in run 271048 (2015) for all lumiblock entries [177]. The black histogram is fitted with a Gaussian. The red numbers are the fitted parameters, the black numbers the quantities of the histogram.

The response variation of TileCal cells is also determined with the help of the cesium calibration system. Since this also measures the response of the scintillators and PMTs at the same time, the variations should be similar for the cesium and MB system. On the other hand, the laser calibration system measures only the PMT gain drifts in time. There is no information on the scintillator's behaviour in time. If cesium, MB and laser measurements coincide with each other the conclusion will be that the response variation of the detector is entirely due to the PMT gain drifts. If the variation measured by the laser system is smaller, then the conclusion is that there is a response degradation in the scintillators as well which is ascribed to *irradiation* effects. By comparing cesium and MB measurements with laser measurements possible irradiation effects of the tile scintillators can be studied.
These studies have been performed separately for the two data taking periods of 2015 and 2016. First, the results for 2015 are presented followed by the 2016 results. For both years, the cells A13, E1, E2, E3 and E4 were studied in more detail since these are the ones that have the highest exposure (highest measured currents) of the TileCal.

D.3.1 Irradiation studies in 2015

In 2015, the total integrated luminosity delivered to ATLAS was 4.2 fb^{-1} [100]. The response variations for the cells A13 and E1, E2, E3, E4 are compared between MB, cesium and laser measurements in Fig. D.7. The laser data points are the ones that are taken with highest frequency throughout the collision period. All measurements shown in these graphs are normalised to the first laser measurement. Down drifts observed by the laser measurement indicate down variations of the PMT gains. These occur during collision runs. Whenever there was a machine stop ($\equiv$ no collisions) the PMTs recover and the blue graphs show up-drifts. For the better understanding the plots are underlayed with the integrated luminosity in grey. Whenever the luminosity is constant there was a period of machine development. The cesium measurements can only be done in these periods. During 2015 data taking, four cesium scans have been performed and the results for A13 are displayed in Fig. D.7(a). MB measurements are done with the actual collision data, hence the green MB points are only present in collision periods. The comparison of the different calibration systems show that there is a good agreement amongst them. There is a slight difference of less than 0.5% between MB and laser for the E3 and E4 cells at the end of the data taking. Overall there is no hint of scintillator irradiation produced in 2015 *pp*-collisions. The irradiation effects can be assessed by subtracting the gain variation measured

by the laser system from the MB variation. In order to see a dependence of an irradiation effect on the collected charge of a PMT, the luminosity coefficient is used. The collected charge Q at a given time t is given by

$$Q(t) = \int_{t_{\text{start}}}^{t} \mathcal{L}\mathrm{d}t' \times \text{luminosity coefficient}.$$

This can be calculated for individual channels of the TileCal. Figure D.8 shows the irradiation effect vs. the collected charge in selected cells during 2015 data taking. Figure D.8(a) shows individual channels of the A-layer of the EB. As anticipated by the plots in Fig. D.7, no irradiation effect is detected on average. The collected charge reaches up to about 450 mC. Figure D.8(b) adds the channels of the E-cells to the plot in Fig. D.8(a). Due to the higher currents measured in the E-cells, the collected charge reaches up to values of 8 C in the region of high $|\eta|$. The data points show the profile of the individual channels. In the region where the collected charge is similar, A-layer cells and E-cells show the same behaviour. For high integrated charges there is a small deviation of the order of 0.5% away from 0 in the irradiation effect. This tendency has been already observed in Fig. D.7. Still, the conclusion is that there was no irradiation effect observed during 2015 data taking.

D.3.2 Irradiation studies in 2016

The same studies have been performed for the 2016 data period. Here, the difference is that the cesium calibration scan was only performed at the beginning of the collision period (problem with hydraulic leak). Therefore, no comparison with cesium measurements could be performed. The delivered luminosity was almost 10 times higher than in 2015, with about 39 fb^{-1} [100]. Since the reference cell D5 itself was experiencing significant gain drifts, this cell was no longer used as reference for the MB studies. Instead, cell D6 was found to be reasonably stable and used as reference. Figure D.9 shows the results of the response variation for MB and laser measurements. Again, the luminosity is underlayed as grey background and phases of machine development are reflected in up-drifts of the PMT gains. Albeit, during 2016 data taking the up-drifts are not as visible as in 2015, also, there is a lack of measurements in the machine development phase in September 2016. The same cells as in 2015 are studied. This time, the MB measurements deviate strongly from the laser measurements. This deviation starts at around ~ 7 fb^{-1}. At the end of the year, the differences between laser and MB range from 3% up to 5%. This deviation is attributed to scintillator irradiation effects. The biggest discrepancy can be observed for E4. The luminosity coefficient for this cell amounts to $\sim 1.6 \cdot 10^{-30}$ nAcm^2s, while for A13 it is $\sim 0.105 \cdot 10^{-30}$ nAcm^2s. This means that the exposure of E4 is about 15 times higher as the one for A13 (see also Fig. D.5(b)). Consequently, the same discrepancy between MB and laser measurements as for E4 is expected for A13 if the luminosity is about 15 times higher. The studies of irradiation effect vs. collected charge are repeated. This time, a slope is expected. Figure D.10 shows the results, here only for A13 and the four E-cells. Figure D.10(a) shows the measurements for the individual channels with their averaged profile overlayed on top. Channels with different pseudo-rapidities but similar integrated charge show a similar irradiation effect. This is expected since there is no known reason why the η-position should have an impact on the robustness against irradiation. The average integrated charge is ~ 63 C (individual channels can reach higher charges due to higher luminosity coefficients, at most ~ 160 C) due to the increased luminosity. The maximal irradiation effect observed is just under 5% at the end of data taking. Following the curve visible in Fig. D.10(a) it seems that the (negative) irradiation effect increases not only linearly with increasing charge collection.

Instead, the irradiation suggests an exponential trend of the kind: irradiation$=-2^{\log_{10}\text{charge [C]}}$. Figure D.11 shows the irradiation studies for the A-layer and B-layer cells for 2016 data taking and the averaged profile per cell only. For the cells in the middle layer in Fig. D.11(b) the irradiation effect is only weak, around 0.6% for the most irradiated cells. For the A-layer the slopes observed in A13 and A14 are different from the ones in A12, A15 and A16. This is at first glance unexpected. However, if it is true that the irradiation does not depend linearly on the collected charge then it might also be true that more exposed cells develop an irradiation robustness leading to a smaller irradiation effect overall (keeping in mind that the same cells/-modules have already been irradiated during Run 1 data taking). A combination of 2015+2016 datasets corresponding to 44 fb^{-1} of integrated luminosity and the measured irradiation vs. total collected charge is shown in Fig. D.12.
Another study can be performed with regard to the irradiation robustness of different materials that have been used as scintillators in different TileCal modules. Modules of E3 and E4 are made of four different materials: the original material, that is PVT-based (polyvinyltoluene), the same, but not irradiated (new), Eljen and Bicron. Figure D.10(b) shows these four materials and their irradiation effect vs. collected charge. Most of the modules are made up of original material. There is a tendency that this seems to be more robust against irradiation compared to the Eljen and Bicron materials. There, the average irradiation effect goes down to more than 8% (Eljen) and more than 10% (Bicron).

D.4 Conclusion

The MB system is capable of monitoring the luminosity as well as the detector response in time. It is a stand-alone system that can quantify the irradiation effect, which is of particular importance for 2016 data taking where no cesium scan could be performed during the data taking period. The observed irradiation effect reaches up to 5% for the most exposed E-cells. The most irradiated regular cell is A13 with about 3% irradiation effect. The effect is minor in the B-layer of the EB with a maximum 0.6%. This implies a similar negligible effect for the A-layer cell of the LB, since the MB currents measured are of the same order. The observed response degradation from the MB system will be used in the reprocessing of the 2016 data (the PMT drifts are immediately forwarded to the data processing). This will have an effect on the jet energy measurement which is likely underestimated but dominated by the measurement of the electromagnetic calorimeter.
The irradiation hardness of different scintillator materials can also be compared via MB measurements. The studies shown here imply that Eljen and Bicron are less irradiation hard than the original scintillator material. The scintillators used in the LB are PSM polystyrene and BASF. Differences of these materials can be studied once a significant irradiation effect can be observed in the future with higher accumulated integrated luminosities.

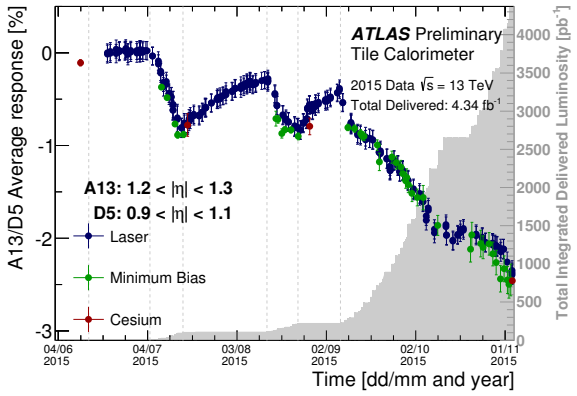

(a) A13

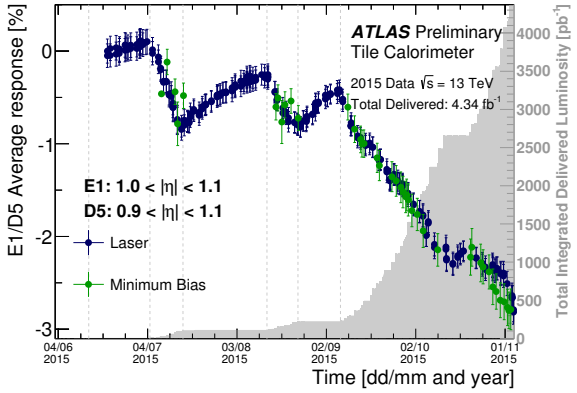

(b) E1

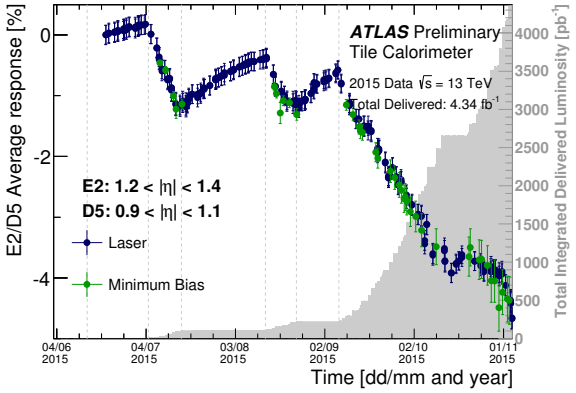

(c) E2

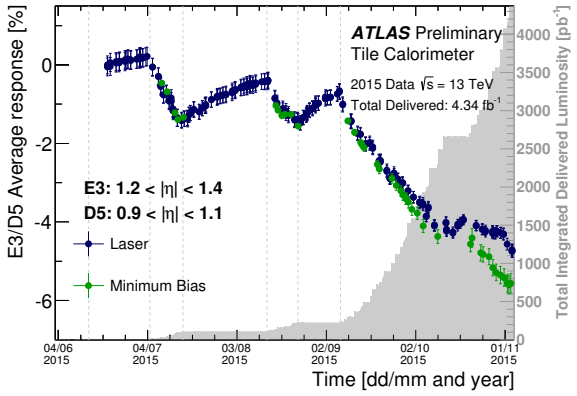

(d) E3

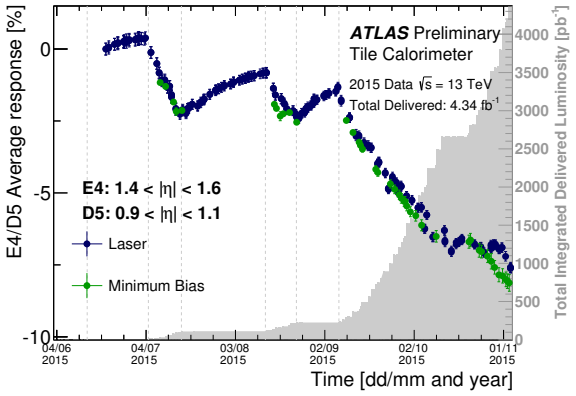

(e) E4

Fig. D.7: Response variation measured from MB currents (green dots) compared to the measurements of the cesium (red) and laser (blue) system for probe cells A13, E1, E2, E3 and E4 w. r. t. D5 during the 2015 data taking period [177, 180].

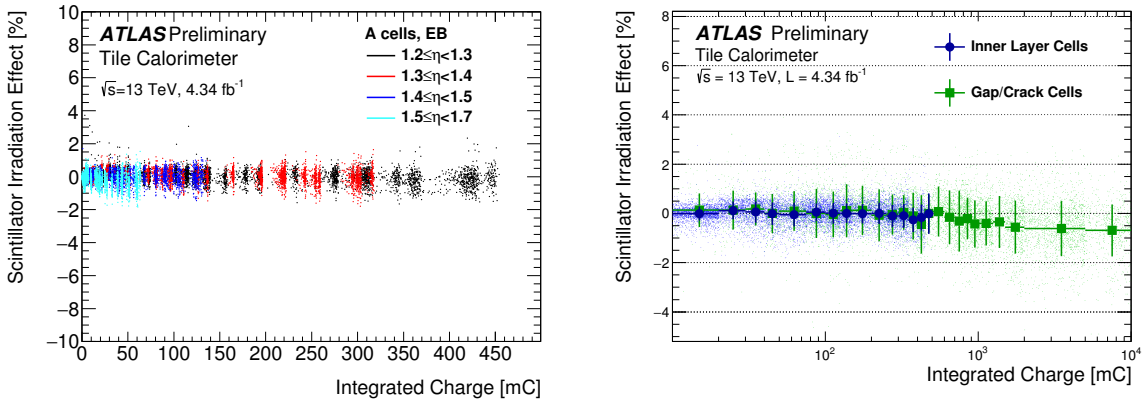

(a) (b)

Fig. D.8: Irradiation effect vs. collected charge [177, 180]: (a) Irradiation effect as measured for A-cells of the EB during 2015 data taking. (b) Irradiation effect compared for A-cells of EB and E-cells.

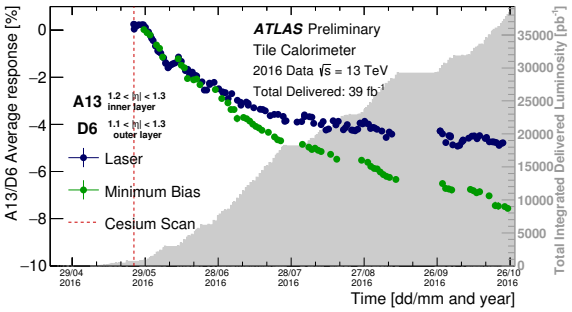

(a) A13

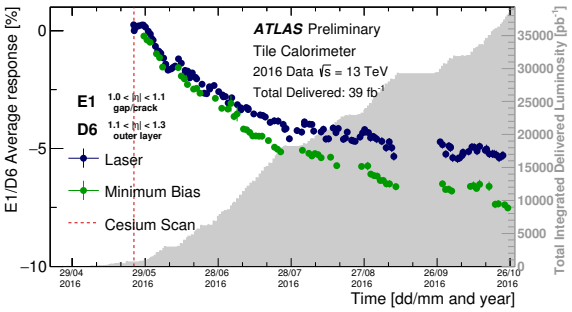

(b) E1

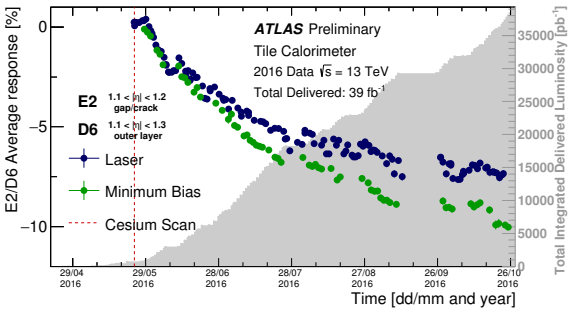

(c) E2

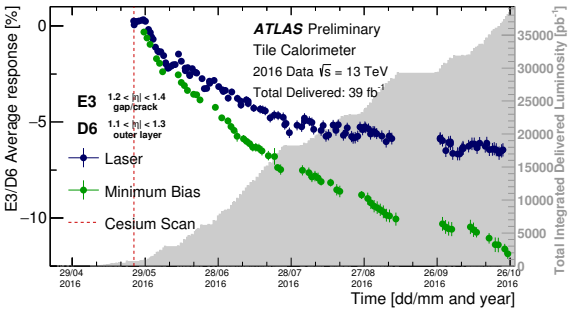

(d) E3

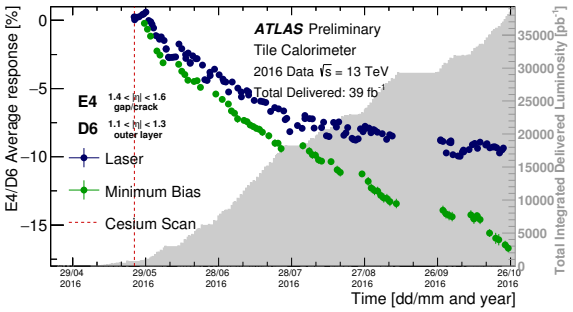

(e) E4

Fig. D.9: Response variation measured from MB currents (green dots) compared to the measurements of the cesium (red) and laser (blue) system for probe cells A13, E1, E2, E3 and E4 w. r. t. D6 during the 2016 data taking period [177].

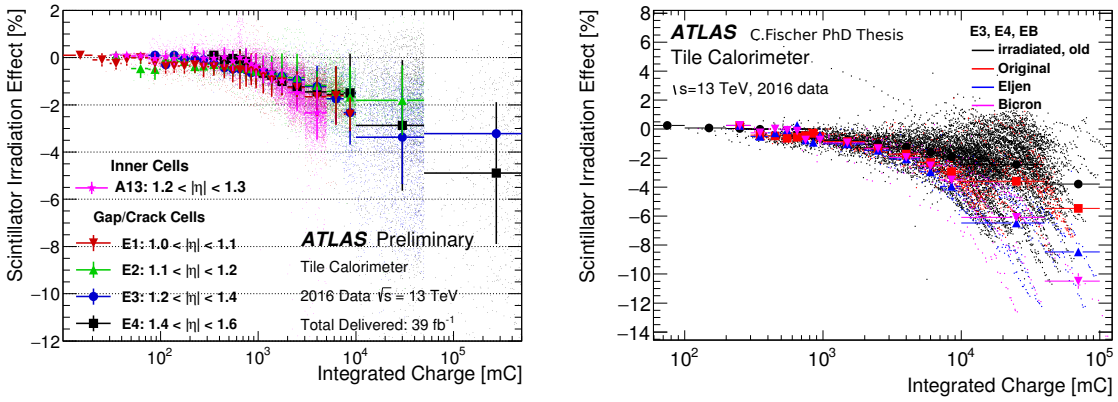

(a) (b)

Fig. D.10: Irradiation effect vs. collected charge measured in 2016 data: (a) Channels of A13 and E-cells with the averaged profile overlayed [177]. (b) Channels of E3 and E4: the profile is shown for different scintillator material (period of about 25 fb^{-1} covered).

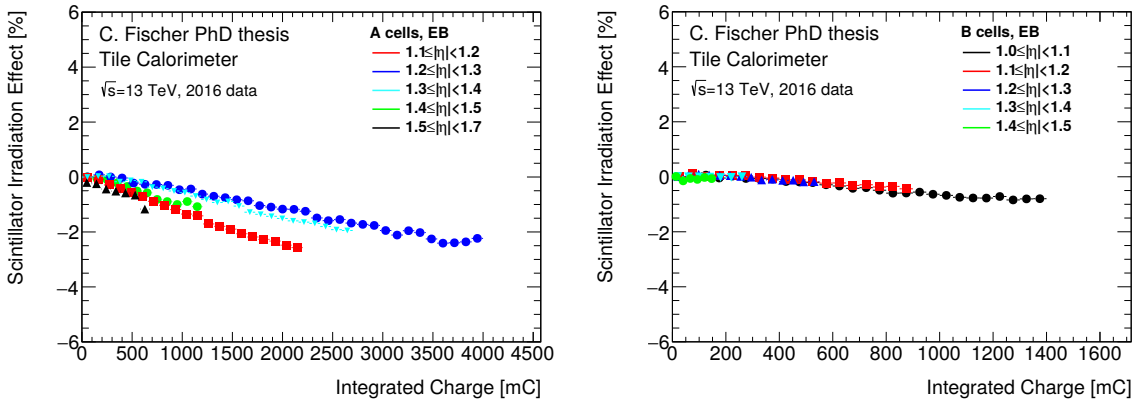

(a) A-layer, EB (b) B-layer, EB

Fig. D.11: Irradiation effect vs. integrated charge for the 2016 dataset. (a) A-layer cells of the EB, (b) B-layer cells of the EB.

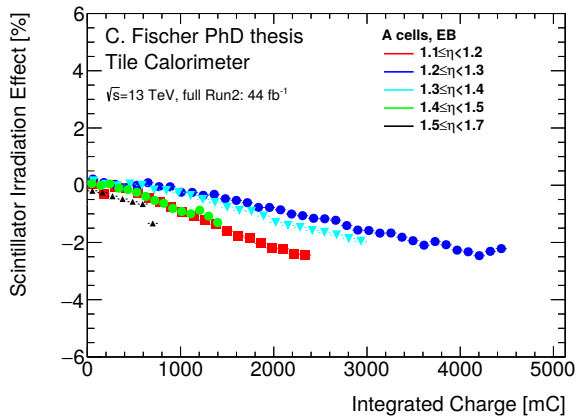

Fig. D.12: Irradiation effect vs. integrated charge for the combined 2015+2016 datasets for cells of the extended barrel A-layer.

Bibliography

[1] ATLAS Collaboration, *Observation of a new particle in the search for the Standard Model Higgs boson with the ATLAS detector at the LHC*, Phys.Lett. **B716**, 1 (2012)

[2] CMS Collaboration, *Observation of a new boson at a mass of 125 GeV with the CMS experiment at the LHC*, Phys.Lett. **B716**, 30 (2012)

[3] S. Weinberg, *The Making of the Standard Model*, Eur. Phys. J. C **34**, 5 (2004)

[4] A. Salam, *Weak and Electromagnetic Interactions*, ed. Nobel Symposium No. 8 (Almqvist & Wiksell, Stockholm, 1968)

[5] D. J. Gross, F. Wilczek, *Asymptotically Free Gauge Theories*, Phys. Rev. D **8**, 3633 (1973)

[6] S. Weinberg, *A Model of Leptons*, Phys. Rev. Lett. **19**, 1264 (1967)

[7] H. D. Politzer, *Asymptotic Freedom: An Approach to Strong Interactions*, Phys. Rept. **14**, 129 (1974)

[8] C. Patrignani, et al. (Particle Data Group), *Review of Particle Physics*, Chin. Phys. **C40(10)**, 100001 (2016)

[9] C. Kraus, et al., *Final results from phase II of the Mainz neutrino mass searchin tritium β decay*, The European Physical Journal C - Particles and Fields **40(4)**, 447 (2005)

[10] V. N. Aseev, et al., *Upper limit on the electron antineutrino mass from the Troitsk experiment*, Phys. Rev. D **84**, 112003 (2011)

[11] K. Assamagan, et al., *Upper limit of the muon-neutrino mass and charged-pion mass from momentum analysis of a surface muon beam*, Phys. Rev. D **53**, 6065 (1996)

[12] R. Barate et al., *An upper limit on the τ neutrino mass from three- and five-prong tau decays*, The European Physical Journal C - Particles and Fields **2(3)**, 395 (1998)

[13] M. Altmann, et al. (GNO COLLABORATION), *Complete results for five years of GNO solar neutrino observations*, Phys.Lett. **B616**, 174 (2005)

[14] M. H. Ahn, et al. (K2K Collaboration), *Measurement of neutrino oscillation by the K2K experiment*, Phys. Rev. D **74**, 072003 (2006)

[15] Y. Fukuda, et al. (The Super-Kamiokande Collaboration), *Measurement of the Flux and Zenith-Angle Distribution of Upward Throughgoing Muons by Super-Kamiokande*, Phys. Rev. Lett. **82**, 2644 (1999)

[16] P. Adamson, et al. (MINOS Collaboration), *Measurement of the Neutrino Mass Splitting and Flavor Mixing by MINOS*, Phys. Rev. Lett. **106**, 181801 (2011)

[17] T. Lasserre, et al., *Comment on Phys. Rev. Lett. 108, 191802 (2012): 'Observation of Reactor Electron Antineutrino Disappearance in the RENO Experiment'* (2012)

[18] H. Georgi, S. L. Glashow, *Unified Weak and Electromagnetic Interactions without Neutral Currents*, Phys. Rev. Lett. **28**, 1494 (1972)

[19] M. Goldhaber, L. Grodzins, A. W. Sunyar, *Helicity of Neutrinos*, Phys. Rev. **109**, 1015 (1958)

[20] N. Cabibbo, *Unitary Symmetry and Leptonic Decays*, Phys. Rev. Lett. **10**, 531 (1963)

[21] M. Kobayashi, T. Maskawa, *CP Violation in the Renormalizable Theory of Weak Interaction*, Prog. Theor. Phys. **49**, 652 (1973)

[22] Z. Maki, M. Nakagawa, S. Sakata, *Remarks on the unified model of elementary particles*, Progress of Theoretical Physics **28(5)**, 870 (1962)

[23] B. Pontecorvo, *Neutrino experiments and the problem of conservation of leptonic charge*, Sov. Phys. JETP **26(984-988)**, 165 (1968)

[24] B. Pontecorvo, *Mesonium and antimesonium*, Zhur. Eksptl'. i Teoret. Fiz. **33** (1957)

[25] P. Higgs, *Broken symmetries, massless particles and gauge fields*, Physics Letters **12(2)**, 132 (1964)

[26] F. Englert, R. Brout, *Broken Symmetry and the Mass of Gauge Vector Mesons*, Phys. Rev. Lett. **13**, 321 (1964)

[27] G. S. Guralnik, C. R. Hagen, T. W. B. Kibble, *Global Conservation Laws and Massless Particles*, Phys. Rev. Lett. **13**, 585 (1964)

[28] *Combined Measurement of the Higgs Boson Mass in pp Collisions at* $\sqrt{s} = 7$ *and 8 TeV with the ATLAS and CMS Experiments*, Phys. Rev. Lett. **114**, 191803 (2015)

[29] F. Zwicky, *On the Masses of Nebulae and of Clusters of Nebulae*, Astrophysical Journal **86**, 217 (1937)

[30] V. C. Rubin, W. K. Ford, Jr., *Rotation of the Andromeda Nebula from a Spectroscopic Survey of Emission Regions*, APJ **159**, 379 (1970)

[31] C. L. Bennett, et al., *First-Year Wilkinson Microwave Anisotropy Probe (WMAP) Observations: Foreground Emission*, The Astrophysical Journal Supplement Series **148(1)**, 97 (2003)

[32] P. Ade, et al. (Planck Collaboration), *Planck 2013 results. I. Overview of products and scientific results* (2013)

[33] E. Majorana, *Teoria simmetrica dell'elettrone e del positrone*, Il Nuovo Cimento **14(4)**, 171 (1937)

[34] R. N. Cahn, *The Eighteen arbitrary parameters of the standard model in your everyday life*, Rev.Mod.Phys. **68**, 951 (1996)

[35] T. Kaluza, *On the Problem of Unity in Physics*, Sitzungsber. Preuss. Akad. Wiss. Berlin (Math. Phys.) **1921**, 966 (1921)

[36] O. Klein, *Quantum Theory and Five-Dimensional Theory of Relativity. (In German and English)*, Z. Phys. **37**, 895 (1926), [Surveys High Energ. Phys.5,241(1986)]

[37] L. Randall, R. Sundrum, *Large Mass Hierarchy from a Small Extra Dimension*, Phys. Rev. Lett. **83**, 3370 (1999)

[38] N. Arkani–Hamed, S. Dimopoulos, G. Dvali, *The hierarchy problem and new dimensions at a millimeter*, Physics Letters B **429(3–4)**, 263 (1998)

[39] S. P. Martin, *A Supersymmetry primer* (1997), [Adv. Ser. Direct. High Energy Phys.18,1(1998)]

[40] H. Nishino, et al. (Super-Kamiokande Collaboration), *Search for Proton Decay via $p \to e^+\pi^0$ and $p \to \mu^+\pi^0$ in a Large Water Cherenkov Detector*, Phys.Rev.Lett. **102**, 141801 (2009)

[41] K. G. Begeman, A. H. Broeils, R. H. Sanders, *Extended rotation curves of spiral galaxies - Dark haloes and modified dynamics*, MNRAS **249**, 523 (1991)

[42] Y. Sofue, *The Most Completely Sampled Rotation Curves for Galaxies*, APJ **458**, 120 (1996)

[43] Y. Sofue, *Nuclear-to-Outer Rotation Curves of Galaxies in the CO and HI Lines*, PASJ **49**, 17 (1997)

[44] R. H. Sanders, M. A. W. Verheijen, *Rotation curves of uma galaxies in the context of modified newtonian dynamics*, Astrophys. J. **503**, 97 (1998)

[45] R. B. Tully, M. A. W. Verheijen, M. J. Pierce, J.-S. Huang, R. J. Wainscoat, *The ursa major cluster of galaxies. I. cluster definition and photometric data*, Astron. J. **112**, 2471 (1996)

[46] D. Clowe, M. Bradac, A. H. Gonzalez, M. Markevitch, S. W. Randall, C. Jones, D. Zaritsky, *A direct empirical proof of the existence of dark matter*, Astrophys. J. **648**, L109 (2006)

[47] C. J. Copi, D. Huterer, D. J. Schwarz, G. D. Starkman, *On the large-angle anomalies of the microwave sky*, Monthly Notices of the Royal Astronomical Society **367(1)**, 79 (2006)

[48] R. Adam, et al. (Planck), *Planck 2015 results. I. Overview of products and scientific results*, Astron. Astrophys. **594**, A1 (2016)

[49] M. Lovell, et al., *The Haloes of Bright Satellite Galaxies in a Warm Dark Matter Universe* (2011)

[50] E. Aprile, et al. (XENON100 Collaboration), *The XENON100 Dark Matter Experiment* (2011)

[51] Z. Ahmed, et al. (The CDMS-II), *Dark Matter Search Results from the CDMS II Experiment*, Science **327**, 1619 (2010)

[52] D. S. Akerib, et al. (LUX), *Improved Limits on Scattering of Weakly Interacting Massive Particles from Reanalysis of 2013 LUX Data*, Phys. Rev. Lett. **116(16)**, 161301 (2016)

[53] R. F. Lang, W. Seidel, *Search for Dark Matter with CRESST*, New J. Phys. **11**, 105017 (2009)

[54] *The Large Area Telescope on the Fermi Gamma-Ray Space Telescope Mission*, The Astrophysical Journal **697(2)**, 1071 (2009)

[55] J. Cortina, F. Goebel, T. Schweizer, for the MAGIC Collaboration, *Technical Performance of the MAGIC Telescopes*, ArXiv e-prints (2009)

[56] J. Ahrens, et al. (IceCube), *Sensitivity of the IceCube detector to astrophysical sources of high energy muon neutrinos*, Astropart. Phys. **20**, 507 (2004)

[57] E. Aslanides, et al. (ANTARES), *A deep sea telescope for high-energy neutrinos* (1999), astro-ph/9907432

[58] J. Goodman, M. Ibe, A. Rajaraman, W. Shepherd, T. M. P. Tait, H.-B. Yu, *Constraints on Dark Matter from Colliders*, Phys. Rev. **D82**, 116010 (2010)

[59] D. Abercrombie, et al., *Dark Matter Benchmark Models for Early LHC Run-2 Searches: Report of the ATLAS/CMS Dark Matter Forum* (2015)

[60] O. Buchmueller, M. J. Dolan, S. A. Malik, C. McCabe, *Characterising dark matter searches at colliders and direct detection experiments: vector mediators*, Journal of High Energy Physics **2015(1)**, 37 (2015)

[61] G. Busoni, A. D. Simone, E. Morgante, A. Riotto, *On the validity of the effective field theory for dark matter searches at the {LHC}*, Physics Letters B **728**, 412 (2014)

[62] M. Papucci, A. Vichi, K. M. Zurek, *Monojet versus the rest of the world I: t-channel models*, JHEP **11**, 024 (2014)

[63] H. An, L.-T. Wang, H. Zhang, *Dark matter with t-channel mediator: a simple step beyond contact interaction*, Phys. Rev. **D89(11)**, 115014 (2014)

[64] U. Haisch, F. Kahlhoefer, T. M. P. Tait, *On Mono-W Signatures in Spin-1 Simplified Models*, Phys. Lett. **B760**, 207 (2016)

[65] M. Wing (ZEUS, H1), *Measurements of deep inelastic scattering at HERA*, in *Proceedings, 32nd International Symposium on Physics in Collision (PIC 2012): Strbske Pleso, Slovakia, September 12-15, 2012*, pages 93–106 (2013)

[66] ATLAS collaboration, *Determination of the strange quark density of the proton from ATLAS measurements of the $W \to \ell\nu$ and $Z \to \ell\ell$ cross sections*, Phys. Rev. Lett. **109**, 012001 (2012)

[67] H.-L. Lai, M. Guzzi, J. Huston, Z. Li, P. M. Nadolsky, et al., *New parton distributions for collider physics*, Phys.Rev. **D82**, 074024 (2010)

[68] *Online PDF plotting and calculation*, retrieved on 27/02/2013, http://hepdata.cedar.ac.uk/pdf/pdf3.html

[69] M. Denny, *Introduction to importance sampling in rare-event simulations*, European Journal of Physics **22(4)**, 403 (2001)

[70] T. Sjöstrand, *Monte Carlo Generators* pages 51–74 (2006)

[71] T. Sjostrand, S. Mrenna, P. Z. Skands, *PYTHIA 6.4 Physics and Manual*, JHEP **0605**, 026 (2006)

[72] G. Corcella, et al., *HERWIG 6: an event generator for hadron emission reactions with interfering gluons (including supersymmetric processes)*, J. High Energy Phys. **0101**, 010 (2001)

[73] T. Gleisberg, S. Hoeche, F. Krauss, A. Schälicke, S. Schumann, J. Winter, *SHERPA 1.α, a proof-of-concept version*, J. High Energy Phys. **0402**, 056 (2004)

[74] G. Altarelli, G. Parisi, *Asymptotic freedom in parton language*, Nuclear Physics B **126(2)**, 298 (1977)

[75] V. Gribov, L. Lipatov, *Deep inelastic e p scattering in perturbation theory*, Sov.J.Nucl.Phys. **15**, 438 (1972)

[76] Y. L. Dokshitzer, *Calculation of the Structure Functions for Deep Inelastic Scattering and e^+e^- Annihilation by Perturbation Theory in Quantum Chromodynamics.*, Sov.Phys.JETP **46**, 641 (1977)

[77] R. K. Ellis, W. J. Stirling, B. R. Webber, *QCD and Collider Physics*, Cambridge Monographs on Particle Physics, Nuclear Physics and Cosmology (Cambridge University Press, Cambridge, 1996)

[78] V. Sudakov, *Vertex parts at very high-energies in quantum electrodynamics*, Sov.Phys.JETP **3**, 65 (1956)

[79] L. Lönnblad, *Ariadne version 4 — A program for simulation of {QDC} cascades implementing the colour dipole model*, Computer Physics Communications **71(1–2)**, 15 (1992)

[80] T. Sjostrand, *A Model for Initial State Parton Showers*, Phys. Lett. **B157**, 321 (1985)

[81] S. Catani, F. Krauss, R. Kuhn, B. Webber, *QCD matrix elements + parton showers*, JHEP **0111**, 063 (2001)

[82] M. L. Mangano, M. Moretti, F. Piccinini, M. Treccani, *Matching matrix elements and shower evolution for top-quark production in hadronic collisions*, JHEP **0701**, 013 (2007)

[83] M. L. Mangano, et al., *ALPGEN, a generator for hard multiparton processes in hadronic collisions*, J. High Energy Phys. **0307**, 001 (2003)

[84] S. Catani, Y. L. Dokshitzer, M. Olsson, G. Turnock, B. R. Webber, *New clustering algorithm for multi - jet cross-sections in e+ e- annihilation*, Phys. Lett. **B269**, 432 (1991)

[85] B. Andersson, G. Gustafson, G. Ingelman, T. Sjostrand, *Parton Fragmentation and String Dynamics*, Phys.Rept. **97**, 31 (1983)

[86] B. Webber, *A QCD Model for Jet Fragmentation Including Soft Gluon Interference*, Nucl.Phys. **B238**, 492 (1984)

[87] T. Sjöstrand, P. Z. Skands, *Multiple interactions and the structure of beam remnants*, Journal of High Energy Physics **2004(03)**, 053 (2004)

[88] T. Sjöstrand, M. van Zijl, *A multiple-interaction model for the event structure in hadron collisions*, Phys. Rev. D **36**, 2019 (1987)

[89] S. Agostinelli, et al. (Geant4), *GEANT4: A Simulation Toolkit*, Nucl. Instrum. Methods A **506**, 250 (2003)

[90] E. Richter-Was, D. Froidevaux, L. Poggioli, *ATLFAST 2.0 a fast simulation package for ATLAS* (1998)

[91] S. Frixione, P. Nason, C. Oleari, *Matching NLO QCD computations with Parton Shower simulations: the POWHEG method*, JHEP **0711**, 070 (2007)

[92] F. Maltoni, Stelzer, *MADEVENT: Automatic Event Generation with MADGRAPH*, J. High Energy Phys. **02**, 027 (2003)

[93] J. Alwall, M. Herquet, F. Maltoni, O. Mattelaer, T. Stelzer, *MadGraph 5 : Going Beyond*, JHEP **06**, 128 (2011)

[94] ATLAS Collaboration, *The ATLAS experiment at the CERN large hadron collider*, Journal of Instrumentation **3**, S08003 (2008)

[95] ATLAS Collaboration, *ATLAS detector and physics performance: Technical Design Report, 1*, Technical Design Report ATLAS, CERN, Geneva (1999)

[96] CMS Collaboration, *CMS Detector and Physics Performance Technical Design Report*, CERN/LHCC-2006-001 (2006)

[97] *ALICE: Technical proposal for a Large Ion collider Experiment at the CERN LHC*, LHC Tech. Proposal, CERN, Geneva (1995)

[98] S. Amato, et al. (LHCb Collaboration), *LHCb technical proposal* (1998)

[99] Luminosity Public Results - ATLAS Public Results (Nov. 2016), https://twiki.cern.ch/twiki/bin/view/AtlasPublic/LuminosityPublicResults

[100] Luminosity Public Results - ATLAS Public Results (Nov. 2016), https://twiki.cern.ch/twiki/bin/view/AtlasPublic/LuminosityPublicResultsRun2

[101] M. Capeans, G. Darbo, K. Einsweiller, M. Elsing, T. Flick, M. Garcia-Sciveres, C. Gemme, H. Pernegger, O. Rohne, R. Vuillermet, *ATLAS Insertable B-Layer Technical Design Report*, Technical Report CERN-LHCC-2010-013. ATLAS-TDR-19 (2010)

[102] *Track Reconstruction Performance of the ATLAS Inner Detector at* $\sqrt{s} = 13$ *TeV*, Technical Report ATL-PHYS-PUB-2015-018, CERN, Geneva (2015)

[103] ATLAS Collaboration, *ATLAS muon spectrometer: Technical design report* (1997)

[104] ATLAS Collaboration, *2015 start-up trigger menu and initial performance assessment of the ATLAS trigger using Run-2 data*, Technical Report ATL-DAQ-PUB-2016-001, CERN, Geneva (2016)

[105] ATLAS Collaboration, *Measurement of the muon reconstruction performance of the ATLAS detector using 2011 and 2012 LHC proton–proton collision data*, Eur. Phys. J. **C74(11)**, 3130 (2014)

[106] ATLAS Collaboration, *Muon reconstruction efficiency in reprocessed 2010 LHC proton-proton collision data recorded with the ATLAS detector*, Technical Report ATLAS-CONF-2011-063, CERN, Geneva (2011)

[107] ATLAS Collaboration, *Electron performance measurements with the ATLAS detector using the 2010 LHC proton-proton collision data*, The European Physical Journal C **72(3)**, 1 (2012)

[108] W. Lampl, S. Laplace, D. Lelas, P. Loch, H. Ma, S. Menke, S. Rajagopalan, D. Rousseau, S. Snyder, G. Unal, *Calorimeter Clustering Algorithms: Description and Performance*, Technical Report ATL-LARG-PUB-2008-002. ATL-COM-LARG-2008-003, CERN, Geneva (2008)

[109] ATLAS Collaboration, *Electron identification measurements in ATLAS using $\sqrt{s}$ = 13 TeV data with 50 ns bunch spacing*, Technical Report ATL-PHYS-PUB-2015-041, CERN, Geneva (2015)

[110] ATLAS Collaboration, *Electron efficiency measurements with the ATLAS detector using the 2015 LHC proton-proton collision data*, Technical Report ATLAS-CONF-2016-024, CERN, Geneva (2016)

[111] ATLAS Collaboration, *Electron and photon energy calibration with the ATLAS detector using data collected in 2015 at $\sqrt{s} = 13$* TeV, Technical Report ATL-PHYS-PUB-2016-015, CERN, Geneva (2016)

[112] ATLAS Collaboration, *Measurement of the inclusive isolated prompt photon cross section in pp collisions at $\sqrt{s} = 7$* TeV *with the ATLAS detector*, Phys. Rev. D **83**, 052005 (2011)

[113] ATLAS Collaboration, *Measurements of the photon identification efficiency with the ATLAS detector using 4.9 fb^{-1} of pp collision data collected in 2011*, Technical Report ATLAS-CONF-2012-123, CERN, Geneva (2012)

[114] ATLAS Collaboration, *Photon identification in 2015 ATLAS data*, Technical Report ATL-PHYS-PUB-2016-014, CERN, Geneva (2016)

[115] ATLAS Collaboration, *Muon reconstruction performance of the ATLAS detector in proton–proton collision data at $\sqrt{s}$ =13 TeV*, Eur. Phys. J. **C76(5)**, 292 (2016)

[116] M. Cacciari, G. P. Salam, G. Soyez, *The anti-k_t jet clustering algorithm*, JHEP **04**, 063 (2008)

[117] M. Cacciari, G. P. Salam, *Dispelling the N^3 myth for the k_t jet-finder*, Phys. Lett. B **641**, 57 (2006)

[118] M. Cacciari, G. P. Salam, G. Soyez, *FastJet User Manual*, Eur. Phys. J. C **72**, 1896 (2012)

[119] ATLAS Collaboration, *Topological cell clustering in the ATLAS calorimeters and its performance in LHC Run 1* (2016)

[120] ATLAS Collaboration, *Luminosity determination in pp collisions at $\sqrt{s}$ = 8 TeV using the ATLAS detector at the LHC*, Eur. Phys. J. **C76(12)**, 653 (2016)

[121] ATLAS Collaboration, *ATLAS LUCID detector upgrade for LHC Run 2*, Technical Report ATL-FWD-PROC-2015-004, CERN, Geneva (2015)

[122] V. Cindro, et al., *The ATLAS Beam Conditions Monitor*, Journal of Instrumentation **3(02)**, P02004 (2008)

[123] T. Barillari, et al. (ATLAS), *Local hadronic calibration* (2009)

[124] M. Cacciari, G. P. Salam, *Pileup subtraction using jet areas*, Physics Letters B **659(1–2)**, 119 (2008)

[125] ATLAS Collaboration, *Jet Calibration and Systematic Uncertainties for Jets Reconstructed in the ATLAS Detector at* $\sqrt{s} = 13$ *TeV*, ATL-PHYS-PUB-2015-015 (2015)

[126] ATLAS Collaboration, *Jet global sequential corrections with the ATLAS detector in proton-proton collisions at sqrt(s) = 8 TeV*, Technical Report ATLAS-CONF-2015-002, CERN, Geneva (2015)

[127] ATLAS Collaboration, *Tagging and suppression of pileup jets with the ATLAS detector*, Technical Report ATLAS-CONF-2014-018, CERN, Geneva (2014)

[128] ATLAS Collaboration, *Optimisation of the ATLAS b-tagging performance for the 2016 LHC Run*, Technical Report ATL-PHYS-PUB-2016-012, CERN, Geneva (2016)

[129] ATLAS Collaboration, *Expected performance of missing transverse momentum reconstruction for the ATLAS detector at* $\sqrt{s} = 13$ *TeV*, Technical Report ATL-PHYS-PUB-2015-023, CERN, Geneva (2015)

[130] ATLAS Collaboration, *Public plots: Missing transverse energy (*$\not{E}_T$*) performance and systematic uncertainties using the full 2015 dataset* (26. Febr. 2016), http://atlas.web.cern.ch/Atlas/GROUPS/PHYSICS/PLOTS/JETM-2016-003/

[131] ATLAS Collaboration, *Search for new phenomena in final states with an energetic jet and large missing transverse momentum in pp collisions at* $\sqrt{s} = 13$ TeV *using the ATLAS detector*, Phys. Rev. D **94**, 032005 (2016)

[132] F. A. Berends, H. Kuijf, B. Tausk, W. T. Giele, *On the production of a W and jets at hadron colliders*, Nuclear Physics B **357(1)**, 32 (1991)

[133] ATLAS Collaboration, *Search for new phenomena in final states with an energetic jet and large missing transverse momentum in pp collisions at* $\sqrt{s}$ *=8 TeV with the ATLAS detector*, Eur. Phys. J. **C75(7)**, 299 (2015)

[134] ATLAS Collaboration, *Search for pair-produced third-generation squarks decaying via charm quarks or in compressed supersymmetric scenarios in pp collisions at* $\sqrt{s} = 8$ *TeV with the ATLAS detector*, Phys. Rev. **D90(5)**, 052008 (2014)

[135] LUX Collaboration, *Results on the Spin-Dependent Scattering of Weakly Interacting Massive Particles on Nucleons from the Run 3 Data of the LUX Experiment*, Phys. Rev. Lett. **116**, 161302 (2016)

[136] XENON100 Collaboration, *Limits on Spin-Dependent WIMP-Nucleon Cross Sections from 225 Live Days of XENON100 Data*, Phys. Rev. Lett. **111**, 021301 (2013)

[137] PICO Collaboration, *Dark matter search results from the PICO-60* CF_3I *bubble chamber*, Phys. Rev. D **93**, 052014 (2016)

[138] PICO Collaboration, *Improved dark matter search results from PICO-2L Run 2*, Phys. Rev. **D93(6)**, 061101 (2016)

[139] R. D. Ball, et al. (NNPDF Collaboration), *Unbiased global determination of parton distributions and their uncertainties at NNLO and at LO*, Nucl.Phys. **B855**, 153 (2012)

[140] P. Z. Skands, *Tuning Monte Carlo Generators: The Perugia Tunes*, Phys. Rev. **D82**, 074018 (2010)

[141] J. Pumplin, D. R. Stump, H. L. Lai, P. Nadolsky, W. K. Tung, *New generation of parton distributions with uncertainties from global QCD analysis*, J. High Energy Phys. **0207**, 012 (2002)

[142] D. J. Lange, *The EvtGen particle decay simulation package*, Nucl. Instrum. Meth. **A462**, 152 (2001)

[143] S. Catani, M. Grazzini, *An NNLO subtraction formalism in hadron collisions and its application to Higgs boson production at the LHC*, Phys. Rev. Lett. **98**, 222002 (2007)

[144] M. Cacciari, M. Czakon, M. Mangano, A. Mitov, P. Nason, *Top-pair production at hadron colliders with next-to-next-to-leading logarithmic soft-gluon resummation*, Phys.Lett. **B710**, 612 (2012)

[145] P. Baernreuther, M. Czakon, A. Mitov, *Percent Level Precision Physics at the Tevatron: First Genuine NNLO QCD Corrections to* $q\bar{q} \to t\bar{t}+X$, Phys.Rev.Lett. **109**, 132001 (2012)

[146] M. Czakon, A. Mitov, *NNLO corrections to top-pair production at hadron colliders: the all-fermionic scattering channels*, JHEP **1212**, 054 (2012)

[147] M. Czakon, A. Mitov, *NNLO corrections to top pair production at hadron colliders: the quark-gluon reaction*, JHEP **1301**, 080 (2013)

[148] M. Czakon, P. Fiedler, A. Mitov, *The total top quark pair production cross-section at hadron colliders through* $\mathcal{O}(\alpha_s^4)$, Phys. Rev. Lett. **110**, 252004 (2013)

[149] M. Czakon, A. Mitov, *Top++: A Program for the Calculation of the Top-Pair Cross-Section at Hadron Colliders* (2011)

[150] J. M. Lindert, et al., *Precise predictions for V+jets dark matter backgrounds* (2017)

[151] A. Manohar, P. Nason, G. P. Salam, G. Zanderighi, *How bright is the proton? A precise determination of the photon parton distribution function*, Phys. Rev. Lett. **117(24)**, 242002 (2016)

[152] C. Schmidt, J. Pumplin, D. Stump, C.-P. Yuan, *CT14QED parton distribution functions from isolated photon production in deep inelastic scattering*, Phys. Rev. D **93**, 114015 (2016)s

[153] R. A. Fisher, *On an absolute criterion for fitting frequency curves*, Messenger of Mathematics **41**, 155 (1912)

[154] J. Aldrich, *R. A. Fisher and the Making of Maximum Likelihood 1912-1922*, Statistical Science **12(3)**, pp. 162 (1997)

[155] F. James, *MINUIT—A System for Function Minimization and Analysis of the Parameter Errors and Correlations*, Computer Physics Communications **10**, 343 (1975)

[156] A. Henrichs, *Precision Measurements of the Top Quark Pair Production Cross Section in the Single Lepton Channel with the ATLAS Experiment*, Ph.D. thesis, Göttingen U. (2012)

[157] A. L. Read, *Presentation of search results: the CL s technique*, Journal of Physics G: Nuclear and Particle Physics **28(10)**, 2693 (2002)

[158] ATLAS Collaboration, *Monte Carlo Calibration and Combination of In-situ Measurements of Jet Energy Scale, Jet Energy Resolution and Jet Mass in ATLAS*, Technical Report ATLAS-CONF-2015-037, CERN, Geneva (2015)

[159] ATLAS Collaboration, *Studies on top-quark Monte Carlo modelling for Top2016*, Technical Report ATL-PHYS-PUB-2016-020, CERN, Geneva (2016)

[160] ATLAS Collaboration, *Measurements of the production cross section of a Z boson in association with jets in pp collisions at* $\sqrt{s} = 13$ *TeV with the ATLAS detector*, Eur. Phys. J. **C77(6)**, 361 (2017)

[161] O. Lundberg, *Searches for Dark Matter and Large Extra Dimensions in Monojet Final States with the ATLAS Experiment*, Ph.D. thesis, Stockholm U. (2016)

[162] S. Ask, *Simulation of Z plus graviton/unparticle production at the LHC*, The European Physical Journal C **60(3)**, 509 (2009)

[163] J. Butterworth, et al., *PDF4LHC recommendations for LHC Run II*, J. Phys. **G43**, 023001 (2016)

[164] ATLAS Collaboration, *Search for Supersymmetry in events with b-tagged jets and missing transverse energy in pp collisions at* $\sqrt{s} = 13$ *TeV with the ATLAS detector*, Technical Report ATLAS-CONF-2017-038, CERN, Geneva (2017)

[165] S. Alioli, P. Nason, C. Oleari, E. Re, *A general framework for implementing NLO calculations in shower Monte Carlo programs: the POWHEG BOX*, JHEP **06**, 043 (2010)

[166] F. Kahlhoefer, K. Schmidt-Hoberg, T. Schwetz, S. Vogl, *Implications of unitarity and gauge invariance for simplified dark matter models*, Journal of High Energy Physics **2016(2)**, 16 (2016)

[167] G. Hinshaw, et al., *Nine-year Wilkinson Microwave Anisotropy Probe (WMAP) Observations: Cosmological Parameter Results*, The Astrophysical Journal Supplement Series **208(2)**, 19 (2013)

[168] A. Albert, et al., *Recommendations of the LHC Dark Matter Working Group: Comparing LHC searches for heavy mediators of dark matter production in visible and invisible decay channels* (2017)

[169] G. Busoni, et al., *Recommendations on presenting LHC searches for missing transverse energy signals using simplified s-channel models of dark matter* (2016)

[170] S. Frixione, *Isolated photons in perturbative QCD*, Phys. Lett. **B429**, 369 (1998)

[171] ATLAS Collaboration, *Jet energy measurement and its systematic uncertainty in proton-proton collisions at* $\sqrt{s} = 7$ *TeV with the ATLAS detector*, Eur. Phys. J. **C75**, 17 (2015)

[172] A. Denner, S. Dittmaier, T. Kasprzik, A. Mück, *Electroweak corrections to monojet production at the Tevatron and the LHC*, The European Physical Journal C **73(2)**, 2297 (2013)

[173] A. Denner, S. Dittmaier, T. Kasprzik, A. Mück, *Electroweak corrections to dilepton + jet production at hadron colliders*, Journal of High Energy Physics **2011(6)**, 69 (2011)

[174] D. Racco, A. Wulzer, F. Zwirner, *Robust collider limits on heavy-mediator Dark Matter*, JHEP **05**, 009 (2015)

[175] ATLAS Collaboration, *Readiness of the ATLAS Tile Calorimeter for LHC collisions*, Eur. Phys. J. **C70**, 1193 (2010)

[176] ATLAS Collaboration, *Approved Tile Calorimeter Plots*, https://twiki.cern.ch/twiki/bin/view/AtlasPublic/ApprovedPlotsTile

[177] ATLAS Collaboration, *Approved Plots Tile Calibration*, https://twiki.cern.ch/twiki/bin/view/AtlasPublic/ApprovedPlotsTileCalibration

[178] P. Jenni, M. Nessi, *ATLAS Forward Detectors for Luminosity Measurement and Monitoring*, Technical Report CERN-LHCC-2004-010. LHCC-I-014, CERN, Geneva (2004)

[179] ATLAS Collaboration, *Approved Tile Calorimeter Plots*, https://twiki.cern.ch/twiki/bin/view/AtlasPublic/ApprovedPlotsTileMinimumBiasSystem

[180] C. Fischer (ATLAS Collaboration), *Study of TileCal scintillators irradiation using the Minimum Bias integrators*, Technical Report ATL-TILECAL-PROC-2016-006, CERN, Geneva (2016)

Acknowledgements

I would like to take the opportunity and thank my supervisor Mario Martínez: Thanks for giving me the chance to work in this very interesting analysis and the possibility to work at CERN. Thanks for all the helpful discussions, your availability for those and numerous valuable inputs for the analysis that we have been a part of.
I would also like to express my gratitude to Arely Cortès Gonzalez: Without your help and competent advice and encouragement and almost unlimited availability you have provided the major building ground for a successful analysis, especially in the 2015 analysis. I was sorry to let you move on, but still, despite not being my responsible post-doc anymore, you were always open for questions and ready to help. A thousands thanks for this!
I also have to thank Remi Zaidan for supporting me in the 2016 analysis and polishing our input code ;). Thanks for your help as well and also thanks to Martin Tripiana for his open ears to software related questions and keeping our common framework in good shape.
I would also like to thank a few members of the monojet-team that I have been part of during the last few years: thanks to Olof and Gabriele for answering ADD related questions, special thanks to Maria Giulia and Giuliano for numerous cutflow comparisons and debugging sessions and the effort to make this analysis a successful one.

I am grateful (again ;)) to Andrea Knue: although far away and no responsibility for your former student anymore, you still always had an open ear to my sorrows. Thanks for the surprise present at the beginning of my PhD and cheering me up whenever needed! Thank you so much for sacrificing your time and proof-reading parts of this thesis. Your comments were, as always, very valuable to me.
I also cannot miss the opportunity to thank my office mates to make this time at IFAE a great experience: thanks to Roger for introducing me to the IFAE analysis, special thanks to Silvia, Arely and Andrea R. for contributing to some enjoyable time in the office despite the load of work that we all had.

Finally, I want to close this last part by thanking my friends and family: thanks for your support, your attempts to cheer me up in difficult times (sometimes succeeded ;)). Despite the distance, your encouragement was invaluable to me.
Na končno: Hvala za vse, Bojan! Thanks for helping me with some graphics for this thesis. Hvala za tvoj pomoč. Veselim se, da si na moji strani. Brez tebe, bi postala nora. Hvala za tvoje potrpljenje. Zdaj pridem k tebi.